Nearshore records of natural hazards of the past millennium, western Washington

Elizabeth J. Davis

A dissertation

submitted in partial fulfillment of the

requirements for the degree of

Doctor of Philosophy

University of Washington

2024

Reading Committee:

Juliet Crider, Chair

Brian F Atwater, Chair

Jody Bourgeois

Program Authorized to Offer Degree:

Department of Earth and Space Sciences

University of Washington

Abstract

Nearshore records of natural hazards of the past millennium, western Washington

Elizabeth J. Davis

Chairs of the Supervisory Committee:

Juliet Crider

Brian F Atwater

Department of Earth and Space Sciences

Since earthquakes cannot be predicted, assessment of earthquake and fault-related hazards relies on knowledge of fault behavior in historic and prehistoric times paired with models based on the physics of how faults work. Historic records of earthquakes in many parts of the world are limited; in these places, paleoseismology extends the earthquake record into the geologic past. In this dissertation, I used field geology and geomorphology at three sites in western Washington to identify, evaluate, and date evidence for earthquakes and lay groundwork for future paleoseismic studies. In chapter 1, submerged shorelines across the Seattle Fault Zone, a crustal fault that crosses Seattle, indicate that the fault produced earthquakes as large as M~7.5 only once in the past 11,000 years, a longer recurrence interval than used in current hazard estimates. In chapter 2, liquefaction records from the Duwamish estuary in Seattle contribute to the regional

earthquake catalog and demonstrate that liquefaction incompletely records regional earthquakes. In chapter 3, I mapped and dated a low-elevation terrace at Rialto Beach on the Pacific coast of Washington, one of many such terraces along the coast, that has been hypothesized to record tectonic uplift. I found that the terrace is ~600–200 years old and that neither formation by tectonic uplift nor formation by beach progradation can be ruled out. The stratigraphic framework developed at Rialto Beach and presented here can be used to evaluate the other terraces to test the hypothesis that these terraces formed via coseismic uplift during Cascadia subduction zone earthquakes. I also found that deep-seated landslides on the slope above the Rialto Beach terrace pre-date the terrace formation, which has implications for their potential use in paleoseismic studies. Findings from all three of these studies will contribute to growing catalog of paleoseismic data in Cascadia that are used to reconstruct earthquake histories and evaluate behavior of the megathrust and crustal faults.

Acknowledgments

Thank-you to my committee, Juliet Crider, Brian Atwater, Jody Bourgeois, Kathy Troost, Andrea Ogston, Harold Tobin, and Peter Lape. All chapters were guided by Juliet Crider and Brian Atwater. I am grateful for their patience, consistency, and wisdom, and for teaching me on all sorts of topics for many years. Thank you to Kathy Troost for inspiration, facilitation, and critiquing my ideas and observations in the field. Thank you to Jody Bourgeois for helping me refine my ideas and writing. Carrie Garrison-Laney was an ongoing source of information, field help, and support. She taught me to clean radiocarbon samples and calibrate the results. Kelsay Stanton read several early drafts. Research and writing groups led by Juliet Crider, Andrea Ogston, and Galya Diment provided helpful reviews of ideas, figures, and text and true community at UW. The remaining mistakes and final interpretations are my own.

These projects have been funded by the University of Washington Department of Earth and Space Sciences, the USGS Earthquake Science Center, the Quaternary Research Center at the University of Washington, the University of Washington M9 Project, the North Pacific Coast Marine Resources Committee, and a P.E.O. Scholar Award.

Chapter 1: This chapter builds on unpublished work from around the early 2000s, including field surveys by Brian Atwater and diatom paleoecology by Eileen Hemphill-Haley. Contributors to those field surveys included Walter Barnhardt, Judith Boughner, Taber Hersum, John Shulene, and Richard Stewart. Kathy Troost provided lab space for preparing radiocarbon samples. Ric Gordon facilitated our access to field sites. The USGS funded radiocarbon ages.

Chapter 2: Ralph Haugerud identified the features and hypotheses I examine and test in this chapter. This work was funded by the U.S. Geological Survey under grant No. G19AP00036 to PIs Emily Roland and Juliet Crider. Emily Roland taught me to develop the seismic survey and process and interpret the results. Ginevra Moore showed me how to process CHIRP data. Dave Thoreson adapted the R/V Weelander for our study and drove the boat along our tedious survey, “mowing the lawn” of Elliott Bay with a new joke ready every hour and zero complaints. Luke Maddux and Kevin Pszczola were essential during collection the seismic data.

Chapter 3: Kathy Troost, Jon Riedel, and Brian Sherrod inspired the line of investigation undertaken in this chapter. Kathy Troost deserves credit for leading and acquiring funding for a multi-year interdisciplinary field campaign at Rialto Beach that has resulted in several MS capstone projects and this dissertation chapter. This project was funded by the North Pacific Coast Marine Resources Committee (MRC). The USGS and Quaternary Research Center at the University of Washington contributed funds for chronology. Test pits and sample collection were permitted by Olympic National Park with the help and support of Matthew Dubeau and Dave Conca of Olympic National Park. Some of the radiocarbon samples described in Ch. 3 were collected and cleaned by Elise Freeman, Chelsea Bush, Kathy Troost, and Mary Alice Benson. Work at Rialto Beach would not have continued without the enthusiasm and material support of Jill Silver and the 10,000 Years Institute in Forks, Washington. Thank-you to Tami Pokorny for sustained interest and facilitation of the project. Thank-you Jill and Tami, and Kathy, Chelsea, Elise, Mary Alice, Monica, Jim, Roger, Sam, and Kevin, for your friendship and for making our trips to Rialto so bright.

Field geology is not accomplished alone. These data would not have been collected without the help, camaraderie, and insights from the following people, who dug holes, surveyed in the rain, drug the canoe, entertained passerby, bushwhacked up gullies, and weathered early mornings, mistaken shortcuts, broken paddles, unstable trees, unseaworthy captains, and more. Thank-you Alyssa Tunnelle, Johnny Paige, J. Padgett, Kevin Cowell, Matt Porter, Tina Andry, Lucas Fifer, Mark Molinari, Nancy Sackman, Kelsay Stanton, Chelsea Bush, Elise Freeman, Roger Troost, Morgan Simon, Ian Miller, Jessie Pearl, Brian Sherrod, Evan Lahr, Zach Yakush, Ginevra Moore, Rick Minor, Megan Mueller, Kalpana Prasad, Jon Rowe, Helena Pfluger, Mary Alice Benson, Sam Bartish, Monica Hill, Jim Miller, Patricia Jessica, Jill Silver, Jonny Parish, David Graham, Juliet Crider, Virginia Davidson, Marquis Richardson, Olivia Fraser, Mary Orrand, Heather Maran, Hannah Greaney, Graham Johnson, Zachary Levitan, Louis Levy, and Mason Steinbrueck.

Table of Contents

List of Figures

List of Tables

Chapter 1. **Submarine terraces in Puget Sound indicate only one M > ~7.5 earthquake on the Seattle fault zone in the past 11,000 years**

ABSTRACT

Submerged marine terraces in Puget Sound, deformed across the Seattle fault zone, indicate that only one earthquake as large as M ~7.5 has occurred in the past 11,000 years. The Seattle fault zone (SFZ), which crosses the city of Seattle, produced a M~7.5 earthquake 923–924 CE, raising coastlines south of the SFZ by as much as ~8 m and resulting in a regional tsunami, landslides, and liquefaction. Marine terraces, now submerged in Puget Sound, are attributed to a late-glacial sea level lowstand ending at about 11 ka. Here I show that these submerged terraces record both glacial isostatic rebound and tectonic deformation across the SFZ. Offset of the 11 ka terraces within the SFZ is similar to the 1100-year-old wavecut platforms, precluding more than one large (M ~7.5) earthquake on the Seattle fault zone in the past 11,000 years. Current hazard estimates allow for a 5000-year recurrence interval for events M>7.1. My results that limit M~7.5 events to one earthquake in the past 11,000 years add specificity to the recurrence estimate. The terrace offsets are also consistent with continuous, but not uniform, block uplift between the Seattle and Tacoma fault zones.

1.1 INTRODUCTION

Worldwide, shallow crustal faults present major hazards. Recent earthquakes on blind crustal faults have resulted in substantial damage and loss of life; e.g., in Northridge, California (1994); Kobe, Japan (1995); Christchurch, New Zealand (2011); and Eastern Turkey (2011 & 2023). Current efforts to address these hazards frequently rely on earthquake recurrence intervals as an expression of the frequency of past earthquakes and thus the probability of future earthquakes. Recurrence intervals simplify complex rupture histories and risks presented by faults into probabilities that can be interpreted in systematic ways. In the U.S., recurrence intervals for individual faults inform National Seismic Hazard maps (Petersen et al., 2023) which forecast the probability that earthquake shaking reaches certain thresholds. These maps regulate building codes and inform emergency plans.

For faults with low slip rates, and especially for blind faults, long-term recurrence intervals are challenging to estimate. Paleoseismic methods have been employed to estimate earthquake recurrence, including trenching fault scarps to identify offset produced during individual earthquakes (e.g., Scharer et al., 2017), evaluating and dating shaking proxies like lake or submarine turbidites (e.g., Moernaut et al., 2017; Goldfinger et al., 2012), liquefaction (e.g., Tuttle, 2001; Tuttle et al., 2017), and landslides (e.g., Struble et al., 2020, Herzig et al., 2023), and mapping deformation of geomorphic features to extract long-term deformation histories (e.g., Rockwell et al., 1988).

Geomorphic features that record crustal deformation include emerged and submerged marine terraces, which exist worldwide and are commonly used in fault studies. Marine terraces are flat or gently sloping platforms cut by marine erosion or constructed by shoreline sediments, and they record periods of relatively stable sea levels (Bradley and Griggs, 1976). Folding, warping, or other deformation of terrace surfaces have been attributed to tectonics in many settings, including coseismic uplift in Alaska (Plafker & Rubin, 1978), Quaternary fold growth in California (e.g., Rockwell et al., 1988), interseismic uplift in southern Chile (Jara-Muñoz and Melgar, 2015), and folding over blind faults in Italy (Santoro et al., 2013). Submerged marine terraces, while more difficult to study, have also been used. Most studies focus on bathymetric benches interpreted as erosional marine terraces of Pleistocene sea level lowstands (e.g., Emery,

1958; Johnson et al., 2014; Jara-Muñoz et al., 2017) and attribute differences in depth to tectonic deformation.

In this study, I use the relative elevation of submerged terraces to extract an 11,000-year deformation history of the Seattle fault zone (SFZ) at Seattle. A large SFZ earthquake would be devastating to the city of Seattle and surrounding urban areas. Despite much study, the structure of the fault zone and recurrence of its earthquakes are not well understood. This is because the fault zone is structurally complex and because it is obscured by thick glacial deposits, urbanization, vegetation, and waterways. Current hazard estimates allow for two M>7.1 earthquakes on the fault in the last 10,000 years (Petersen et al., 2023; Frankel et al., 1996 citing personal communication with R. Bucknam, 1996). Here, I propose a longer recurrence interval for the largest known events on the fault zone (M~7.5). I map and quantify fault-related offset of submerged marine terraces that limit deformation to only one M~7.5 earthquake in the past 11,000 years.

1.1.1 Geologic and tectonic setting

The submerged marine terraces studied here are located in Puget Sound, in the forearc basin of the Cascadia subduction zone (Fig. 1.1A). Puget Sound sits in a topographic and structural low between the Olympic mountains coast range and the Cascade volcanic arc. North-south shortening of the Puget Lowland (McCaffrey et al., 2007) is accommodated on several thrust or oblique faults that divide the Puget Lowland into fault-bounded uplifts and basins (Pratt et al., 1997; Brocher et al., 2001; Blakely et al., 2002). These faults generally trend northwest-southeast and include the Seattle fault zone, which crosses the city of Seattle (Fig. 1.1B). Slip on the Seattle fault has juxtaposed Tertiary marine and volcaniclastic bedrock on the south side of the fault with a deep basin of Quaternary sediments to the north (Troost and Booth, 2008). The Seattle fault zone bounds the northern edge of the Seattle uplift, a structural horst that extends south to the Tacoma fault zone and west to the Saddle Mountain fault (Pratt et al., 1997).

Despite representing a major seismic hazard, many questions remain about the structure of the Seattle fault zone and its earthquake hazard. The SFZ is complex and surface indicators are partially obscured by water, sediment, and urban land modification. Thus, major questions

remain about the locations of individual faults, their structures, and the style and recurrence of possible earthquakes. Geophysical studies from the past several decades (e.g., Pratt et al., 1997; Johnson et al., 1999 and 2002; Pratt et al., 2015; Moore et al., 2022) indicate that at least three north-vergent thrust strands exist at depth (Fig. 1.2). Slip on these main thrusts produces broad surface folding that raises the bedrock south of the fault and drops bedrock north of the fault. This fold is dissected by laterally discontinuous antithetic south-vergent thrusts ("backthrusts") that break the surface. Uncertainty remains about the structure of the SFZ, including the interaction between blind thrusts and smaller backthrusts.

There is an abundance of geologic evidence for one rupture along a main thrust of this fault in the winter of 923–924 (Black et al., 2023). This event, known as the Restoration Point earthquake, produced a M 7.5 earthquake (magnitude estimated by ten Brink et al., 2006; Styron and Sherrod, 2021) that uplifted shorelines around Puget Sound. This earthquake is also blamed for triggering a tsunami in Puget Sound (Atwater and Moore, 1992), large block landslides that dropped hillside forests into Lake Washington (Karlin and Abella, 1992), rockfalls in the Olympics (Schuster et al., 1992), and liquefaction around Puget Sound (Bucknam et al., 1992; Jovanelly and Moore, 2009; Whisler et al., 2002; Bourgeois & Johnson, 2001; Sherrod, 2001; Sherrod et al., 2004; Barnhard and Sherrod, 2006; Martin, 2011; Martin & Bourgeois, 2012). Careful radiocarbon dating and tree ring width pattern matching have indicated that the tsunami and landslides were coincident and assigned an age to these effects, and therefore the earthquake: 923–924 CE (Atwater and Moore, 1992; Atwater, 1999, Black et al., 2023).

Evidence for uplift in similar time ranges comes from marshes at Burley and Oakland Bay (Bucknam et al., 1992), Lynch Cove (Bucknam et al., 1992 and Garrison-Laney, 2017), and Gorst (Arcos, 2012), and elevated beaches have been mapped in geologic maps as far south as the Tacoma fault zone (Tabor and Booth, 2017; Tabor, et al., 2014). However, paleoseismic studies using coastal terraces to constrain structural models have used terraces only as far south as the northern tip of Vashon Island. The Restoration Point earthquake occurred within a 6-month period of an earthquake on the Saddle Mountain fault (Black et al., 2023); these events also fall within the time estimate for an earthquake on the Tacoma fault zone (Nelson et al., 2014).

1.1.2 Emerged marine terraces in the Seattle fault zone

Emerged marine terraces along the coast of Puget Sound provided geologic evidence for recognizing the Restoration Point earthquake, and these onshore terraces provide a basis for comparison with the submerged terraces described and evaluated here. These emerged terraces are seaward-sloping bedrock platforms that truncate steeply dipping beds of Tertiary sediments and have been mapped up to eight meters above modern sea-level (e.g., Waldron, 1967; Yount et al., 1985; Gower et al., 1985; Troost et al., 2005, Ota et al., 2006). The bedrock platforms were described in detail by Bucknam et al. (1992), who first attributed their emergence to tectonic uplift in the SFZ. Because the most conspicuous terraces appear to be continuous, this uplift was interpreted to have occurred during one blind thrust earthquake. Gradual emergence or multiple events separated by time are unlikely to have raised the shorelines. The surfaces of the bedrock terraces, which are ridged with continuous, steeply dipping beds of sandstone and mudstone, lack erosional features that are likely to have formed if uplift were slow or punctuated. One of the best exposures of this terrace wraps around Restoration Point on Bainbridge Island (Fig. 1.3).

Several researchers have used the pattern of deformation on the emerged marine terraces to define a fold and evaluate the structure of the SFZ. Back edges (the up-dip inflections on these terraces, also known as shoreline angles) are typically used as markers of MSL (mean sea level) within a few meters (Lajoie, 1986). In Puget Sound, Ota et al. (2006) measured modern shoreline angles to rest between 1 and 1.5 m above modern MSL (Fig. 1.4). ten Brink et al. (2003) showed that 20 terrace elevations derived from field observations (mostly those of Bucknam et al., 1992) were not well-fit by rupture on one or more south-dipping reverse faults and required more complicated near-surface geometries including antithetic backthrusts. ten Brink et al. (2006) tested four different structural models involving slip on both blind main thrusts and antithetic backthrusts, preferring a roof-thrust geometry that includes slip on main thrusts at depth and secondary backthrusts at the surface. Ota et al. (2006) measured additional coastal terrace elevations at 97 sites from LiDAR and field levelling to define a zone of deformation rising to 8.5 m above MSL, defining a complex folded surface within the Seattle fault zone (Fig. 1.5). Measurements extended to at most 8 km south of the deformation front on both sides of Puget Sound and crossed several locations where the surface was dissected and deformed by the north-facing scarps thrusts and associated localized raised surfaces. Muller and

Harding (2007) demonstrated an automated process for mapping terrae elevations in West Seattle, and mapped a nearly continuous swath of deformation using updated LiDAR to define a fold with an amplitude of 5 m. Pratt et al. (2015) used slip modeling to reach a different interpretation of the structure than ten Brink et al. (2006): that the pattern of uplifted terraces and subsidence north of the fault requires slip on the main thrusts near the surface. Moore et al. (2022) interpreted shallow seismic CHIRP to produce a new structural model that involves northward propagation of the active thrust strand over time.

The emerged terraces that define the surface of the fold are offset across at least three backthrusts (Ota et al., 2006; Kelsey et al., 2008; Nelson et al., 2014), suggesting that these faults ruptured either during fold growth or subsequently. Paleoseismic trenches across the backthrusts suggest that these smaller faults slipped independently from both each other and from slip on the deeper main thrust(s) (Nelson et al., 2003a). Trenches suggest slip on different backthrusts up to 5 times in the past 3500 years (Nelson et al., 2014), with different faults and different trenches on the same fault recording different slip events.

Earlier slip on some of these faults may also be recorded in the emerged coastal marine terraces. Kelsey et al. (2008) used LiDAR and field mapping, including leveling and soil augers, to map three terrace segments above the Restoration Point earthquake fold surface, each of them north of a north-side-up backthrust. These terrace segments are truncated by the Restoration Point platform and interpreted as evidence of localized backthrust rupture prior to 923–924 CE.

In this study, I identify submerged marine terraces and argue that they are substantially older than the emerged marine terraces uplifted by the Restoration Point earthquake. I then use the submerged terraces as a structural datum from which I extract fault-related deformation.

1.1.3 Glacial and sea-level history

The presence of submerged marine terraces in Puget Sound can be attributed to a regional post-glacial sea-level lowstand. Understanding the characteristics and timing of this lowstand is essential to using it as a structural datum.

At least six Pleistocene glaciations have reworked the topography and materials in the Puget Lowland, modifying landforms and depositing and removing sediments (Troost and Booth, 2008). The most recent glaciation, marine isotope stage 2, is locally called the Vashon stade of the Fraser glaciation (Armstrong et al., 1965). Here, a broad tongue of the Cordilleran ice sheet, known as the Puget Lobe, filled the Puget Lowland (Bretz, 1913). The maximum ice extent of this Puget Lobe stretched south of the current location of Olympia, Washington, and likely occurred between 16,000 and ~14,500 cal. yr BP (Haugerud, 2020).

Glacial retreat was accompanied by dramatic changes in relative sea level (RSL) in Puget Sound (Fig. 1.6). Relative sea-level at any given site and time reflected the interplay between glacial isostatic rebound and eustatic global sea-level change. Glacial isostatic adjustment models have been constructed for Puget Sound that use physical properties of Earth's structure to model RSL response to geologically inferred ice histories (e.g., Yousefi et al., 2018; Yousefi et al., 2021). Though model outputs vary depending on the input ice history and model structure, all published models for Puget Sound show a rapid RSL fall upon deglaciation until about 14 ka, followed by relatively stable sea levels below -50m between ~14 ka and ~11 ka, followed by monotonic RSL rise until sea-levels stabilize near their present height around ~6 ka (Appendix 1.1). Farther north, sea-levels start higher and fall to a later and higher lowstand before rising to present levels (Fig. 1.6). For the past 15 ka, all sites show an initial high RSL tens to >100 m above modern (Figure 1.6; James et al., 2009; Haugerud, 2017), followed by initial rapid RSL fall as isostatic rebound outpaced eustatic sea-level rise. As local isostatic rebound began to slow, sea-level fall also slowed, reaching a lowstand below modern sea-level in the late Pleistocene-early Holocene. Once the rate of eustatic sea-level rise outpaced the slowing rate of isostatic rebound, RSL began to rise, stabilizing in the mid-Holocene.

The late Pleistocene-early Holocene lowstand has been inferred to have produced the submerged shorelines in Puget Sound, which I map and evaluate herein. These features, identified by Haugerud (2017) in Puget Sound (as well as by Mosher and Hewitt (2004) in the Strait of Juan de Fuca), consist of flat benches around 60 m depth (Fig. 1.3) that can be traced across Puget Sound from at least Whidbey Island to south of Tacoma (Fig. 1.4). Their depth persistence and presence across Puget Sound on offshore land underlain by both bedrock and glacial deposits

supports the interpretation that these features were formed by a sea-level stillstand and not by localized processes or geologic contacts. Haugerud (2017) used the depths of these shorelines at Seattle to bound the lowstand elevation of the Seattle sea-level curve (Fig. 1.6). This lowstand would have occurred ~15-11 cal ka BP: after deglaciation but before eustatic sea-level rose higher than 55 m (Lambert et al., 2014).

If these shorelines represent a sea level from a period >11,000 years ago, the amount of deformation in the shorelines across the SFZ ought to record the number of earthquakes that have occurred. Thorson (1981, 1989, 1993) used this framework in the Puget Lowlands, measuring the elevations of glacial lake shorelines (13.5-14 ka) and estimating 7 +/- 2 m of offset across the SFZ. Thorson (1996) expanded this analysis to include the contact between glacial lake and advance outwash sediments (15-18 ka) to find 8-14 m of offset. Haugerud (2017) proposed the use of sea-level lowstand shorelines (ca. 11 ka) in this way and tested the idea using nine shorelines, noting an apparent 8 m of offset across the SFZ. The submerged shorelines may have been created any time 14–11 ka. The lowstand need not have produced completely isochronous features, as rebound rates may have varied. For the purposes of discussing earthquake recurrence, I select 11 ka as the minimum age for the shorelines. Here, I map over 60 such shorelines across the Seattle fault and extract over 150 elevation profiles to compare their deformation with the emerged marine terraces raised by the last known large earthquake, the Restoration Point earthquake.

1.2 METHODS

In this study, I mapped submerged terraces in Puget Sound, attributed them to the sea-level lowstand ending about 11,000 years ago, and measured their deformation across the Seattle fault zone. I then compared this deformation with deformation recorded in the onshore emerged terraces that occurred during the Restoration Point earthquake.

1.2.1 Datasets

1.2.1.1 Bathymetry

I used 72 publicly available bathymetry datasets (.bag files) from NOAA National Ocean Service (NOS) for central Puget Sound. The grid sizes of the datasets vary from <1 m to 16 m, with all

datasets increasing in grid size with depth. Datasets were layered in ArcGIS with the highest resolution on top, stitched together to a 1m x 1m grid size, and contoured. Depth uncertainty of bathymetric layers constitutes the 2nd band of the original rasters, and across the terraces studied ranges from <0.1 m to 1.5 m.

1.2.1.2 CHIRP seismic reflection data

CHIRP seismic reflection data were collected by Emily Roland, Juliet Crider, Ginevra Moore, and myself in October, 2019 aboard the R/V Weelander, a 15-ft vessel operated by the University of Washington School of Oceanography. The survey was collected with an ultra-high resolution, 2-16 kHZ Edgetech 216s CHIRP system and crossed Elliott Bay, the Duwamish Waterway, and terraces offshore Bainbridge Island. Data were processed using a standard CHIRP processing workflow that included heave correction and conversion to envelope. After processing, the data were collected in an interpretation project along with complementary datasets using the IHS Kingdom Suite software. One seismic line is used in this project; it is shown in Appendix 1.3.

1.2.1.3 Legacy seismic reflection data

Seismic mini-sparker data were collected aboard a UW student cruise (R/V Onar 1001 in April, 1982) led by UW Oceanography professor and USGS scientist Mark Holmes. The data, which have not been published except for a few strands found in Loeffler et al. (1989), are printed on paper scrolls and are accompanied by a paper location map (Appendix 1.3). Depths had been written on the seismic lines.

1.2.1.4 Onshore LiDAR

I compiled public LiDAR datasets from the Washington DNR LiDAR Portal. These comprised DTMs and hillshade datasets from 2018 and 2020 which I used to create slope and contour maps.

1.2.2 Mapping terraces

1.2.2.1 Submerged terraces

Submerged terraces were mapped manually in ArcGIS using a 3 m contour laid over hillshade imagery from NOAA NOS. Terraces were defined as relatively flat areas bounded by a back

slope and front slope. Some areas in Puget Sound are flat and smooth but were not classified as terraces--for example, the floor of the main basin of Puget Sound.

1.2.2.2 Onshore terraces

I digitized boundaries of onshore emerged terraces in ArcGIS, guided by published geologic maps and papers where investigators undertook field mapping (Ota et al., 2006; Kelsey et al., 2008; Troost and Booth, 2005; Waldron, 1967; Yount et al., 1985; Gower et al., 1985; Tabor and Booth, 2017; Tabor et al, 2014). Where boundaries were unclear from these publications, or the updated LiDAR shows an obvious other feature, I based the mapping on a slope map and contours constructed from Lidar data. I avoided obvious cuts or fills and road grades where they diverge from surrounding topography. I did not field check any of the mapping.

I compared submerged terraces with onshore terraces by subtracting amounts of uplift attributed to the Restoration Point earthquake from the depths of co-located submerged terraces. Many researchers have mapped the uplifted coastal shorelines, which lie adjacent to and above modern beaches on both sides of Puget Sound, south of the Seattle fault deformation front. Amongst these, Ota et al. (2006) mapped shorelines in LiDAR imagery, measuring back edge elevations at 97 points, and ground-truthing a subset of those point elevations.

The dataset produced by Ota et al. (2006) provides the best spatial coverage for a direct quantitative comparison with the submarine data; I compared the other datasets qualitatively. Ota et al. (2006) mapped shorelines on both sides of Puget Sound, including Bainbridge Island and Waterman Point in the west and from Alki Point to south of Lincoln Park in the east (Fig. 1.4). They were careful to measure shoreline elevation away from colluvium at the slope toe and estimated a LiDAR error of +/- 30 cm. (For some shorelines, they also surveyed elevation with a level; here, I use only their measurements from lidar.) These measurements cross the main fold above the SFZ and are offset across multiple back thrusts: west end of Toe Jam Hill fault (Fig. 1.3), Point Glover fault, Waterman Point fault, and West Seattle fault (Kelsey et al., 2008; Nelson et al., 2014).

1.2.3 Measuring profiles and back edge depths

In order to use terraces as sea-level indicators, it is necessary to extract the elevation of the back edge of each terrace, where the inferred former shore platform meets the inferred seacliff of bluff above—that is, the "back edge," or shoreline angle. In order to estimate the depths of submerged terraces, I drew slope profiles across each submerged terrace, perpendicular to the slope, spaced 100–200 m apart. Where possible, I drew several profiles across each terrace.

Back-edge depths were measured at the concave inflection point at the base of the slope, which I picked manually (Fig. 1.7), and sediment thickness at that point was estimated to produce a "true depth" to the bedrock shoreline angle. Because this inflection point is more apparent in some profiles than in others, I estimated a vertical picking error for each back edge measurement. These errors range from 0.5 m to 5 m, with most picking errors being 1–2 m. I estimated thickness of sediment cover over the back edge of the terrace using seismic reflection data, available at two locations in the study area. CHIRP data collected by the authors crossed one terrace; another terrace was crossed by legacy seismic minisparker data collected by UW Oceanography. I formally propagated uncertainties in back edge depth due to picking, the uncertainty in the bathymetric dataset, and uncertainty in sediment cover thickness; the calculations are described in Appendix 1.4.

1.2.4 Comparing onshore and offshore datasets

Comparing the back edge elevations of onshore terraces with the back edges of submerged terraces required several conversion steps, which I outline below. The final goal was to subtract the amount of onshore deformation from the submerged shoreline elevations in order to evaluate how much deformation could be accommodated by the submerged shorelines. First, in order to convert the elevation of onshore back edges to offset, I assumed all of the shoreline angles (emerged and submerged) formed at approximately MSL (Ota et al. (2006) measured modern shoreline angles to sit 1–1.5 m above MSL). Then, I calculated the offset of each emerged terrace from current MSL, to use this offset as the record of tectonic deformation at each terrace. This amount of offset records both the tectonic deformation and any other net sea-level change over the past few thousand years. The next step was to compare the amount of offset recorded by the onshore terraces with the amount of offset in co-located submerged terraces. Since

onshore and offshore data points were not co-located, I projected both datasets onto a line perpendicular to the SFZ deformation front, and linearly interpolated offset values from the onshore dataset to points co-located with the offshore dataset. This produced two datasets co-located with respect to their distances from the SFZ deformation front; the results of this interpolation are shown in Appendix 1.5. Finally, I subtracted the amount of deformation recorded by the emerged terraces from the depth of the submerged terraces.

1.3 RESULTS

1.3.1 Results of mapping

Submerged terraces are distributed across Puget Sound (Figure 1.4). While individual terraces exist at many depths, and as deep as 172 m, 80% of the mapped terrace surfaces lie above 64 m depth, with 52% of the surfaces resting between 64 m and 25 m deep. Depths to each pixel of mapped terraces are shown in a histogram in Appendix 1.2. The rest of the descriptions focus on terraces only in the 66–25 m depth range.

The mapped terraces are 100–200 m wide with the widest extending more than 800 m along the edge of the slope. They are typically located approximately 500–700 m from the current shoreline, and are ubiquitous on both flanks of Puget Sound, especially within and south of the Seattle fault zone.

1.3.2 Morphology of profiles

Slope profiles across the submerged terraces are morphologically similar (examples are shown in Fig. 1.7; all profile locations are shown in Supplementary Figure 1; data from all the profiles are available as .txt files in the Data Supplement). The seafloor falls from the modern shoreline at various rates to meet a smooth, comparatively flat terrace surface. Terrace surfaces are characterized by a gentle seaward slope (mostly 1-6˚, up to 9˚) with a sharp break in slope at the seaward edge. Below this break, slope morphology varies considerably, descending into the main basin of Puget Sound, which is about 200 m deep. While some of the slope profiles fall steeply in concave profiles to the terrace surface, meeting at an obvious inflection point, others fall gently, forming a convex profile before approaching the terrace surface. Sediment cover on

the profiles, as interpreted from seismic reflection lines, changed the elevation of the inflection point by at most 3 m.

1.3.3 Longitudinal distribution of back edge depths

In order to identify whether submerged terraces are offset across the SFZ, I projected depths to the back edge of terraces on a northeast-southwest transect perpendicular to the trend of the SFZ deformation front (Fig. 1.8). The trend of the deformation front is complex and varies from east to west; I estimated the trend of the fault zone where it crosses Puget Sound by a line between Alki Point and Restoration Point (referred to here as "distance from Alki Point"). Coordinates with respect to this datum are shown in Figure 1.4.

Depths to back edges in profiles on adjacent terraces are persistent; they typically vary by less than 5 m (within uncertainty) (Fig. 1.8). Clusters of points along the transect reflect adjacent profiles drawn across the same terrace. For example, the cluster of three points at -15 m from Alki Point along the east margin of Puget Sound represent three profiles drawn across the same terrace. Adjacent clusters, and therefore adjacent terraces, also tend to be similar in elevation. The spatial distribution of depth points on the east and west margins of Puget Sound reflects the distribution of the terraces. For example, terraces are absent north of the SFZ on the west flank of the Sound but are present on the east flank of the sound (Fig. 1.4).

1.3.4 Depth trends outside of and within the SFZ

Depths to the back edges of terraces are different outside of the SFZ than they are within it (Fig. 1.8). Below, I discuss the depths to the terraces in three sections: those north of the SFZ deformation front, those within the zone of previously mapped SFZ deformation, and those south of the deformation zone.

North of the deformation front, back edges range in depth from a maximum of -65.5 m depth to a minimum of -37 m depth (Fig. 11). Terraces systematically decrease in elevation at between 0.22 and 0.3 m/km. The best-fit line slopes at 0.27 m/km. All the linear models tested including fit statistics, are shown in Appendix 1.6. I follow prior workers (e.g., Thorson, 1981; Haugerud et al., 2017; Haugerud, 2020) and interpret this slope to represent differential glacial isostatic

adjustment since the formation of the terrace surface. The slope of 0.27 m/km is roughly one-third of the 1 m/km rule-of-thumb proposed by Thorson (1981) to account for post-glacial rebound of older surfaces. James et al. (2000) found 0.78 m/km over a different distance interval with some corrections for the SFZ.

Within the SFZ, on both flanks of Puget Sound, back edges of the submerged terraces are well above the glacio-isostatic trendline defined by the more northerly points (Fig. 1.8). Back-edge depths within the SFZ range from -25.6 m to -59 m (with the exception of the anomalies discussed below). The points on both sides of Puget Sound lie 6–9 m above the glacio-isostatic trendline, though uncertainties allow for a distribution 0–11 m above the trend. More than of 10 km south of the datum, on both sides of Puget Sound, depths to terraces are more scattered, but remain largely elevated above the glacial isostatic trend line. This is about the same latitude that the levels of onshore terraces stabilize around 2 m above sea level and are no longer used in fault reconstructions.

Terraces are shallower within the fault zone on both sides of Puget Sound, but the pattern of deformation is different on the east vs. the west flanks of the sound (Fig. 1.8). On the east side, the shallowest terraces are located between 0 km and 5 km south of the deformation front, while on the west side they shallow farther north: between -3 km and 5 km south of the datum.

1.3.5 Anomalies

Three terrace measurements on the east margin of the sound are anomalously deep: near and below 60 m depth (Fig. 1.8, x = -10.4 km). The profile at -10.4 km with respect to Alki Point (profile e37 in the Data Supplement) is located on the edge of a terrace and may not capture the back edge; the location was noted as low confidence during mapping. An adjacent profile crosses the same terrace more squarely and has a picked depth of -50 m. Profiles at -2.76 km and 2.8 km with respect to Alki Point (profiles e69bay and e70bay, respectively, in the Data Supplement) were drawn across a knickpoint on a possible drumlin in Elliott Bay. This knickpoint may not represent a marine terrace.

1.4 DISCUSSION

1.4.1 Submerged terraces as a Puget Sound sea-level indicator about 11 ka

The ubiquitous presence of submarine terraces around a consistent depth throughout Puget Sound, and the lack of other terraces at different depths, suggests that these features can be attributed to a regional, rather than localized, phenomenon. I agree with the interpretation of these features as stranded shorelines (Haugerud et al., 2017; Haugerud, 2020) and that substantially low sea levels, like those that closely followed deglaciation, would be required to form them.

Since the most recent time sea-level was relatively steady and lower than modern was more than 11,000 years ago, I infer that the terraces are at least 11,000 years old. While earlier sea-level lowstands likely occurred under similar conditions during the earlier 6+ glaciations in Puget Sound, every subsequent glaciation reworked the landscape, making the most recent glaciation the most likely candidate for forming preserved features across the Sound. This means that while earlier ages for lowstands that formed the terraces cannot be ruled out, the most likely timing for the lowstand would be the end of the most recent glaciation.

1.4.2 Submerged terraces as recorder of glacio-isostatic adjustment

Submerged shorelines of the post-glacial lowstand may be used to evaluate how much rebound occurred since the shorelines formed. Submerged terraces in Puget Sound, like onshore terraces in Whatcom county (Kovanen et al., 2020) and glacial lake shorelines (Thorson, 1981), are higher to the northeast than in the southwest. All lines fit to submerged shoreline depths north of the SFZ deformation front slope up to the NE; the best-fit does so at a rate of 0.27 m/km (Fig 1.8; Appendix 1.6). This is about a third of the estimate for the older glacial lake shorelines and highstand shorelines farther north. The submerged terraces were cut ~2000 years after the glacial lake shorelines (Thorson et al.,1989), during which GIA was already occurring (Yousefi et al., 2021). If this trend reflects GIA, it would be consistent with a slowing of adjustment as isostatic rebound decayed with time, a smaller magnitude of adjustment to the south, or both. The submerged terraces have not been independently dated; therefore, they can be used to constrain magnitudes of RSL GIA models but not timing.

1.4.3 Submerged terraces as a recorder of tectonic deformation

Terrace depths diverge upward from the linear trendline south of the Seattle fault zone (Fig. 1.8); I interpret this divergence to record tectonic uplift.

1.4.3.1 The distribution of submerged terrace depths within the SFZ can mostly be accounted for by uplift during the 923–924 CE Restoration Point earthquake

Within the Seattle fault zone, submerged terraces appear to define a folded surface (Fig. 1.8), similar in form and amplitude to the fold traced by the subaerial wavecut platform (Fig. 1.5). If submerged shorelines were offset by more than one Restoration Point-style earthquake, they ought to be deformed at magnitudes notably greater than coastal terraces uplifted in 923–924 CE.

This is not the case; most submerged terraces are offset by similar amounts within the SFZ as their onshore counterparts. With the exception of six points ~5 km south of Alki Point on the east margin of Puget Sound (which are discussed below), within the Seattle fault zone depths of submarine terraces align to the GIA datum once deformation from the Restoration Point earthquake has been removed (Fig. 1.8). If the equivalent of two Restoration Point earthquakes is subtracted from the elevation of the submerged terraces, the points fall well below the GIA datum. This suggests that no two such deformation events have occurred; the Restoration Point was unique in magnitude and spatial extent of deformation since the formation of the submerged terraces around 11 ka.

1.4.3.2 Offsets of submerged terraces indicate no uplift in Seattle north of Alki Point during Restoration Point earthquake

Published studies disagree about the northernmost extent of Seattle fault deformation where the fault crosses Seattle. Initial interpretations of seismic reflection lines (e.g., Pratt et al., 1997; Johnson et al., 1999) mapped the northernmost fault south of downtown Seattle, running through south Seattle and near Alki Point. Blakely et al. (2002), based on aeromagnetic anomalies and geology in combination with the earlier seismic reflection data, place the northern thrust about a kilometer farther north based on aeromagnetic anomalies and geology in combination with the earlier seismic reflection data. Pratt et al. (2015) interpret new seismic reflection data to place the frontal thrust even further north, through downtown Seattle.

Both Blakely et al. (2002) and Pratt et al. (2015) place one or more thrusts north of Alki Point. However, submerged terraces suggest that folding has not occurred this far north on the west side of Puget Sound since deglaciation, a finding consistent with elevations of glacial contacts (Thorson, 1996). The lack of deformation suggests that, at least in the most recent event, deformation did not occur adjacent to these proposed fault placements.

1.4.3.3 Offsets of submerged terraces are consistent with fault segmentation across Puget Sound

Submerged terraces permit right-lateral tear faults with offsets of > 1 km in Puget Sound. Johnson et al. (1999) interpreted from seismic reflection data two right lateral tear faults in Puget Sound that offset the Seattle fault deformation front by several kilometers. Based on continuity of gravity anomalies in Puget Sound, Blakely et al. (2002) identified two locations where such faults are permissible but constrain the amount of offset on these faults to <1 km. Submerged terraces on the west side of Puget Sound are elevated as far north as -3 km north of Alki Point (Fig 1.8); on the east side of Puget Sound the submerged terraces are elevated only south of Alki. This ~3 km north-south difference in the northernmost extent of deformation is consistent with the interpretations from the seismic data and suggests the Seattle fault is segmented crossing Puget Sound. Moore et al. (2022) found a similar north-south offset between growth strata along the west side of Puget Sound and in Lake Washington. Blakely et al. (2002) suggested the frontal fault, which has stepped forward through time (Moore et al., 2022), may have stepped forward on the west side of Puget Sound but not on the east. If this were the case, slip on both segments of the frontal faults occurred during the Restoration Point earthquake to produce the uplifted wavecut platforms at both Restoration Point and Alki.

1.4.3.4 Six anomalous profiles may be explained by non-tectonic processes

Six points from profiles drawn across three submerged terraces ~5 km south of Alki Point remain elevated above the GIA datum even after removing the signal of uplift attributed to the Restoration Point earthquake (Fig. 1.8). These high points are unlikely to be random anomalies or picking errors, since they persist at a similar depth across three adjacent terraces that span 900 meters.

There are several possible hypotheses for their higher elevation, none of which can be ruled out with existing data. First, these terraces could represent a different surface, like a lithologic contact. Second, the surfaces of the terraces could be covered with a thick (~10 m thick) package of sediment that is not present atop adjacent terraces. Third, a tectonic explanation is also a possibility.

I favor an explanation that recessional outwash, flowing eastward from the land, provided a local sediment source to mantle these terraces with unusually thick deposits. While the modern depositional context of each terrace is different, geologic maps show that all three are downstream from mapped recessional outwash (sands and gravels deposited by rivers draining a receding glacier). Geotechnical borings at the Fauntleroy Ferry Terminal, 200 m upstream from the middle terrace, show at least 6-10m of loose to medium dense sand (likely post-glacial deposits) atop stiff clay (likely glacial deposits).

A tectonic explanation remains a possibility. For example, the nearby Blake Island anticline (Pratt et al., 1997) is a structure that could have uplifted these points locally (Fig. 1.1B). Notably, Fauntleroy Cove just onshore from these terraces, is one of several locations associated with Indigenous earthquake records within the Seattle fault zone (Ludwin et al., 2005).

1.4.4 Implications for earthquake hazard

1.4.4.1 Recurrence of M ~7.5 earthquakes

Limiting SFZ earthquake history to one M~7.5 earthquake in the past 11,000 years, as proposed here, would specify and lengthen the recurrence for large earthquakes compared with current seismic hazard estimates. The National Seismic Hazard Map currently allows for one M 7.1 or greater earthquake on the Seattle fault in a 5,000-year period (Petersen et al., 2023; Frankel, et al., 2007). The Restoration Point earthquake is estimated as a M 7.5 event (ten Brink et al., 2006; Styron and Sherrod, 2021), though trench studies indicate smaller earthquakes may have occurred on individual backthrusts. Results here corroborate the findings from glacial contacts (Thorson, 1996) and glacial lake shorelines (Thorson, 1981; Thorson, 1993), and quantify earlier work on submerged terraces (Haugerud, 2020) that there has not been another earthquake like the M 7.5 Restoration Point event in the past 11,000 years.

One such earthquake in the past 11,000 years is consistent with the most recent estimates of long-term geologic slip rates on the SFZ. Moore et al. (2022) modeled slip over 24.5 Ma on three SFZ main thrusts that step sequentially northward to produce a total shortening rate of 0.42–0.83 mm/yr. Using their preferred fault geometries, this translates to 4.6–9.1 m of uplift in the past 11,000 years, 4.9–9.7 m of uplift over the Holocene (11.7 ka) and 6.0–11.9 m since deglaciation (14.3 ka). This is consistent with one earthquake that produces ~8 m of uplift above the fault tip.

Shortening across the SFZ is driven by regional north-south shortening across western Washington that has been estimated geodetically at 4–6 mm/yr (Mazzotti et al., 2002; McCaffrey et al., 2007; McCaffrey et al., 2013). One episode of fault slip (8 m of uplift) in the past 11,000 years translates to 8 m of north-south shortening on a fault that dips 45 degrees, suggesting the SFZ has accommodated ~12–18% of the regional shortening in that time period. This estimate is consistent with a long-term shortening estimate by Moore et al. (2022) who calculate the SFZ has accommodated ~7–21% of regional shortening over the past 23.8 Ma.

The one-earthquake estimate presented here is limited to broad-scale regional deformation produced by slip on main thrusts of the Seattle fault and does not provide information about earthquakes of smaller magnitude that could occur on Seattle fault backthrusts (e.g., Kelsey et al., 2008). Paleoseismic trenches suggest several such earthquakes may have occurred in the past several thousand years. Styron and Sherrod (2021) modeled possible magnitudes of these events, providing a 95% confidence interval of M 6.2–7.2.

One M~7.5 earthquake in the past 11,000 years, as inferred here, is fewer than estimates made at individual paleoseismic sites. Angster et al. (2023) interpret a second SFZ earthquake, distinct from the Restoration Point event, at ~10.8 ka by correlating radiocarbon ages in two paleoseismic trenches on Bainbridge Island and on the western shore of Lake Sammamish (31 km apart), bringing the post-glacial number of earthquakes to two. Moore et al. (2022) propose a possible much larger number of events from the dips of recessional lake and outwash sediments as seen in shallow seismic reflection data in Lake Washington. Dips increase with depth in the southern limb of the frontal fold of the SFZ; the increase in dip is consistent with 9-15

postglacial times of fold growth, 50% of which would have occurred in the 1.1 ka immediately following deglaciation. The Lake Washington data have unusually good stratigraphic constraints, but Moore et al. (2022) noted that dips could be explained in other ways, such as a primary southward dip, possible differential settlement, or deformation on another localized structure.

Taken in context with the broad-scale deformation defined by the submerged terraces, reinterpreting the discrepancies outlined above has the potential help refine the structure of the Seattle fault zone and the relationships among smaller backthrusts and the main fault. The discrepancies outlined above motivate further research to interpret paleoseismic datasets produced at a single location (e.g., backthrusts or other local structures) in the context of the broad scale deformation history defined by the submerged terraces.

1.4.4.2 Block uplift between the Seattle and Tacoma fault zones

The depths of submerged terraces support existing structural interpretations of block uplift south of the Seattle fault zone. Submerged terraces south of the SFZ remain elevated above the GIA datum ("Possible glacio-isostatic datums" on Fig. 1.8) for at least 20 km south of Alki Point (Fig. 1.8), extending nearly to the hanging wall of the Tacoma fault zone (TFZ) (Fig. 1.4). Long-term uplift in the Seattle uplift, bounded by the SFZ (north), Tacoma fault zone (south), and Saddle Mountain fault zone (SMFZ) (west) is supported by several lines of geophysical evidence including deep seismic reflection data (e.g., Pratt et al., 1997), gravity maps (e.g., Daneš et al., 1965; Finn et al., 1991), magnetic anomalies (e.g., Blakely et al., 2002), and maps of surficial bedrock (e.g., Gower et al., 1985). While geophysical data suggest the entire block has risen over millions of years to juxtapose the Tertiary bedrock within the uplift with Quaternary sediments in the basins to the north and south, paleoseismic studies have focused only on uplifted terraces within or immediately adjacent to the fault zones.

Onshore terraces south of the SFZ also appear to span the entire length of the Seattle uplift, though have mostly escaped paleoseismic study outside of the few kilometers south of the SFZ deformation front. Lidar-updated geologic and geomorphic maps show "old beach" deposits at supra-tidal elevations at shorelines as far south as Tacoma (Haugerud, 2009; Tabor et al., 2014;

Booth et al., 2015; Tabor et al., 2017), though they have not been the subject of paleoseismic study to determine their age and the likelihood that they were formed during uplift of the Restoration Point earthquake. Most study has focused on terraces in the few kilometers south of the SFZ deformation front, where uplift during the Restoration Point earthquake was the greatest. The paleoseismic studies at Gorst are an exception, where uplift recorded in marsh sediments was described ~10 km south of the deformation front (Arcos, 2012).

These observations are consistent with block uplift bounded by the SFZ, Tacoma Fault Zone, and Saddle Mountain fault. A similar structural model for block pop-up has been proposed for the uplift bounded by the Doty fault (Anderson et al., 2023).

The findings that trees died due to movement on the SFZ and Saddle Mountain Fault within a 6-month window, and within 100–200 years of movement on the Tacoma Fault Zone, has led to the hypothesis that all of these faults can rupture in a multi-fault earthquake or closely timed earthquake sequence (Black et al., 2023). While deformation of submerged terraces would not distinguish between synchronous or sequential uplift on these three structures, uplift within the Seattle uplift block indicates that all of these faults have been active since the 11 ka lowstand terminus. The possibility of synchronous or near-synchronous deformation on all of these structures has implications for fault kinematics, earthquake hazard, and tsunami modeling.

In order to flesh out these interpretations and evaluate their implications, further investigations could: (1) solidify the origin, establish the age, and measure the inner-edge elevation of potentially uplifted beach deposits and wavecut platforms south of the SFZ and north of the TFZ; (2) extend the survey of submerged terrace depths across the TFZ to evaluate their offset; and (3) establish a geologically derived quantitative estimate for magnitude of uplift immediately adjacent to the TFZ.

1.5 CONCLUSIONS

Submerged terraces in Puget Sound, attributable to a sea-level lowstand ~11,000 years ago, are used as a structural datum to map and quantify tectonic deformation south of the Seattle fault zone. I find that terrace depths allow no more than one M~7.5 earthquake in the past 11,000

years, half the number of large earthquakes allowed by current hazard estimates. The pattern of deformation also suggests that uplift may represent continuous block uplift between the Seattle, Tacoma, and Saddle Mountain fault zones, and that, at Seattle, uplift did not extend further north than Alki Point. These results motivate further research to define the southern extent of possible block uplift.

1.6 FIGURES

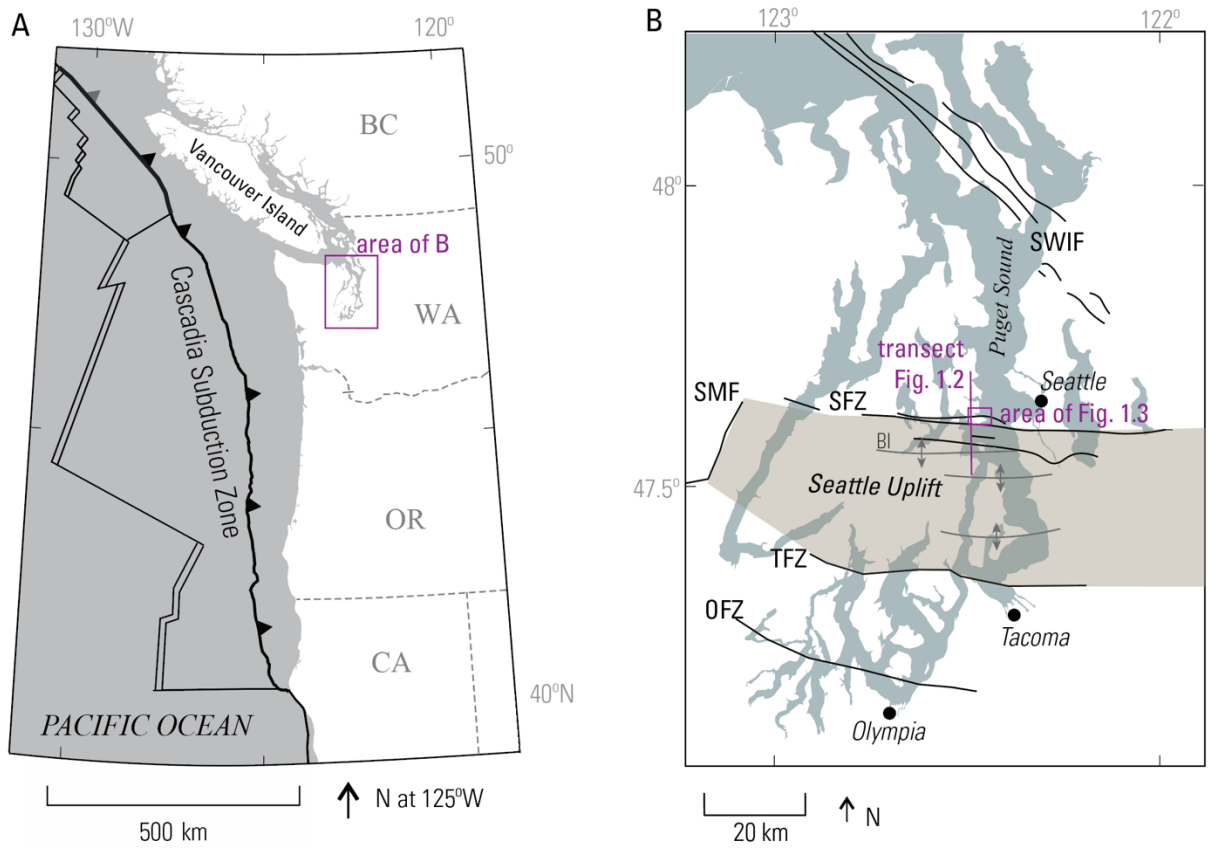

Figure 1.1. Location of the study area, Puget Sound, in western Washington. (Left) location of Puget Sound in Washington State, in the forearc of the Cascadia subduction zone. (Right) Crustal faults (black lines) cross Puget Sound, including the South Whidbey Island fault (SWIF), Seattle fault zone (SFZ), Saddle Mountain fault, (SMF), Tacoma fault zone (TFZ), and Olympia fault zone (OFZ). Smaller anticlines (gray lines with arrows) include the Blake Island anticline (BI). The cities of Seattle, Tacoma, and Olympia are located in the vicinity of these structures. The Seattle Uplift (gray shaded area) is bounded by the Seattle fault zone, Tacoma fault zone, and Saddle Mountain fault (Pratt et al., 1997).

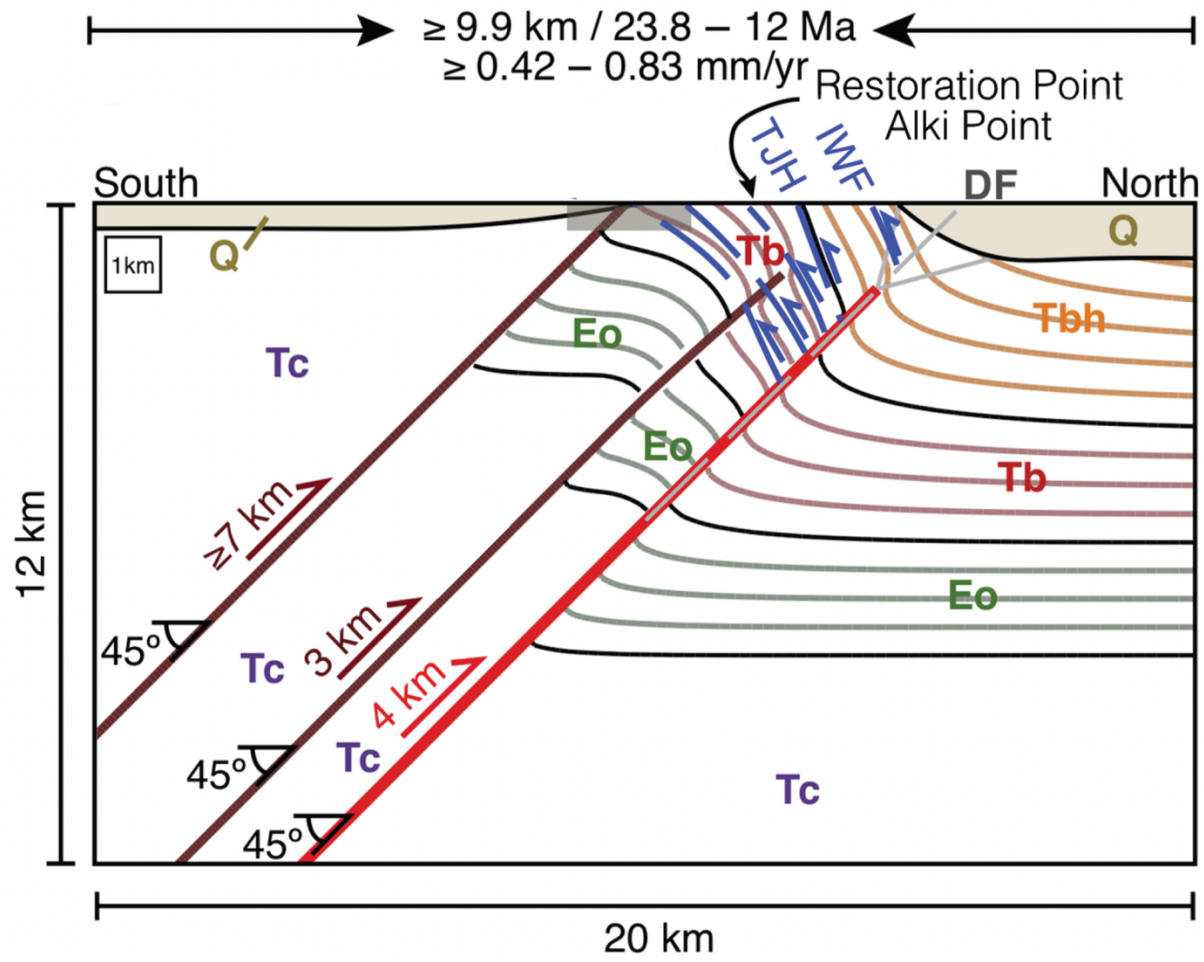

Figure 1.2. Structural model of the Seattle fault zone in cross-section proposed by Moore et al. (2022). The location of this cross-section is shown on Figure 1.1. Three north-vergent main blind thrusts (red lines) produce surficial folding, which is cut by additional smaller south-vergent backthrusts (blue lines). Backthrusts include Toe Jam Hill fault (TJH) and Islandwood fault (IWF) shown on Figure 1.3. Convergence rate listed is that of Moore et al. (2022). Figure adapted from Moore et al. (2022).

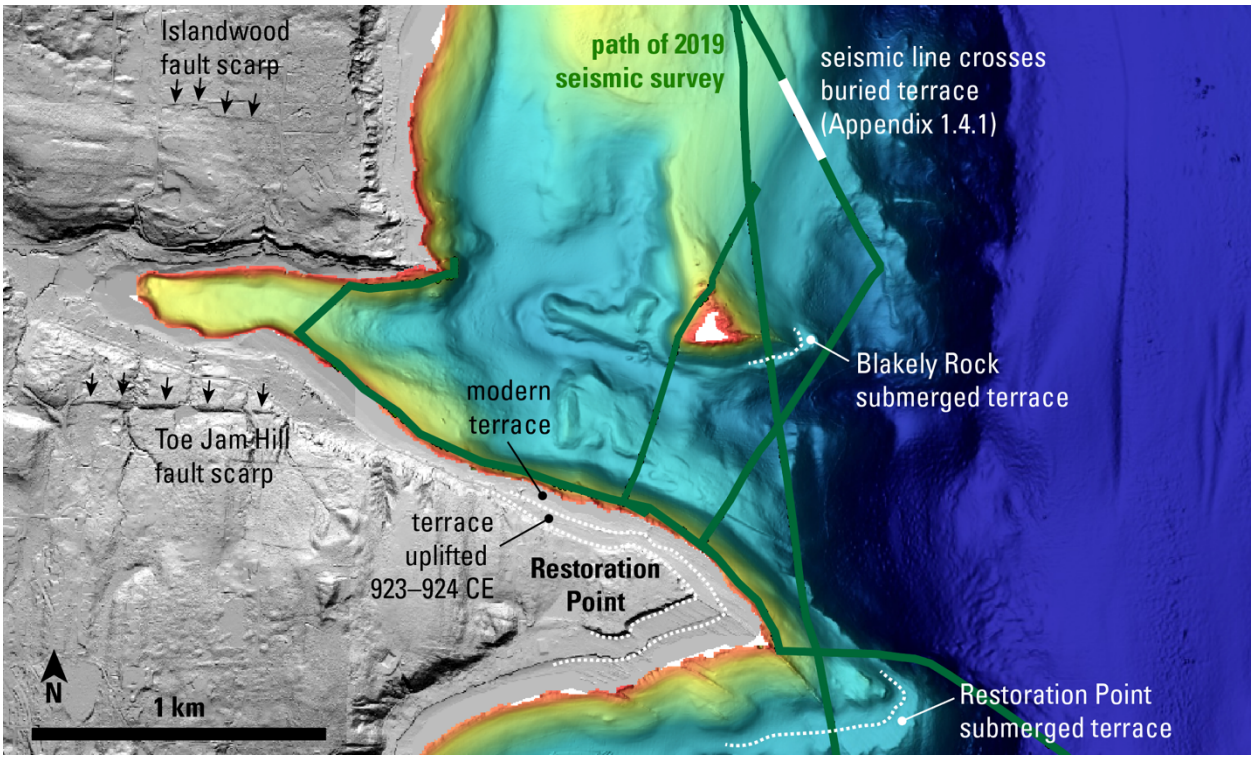

Figure 1.3. Map of restoration point showing bathymetric terraces, onshore terraces, faults, and seismic survey lines. Terraces obvious in bathymetry are present off many shorelines in Puget Sound, including those offshore Restoration Point. At Restoration Point, three levels of inferred shorelines are visible in topography and bathymetry (white dashed lines mark approximate back edges). The break in slope at the back edge of the Restoration Point submerged terrace is under the white dashed line. The modern shoreline sits between a terrace uplifted in the Restoration Point earthquake of 923–924 CE and the offshore submerged terrace. South-facing fault scarps of backthrusts, including the Islandwood fault scarp and Toe Jam Hill fault scarp cross topography. Black arrows are on the upthrown side of the scarp. Seismic reflection data collected by the authors in 2019 (green lines) crosses submerged terraces visible in bathymetry and images a terrace buried in the subsurface. Bathymetry is NOAA NOS Color Shaded Relief.

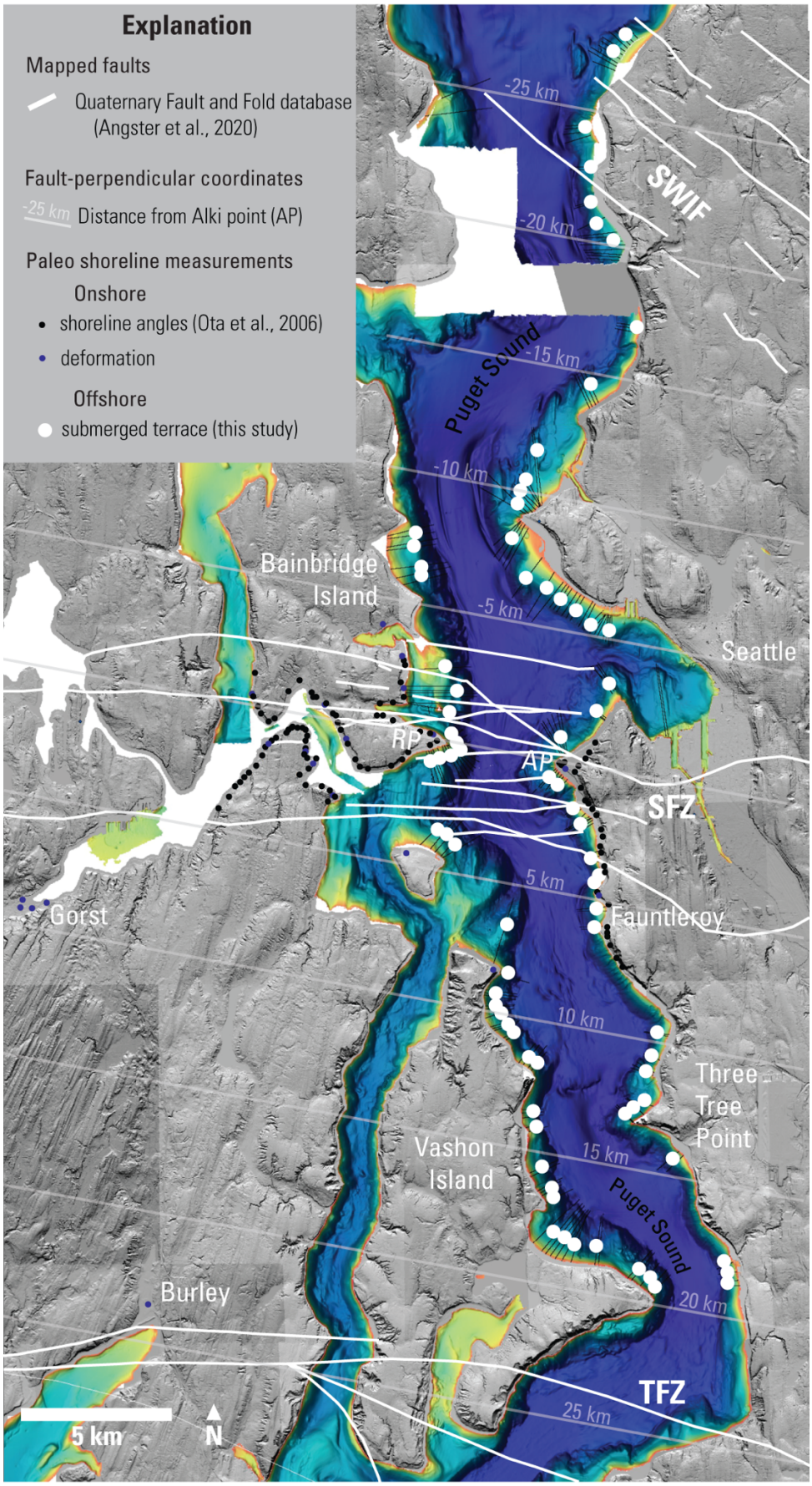
Explanation
Mapped faults
Quaternary Fault and Fold database (Angster et al., 2020)
Fault-perpendicular coordinates
-25 km Distance from Alki point (AP)
Paleo shoreline measurements
Onshore
shoreline angles (Ota et al., 2006)
deformation
Offshore
submerged terrace (this study)
-25 km
-20 km
-15 km
-10 km
-5 km
5 km
10 km
15 km
20 km
25 km
SWIF
Puget Sound
Bainbridge Island
Seattle
RP
AP
SFZ
Gorst
Fauntleroy
Three Tree Point
Vashon Island
Burley
TFZ
5 km
N

Figure 1.4. (prior page) Locations of submerged terraces mapped in this study (circles). Other terraces extend beyond the north and south boundaries of this map but were not used in this study. Fault locations are from the USGS Quaternary Fault and Fold database (Angster et al., 2020) for the Seattle fault zone (SFZ), South Whidbey Island fault zone (SWIF), and Tacoma fault zone (TFZ) and represent both projections of blind main thrusts and surface-breaking backthrusts compiled from multiple structural interpretations. Shoreline angles of uplifted terraces (black dots) measured by Ota et al. (2006) were compared with the bathymetric terraces. Other deformation measurements (blue dots) were measured at Gorst by Arcos (2012), at Burley by Bucknam et al. (1992), and compiled elsewhere by ten Brink et al. (2006).

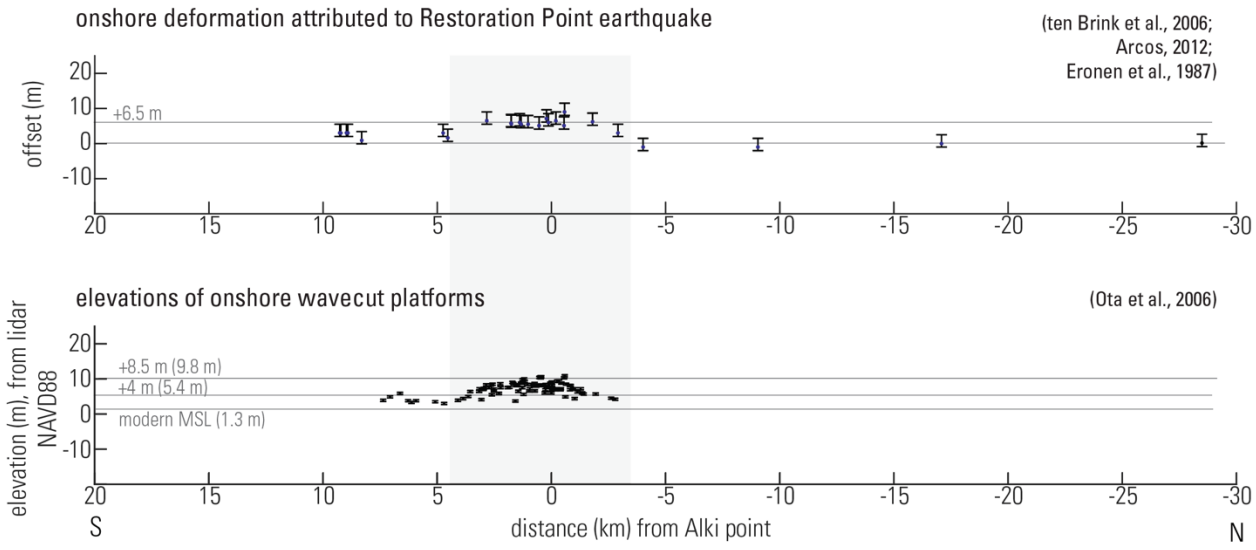

Figure 1.5. Other datasets of paleo shorelines show upward offset within and south of the Seattle fault zone. Gray box represents zone of mapped faults (Angster et al., 2020). (Top) Uplift measurements compiled by ten Brink et al., (2006) plus data from Arcos (2012) and Eronen et al. (1987). ten Brink et al., (2006) data were compiled from other studies that measured or estimated meters offset of coastal terraces attributed to Restoration Point earthquake. Errors are plotted as reported plus an additional 1.5 m positive error to account for possible subsidence in the Puget Lowland in the past 1100 years, as described by Arcos (2012). (Bottom) Uplifted shorelines measured by Ota et al. (2006). Ota et al., mapped shorelines along West Seattle, at Restoration Point, and Point Glover. Elevation values are listed in meters NAVD88. Gray horizontal lines show estimated elevations associated with 4 m and 8.5 m of offset compared with modern MSL (though Ota noted that modern shorelines form at ~1-1.5m above MSL). The values in parentheses are the elevations in m NAVD88. Overall, both compilations evidence a several-meter-high fold within the zone of mapped faults that descends to the south. Neither dataset shows a return of modern terraces to at or near MSL.

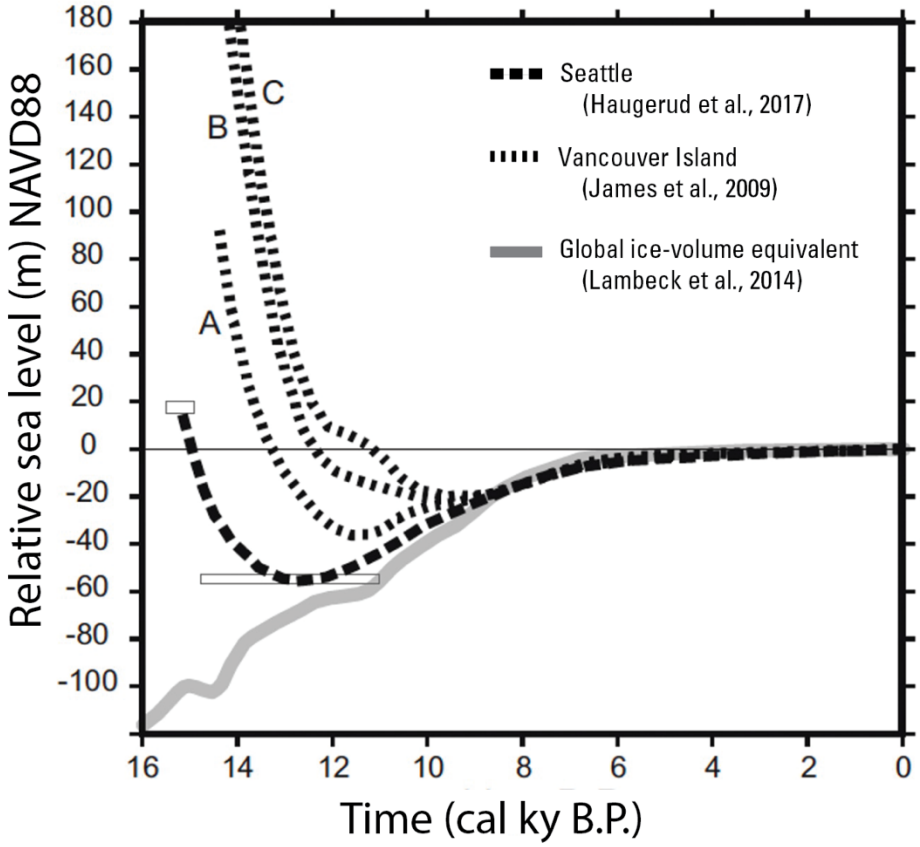

Figure 1.6. Relative sea-level histories for regional locations. The heavy dashed line represents relative sea level at Seattle. The relative highstand in Seattle ca. 15 ka (short white bar) is projected from the marine limit of Thorson (1989) and Dethier et al. (1995). The relative lowstand (long white bar) is based on Haugerud's (2017) interpretation of the submerged benches studied here. Similar predictions from GIA models using different data are shown in Appendix 1.1. After Haugerud et al. (2017).

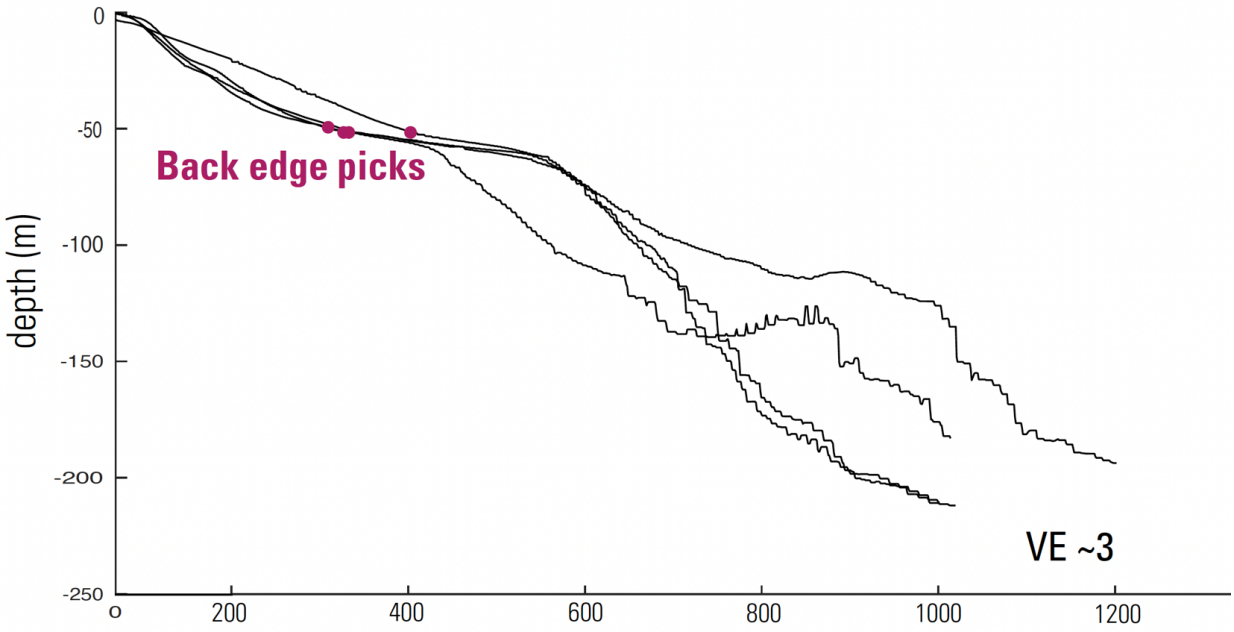

Figure 1.7. Four slope profiles across the submerged terrace offshore Three Tree point (location in Figure 1.4). Noise at deeper depths reflects the decreased resolution of the bathymetric data as depth increases.

One Restoration Point earthquake

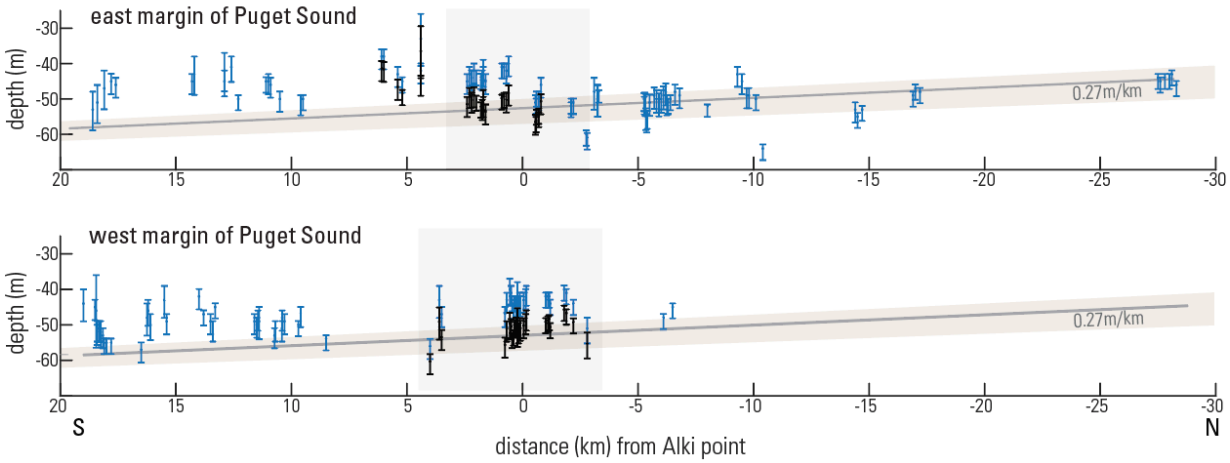

Two Restoration Point earthquakes

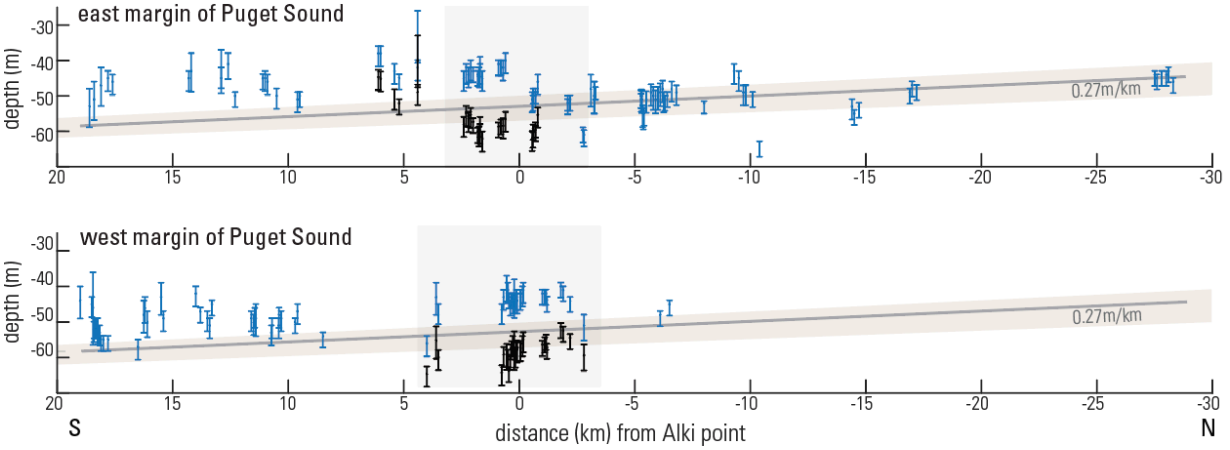

Explanation

Submarine terraces

Picked depth to back edge of submarine bench. Formally propogated error includes picking error, bathymetric error, and 3m possible sedimentcover.

Submarine terrace depths and error minus offset from one or two Restoration Point earthquake(s) as measured by Ota et al., (2006).

Location of Seattle Fault Zone

Range of mapped faults (Angster et al., 2020)

Possible glacio-isostatic datums

Range of linear models fit to points north of SFZ.

Best fit line rises to north at rate of 0.27 m/km

Figure 1.8. (prior page) Picked depths to back edges on the east and west flanks of Puget Sound. Error bars include estimated picking error of 0.5-5 m, a potential 3 m of sediment cover, and uncertainty from bathymetric and lidar datasets. Formal error propagation is described in Appendix 1.4. Blue points represent submerged terrace back edges; black points represent the expected depth of terrace back edges with deformation from one Restoration Point earthquake (upper plot) or two such events (lower plot) removed. A range of glacial trendline fits is represented by the south-dipping gray bar (see Appendix 1.6 for discussion of trendline fits); the best fit line is labeled. The light blue-gray box represents the zone of mapped faults (Angster et al., 2020).

Chapter 2. **Paleo-liquefaction features of the past 1,100 years at the Duwamish delta in Seattle, Washington**

ABSTRACT

Small exposures of Holocene liquefaction features at the Duwamish delta evidence two or more earthquakes in the past 1100 years in Seattle. The modern delta, inset into a terrace uplifted in an earthquake on the Seattle fault zone (SFZ) 923–924 CE, consists of lahar-runout sand deposits capped with intertidal deposits. Liquefaction features comprise dikes and lenses of andesitic sand in outcrops of peaty mud. Andesitic sand is likely derived from Mount Rainier lahar runout that underlies the mud; liquefaction and fluidization of these deposits during earthquake shaking produced sand dikes intruded into the overlying mud. Some dikes extruded sand blows onto paleo-surfaces; others apparently did not reach the ground surface. All outcrops show marsh aggradation through time. Radiocarbon ages on in-situ marsh plants constrain timing for episodes of sand venting: as few as two and as many as six episodes are possible. Most evidence consists of dikes that did not reach the ground surface, leaving ambiguity in the timing of the episodes. The earlier event ejected sand atop *Triglochin maritima* plants. The fossil leaf bases of these plants provide a stratigraphically precise way to date the event: the age of the earthquake is the same age of the leaf bases: 990–1150 cal yr CE. The lack of precision inherent in radiocarbon dating means the age range is too broad to connect to a particular earthquake, though it overlaps with similarly broad age estimates of one of the most recent of the Cascadia megathrust earthquakes and ages of other regional liquefaction. Nonetheless, the stratigraphic position of this event—inset into the terrace uplifted in the SFZ earthquake 923–924 CE—confirms that an earthquake of unknown source produced ground shaking in Seattle at most a few centuries after the uplift. A later earthquake or earthquakes produced sand dikes at five sites; at only one site did dikes reach a ground surface and eject sand. The extrusions date, in cal yr CE, to before 1490–1630. The dikes at other sites occurred after 1030–1150, 1220–1280, 1230–1300, and 1400–1630. Any of these dikes could have been produced in a known megathrust earthquake in 1700, though this earthquake did not obviously produce sand venting that reached a ground surface, even in outcrops where the stratigraphic position of 1700 is probably recorded.

This observation does not necessitate a lack of strong ground shaking in 1700, as none of the outcrops record multiple episodes of sand venting at the same outcrop, demonstrating that liquefaction at this site incompletely records regional earthquakes. Lack of completeness of the Duwamish liquefaction record is likely due to a paucity of available outcrops and changes in the outcrops through time as the marsh aggraded, moved northward, and likely compacted.

2.1 INTRODUCTION

Liquefaction and other ground shaking proxies contribute to earthquake catalogs in places where the historic record of earthquakes alone is not sufficient to evaluate seismic hazards. In many places that lack other paleoseismic indicators (e.g., surface-breaking faults, records of sudden land-level change, or tsunami deposits), paleo-liquefaction becomes the primary evidence for earthquakes. Since paleo-liquefaction records are used to infer the long-term earthquake potential of seismic sources, it is important to understand to what extent these catalogs can be inferred to be complete. Several outstanding questions pertain to the development and interpretation of liquefaction catalogs as records of earthquakes: How can liquefaction features be dated with enough precision to link them to a particular earthquake? What features of geologic settings make them more likely to completely record of earthquake-induced liquefaction? Under what conditions might an absence of liquefaction be confidently interpreted as evidence that an earthquake did not occur?

In the Pacific Northwest of the United States (Fig. 2.1), these general questions play out in specific ways. Three earthquake sources contribute to regional seismic hazard: the Cascadia subduction zone (CSZ), crustal faults (some of them blind) in the overlying plate, and the subducting plate, which produces deep intraslab earthquakes. Only the last of these three sources has produced earthquakes recently enough to be recorded instrumentally (PNSN). Therefore, substantial uncertainty remains about the recurrence, magnitude, effects, and variability of earthquakes on the CSZ and on crustal faults. In order to address these uncertainties, major efforts are underway to produce and compile paleoseismic data (e.g., compilation described by Walton et al., 2021), including paleo-liquefaction data (Rasanen et al., 2021a). By leveraging a regional view of paleoseismic data, we may be able to infer some nuances of the behavior of

these disparate seismic sources. These potential analyses rely on both a thorough catalog of evidence and precise ages for the events in the catalog.

In this chapter, I contribute to this regional catalog of paleoseismic data by mapping and dating paleo-liquefaction features at the Duwamish delta (Fig. 2.2) in Seattle, Washington. In doing so, I illustrate a method for dating liquefaction with exact stratigraphic precision and demonstrate that the liquefaction catalog at the Duwamish delta incompletely records regional earthquakes.

2.2 BACKGROUND

2.2.1 Liquefaction features as a proxy for ground shaking

Earthquake shaking provides a mechanism for causing liquefaction, fluidization, and their resulting features; therefore, relict "liquefaction features" can be used as evidence for earthquakes. Liquefaction has been defined by Youd (1973) as "transformation of a granular material from a solid into a liquefied state as a consequence of increased pore water pressures." Cyclic shear waves produced by earthquakes propagate upwards, eventually reaching saturated sediments near a ground surface (Obermeier, 1996). This increases pore water pressures and can trigger the process of liquefaction. The process of liquefaction, the temporary loss of contact between grains of a saturated sedimentary layer, is differentiated from the process of fluidization, where upward-moving pore fluids suspend and move sediment grains (Lowe, 1975). Both liquefaction and fluidization may result in recognizable "liquefaction features," including altered or convoluted strata (e.g., resulting from liquefaction alone), injected dikes or sills, or extrusions onto a ground surface (e.g., resulting from liquefaction and fluidization) (Lowe, 1975; Obermeier, 1996). Specific characteristics of liquefaction features used in this study are described in section 2.3.2.

2.2.2 Paleo-liquefaction features have been used as evidence for ground shaking worldwide

Paleo-liquefaction studies are useful where seismogenic faults are difficult to identify and have been most common in intraplate settings (Tuttle et al., 2019). In the U.S., paleo-liquefaction data were used to develop seismic source models for the U.S. National Seismic Hazard Map and for central and eastern U.S. seismic source characterization for nuclear facilities. Studies use extensive catalogs of regional liquefaction features to identify the source and strength of shaking

during earthquakes. For example, in the New Madrid Seismic Zone of the Mississippi Valley, earthquakes in 1811–1812 triggered large-scale liquefaction which resulted in injected sand dikes and erupted of sand blows that recurred multiple times at the same sites (Tuttle, 2000). At least four earthquakes have been inferred from recurrent liquefaction in this record, and the size of earthquakes has been estimated up to M7.8–8.1. Lack of observed liquefaction has also been used as evidence for a lack of earthquake shaking (as described in Obermeier & Pond, 1998).

The construction of useful earthquake catalogs relies on precise enough dating to distinguish between successive earthquakes. Where liquefaction features are present, age estimates for the earthquakes that produced them can be ascribed by dating sediments that surround the features, for example by comparison with in-situ or detrital radiocarbon samples (Tuttle et al., 2000).

2.2.3 Prior work on liquefaction in the Puget Lowland

In the Pacific Northwest, Rasanen et al. (2021a, 2021b) compiled published geologic evidence for liquefaction at 185 sites. In the Puget Lowland, paleo-liquefaction has been mapped and dated at seven sites (Table 2.2). Evidence at all sites consists of sand dikes that meet vented sand lenses. In some places, evidence for liquefaction accompanies evidence for land-level change or tsunami.

As in the present study, the quality of age control on regional liquefaction features is variable. Table 2.1 lists the ages bearing on liquefaction as reported by the authors. At the Snohomish and Skokomish deltas (Bourgeois & Johnson, 2001; Martin, 2011), timing of liquefaction emplacement is constrained by ^{14}C ages of in-situ, growth-position marsh-plant fossils that correspond in time with events in addition to providing age maxima and minima. Elsewhere, liquefaction timing is bracketed only by a maximum or minimum, leaving many possibilities for the timing of the earthquake that would have produced the feature.

The largest individual sand blows recognized to-date in the Puget Lowland were identified at Issaquah Creek, 0.7–1.5 km upstream (SE) of a delta feeding inland Lake Sammamish. Vented sand volcanoes are exposed in cutbanks of the creek (Whisler et al., 2002; Martin and Bourgeois, 2012). Sand blows, capping floodplain soil, contain mud laminae, peat, and mud intraclasts, soft

sediment deformation, and fluid escape structures, and reach over 100 cm thick (Martin and Bourgeois, 2012). At least one dike terminates at a sand blow (Whisler et al., 2002). The base of the vented sand contains well-preserved leaves; three of these detrital leaves constrain the timing of liquefaction to before 660–992 cal yr CE (Table 2.3) (Martin and Bourgeois, 2012). Liquefaction also occurred at this site in the historic 2001 earthquake (Nisqually Clearinghouse via Martin and Bourgeois, 2012).

At Lynch Cove, a tidal marsh at the end of Hood Canal, evidence for liquefaction has been inferred to accompany uplift (Jovanelly and Moore, 2009; Martin and Bourgeois, 2012). Evidence for abrupt uplift, followed by subsidence, was described and dated by Bucknam et al. (1992). Evidence for liquefaction consists of sand unit of variable thickness exposed in cores and creek banks across at least 0.5 km (Jovanelly and Moore, 2009; Martin and Bourgeois, 2012). Many dikes terminate at the sand unit (23 seen in outcrops by Martin and Bourgeois, 2012; two seen in cores by Jovanelly and Moore, 2009). The sand layer, which reaches 100 cm thick, contains intraclasts, mud laminae, soft sediment deformation, cross-stratification, and micro faults. The sand layers were interpreted as a combination of tsunami and liquefaction deposits by Jovanelly and Moore (2009). Martin and Bourgeois (2012) reinterpret the sand as only vented sand deposits (i.e., with no evidence for tsunami) on the basis of its characteristics, including the variable thickness of the deposit and its failure to thin moving landward. The liquefaction is dated by its correspondence with the uplift to before 880–980 cal yr CE (Bucknam et al., 1992; Sherrod et al., 2004).

At the Skokomish delta, differential uplift was accompanied by liquefaction before 780–1000 CE (Polenz et al., 2010; Martin, 2011; Martin and Bourgeois, 2012; Arcos, 2012). Evidence for liquefaction consists of intruded dikes and vented sand blows that reach over 30 cm thick.

At the Snohomish delta, three episodes of liquefaction are described from numerous outcrops (Bourgeois and Johnson, 2001; Martin, 2011). Event B, contemporaneous with local subsidence and a tsunami, consists of sand dikes terminating in sand blows and is dated to 800–980 CE. The authors note that subsidence may be the result of localized settlement and not tectonic. Event C consists of sand dikes that crosscut the Event B horizon, meet a sand lens, and are dated to 910–

990 CE. Event E consists of sand dikes that crosscut the Event B horizon, meet a sand blow, and are dated to after 1400–1600 CE.

At the Nisqually delta, evidence for liquefaction consists of beds of sand with internal deformation, sand blows, and at least one sand dike observed in a core (Sherrod, 2001; Sherrod, 2004; Barnhardt and Sherrod, 2006). At the McAllister creek site (Sherrod, 2001), a sand blow is dated to after 770–1000 CE. Elsewhere, liquefaction is dated to after 680–1030 CE (Sherrod, 2001; Barnhardt and Sherrod, 2006).

At Burley, evidence for liquefaction consisting of sand blows is associated with uplift (Sherrod, 2004). The liquefaction features are dated to after 770–1000 CE.

2.2.4 Geologic and tectonic setting

The Duwamish delta, now an industrial corridor, is located at the mouth of the Duwamish River (Figs. 2.1, 2.2, 2.3) where it meets Elliott Bay, an embayment of Puget Sound. The delta has geologic conditions highly susceptible to liquefaction (Kayen and Barnhardt, 2005).

2.2.4.1 Earthquake sources for liquefaction

Three types of earthquakes may produce liquefaction at the Duwamish delta: crustal fault earthquakes, deep intraslab earthquakes, and megathrust earthquakes on the Cascadia subduction zone (CSZ). First, several east-west trending crustal faults cross the region (Pratt et al., 1997; Brocher et al., 2001; Blakely et al., 2002), including one structure, the Seattle fault zone (SFZ), that crosses the Duwamish delta itself (Fig. 2.1B). The SFZ produced a M~7.5 earthquake (magnitude estimated by ten Brink et al., 2006; Styron and Sherrod, 2021) in 923–924 CE (Black et al., 2023) that caused several meters of uplift in a broad fold over the main thrusts (Bucknam et al., 1992; ten Brink et al., 2006) and a tsunami in Puget Sound (Atwater and Moore, 1992; Atwater, 1999; Bourgeois and Johnson, 2001). Liquefaction features at several sites around Puget Sound (Fig. 2.1; Table 2.5) have been attributed to this earthquake by age correlation and by comparison with coincident geologic evidence. Second, deformation within the subducting Juan de Fuca slab produces deep earthquakes. Historically, such earthquakes with hypocenters near Seattle produced liquefaction in 1949 (M6.7), 1965 (M6.5), and 2001 (M6.8) (Chleborad

and Schuster, 1998, Filiatrault et al. 2001, PNSN) (Fig. 2.3). Last, the Cascadia subduction zone (CSZ), off the coast of Washington, has produced M~8–9 earthquakes that recur every few hundred to >1000 years (Atwater and Hemphill-Haley, 1997; Goldfinger et al., 2017). The last earthquake, in 1700 CE (Satake et al., 1996), produced liquefaction along the Washington coast and on the banks of the lower Columbia River (Obermeier, 1993; Obermeier, 1995; Peterson and Madin, 1997; Takada and Atwater, 2004, Atwater, 2020). Lower Columbia River outcrops record liquefaction from at least one prior earthquake, likely ca 1013–1064 cal yr CE. (Obermeier, 1995; Atwater, 2020). Late Holocene liquefaction features have also been noted in Oregon (Kelsey et al., 2002; Peterson et al., 2014). Locations of late Holocene liquefaction features are shown in Figure 2.1. Other geologic records of strong ground shaking in 1700 have been searched for but largely not found (e.g., Struble et al., 2020; LaHusen et al., 2020; Grant et al., 2022).

2.2.4.2 Duwamish delta stratigraphy is favorable to record earthquake liquefaction

Geologic and human influences contribute to the Duwamish delta's susceptibility to earthquake-induced liquefaction and its capacity to record traces of past earthquakes. In particular, the lahar-runout sand that forms the delta, which is capped by intertidal mud and anthropogenic fill, provides abundant source material for liquefaction during earthquakes.

Strata below the Duwamish delta consist, from low to high, of a trough in glacial sediments filled by alluvium, intertidal deposits, and unconsolidated anthropogenic fill (Zehfuss, 2005). The glacial trough was deposited, scoured, and overconsolidated during seven or more Pleistocene glaciations (Troost and Booth, 2008). This trough is overlain by mud of freshwater glacial lakes and a marine embayment of Puget Sound (Mullineaux, 1970). This embayment was progressively filled with alluvium, emplacing tens of meters of unconsolidated sand atop the mud. Much of this sediment came from Mount Rainier, which is in the headwaters of the Duwamish drainage (Zehfuss, 2005). By 2200–2900 cal yr B.P., eruptive episodes began on Mount Rainier, introducing an abundance of sediment into the White River in the form of clay-poor lahars (Luzier, 1969; Zehfuss, 2005). The White River reworked and transported this material downstream, prograding the Duwamish delta northward at an average rate of 7 m/yr.

The delta established in its current position about 1100 years B.P., roughly coinciding with the earthquake 923–924 CE.

Uplift 923–924 CE raised the lahar-covered delta mud 5.5 m (ten Brink et al., 2006, citing unpublished data) raising it out of the intertidal zone and Duwamish floodplain. Subsequently, the river incised this uplifted terrace. Terraces flank either side of the river incision (Fig. 2.2). Since then, a sequence of subtidal to supratidal marsh deposits has filled the incision. This fill, which postdates the earthquake 923–924 CE, is the subject of this study.

The newly dry uplifted terrace on the west side of the valley became a permanent village site for Indigenous Duwamish people (Campbell, 1981; URS, 1987). Historical maps (Fig. 2.2) show remnants of the terrace on both west and east edges of the valley, where freshwater vegetation grew in the late 1800s (Collins and Sheikh, 2005). Between 1875 and 1901 CE, early European settlers farmed at the Duwamish delta, diking parts of the salt marsh (Fig. 2.3) (Lawson, 1875; Westdahl, 1901). More recently, the tidelands were anthropogenically modified to provide land for industry: over 2700 acres of tideland were filled at the delta and Elliott Bay, creating new land (Bagley 1929, p356). New, straight, channels were dredged, turning 21.7 km of river into 7.2 km of straightened waterway. Present-day banks of the lower waterway have been nearly completely developed by manufacturers and the Port of Seattle. In 2001, contamination with industrial contaminants such as PCBs, PAHs, and heavy metals led to the designation of the lower waterway as a superfund site (EPA, 2014). Measurements of contaminants are highest in the sediment that lines the dredged channels.

2.2.4.3 Early liquefaction seen in sediment peels and excavations

Excavations and sediment peels collected from giant vertical slices (geoslices) from meters below the surface of the terrace east of the modern waterway (VM in Fig. 2.3) display convolute bedding of lahar-runout sand and other structures attributed to liquefaction (Zehfuss, 2005). Excavations and peel collection were carried out in 2000. The methods for collecting the geoslices and producing peels, which are about 50 cm wide and several meters long, are described in detail by Takada & Atwater (2004). Detailed descriptions of the Georgetown

terrace peels and others, including comprehensive photos and sketches, can be found in the CD-ROM Appendix to Zehfuss (2005).

Generalized stratigraphy displayed in the peels and excavation consists of meters of planar- and cross-laminated andesitic sand with beds a few centimeters to 80 cm thick, some distinct and traceable between peels (Zehfuss, 2005). The sand is capped by a buried soil consisting of 1–10 cm thick dark brown organic sand that was present in all the peels. In the excavation, Douglas fir roots extended into the subsoil. The sand is mantled by 2 m of olive brown mud and well-laminated fine-to-coarse sand. Zehfuss (2005) interpreted the sequence as packages of lahar-derived hyperpycnal flows deposited into the shallow subtidal and possibly intertidal zone, overlain by a forest soil that existed until 1914 when it was covered by hydraulic dredge spoils.

Both the excavation and peels displayed sandy intrusions (Zehfuss, 2005). In the excavation, a sand dike a few centimeters wide crossed > 1 m of bedded sand reaching to within 50 cm of the base of the buried soil. The dike narrowed and fined upward, grading from fine to medium sand near the base of the exposure to silty very fine sand at the uppermost traceable limit of the dike. The trace of the dike became unclear at its upper margin; it could not be traced to the soil. The dike must post-date the sand it cuts across but may be older or younger than the development of the forest soil.

Four sediment peels (peels 3-6 of Zehfuss, 2005) display large intrusions, which are common in the lahar runout sand between -62 cm and -130 cm NAVD88. Intrusions crosscut and deform laminae or bedding structures and consist of massive sand or sand with silty flow structures. In peel 4, a sandy intrusion contains silt intraclasts.

Age constraint comes from peel 6, where intrusions disturb strata bearing a twig that dates to 132–380 cal yr CE (CAMS 88806). Intrusions in other peels are located higher in elevation than a stratigraphically higher twig (intrusions in 2 peels < 1 m higher, and an intrusion in one peel > 2 m higher) dated to 278–535 cal yr CE (CAMS 88805).

The presence of fluidized intrusions in every peel suggests disturbance was widespread. While rapid loading of soft sediments during lahar-deposition episodes may have produced some of the deformation, it is unlikely to have resulted in the rip-up clasts that occupy some of the intrusions, or the tall and narrow dike exposed in the excavation. Seismically induced liquefaction and fluidization of the unconsolidated sand is a more likely explanation. While the timing of the earthquake(s) is not well-constrained in the peels recorded by Zehfuss (2005), one must have occurred following the deposition of the twig 132–380 cal yr CE, and some features, including the dike that reaches nearly to the post-900 CE buried soil, are likely to have occurred later, perhaps coincident with or following the uplift of that terrace in 923–924 CE that allowed the forest soil to form.

2.2.4.4 Liquefaction during earthquakes of 1949, 1965, and 2001

Liquefaction along the Duwamish River also occurred in all three of the region's large historic earthquakes, all of them deep earthquakes, in 1949, 1965, and 2001 (Fig. 2.2). However, this liquefaction may not have occurred in the deep lahar-runout sands described in the last section, but rather in unconsolidated modern fill.

Chleborad and Schuster (1998) compiled reports of ground failures of the 1949 and 1965 earthquakes, including liquefaction-induced features. The 1949 M 7.1 event occurred just north of Olympia while the 1965 M 6.5 event was between Seattle and Tacoma. Both events produced extensive ground failures including landslides, settlement, ground cracks, and sand boils. Sand boils occurred most frequently in floodplains, valley floors, and at river deltas emptying into Puget Sound where tidal deposits or alluvium have been covered with artificial fill.

The 1949 earthquake produced extensive sand boils, cracks, settlement, and lateral spreads, based on reports summarized in Chleborad and Schuster (1998). The reports are chiefly limited to populated areas and usually include limited detail. Many of the reports describe extensive failures in and around Puyallup and include sand boils consisting of white fine sand, clean black sand, or blueish sand. Sand boils ranged from small mounds to boils several meters across. In Seattle, there are fewer reports of failure. Sand boils were reported on the north and west sides of the Duwamish Waterway and adjacent the Elliott Bay waterfront (Fig. 2.2).

The 1965 earthquake produced similar ground failures, though fewer reports of sand boils. Some sand boils were reported in Olympia and in Seattle (Chleborad and Schuster, 1998). The heaviest earthquake damage to buildings occurred in the Duwamish valley, south of downtown Seattle (Mullineaux et al., 1967). Three fatalities and many injuries were incurred by falling building debris. Mullineaux et al., 1967 attribute most of this damage to structures to liquefaction and settlement. The effects of these two earthquakes are likely underestimated, as most reports were made in more populated areas.

A report following the 2001 M6.8 Nisqually earthquake described regional ground failures including landslides, lateral spreads, and liquefaction of alluvial sediment (Filiatrault et al., 2001). The earthquake epicenter was near the 1949 epicenter, though the magnitude smaller. Liquefaction was reported at several sites in the Duwamish valley. With the exception of a few points, liquefaction in 2001 was mapped entirely in areas of artificial fill.

2.3 METHODS

This chapter presents observations of liquefaction-induced features from explorations at the Duwamish Waterway between 1996 and 2021. Observations prior to 2017 include field surveys and diatom paleoecology by those listed in the Acknowledgments of this dissertation.

Searches for liquefaction features were conducted at outcrops along the banks of the dredged Duwamish Waterway. These outcrops are exposed at low tide between walls of rip-rap and industrialized shoreline. Hardening of the channel walls (e.g., rip-rap and seawalls) significantly restricts the number and locations of available outcrops.

2.3.1 Surveying

At each site, vertical benchmarks were established and related to Mean Lower Low Water (MLLW) by surveying each day's low tide and comparing low tide measurements with the 1-min observed tides at the Seattle tide gauge (NOAA, 2020). Transects and surveyed stratigraphic markers were measured according to these benchmarks.

2.3.2 Attribution to liquefaction

I inferred episodes of sand liquefaction, fluidization and surface venting through the morphology and sedimentology of sand deposits. Martin and Bourgeois (2012) summarized the morphology of earthquake-induced vented sediments in general and with specific examples in the Puget Lowland. Vented sand deposits can consist of dikes and sills injected into the surrounding material, domes or volcanoes ejected onto a free surface, or infilled lateral spreading cracks (Obermeier, 1996; Martin and Bourgeois, 2012). Vented sand deposits typically fine upwards and can contain intraclasts of deeper sedimentary units (Tuttle, 2001), massive or graded bedding, and structures such as laminae, soft-sediment deformation, or fluid-escape structures. Here, I ascribe persistent sand lenses met from below by subvertical sand dikes to earthquake-induced liquefaction and fluidization. A presence of silty intraclasts within sand lenses or dikes strengthened evidence for fluidization.

2.3.3 Radiocarbon dating

2.3.3.1 Selection of samples

I used ages of marsh plants growing stratigraphically above and below liquefaction horizons to provide age constraints for the timing of liquefaction. For almost all ages, I collected growth-position plant fossils identifiable to the species level. A few ages are derived from detrital bark found in the outcrop, where identifiable marsh plant fossils were not present. I used bark to constrain loose maximum ages only. Because the modern Duwamish delta is an industrial waterway, there are few live tidal marsh plants for comparison, most of which are located in restoration areas. Two species were described based on literature and other sites: *Triglochin maritima* and *Bolboschoenus maritimus*.

T. maritima colonizes tidal marshes and may be found from incipient marsh to high marsh (Shennan et al., 1998). While alive, the blond feathery leaf base of this species sits at or just below the marsh surface. Sub-fossil remains of these characteristic leaf bases are abundant in Duwamish outcrops. *T. maritima* leaf bases serve as markers of time, a tidal marsh environment, and marsh surface level.

B. maritimus, a tuberous bulrush, is widespread in modern West Coast marshes and wet meadows, especially where saline (Hitchcock & Cronquist, 2018). The living bulrush stems from networks of rhizomes that live tens of centimeters below the ground surface. The corms and culms of fossil rhizomes can be found in Duwamish outcrops, which I used to infer a time of tidal marsh environment some tens of centimeters above. I inferred that liquefaction features below a *B. maritimus* rhizome predated tuber growth, but because the depth of the rhizomes below the ground surface is not well-defined, I did not assume that liquefaction features above a tuber post-date the growth of the rhizome.

2.3.3.2 Estimating uncertainty with added variance

Each ^{14}C age includes errors to account for variations that occur during ^{14}C measurements. Lab-reported errors estimate the reproducibility of a repeat measurements of a single sample; "added variance," described below, estimates reproducibility of replicate samples, including uncertainty introduced in collection or processing (Luk, 2020).

Added variance modifies the reported error for a sample. For a modern sample, the added variance calculated for NOSAMS for the years 2015 and 2016 was 2.6 per mille (Mark Roberts, pers comm, 2019). This value was used to inform the following equations for added variance error, where *Fmodern* and *Fme* are lab-reported values and Added Variance Error is the updated calculated error for a given age.

$$(1) \qquad Added\ variance = Fmodern * 0.0026$$

$$(2) \qquad Total\ error = \sqrt{(Fme^2 + Added\ variance^2)}$$

$$(3) \qquad Added\ Variance\ Error = \frac{8033 * Total\ error}{Fmodern}$$

2.3.3.3 Combination of ages pertaining to the time of an event

Oxcal version 4.4 (Bronk Ramsey, 1995; Bronk Ramsey, 2009; Bronk Ramsey, 2017) and the IntCal20 atmospheric curve (Reimer et al., 2020) are used to convert calibrated radiocarbon ages

to calendar ages. Calibrated ages were rounded to the nearest decade. Where possible, I used prior knowledge of stratigraphy to construct sequence models, which serve as a Bayesian prior for Oxcal's calculated posterior likelihoods. Posterior age ranges are reported as a 95% confidence interval of calibrated years CE.

2.4 RESULTS

2.4.1 Intertidal deposits along the Duwamish Waterway

Muddy deposits crop out along small undeveloped segments of the edges of the modern dredged channel (Fig. 2.2). At the times of observations, these sites were accessible by foot or canoe only during low tides and were submerged at higher tides. I visited five outcrops along both cut banks of the modern dredged channel. Prior to dredging and filling of the delta, all these outcrops were located in the interior of an elongate tidal marsh island (Fig. 2.3) (Lawson, 1875). The island occupied the cut between the terraces on either side, flanked by two river channels.

From lowest to highest, deposits include interbedded dark gray silts and sands in the lowest exposures which grade into massive gray or olive mud containing *B. maritimus* and *T. maritima* rhizomes. At most sites, *B. maritimus* appears lower than *T. maritima*. Above are units of peaty brown mud (and at a few sites dark-brown peaty soil), frequently bearing well-defined laminae and abundant plant remains, typically *T. maritima* and others. Laminae form distinctive notches in weathered outcrops, suggesting textural variation, and range in thickness from 8 mm to 2 cm. Generally, laminae are about 0.5 cm thick and alternate in color from white, dark gray, light gray, to reddish brown.

Depositional environments that produced these outcrops include structureless mud and interbedded mud and sand layers of unvegetated and vegetated intertidal mudflats, peaty mud (some places laminated) of salt marshes, soil of a historical pasture that was created following the diking of the salt marsh in the early 1900s, mud and sand of intertidal environments that reinhabited the marsh following the removal of the dikes, and rubble, sand, and mud of 20th-century artificial fills. Environments at each site were inferred from sediment texture and color, strata, and presence or absence of in-situ plant fossils.

2.4.2 Deposits at site FC

The best exposed and most representative section of intertidal fills was described at site FC (Figs. 2.4 and 2.5), The outcrop at site FC (Fig. 2.4) consists of 60 m of 2-3 m high mostly continuous mud banks on the east edge of the waterway. Stratigraphic markers (CC, LZ, LL, UZ, and PS of Fig. 2.4) are mostly persistent over the length of the outcrop. The following section describes the stratigraphy of this outcrop from low to high.

The basal unit, observed in pits and gouge cores up to 2 m below outcrop level, consists of several decimeters of interbedded layers of light gray silts (0.5–1 cm thick) and dark gray silty fine to very fine sands (3–5 cm thick). This unit grades upward into brown mud that forms the base of the outcrop. The brown mud (10 cm–1 m thick) contains individual *B. maritimus* rhizomes and patches of *T. maritima*, some of which were sampled for ^{14}C dating (open circles and triangles of Fig. 2.4A). The upper contact of this unit is defined by a color change to gray mud (CC of Fig. 2.4). At many places along the length of the outcrop the patchy lenses of black sand (reaching 12 cm thick) sit at the CC contact. The sand lenses are met from below by at least three dikes; more dikes reach the surface of the eroded bench in front of the outcrop.

Gray mud (30–66 cm thick) overlies the CC contact and contains scattered rhizomes of *B. maritimus* and less common patches of *T. maritima*. A patchy tabular silt layer up to 2.5 cm thick (LZ of Fig. 2.4) lies within this unit and was traced across 30 – 60 m of outcrop. This LZ silt layer is roughly horizontal, gray, and exhibits no internal stratification. Above LZ, the mud is generally structureless; up to 10 cm of mottling is present in places within 20 cm of the unit's upper margin. The upper contact of the unit (marker LL of Fig. 2.4) is defined by the lowest appearance of rhythmic laminae within brown peaty mud.

The unit above LL consists of brown peaty mud with rhythmic laminae, is 1 – 1.5 m thick and forms the bulk of the outcrop (Fig. 2.4). Low in this unit, both *B. maritimus* and *T. maritima* are abundant; however, *B. maritimus* rhizomes are not present high in the unit. About 20 cm above the base of this unit is a ~1-cm thick, tabular silt layer (marker UZ of Fig. 2.4) exposed nearly continuously for 60 m. This UZ silt layer and the LZ silt layer in the underlying unit are the only

two such thick and persistent silt layers in the outcrop, though there are other, thinner silt laminae present (not noted on sketch).

The section is capped by a sequence of 1–2 cm of peaty soil (PS of Fig. 2.4), 3 -14 cm of massive gray mud with *T. maritima*, and 2–12 cm of brown mud containing sand, roots, wood, and debris.

2.4.3 Interpreted environments at FC

I attribute deposition of the sequence at FC to an aggrading sequence of subtidal to upper intertidal environments. The basal unit of unvegetated interbedded silts, sands and mud that grades upward to brown mud likely represents subtidal and lower intertidal deposition. The appearances of singular and patches of *B. maritimus* and *T. maritima* that appear in places at the higher end of this unit likely grew in incipient tidal marshes (mid- to upper intertidal). The color change of the mud at CC and the reduction in the abundance of plant fossils suggests the gray mud between CC and LL was deposited on unvegetated tide flats of low incipient marshes (lower to mid-intertidal), maybe as the result of localized submergence, as evidenced by diatom counts (E. Hemphill-Haley, unpublished data, 2001). This submergence would have been local to only the FC outcrop, as it is not seen in other outcrops.

Between markers LL and PS, the more plant-rich, massive and laminated unit I interpret as upper intertidal to supratidal salt marsh deposits. Laminae in intertidal environments typically represent tidal or seasonal fluctuations; the white laminae might represent annual varves sourced from spring glacial melting at Mount Rainier.

The two silt layers LZ and UZ that are within the peaty brown mud are likely to be Duwamish River flood deposits. Their thickness and persistence in the outcrop differentiate them from other laminae, suggesting they represent unusual events. While river floods or tsunamis can both produce tabular silt layers in outcrops (Martin and Bourgeois, 2012), these silt layers lack an obvious marine diatom signature that should exist if they were tsunami deposits (Hemphill-Haley, pers. comm., 2001). Therefore, they likely represent river floods from upstream.

The capping peaty soil I attribute to pasture following early 1900s diking. An 1875 survey map (Lawson, 1875) shows the predecessor of Kellogg Island prior to dikes, though dikes are mapped along the edge of Georgetown Terrace (Fig. 2.3). A map from 1899 (T-2421, Gilbert, 1899) and 1901 (Westdahl, 1901) include the dikes. By the 1940s (Fig. 2.3), the dikes had been removed, allowing tides to deposit mud atop the sequence; this is the likely source for the gray mud with *T. maritima* that overlies the peaty soil. The uppermost unit (mud and debris) I interpret as historical fill deposited during tide flat reclamation projects.

2.4.4 Stratigraphic age model at FC

To model the age of sediments and stratigraphic markers at the FC site, I constructed a stratigraphic model in Oxcal that aligns ages in stratigraphic order in a simple, uniformly distributed sequence (Fig. 2.6). I placed ^{14}C ages sequentially and contiguously where stratigraphic order was obvious from the outcrop. Where the position or species of the ^{14}C sample made its stratigraphic position unclear, I grouped it in a "Phase" with other adjacent samples within a well-defined stratigraphic zone. "Phase" function in Oxcal assumes that ages are uniformly distributed within the Phase, but that they can occur in any order (i.e., every sample in the phase has an equal likelihood of occurring at any time within that phase). I did not include a modeled sedimentation rate or information about the spacing between the samples. This induces some error into the model, since the uniform distribution will consider each sample in sequence without taking into account that some samples may be much more widely spaced than others. This may have the result of skewing the posterior ages away from times where many samples were collected and towards times where fewer samples were collected. For the same reason, I did not include in the sequence model known ages of the earthquake in 923–924 CE that occurred prior to the formation of the marsh, or the formation of the soil inferred to ca. 1915 CE.

From stratigraphically low to high, the model includes a phase of three *T. maritima* draped by sand at contact CC (Fig. 2.5). The three *T. maritima* grew in the same clump and likely died around the time the sand was deposited, as the sand mantles them, and they do not continue above the sand. In phase, the three *T. maritima* and modeled time of venting output to 990–1130 cal yr CE. (Note that this age is constrained by the overlying ages in the model; I use a broader

range (990–1150 cal yr CE), derived from only the *T. maritima* that underlie the sand, as a more conservative age for the timing of sand deposition, as described in section 2.4.6 and Appendix 2.2.)

Two *B. maritimus* corms directly overlie the sand; these serve as minimum ages and are modeled in phase (Fig. 2.6) since *B. maritimus* corms are injected below the ground surface, so it is unclear whether one grew first, or whether the plants were growing concurrently. These likely predate or overlap in time with LZ, the posterior age for which is 1025–1159. This age is sensitive to model parameters because the geologic constraint is not good. I added a boundary to denote non-overlapping time between the lower silt and following strata. After the lower silt is a phase including a *B. maritimus* corm that sits atop of the lower silt and a *T. maritima* leaf base collected 4 cm above LZ.

Above this are a sequence of eight *T. maritima* in stratigraphic order, placed centimeters apart. Three predate UZ and five postdate it, limiting the posterior age of UZ to 1349–1436. Two samples of T. maritima, samples 6 and 9 of Table 2.1, were collected ~37 m to the north. I excluded these samples from the model because their lateral distance from the other samples made it unclear where they should be placed in the sequence. Instead, I used them as an independent test on the age of UZ (Oxcal sequence model and output in Appendix 2.3); the output age is consistent at 1326–1424 cal yr CE.

The youngest dated *T. Maritima*, among the highest seen in the outcrop, has a posterior age of 1488–1631. Above this, 40 cm of outcrop contains at least one more distinctive gray silty layer before reaching the peaty soil attributed to ~1914 pastures. If 40 cm of sedimentation occurred at the same rate as the 40 cm of tidal marsh sediments below it, the sediment between the highest *T. maritima* (1488–1631 cal yr CE) and the peaty soil emplaced in ~140 and ~490 years.

2.4.5 Deposits and interpreted environments at other sites

Muddy sandy deposits were also described and interpreted at the other sites in the post-uplift intertidal fill (sites SN, SS, KN, KC, KCS, and KS of Fig. 2.3; observations presented in Figs. 2.8–2.15). These deposits largely follow a similar sequence to that at FC (interbedded silts and

sands of lower-intertidal tide flats grading to mud and peaty mud of mid-to supratidal tidal marshes), and in some places a cap of historical soil. Individual outcrops display occasional localized divergences from this sequence (e.g., a channel and fill at site KN, Fig. 2.11, and the sand deposits described as evidence for liquefaction below). None of the other sites studied displayed persistent tabular silt layers that could correlate with LZ and UZ, nor did they display evidence for localized submergence seen at the CC contact at site FC.

2.4.6 Evidence for liquefaction

Evidence for liquefaction and fluidization during earthquakes consists of sand dikes and sand blows that I infer to have been injected into or ejected atop intertidal mud (examples shown in Fig. 2.7). Sand was seen at all sites; sand deposits at five out of seven sites are attributed to liquefaction. Evidence consists of 21 tabular sand dikes and two sand-blow horizons. Both horizons consist of multiple coalescing sand blows. The horizon at FC contains abundant silty intraclasts. Dikes vary in width from < 1 cm to 6 cm, consist of gray-to-black fine to medium sand, commonly contain silty intraclasts and rare silt laminae. Dikes crosscut visible strata and end either at the ground surface, within an outcrop, or at a sand lens; some branch, anastomose, or form en echelon steps.

Radiocarbon dating and cross-cutting relationships show that at least two and as many as six episodes of liquefaction are recorded in Duwamish outcrops (Table 2.4; Figs. 2.17, 2.18). Since all of these outcrops consist of intertidal mud that formed inset into the terrace uplifted in the 923–924 CE SFZ earthquake, all of these episodes of liquefaction post-date that event. Event A is evidenced by convoluted beds of lahar-runout sand as seen in peels and described by Zehfuss (2005). Event B is evidenced by widespread sand blows and dikes at contact CC of site FC (Fig. 2.4). One or more events, herein called Event(s) C, is evidenced by sand blows and dikes at site KC (evidence KC-e, Figs. 2.8, 2.9), and dikes at four other sites; these features overlap in time with one another and may represent the same or disparate events. At FC, dikes crosscut the Event B horizon (evidence FC-i, Fig. 2.4). Dikes are present at three other sites (evidence SS-i, KN-i, KCS-i) (Figs. 2.10-2.14).

Earthquake-induced liquefaction is the most likely process that emplaced the observed sand dikes and associated sand blows. Artesian conditions can produce sand boils that may resemble seismically induced features (Obermeier, 1996), but tend to form spherical, rather than tabular dikes. Streambank slumps and landslides can also produce sand dikes not associated with earthquake shaking, though are unlikely to produce sand blows. While I noted evidence for localized slumps in the riverbank outcrops, these were relatively small (a few meters in extent) and evidenced mostly by disruption of the horizontal laminae in the mud. Flood or tsunami deposits could explain a sand deposit at a stratigraphic contact, though such deposits more typically form more uniform and extensive sheets that thicken landward or seaward (Martin and Bourgeois, 2012) and would lack a mechanism to the produce sand dikes that are associated with the sand blows.

Timings of events are constrained by individual radiocarbon ages. For Event B, though I constructed an Oxcal sequence for the outcrop, I estimated the age of the venting conservatively by only using the age of the nearest ^{14}C samples, which is described more in the next section. Maximum ages of dikes of Event(s) C are constrained by ^{14}C ages that date the strata they pass through. Evidence KC-e of Event(s) C, sand blows observed and dated in 1997–1998 (Figs. 2.8G, H; 2.9A, C), occurred prior to *B. maritimus* rhizomes that grew in mud deposited atop the sand blows. The events are described in detail below.

2.4.7 Event A – disturbed bedding at depth described by Zehfuss (2005)

Event A is reserved for the large-scale subsurface liquefaction of lahar-runout deposits that were described by Zehfuss (2005) and detailed in section 2.2.4.3. This evidence consists of disturbance of bedding at depth that postdates 278–535 cal yr CE and one dike that approaches the pre-923–924 ground surface. This liquefaction might have occurred during the 923–924 CE SFZ earthquake or later.

2.4.8 Event B – sand blows and dikes at FC

Event B represents the first event known to post-date the SFZ uplift of 923–924 CE. Sand dikes and blows at the FC outcrop evidence an earthquake that produced liquefaction reaching the ground surface above horizon CC (Fig. 2.4). Along the outcrop, seven sand dikes terminate at

or near the level of sand lenses: either at the eroded bench in front of the outcrop (n = 4), at the base of a sand lens (n = 3.). The sand dikes are tabular, widen downwards, and are mostly parallel. Several persistent sand lenses are horizontally aligned at a stratigraphic level across more than 50 m of outcrop (Fig. 2.4). The lenses range in thickness from < 1 cm to > 12 cm. At one location, a sand lens drapes over a mound of *T. maritima* leaf bases (Fig. 2.5). Many intraclasts similar to the underlying mud are present within the sand lenses. Horizontally aligned sand lenses were likely vented onto the ground surface, fed by dikes. The sand lenses are unlikely to have formed as sills since leaf bases of *T. maritima* grew at the surface of the former marsh and the sand drapes them.

The tabular and subvertical, and largely parallel nature of the sand dikes suggests they may have been produced as lateral spreads. For example, the 1964 Alaska earthquake produced extensive liquefaction that resulted in landspreading, in which land moved towards channels and other topographic depressions (McCulloch and Bonilla, 1970). This spreading resulted in a network of cracks, highest in density adjacent stream channels, from which extruded sediment and water. Not all of the field evidence supports an interpretation as lateral spread: the dikes tend widen downwards (lateral spreads tend to widen upwards), and the dikes are filled with sand (lateral spreads may eject sand, but may not be filled with sand). Regardless, proximity to a tidal channel of the Duwamish River may have influenced the location and density of the dikes at FC and other sites, similar to the 1964 Alaska example.

The implied earthquake likely dates to 950–1150 cal yr CE, the combined age of the three T. maritima that are draped by the sand (Fig. 2.5). The derivation of this age is discussed in Appendix 2.2. The *T. maritima* leaf bases that directly underlie the vented sand provide uncommon stratigraphic precision for ^{14}C dating of liquefaction. Where typically there is an unknown period of time between the age of a ^{14}C sample and the age of event, in this example, there is good stratigraphic evidence that the sand was deposited at the time the *T. maritima* were absorbing carbon at the ground surface. Therefore, the age of death of the *T. maritima* is the same as the age of the event.

2.4.9 Event(s) C – later sand blows at KC and sand dikes at four sites

At least one and up to five later events are evidenced by sand blows at KC and sand dikes at four sites (Fig. 2.15). Sand blows and dikes at site KC (evidence KC-e) (Figs. 2.8, 2.9) indicate an event that post-dates Event B and may predate, postdate or correspond with dikes at other sites (described below). At KC, fine horizontal sand lenses met by vertical dikes were observed by B. Atwater and others in the early 2000s (Fig. 2.8). Thirty grams of *B. maritimus* corms and culms sampled above the lens limit the age of emplacement to before 1489–1635 cal yr CE.

Additional sand dikes at four sites must also post-date Event B, but may have occurred in the same event as the sand blows KC-e. At site FC (Fig. 2.4), four dikes extend above the Event B sand horizon (evidence FC-i of Fig. 2.17). Two of these crosscut the sand horizon and three are present above LZ, suggesting at least some of these dikes post-date the age of LZ, 1030–1160 cal yr CE. At KN (Fig 2.10, 2.11), a bifurcating dike crosscuts strata bearing two chunks of detrital bark that date the dike to some time after 1220–1280 cal yr CE (KN-i). At SS (Fig. 2.12), a dike crosscuts strata bearing a growth-position *T. maritima* that limits the age of the dike to after 1230–1300 cal yr CE (SS-i). At KCS (Figs. 2.13, 2.14), a sub-horizontal dike crosscuts laminae bearing a *B. maritimus* corm that dates to 1460–1630 cal yr CE. Another *B. maritimus* corm above the sand dike dates to a similar age range, suggesting the dike was emplaced around or after 1450–1630 cal yr CE (KCS-i). These dikes (FC-i, KN-I, SS-i, and KCS-i) all post-date Event B but could have all been produced by the same or separate Event(s) C.

2.4.10 Sand lenses or layers not attributed to liquefaction

A sand horizon within mud at SN (Appendix 2.1.2) may have been emplaced by sand venting onto the ground surface, but can instead be explained as a channel fill, so it is not included in the catalog. No dikes terminate at the sand and the sand layer rests unconformably above gray mud. Ages on *T. maritima* below the layer and *B. maritimus* above the layer were put in sequence (Appendix 2.1.2) to model the age of deposition of this layer. Sand deposition occurred between 1428–1592 cal yr CE.

A bedded sand horizon at KS (Appendix 2.1.1) is also not attributed to sand venting. The horizon, 11 cm thick, consists of dark gray silty sand with few silt seams. Thinner beds of sand

are interbedded with gray peaty laminated mud. Two *T. maritima* growth-position leaf bases that extend into the base of the sand limit the age of deposition to near or just after 1041–1215 cal yr CE.

2.5 DISCUSSION

2.5.1 Evolution of the Duwamish marsh following uplift 923–924 CE

Ages presented here suggest marsh plants had established in the post-earthquake Duwamish marsh within 100 years of the uplift (Fig. 2.15). The oldest age of an in-situ marsh plant (*T. maritima* at FC, 987–1150 cal yr CE) suggests the Duwamish tidal marsh had begun establishing by at least ~60-230 years following the uplift. Based on outcrop ages, the marsh moved northward and it aggraded with time (Fig. 2.16). The first post-uplift liquefaction (Event B) occurred in the incipient marsh at FC while only the southernmost outcrops existed. Following localized subsidence at FC, perhaps accompanying compaction associated with the liquefaction of Event B, the marsh aggraded at FC and incipient marsh developed farther north. By ~1400 CE, all of the outcrops studied had begun to aggrade. By 1875 CE, the marsh existed as shown on historic maps (Lawson, 1875; Fig. 2.2).

2.5.2 Challenges in attribution of liquefaction events to particular earthquakes

Attributing ages of liquefaction to specific earthquake sources or even the type of source in the Puget Lowland is challenging because deep earthquakes, which have no other geologic signatures than shaking proxies, can never be ruled out. At localities like the Duwamish, where evidence for liquefaction is not accompanied by other evidence for fault rupture (e.g., land-level change or tsunami), age provides the only basis for correlating liquefaction at a site with other regional events.

The geologically precise age of the Event B venting provides an age constraint for ground shaking to which other regional liquefaction events can be compared (Fig. 2.17). Prior to this study, liquefaction features in the Puget Lowland that span the centuries around the 923 CE Seattle Fault earthquake have been attributed to that event or to the cluster of other crustal fault ruptures that occurred in the same century (Table 2.3). With the exception of event B at the Snohomish delta (Bourgeois & Johnson, 2001), the age constraints for any of these liquefaction

features permit them to correspond instead to Duwamish earthquake B, which occurred about a century after the 923 event. The stratigraphic context within the Duwamish delta – inset into the 923–924 CE uplift terrace infilled by strata bearing earthquake B liquefaction features – uniquely distinguishes these two events. If Puget Lowland liquefaction features are to be used to inform ground shaking estimates from the 923 earthquake or other events, we must first acquire higher-resolution ages that can distinguish whether to attribute liquefaction to 923 or to the time of Duwamish earthquake B, prior to analyzing the regional catalog.

2.5.3 Possible sources and correlations for Event B

Duwamish Event B overlaps in age with a known Cascadia earthquake (event B of Nelson et al., 2021) (Fig. 2.15, 2.17). This age also overlaps with broad ranges for crustal fault events: an earthquake on the Tacoma fault, 770–1160 C.E. (Sherrod et al., 2003a) and a time of motion on the Seattle Fault backthrust Waterman Point scarp between 1010 and 1570 cal yr CE (Nelson et al., 2014). Deep slab earthquakes could also be a source for liquefaction of Event B, similar to the historical events in 1949, 1965, and 2001. If this were the case, liquefaction could be present at other regional sites without evidence for movement on a crustal fault.

Liquefaction that overlaps in time with Event B has been observed at all Puget Lowland sites where liquefaction has been observed (Table 2.3; Fig. 2.17). However, as noted above, with the exception of the Snohomish delta, ages for liquefaction at most of these sites cannot distinguish between liquefaction in 923–924 CE and Duwamish Event B. Snohomish Event B overlaps in time with 923–924 CE, and Snohomish Event C overlaps in time with Duwamish Event B (Bourgeois and Johnson, 2001). Turbidite deposits described from Lake Washington, another type of shaking proxy (Event B of Karlin et al., 2004), also overlap in time with this event. It is possible that these three events occurred as the result of the same earthquake.

2.5.4 Possible sources and correlations for Event(s) C

Ages of dikes and sand blows of Event(s) C are poorly constrained. They may overlap in time with dikes at the Snohomish delta (Snohomish Event E), turbidites in Lake Washington (Lake Washington Events C and D), and/or liquefaction at Issaquah Creek or the Nisqually delta (Fig. 2.17). The possibility that a subduction zone earthquake in 1700 produced one or more of these

dikes cannot be ruled out. However, it is notable that none of the dikes reaches the stratigraphic position of 1700, even at outcrops that were probably accumulating mud in that year (Fig 2.17).

2.5.5 Issue of completeness: Duwamish largely lacks recurrent liquefaction

The Duwamish liquefaction record largely lacks evidence for recurrent large-scale liquefaction, suggesting the Duwamish record is incomplete. Recurrent sand venting at the same outcrop, such as that described at Charleston, South Carolina (Obermeier et al., 1985; Talwani and Cox, 1985), the New Madrid Seismic Zone (Tuttle et al., 2000), and Christchurch, New Zealand (Giona Bucci et al., 2017), provides a baseline level of confidence that the geologic record of liquefaction approaches a complete earthquake catalog. The assumption that an earthquake record is near-complete is a precursor to inferring long-term fault behavior from liquefaction catalogs alone.

Unlike these other localities, no Duwamish site displays multiple episodes of sand venting (Fig. 2.15). At FC, a few sand dikes postdate the Event B venting, but there is no evidence that they reached a ground surface. Similarly, the venting (KC-e of Event(s) C) at KC, appears not to have occurred at the FC outcrop. Furthermore, none of the other sites obviously records multiple times of liquefaction. This "patchiness" of the Duwamish liquefaction record has several possible explanations: it could be the result of substantial limitations in the search for liquefaction or the result of a change in site conditions over time that changed each site's susceptibility to liquefaction.

The search for liquefaction features at the Duwamish delta is severely limited by the availability of outcrops. Industrialization has obscured nearly all of the delta sediments; most of the mud currently accessible is in the seven sites studied herein. Liquefaction, even widespread liquefaction, could have occurred at the delta and "missed" the seven sites studied in this chapter.

Furthermore, liquefaction susceptibility at each of these sites has almost certainly changed with time. As the marsh aggraded and expanded northward, the intertidal mud that forms the outcrops built upwards, thickening the impermeable cap atop the liquefiable layer(s) of lahar-runout sand below. Increasing the thickness of such a confining cap generally increases the peak ground

acceleration required to induce liquefaction of a buried sand body and reduces the height sand dikes can inject into the cap (Ishihara, 1985). An increased cap thickness of 1 m may be large enough to have an impact on the surface manifestation of liquefaction, though this also depends on the thickness of the liquefiable sand layer at depth and the strength of the shaking.

The following paragraph illustrates the possible scenario in which changes in the FC outcrop over time changed its capacity to record surface manifestations of liquefaction. The FC outcrop recorded sand venting 990–1160 cal yr CE, when the site was an incipient marsh (Fig. 2.16). By the 1400s, when dikes were injected at other sites, the outcrop had aggraded by 1 m, almost certainly reducing the liquefaction susceptibility of the sand below. Dikes at FC may date from this time period, but the dikes did not reach a ground surface. By 1700, when the CSZ earthquake occurred and the outcrop again failed to record liquefaction, the outcrop had aggraded ~20 cm more.

Proximity of the outcrops to a channel, in addition to vertical accretion, likely also changed with time and could have influenced the capacity of outcrops to record liquefaction. For example, the dikes at some or all sites could represent ground cracks that formed in proximity to a tidal channel, such as the cracks described after the 1964 Alaska Earthquake by McCulloch and Bonilla (1970). If this were the case, lateral migration of the tidal marsh away from each site would likely have reduced each site's capacity to record surface manifestations of liquefaction. In the Alaska example, sites less than 150 m from a channel experienced the most ground cracking, and ground cracking diminished substantially by 300 m away from a channel. Lateral migration of Duwamish tidal channels on this order is possible within the time frame studied, and may play a part in determining the liquefaction record at each outcrop.

Densification may also have resulted in a decrease in liquefaction susceptibility over time. An episode of liquefaction, such as that of Duwamish Event A or B, typically densifies sediments, which in theory reduces liquefaction susceptibility in subsequent earthquakes (Obermeier, 1996). Densification need not be uniform or ubiquitous, as demonstrated by counterexamples at many localities (e.g., Charleston, New Madrid Seismic Zone, and Christchurch as described above).

Nonetheless, densification provides one mechanism by which Duwamish outcrops might display liquefaction features from one earthquake and not subsequent ones.

These examples demonstrate that the Duwamish delta does not constitute a site where the record of liquefaction can be considered to be complete, and that an absence of liquefaction seen from these outcrops should not constitute evidence that no liquefaction occurred. This demonstration of patchiness motivates more detailed liquefaction mapping at similar sites in order to improve the regional liquefaction catalog. In particular, this could include revisitation of sites already studied, because as outcrops erode, different records may be exposed.

2.5.6 CSZ earthquake in 1700 not represented

Given the patchiness of the Duwamish catalog, it may not be a surprise that no evidence for liquefaction from 1700 was encountered. Nonetheless, the Duwamish delta adds to the localities where evidence for ground shaking associated with the M~9 CSZ earthquake in 1700 has been searched for and not found. Models of subduction zone earthquakes of this magnitude produce substantial ground shaking around Puget Sound (Wirth and Frankel, 2019) that is predicted to produce liquefaction (Rasanen et al., 2021). However, no liquefaction studies have yet identified these features. If these features exist at the Duwamish delta, they might be located farther seaward than the outcrops studied in this chapter.

2.5.7 Historic earthquakes not represented

Similarly, liquefaction occurred historically in the Duwamish valley in 1949, 1965, and 2001, though not at the Duwamish outcrops I studied (Fig. 2.2). Historically recorded liquefaction, with the exception of two sites, was concentrated in former tidal marshes that were filled, raising the question of whether it was the fill that liquified and fluidized instead of the underlying sediments. Alternatively, perhaps the earthquakes that produced Duwamish events A, B, and C were more strongly felt at the delta than the historic events.

2.5.8 Cascading hazards

Locally, modern liquefaction in the Duwamish estuary compounds potential hazards such as contaminated sediments. The waterway was named a Superfund site in 2001; contaminants are

concentrated in the sediments on the river bottom (EPA 2014). Contaminants come from multiple sources, including stormwater runoff, wastewater, and industrial practices. The potential for sediment disruption as has occurred during prior earthquakes and liquefaction to remobilize or move contaminants and disrupt cleanup or capping efforts has not been studied.

2.6 CONCLUSIONS

Liquefaction features from the Duwamish delta record at least two earthquakes. The geologic environment here provides an unusual opportunity for stratigraphically exact dating of liquefaction using in-situ marsh plants. The first recorded Duwamish liquefaction occurred a century or two later uplift of the delta during the 923–924 Seattle fault earthquake, at least one prior to 1489–1635, and possibly one between the two or after. Despite this evidence, though there are several unattributed dikes, there are no signs of vented sands emplaced during well-known earthquakes in 1700 CE or historically in 1949, 1965, or 2001, highlighting that the earthquake record as derived from liquefaction at this site is incomplete. These results suggest that in the Duwamish marsh, liquefaction has been a patchy recorder for earthquake shaking. If liquefaction occurred during all earthquakes, it did not produce features that persist in the limited remaining outcrops. Here, absence of observed liquefaction features does not suggest absence of earthquake shaking. Patchiness of recording at this site and evidence that the visible record has changed as outcrops erode motivates more efforts to produce a regional liquefaction catalog, including revisitation of old sites.

2.6 FIGURES

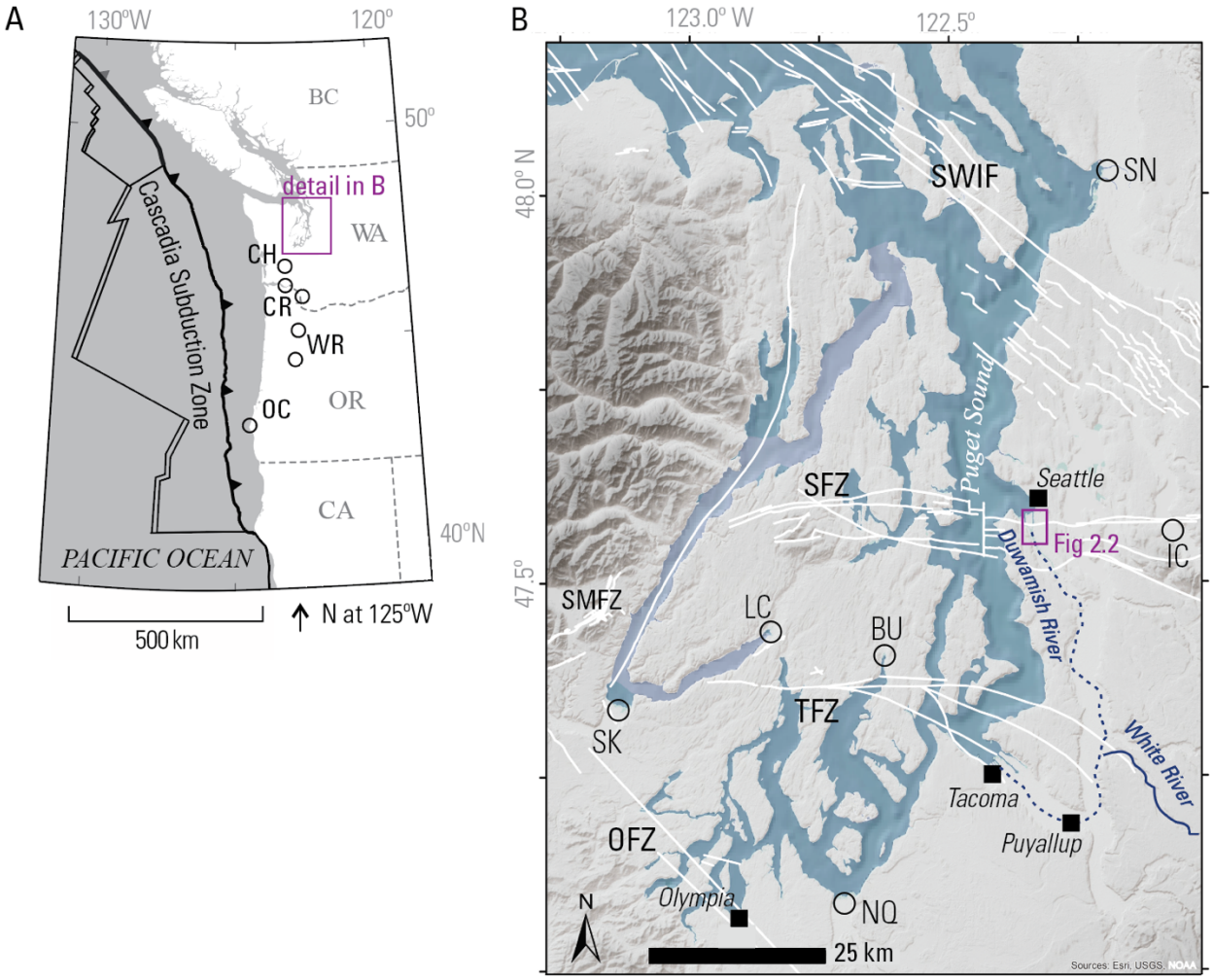

Figure 2.1. Index map. (A) Location of Puget Sound inland of the Cascadia subduction zone. Circles denote sites where late Holocene liquefaction has been reported and dated: at the Chehalis River (CH) (Obermeier and Dickenson, 2000), along and near the Columbia River (CR) (Obermeier et al., 1993; Atwater, 1994; Obermeier, 1995; Peterson and Madin, 1997; Obermeier and Dickenson, 2000; Takada and Atwater, 2004; Atwater, 2020), at the Willamette River (Peterson et al., 2014), and along the Oregon coast (OC) (Kelsey et al., 2002). (B) Puget Lowland and locations mentioned in the text, including Seattle, the Duwamish River, and crustal faults (white lines) (Angster, 2020): South Whidbey Island fault (SWIF), Seattle fault zone (SFZ), Tacoma fault zone (TFZ), Olympia fault zone (OFZ), and other deltas where liquefaction features have been described (citations in Fig. 2.17): Snohomish (SN), Issaquah Creek (IC), Nisqually (NQ), Skokomish (SK), Burley (BU), and Lynch Cove (LC).

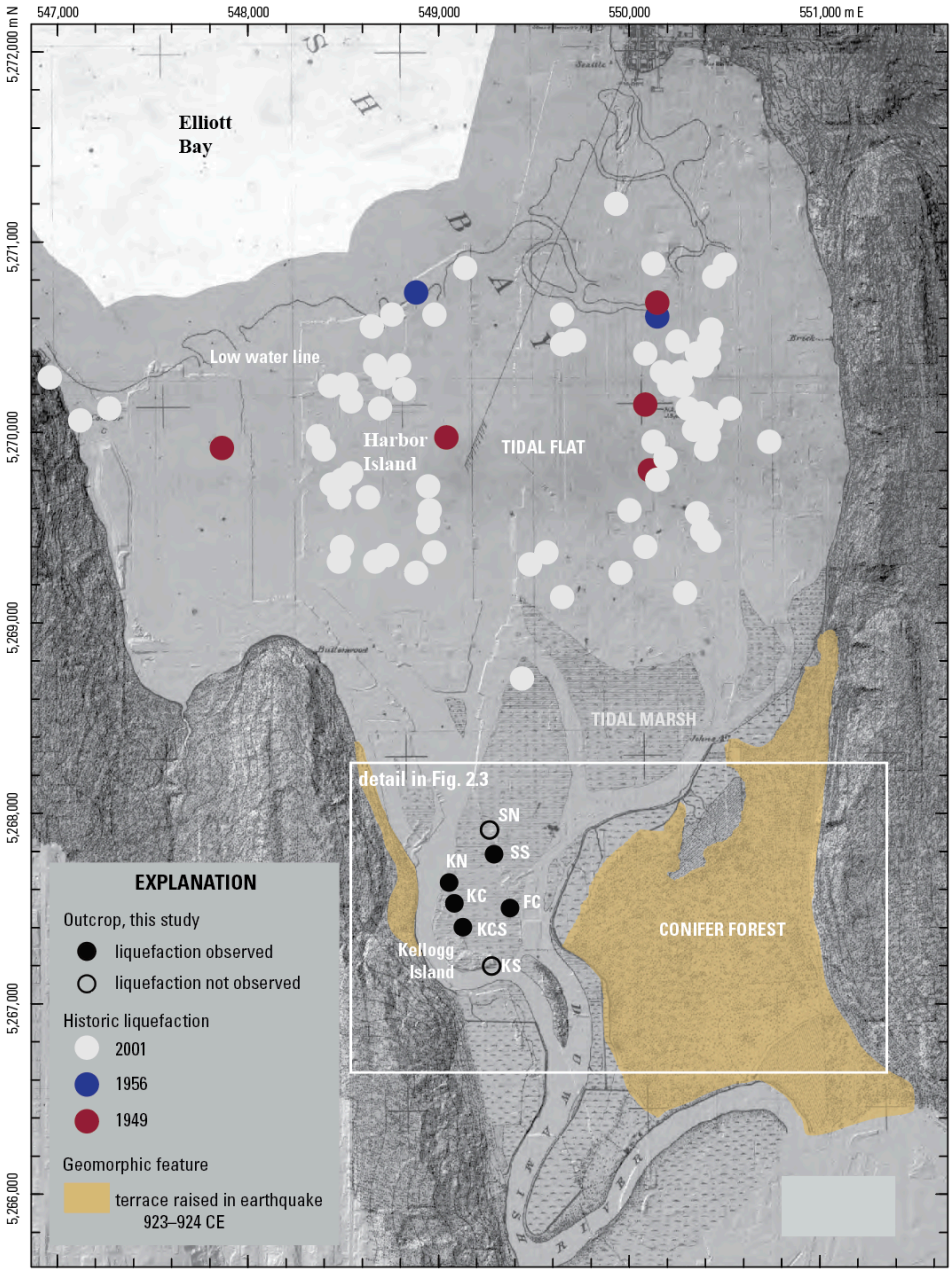

Figure 2.2. Map of the Duwamish delta showing places where historical earthquakes produced liquefaction, probably in artificial fill and locations of paleo-liquefaction features observed along the Duwamish Waterway. The base map shows an 1875 topographic survey (Lawson, 1875); different textures represent different vegetation types. Modern LiDAR is in faint relief in the background. Locations that were tidal flats in 1875 have now been covered by unconsolidated fill. Paleo-liquefaction may also have occurred in those locations, but if so, the geologic data are not accessible. The sites described in this chapter are in the former tidal marsh; liquefaction was preserved amongst the marsh strata. Historical liquefaction, documented following deep earthquakes in 2001 (Troost, pers. comm, 2019), 1965 (Chleborad & Schuster, 1998), and 1949, was digitized from paper maps for this study. Digitized historical datasets are available as supplemental data to this dissertation. Yellow shading shows the geomorphic terrace probably raised during the earthquake 923–924 CE (after Collins and Sheikh, 2005).

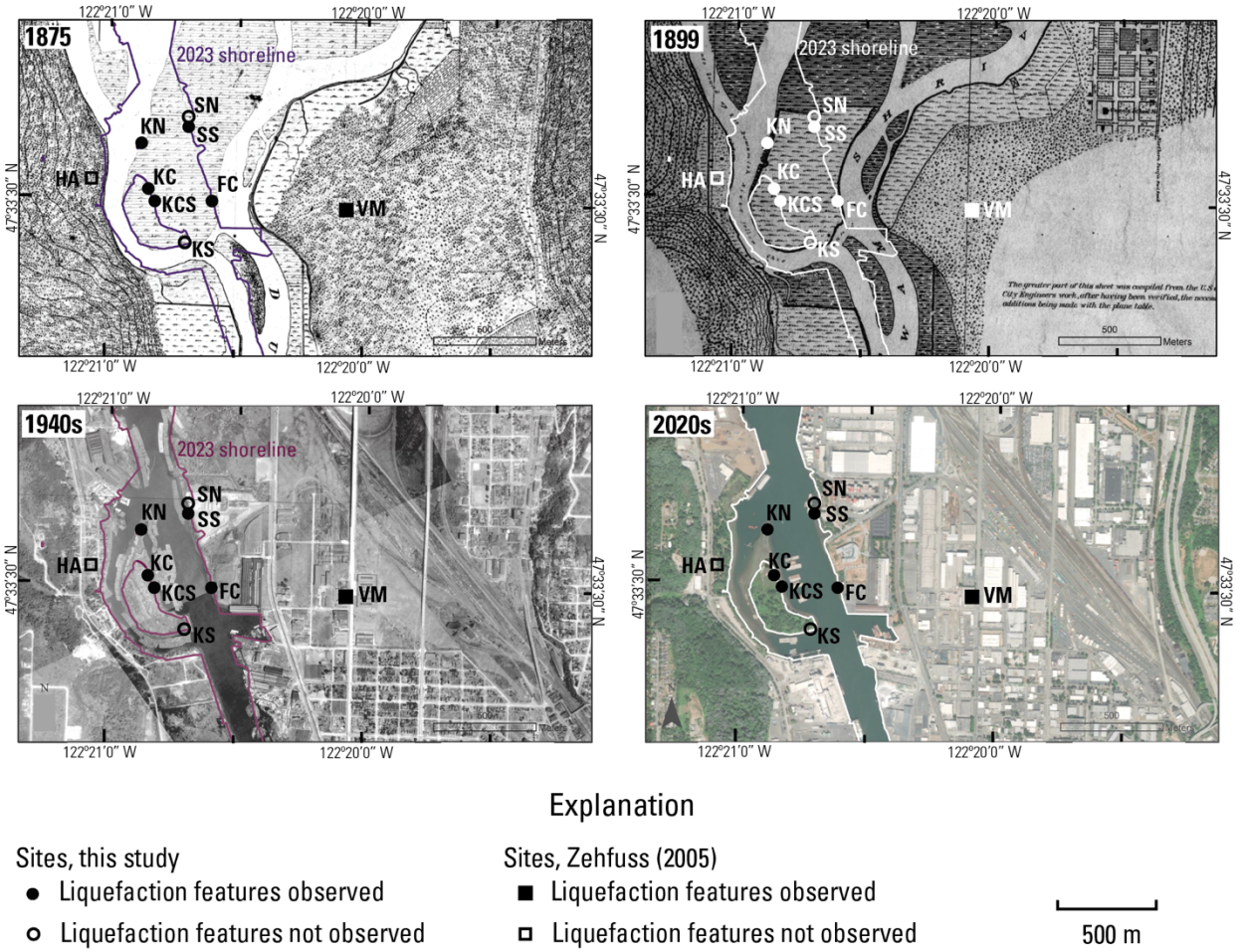

Figure 2.3. Locations of sites in this study and sites of prior observations presented by Zehfuss (2005). Sites are at Ha-ah-poos Village Park (HA), Kellogg Island (KN, KC, KCS, KS), Sbaquah (SN, SS), Federal Center (FC), and Vincent Metals (VM). Four maps from different years show progressive modification of the Duwamish delta; the trace of the 2023 shoreline is shown as lines on each map. In 1875 (upper left), a tidal marsh covered the sites (Lawson, 1875). Sites described by Zehfuss (2005) were forested terraces. The 1899 map (upper right) shows a diked pasture at the locations of the study sites (Gilbert, 1899). The 1940s (lower left) and 2020s (lower right) maps show the configuration of the modern shoreline. Outcrops described in this dissertation are located on the banks of the dredged waterway that cuts across the former tidal marsh island.

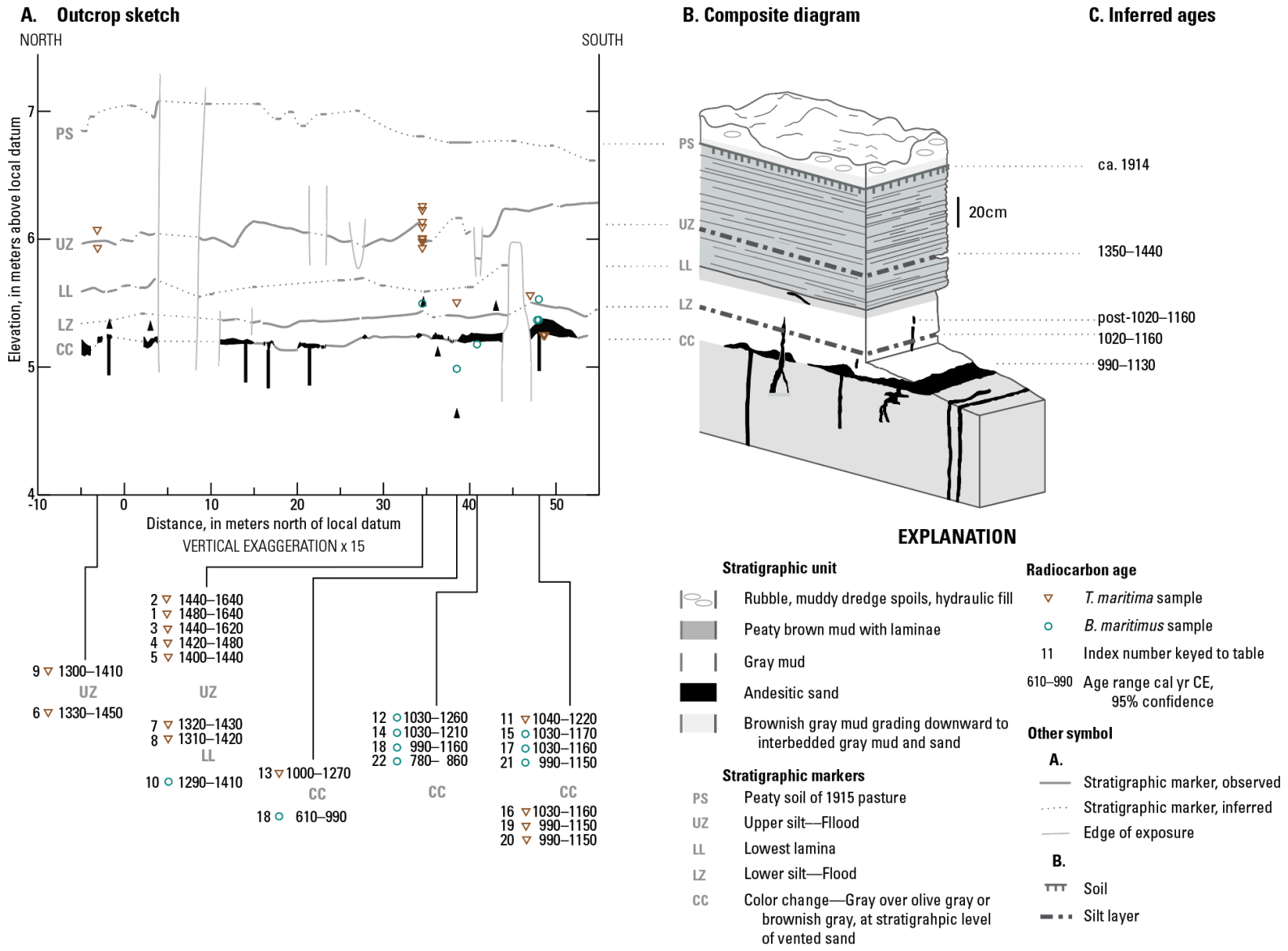

Figure 2.4. Stratigraphy at FC.

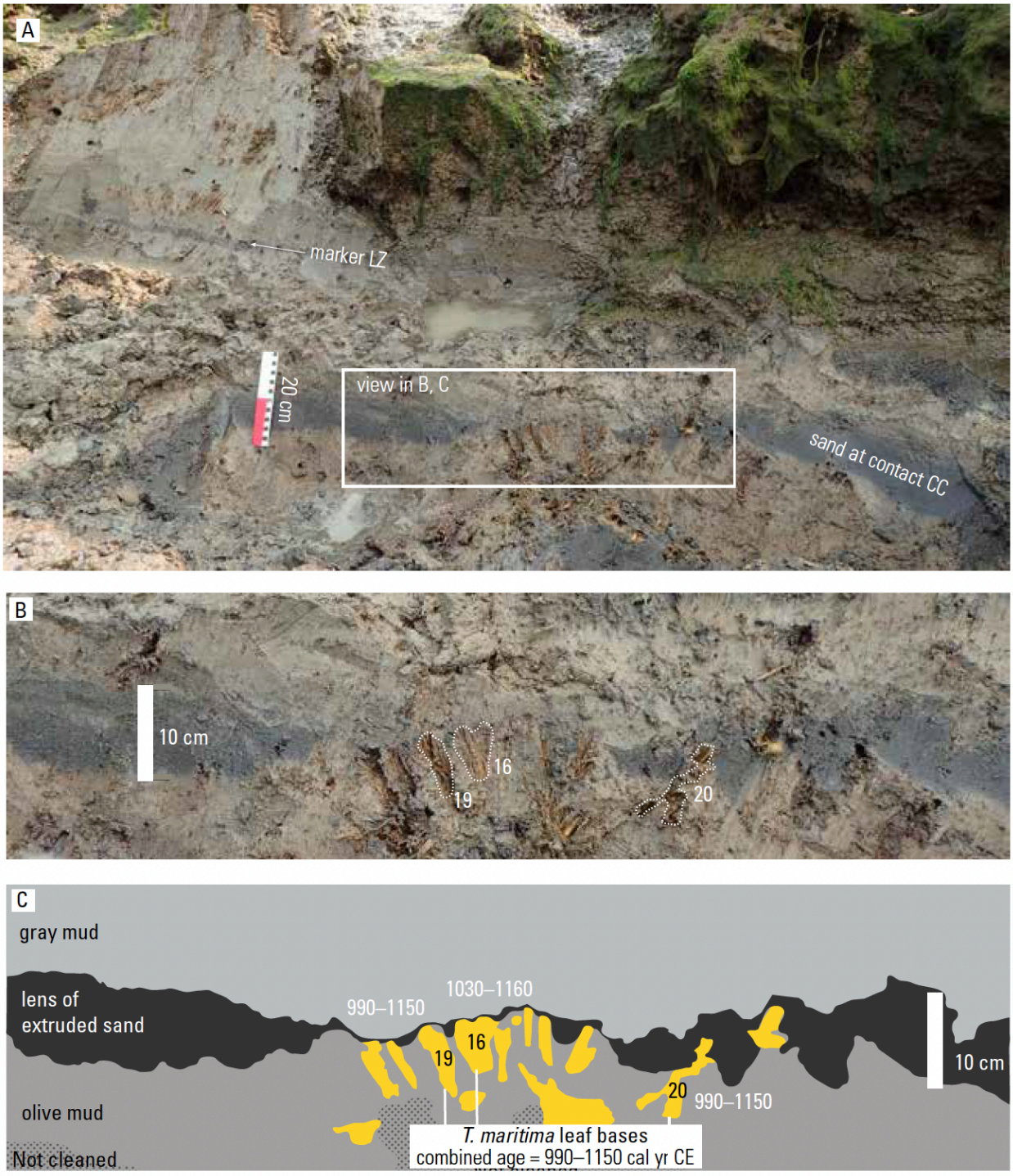

Figure 2.5. Context (A), photo (B), and sketch (C) of *T. maritima* leaf bases draped by sand of Event B at FC, (Figure 5, x = 48.5 m). Leaf bases of *T. maritima* grow at or just under the surface of a tidal marsh. The sand blow vented atop the surface of the marsh, covering the leaf bases, so the age of the leaf bases can be used as the age of the venting for Event B. Leaf bases are numbered according to 14C sample numbers listed in Table 2.1. Ages listed are 95% CI cal yr CE. (C) shows calibrated ages for each sample and the combined age for the three samples.

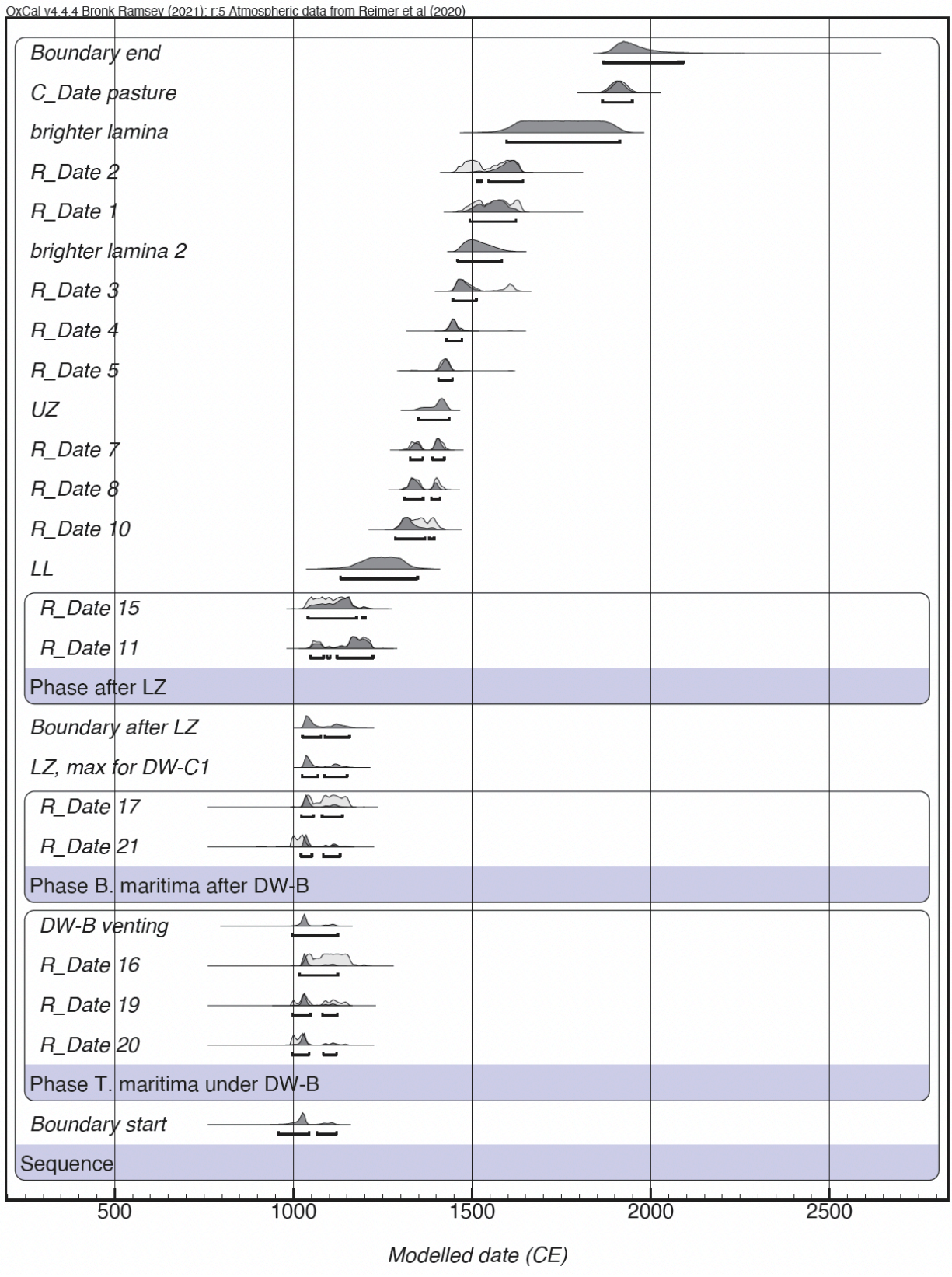

Figure 2.6. Age model at site FC.

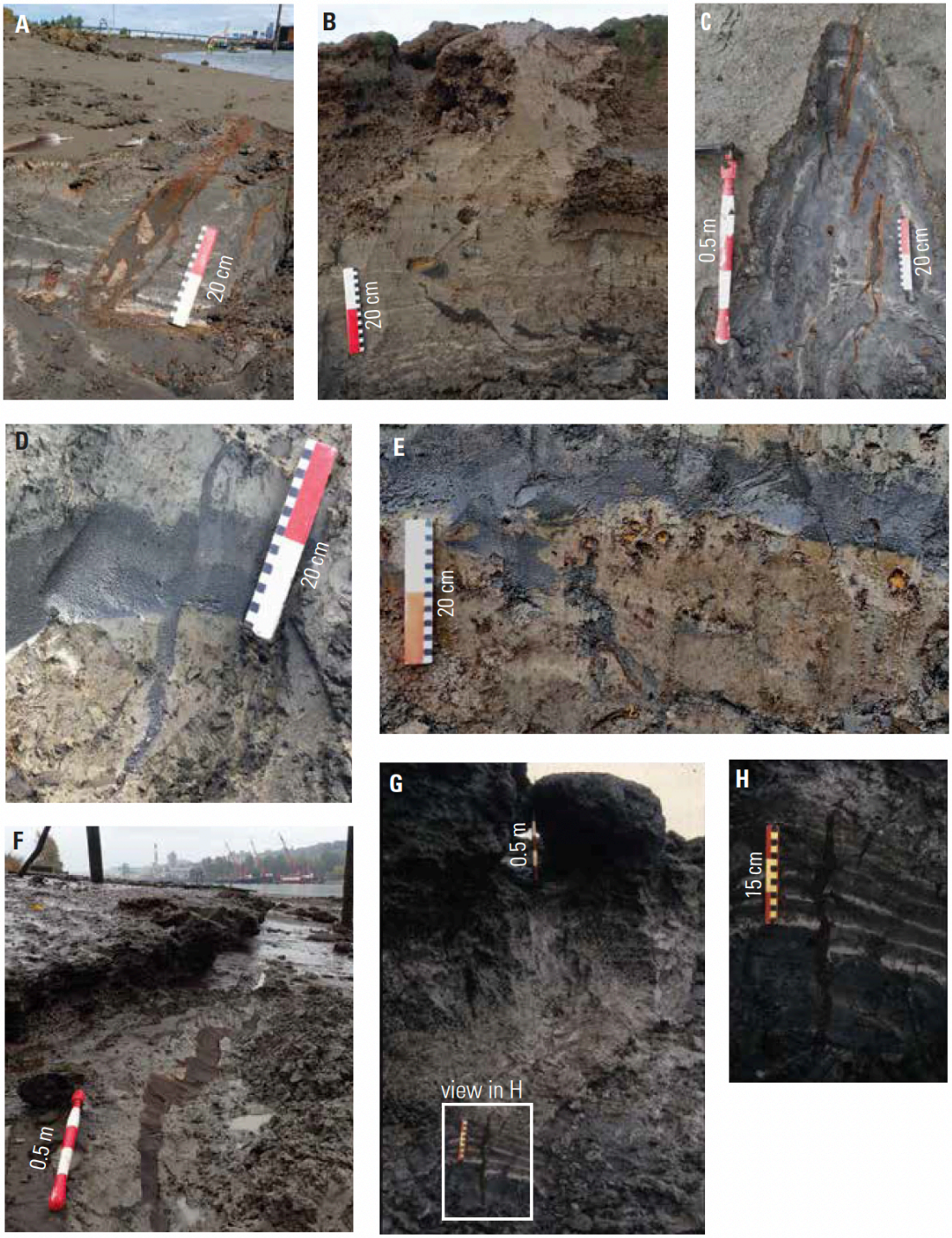

Figure 2.7. Examples of paleo-liquefaction features seen along the Duwamish Waterway. (A) Sand dike crosses tidal laminae and contains silty intraclasts, site KC. (B) Sand dike steps upwards across the outcrop at site KN. (C) Photo looking down: Sand dike forms en echelon steps in the intertidal bench at site KC. (D) Sand dike crosses vented sand horizon at FC. (E) Sand dike meets sand lens at site FC. (F) Sand dike crosses intertidal mud at site SS. (G, H) Sand dike crosses rhythmic laminae at site KC. In G, the dike extends from box for H up to the shovel handle in the background. Photo by Brian Atwater, 1998, used with permission.

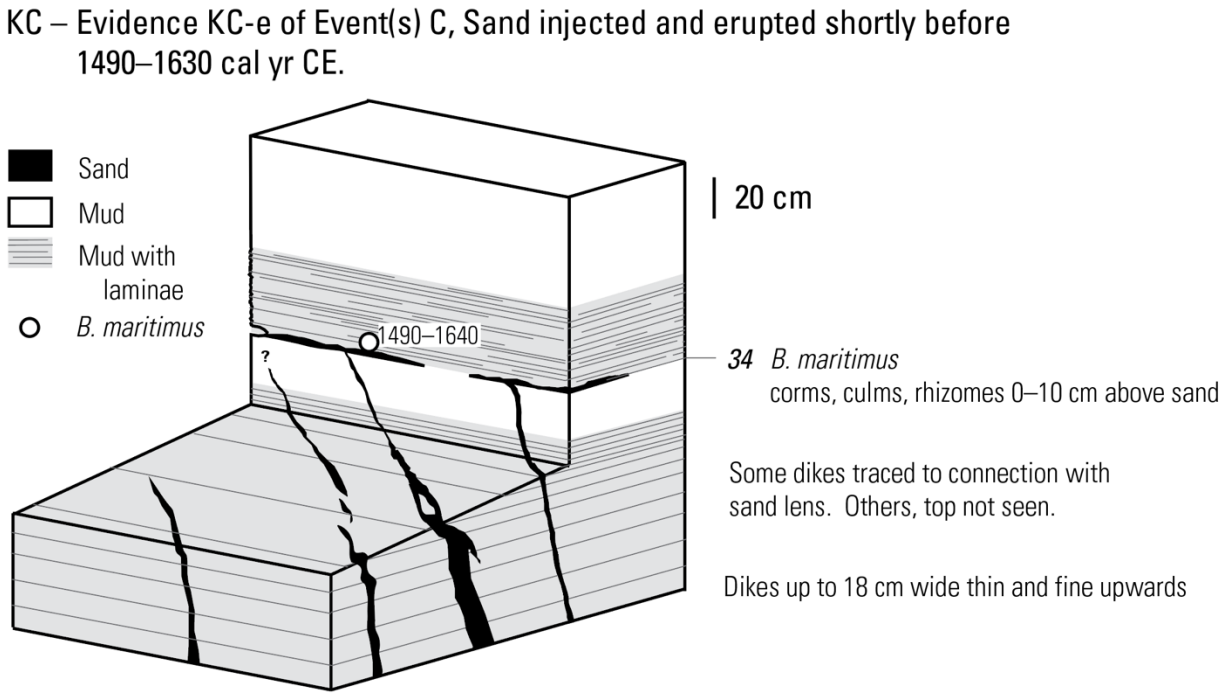

Figure 2.8. Stratigraphy, chronology, and liquefaction features (KC-e) of Event(s) C at site KC.

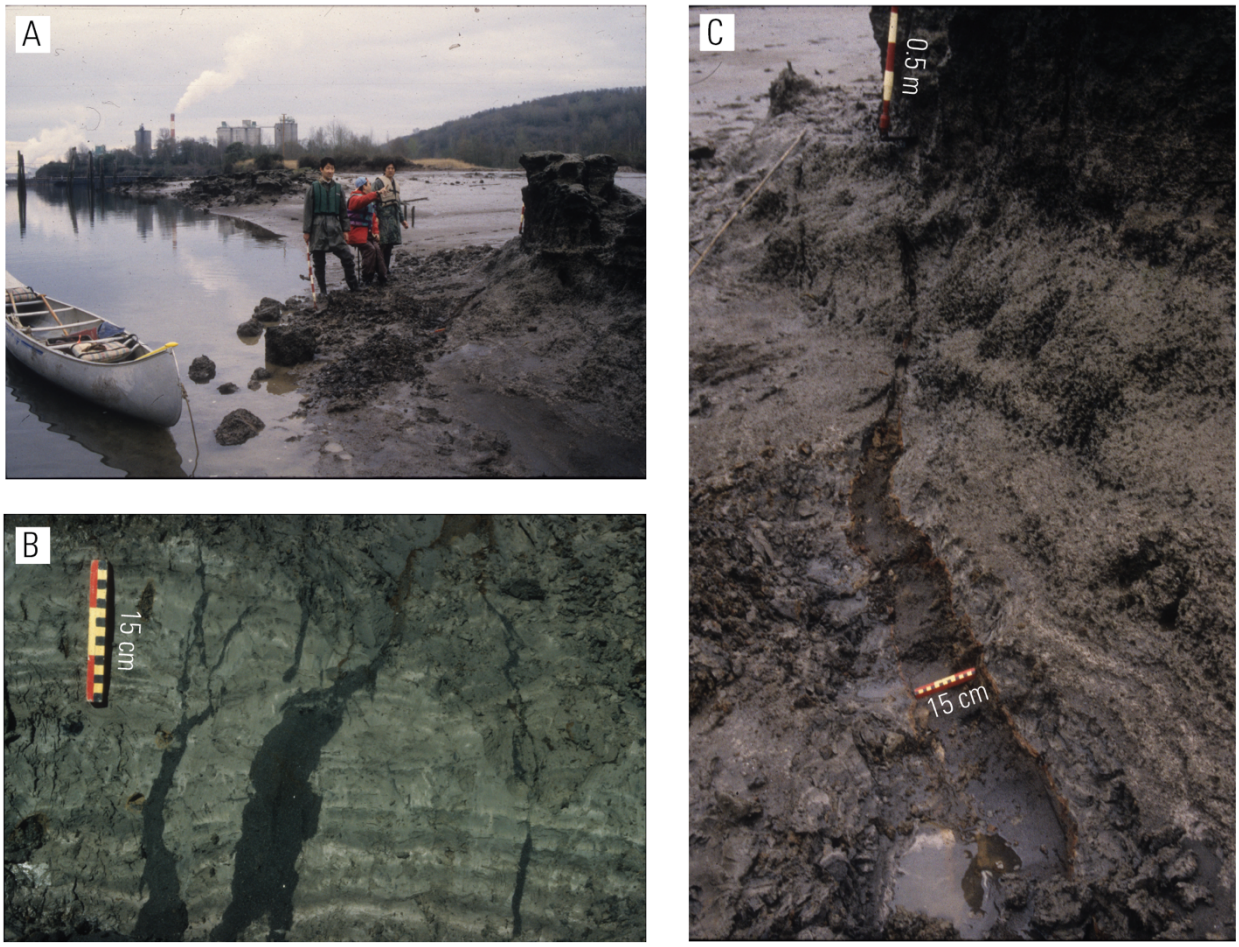

Figure 2.9. Photos at site KC, 1998 and 2000. (A) Outcrop on Kellogg Island in 1998, at the edge of the Duwamish Waterway, looking south. The muddy outcrop to the right of the people was largely eroded between the early 2000s and 2017. (B) Dikes anastomose and branch crossing white and gray laminae. Photo taken facing a cleared outcrop face in 2000. (C) A 15-cm wide dike crosses the intertidal bench and rises into the outcrop in the background in 1998, probably to the stratigraphic position of the shovel blade. Dikes such as this were traced to a vented sand lens (Fig 2.7). The venting occurred before 1485–1635 cal yr CE. This dike is in the same area as en echelon dikes pictured in Fig. 2.4C and dikes in Figs. 2.4G and H. Photos by Brian Atwater, used with permission.

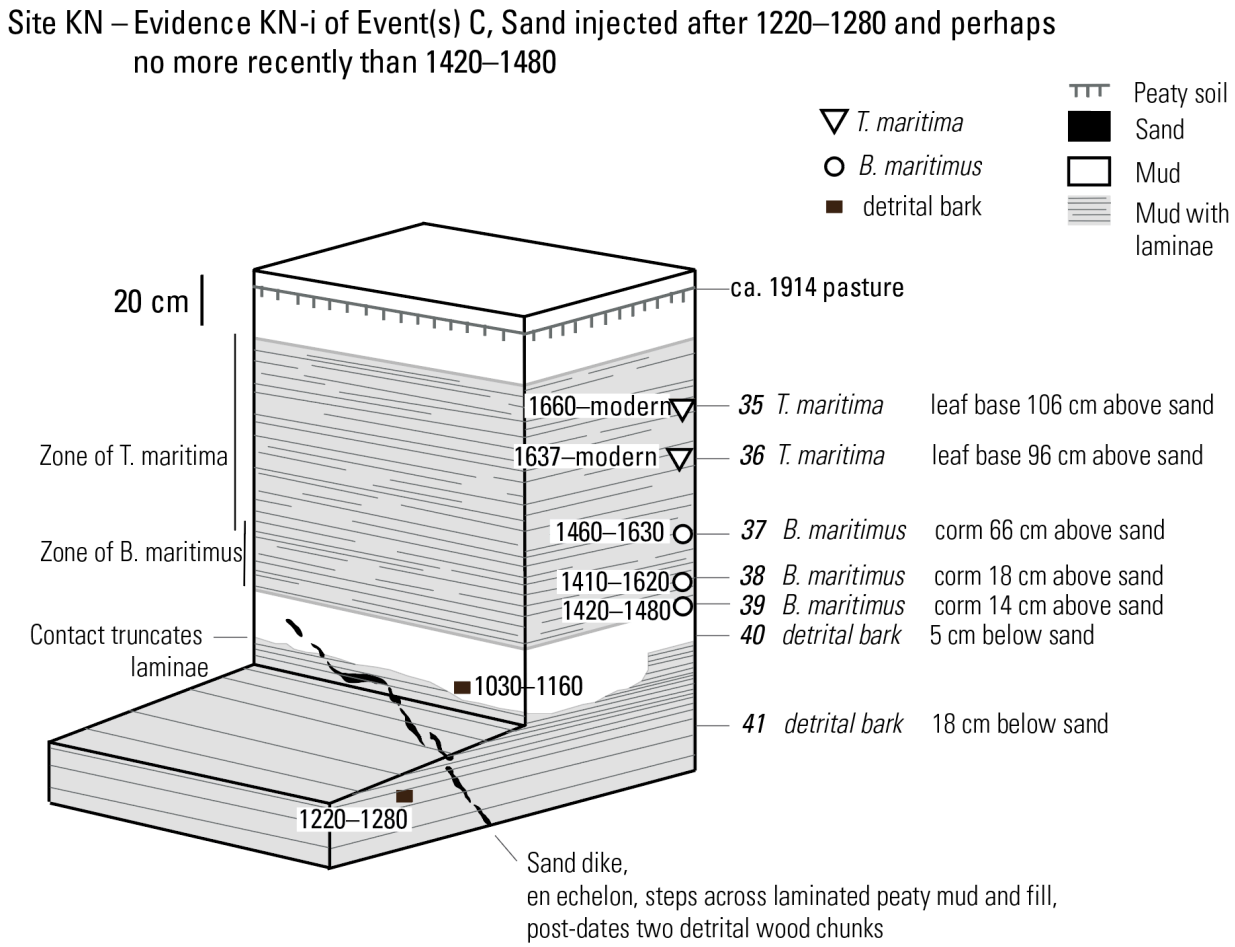

Figure 2.10. Site KN stratigraphy, chronology, and liquefaction features, evidence KN-i of Event(s) C.

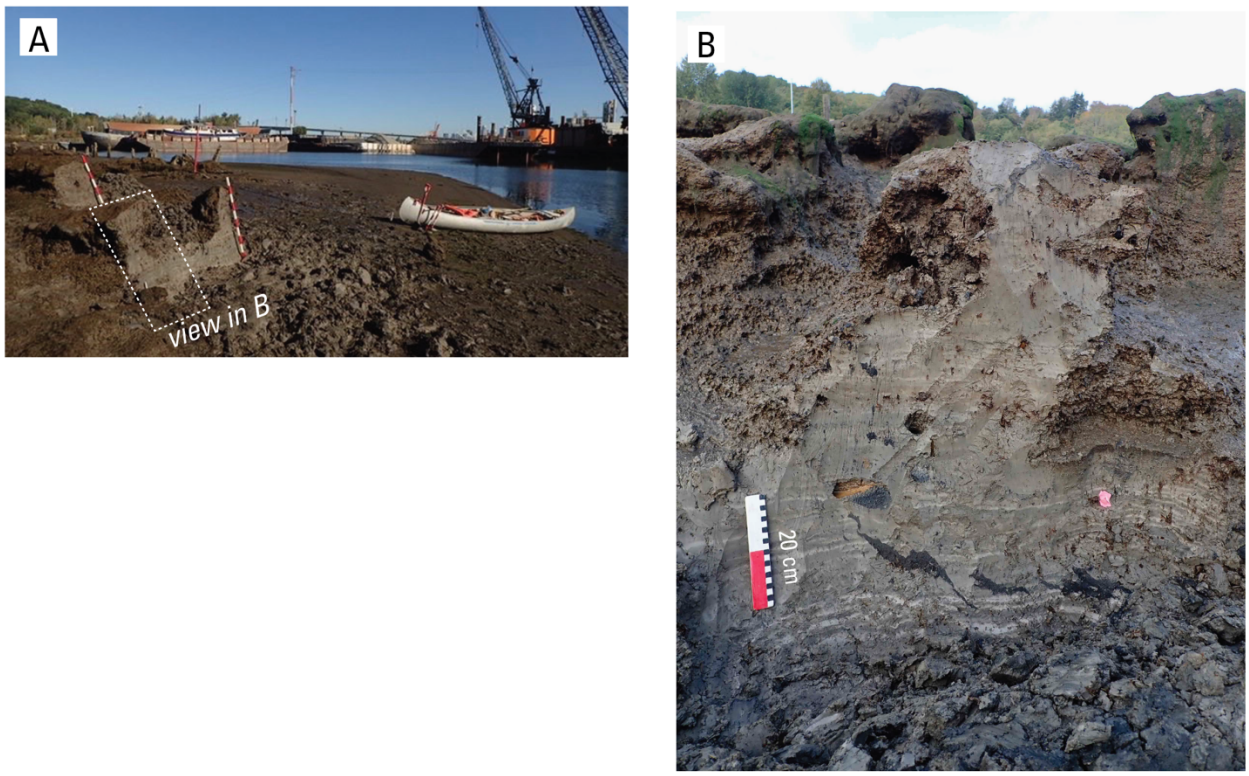

Figure 2.11. Site KN photos. (A) Outcrop at the northern end of Kellogg Island, on the west side of the modern Duwamish Waterway. Photo looks north. (B) Cleaned outcrop showing a dike of Event(s) C crossing white and gray laminae.

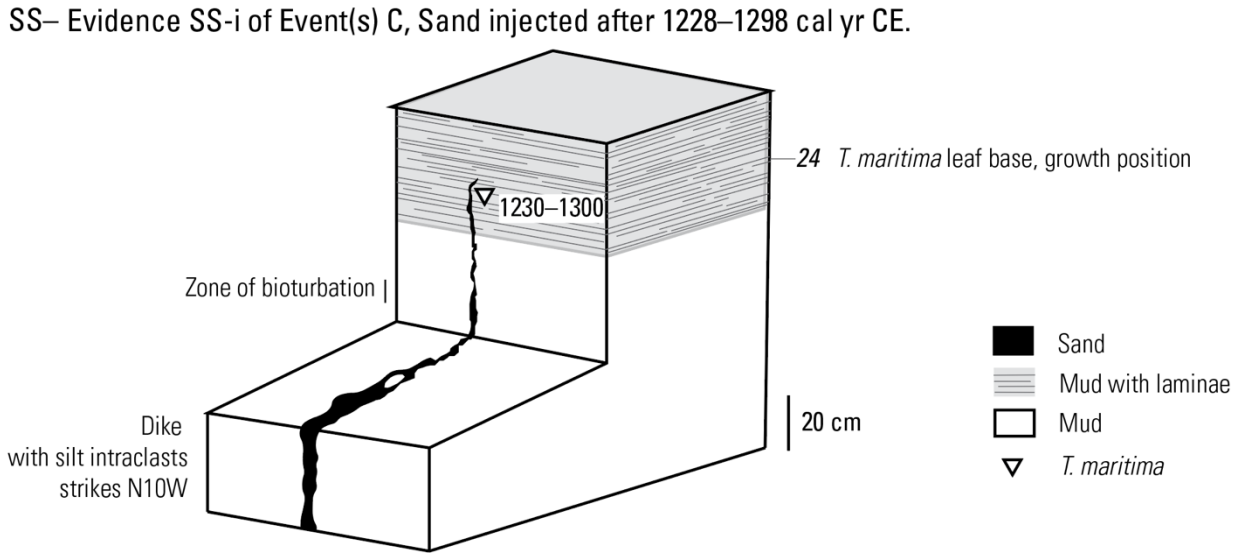

Figure 2.12. Stratigraphy, chronology, and liquefaction features at SS, evidence SS-i of Event(s) C.

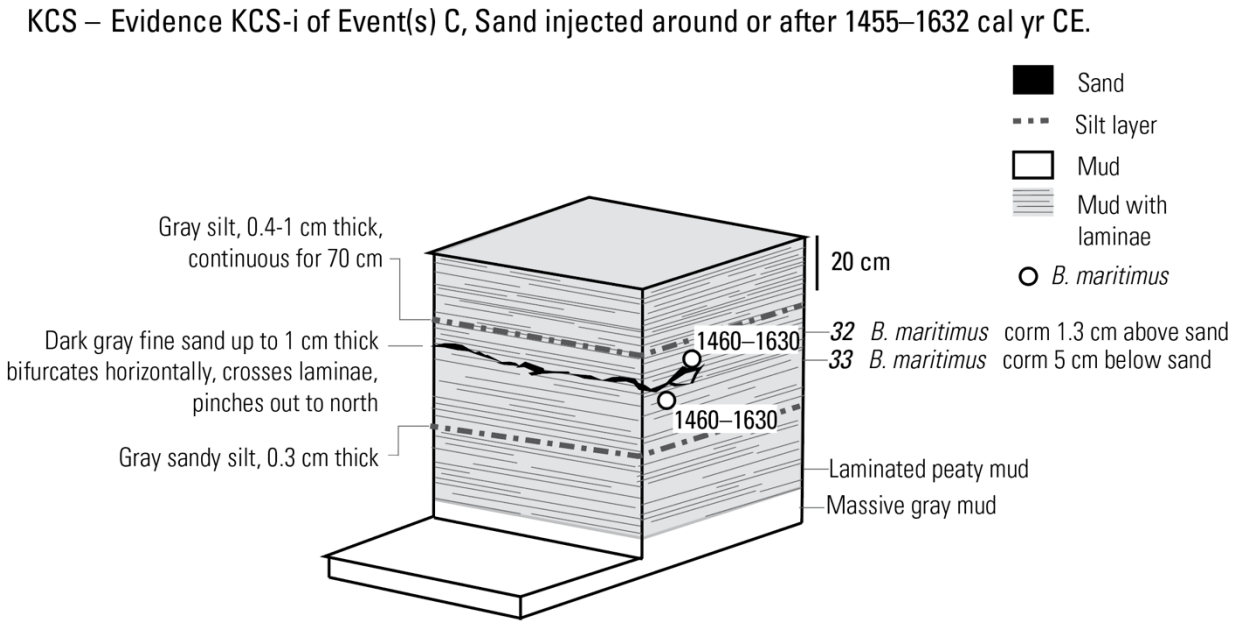

Figure 2.13. Site KCS stratigraphy, chronology, and liquefaction feature KCS-i of Event(s) C.

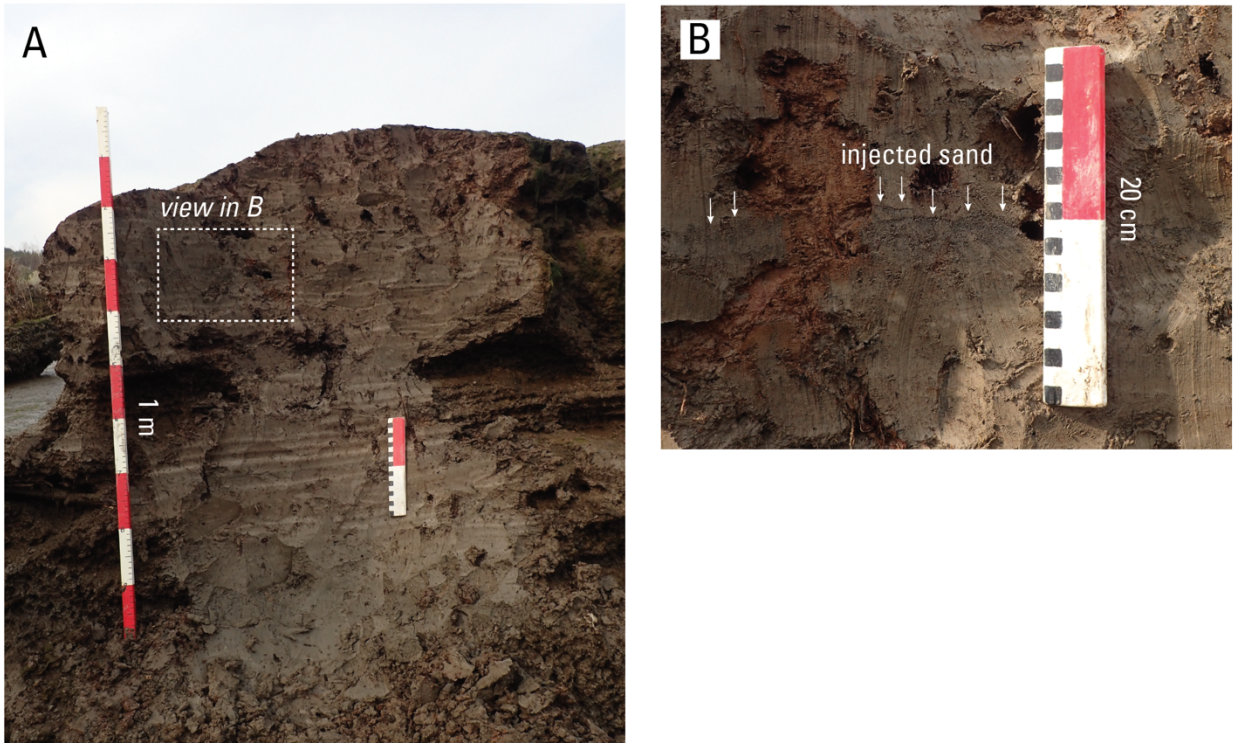

Figure 2.14. Photos at Site KCS. (A) An east-facing outcrop displays rhythmic laminae. (B) A thin sand dike of Event(s) C crosses these laminae.

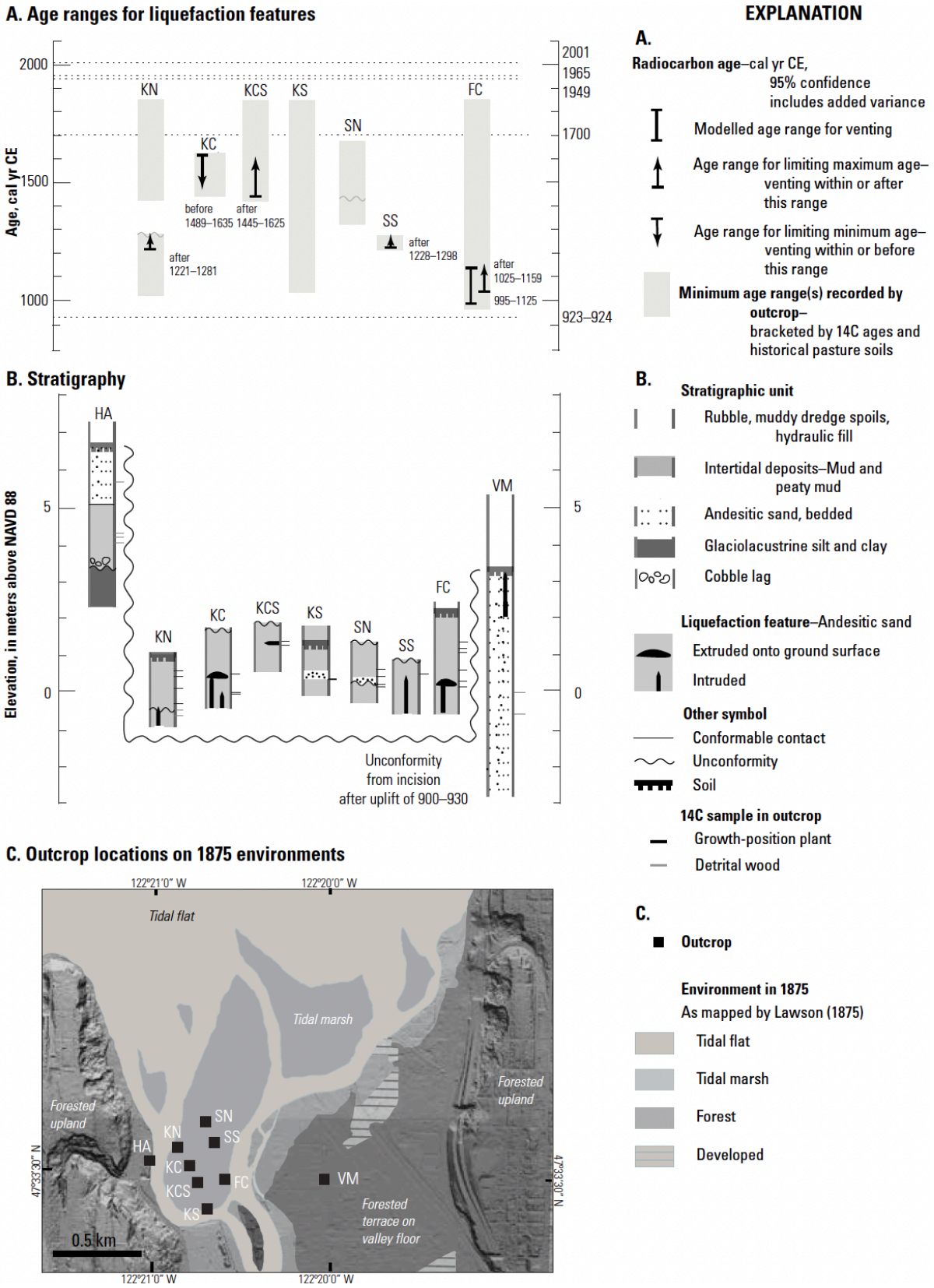

Figure 2.15. Chronology, stratigraphy, and locations of outcrops described in this study.

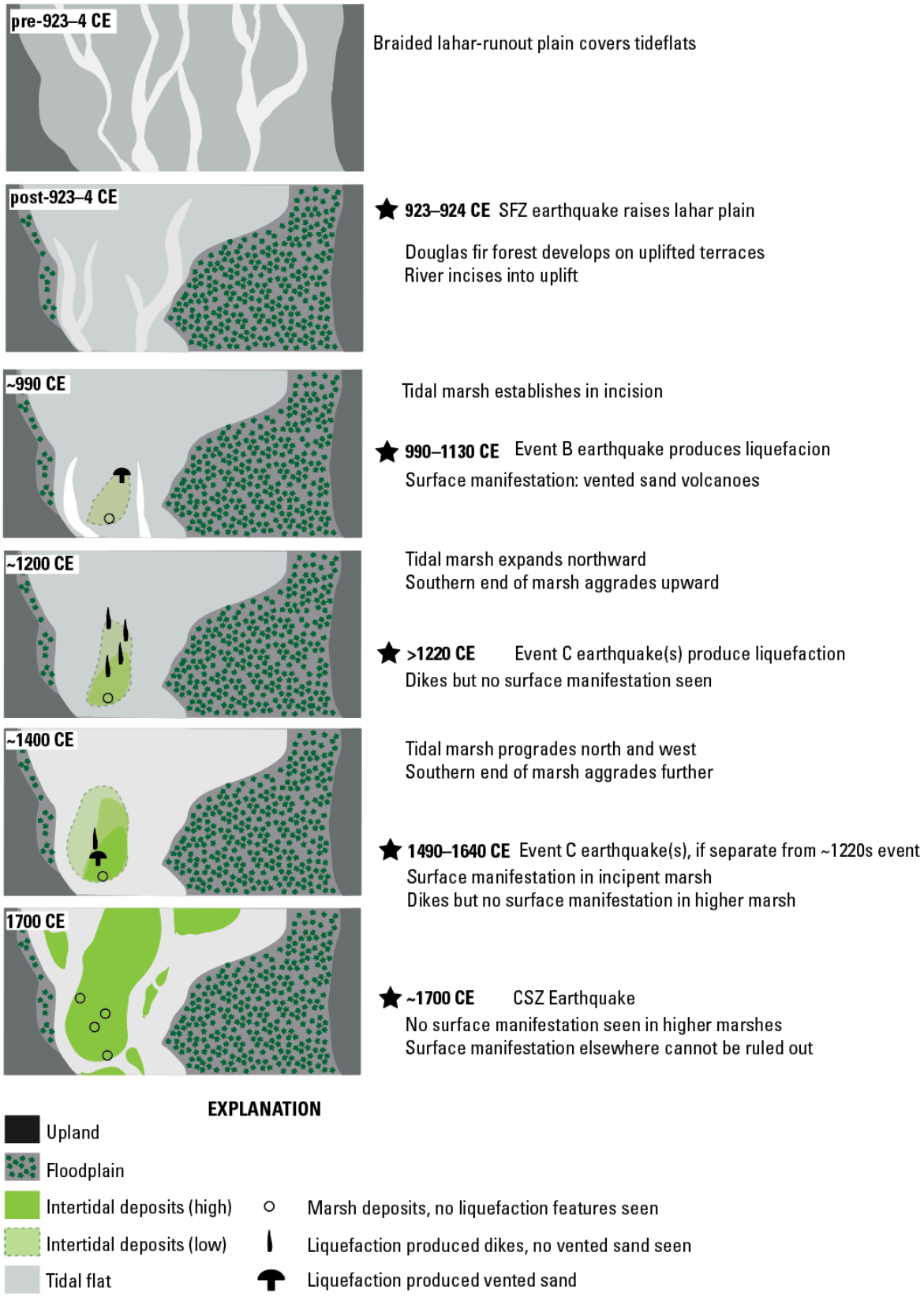

Fig. 2.16. Evolution of the Duwamish marsh over time.

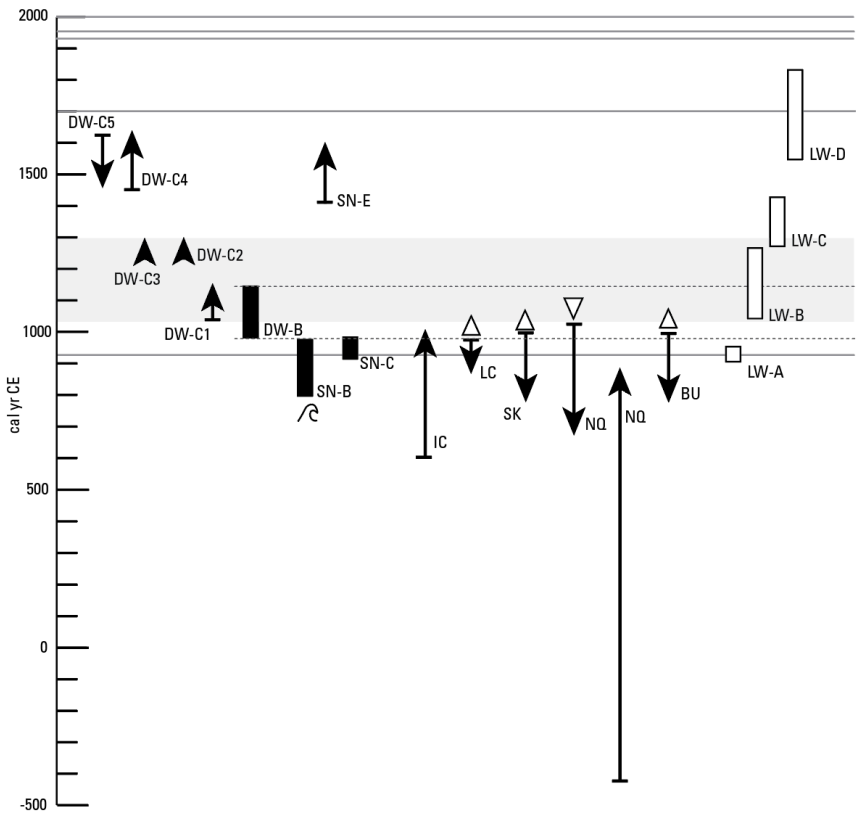

Earthquake age	Source	Magnitude	Description
2001 CE	intraslab	M 6.8	hypocenter ~50 km SSW of Duwamish
1965 CE	intraslab	M 6.5	hypocenter ~24 km S of Duwamish
1949 CE	intraslab	M 7.1	hypocenter ~60 km SSW of Duwamish
1700 CE	CSZ	M~9	Subsidence ~150 km SW of Duwamish
1020–1300 CE	CSZ	M<9?	Subsidence ~150 km SW of Duwamish
995–1125 CE	?	M ?	Duwamish liquefaction stratigraphically after 923–924 uplift
923–924 CE	SFZ	M~7.5	Regional uplift and subsidence around Puget Sound, tsunami

EXPLANATION

Timing of evidence for ground shaking

- Limiting minimum age (liquefaction during or before time spanned by arrow)
- Limiting maximum age (liquefaction during or after time spanned by arrow)
- Age range for liquefaction (liquefaction during time spaned by box)
- Age range for Lake Washington turbidites

Evidence for fault activity coincident with liquefaction

- Coincident uplift
- Coincident subsidence
- Coincident tsunami

Figure 2.17. (prior page) Duwamish liquefaction events compared with other regional paleo-liquefaction features and known earthquakes. Paleo-liquefaction features have been dated at the Snohomish delta (SN) (Bourgeois and Johnson, 2001), Issaquah Creek (IC) (Whisler et al., 2002; Martin and Bourgeois, 2012), Lynch Cove (LC) (Hemphill-Haley, 1996; Sherrod et al., 2004; Jovanelly and Moore, 2009; Martin and Bourgeois, 2012), the Skokomish delta (SK) (Polenz et al., 2010; Martin, 2011; Martin & Bourgeois, 2012), the Nisqually delta (NQ) (Barnhardt and Sherrod, 2001; Sherrod, 2001), and Burley (BU) (Sherrod et al., 2004). Also plotted are ages of terrigenous layers in the lakebed of Lake Washington, which have been interpreted as possible seismites (Karlin et al., 2004). They note that the LW-C deposit(s) may encompass multiple events. The age of the penultimate CSZ earthquake is derived from Nelson et al. (2021).

2.6 TABLES

Table 2.1. Radiocarbon ages from FC outcrop, most of which are used in the age model in Figure 2.7. Samples collected in 2000 or earlier were collected by Brian Atwater and are not used in the age model. Calibrated ages are rounded to the nearest 10 years. The calibrated ages are the priors for the age model; the modeled posterior ranges for marker beds are listed in this table. The modeled posterior ranges for individual 14C ages are shown on Fig. 2.7.

ID	Year collec-ted	Horiz. coord (m)	Vert. coord. (m)	Event or horizon	Height above horizon (cm)	Plant genus and parts dated	Stratigraphic position	Interpretation	Lab number	Quoted age	Age with added variance	Calibrated age, 95% confidence, cal yr CE
2	2018	34	6.26	UZ	25.5	*Triglochin*, leaf base	23.5 cm above UZ	Loose minimum age for UZ	OS-171115	355 +/- 20	356 +/- 29	1460–1640
1	2018	34	6.22	UZ	21.5	*Triglochin*, leaf base	19.5 cm above UZ	Loose minimum age for UZ	OS-171117	330 +/- 15	332 +/- 27	1480–1640
3	2018	34	6.13	UZ	12.5	*Triglochin*, leaf base	12.5 cm above UZ	Loose minimum age for UZ	OS-145731	390 +/- 15	391 +/- 26	1440–1620
4	2018	34	6.09	UZ	9	*Triglochin*, leaf base	9 cm above UZ	Minimum age for UZ	OS-171116	440 +/- 15	440 +/- 26	1420–1480
6	2017	-3.1	6.10	UZ	4	*Triglochin*, leaf base	4 cm above top of UZ	Minimum age for UZ	OS-147272	585 +/- 15	585 +/- 26	1300–1410
5	2018	34	6.01	UZ	0.5	*Triglochin*, leaf base scar on rhizome	Just above UZ, not quite touching	Close minimum age for UZ	OS-145735	510 +/- 15	508 +/- 26	1400–1450
			5.9–6.3	**UZ: tabular silt layer, ~1 cm thick**								**Modeled posterior age: 1350–1440**
7	2018	34	6.00	UZ	-1	*Triglochin*, leaf base and scar	1 cm below UZ, touches UZ	Close maximum age for UZ	OS-145734	555 +/- 20	554 +/- 29	1320–1430
9	2017	-3.05	6.10	UZ	-1	*Triglochin*, leaf-base scar on rhizome	1 cm below base of UZ	Maximum age for UZ	OS-135960	510 +/- 20	511 +/- 28	1330–1450
8	2018	34	5.94	UZ	-6	*Triglochin*, leaf base with scar	6 cm below base of UZ, lowest observed *Triglochin*	Maximum age for UZ, local first appearance of *T. maritima*	OS-145733	570 +/- 15	571 +/- 27	1310–1420
10	2018	34	5.50	LL	-3	*Bolboschoenus*, culm and its corm	Corm 3 cm below LL, Culm cuts LL.	Close minimum age for LL. Loose minimum age for LZ.	OS-145003	615 +/- 35	613 +/- 40	1290–1410
			5.5–5.8	**LL: lowest thin lamina**			*No surveyed intrusion reaches the stratigraphic level of LL*					**Modeled posterior age: 1130–1350**
				Event C: sand dike below LL, crosses strata								**Modeled posterior age: after 1020–1160**

13	1996	38	5.50	LZ	25–35	*Triglochin*, leaf bases and rhizomes	25–35 cm above LZ	Minimum age for LZ if silt marker on 1996 reconnaissance sketch is LZ	Beta-92273	910 +/- 80	n/a	1000–1270
11	2017	47	5.54	LZ	4	*Triglochin*, leaf-base scar on rhizome	4 cm above lower silt Minimum age for LZ, and the closest to that layer.	Minimum age for LZ	OS-136966	890 +/- 20	889 +/- 28	1050–1220
15	2018	48	5.51	LZ	1	*Bolboschoenus*, culm and its corm	Corm just above LZ	Minimum age for LZ	OS-145725	935 +/- 15	936 +/- 26	1030–1170
			5.3–5.5	**LZ: tabular silt layer, 2.5 cm thick**					**Modeled posterior age: 1020–1160**			
17	2018	48	5.35	Event B		*Bolboschoenus*, culm and its corm	Corm just above sand, 11 cm below bottom of LZ	Minimum age for sand lens. May have been injected through LZ	OS-171114	960 +/- 15	962 +/- 26	1030–1160
21	2018	47.8	5.35	Event B		*Bolboschoenus*, culm and its corm	Corm just above sand, 12.3 cm below lower silt, 25 cm north of 180716-5	Minimum age for sand lens. Culm may have been injected through LZ	OS-145724	1020 +/- 20	1018 +/- 28	990–1150
				Event B: Vented sand volcanoes met by several dikes					**Modeled posterior age: 990–1150**			
19	2017	48.5	5.2	Event B		*Triglochin*, leaf base and scar	Bottom 4 cm below sand, top covered by sand, x=48.5	Close maximum age for DW-B	OS-145732	995 +/- 15	994 +/-27	990–1150
16	2017	48.5	5.2	Event B		*Triglochin,* leaf base	Bottom 2 cm below sand, top covered sand, x=48.5	Close maximum age for DW-B	OS-136964	950 +/- 20	951 +/- 30	1030–1160
20	2017	48	5.2	Event B		*Triglochin*, leaf base	Bottom 2 cm below sand, top covered sand, x=48.5	Close maximum age for DW-B	OS-147271	1010 +/- 20	1014 +/- 27	990–1150
14	2000	41	5.2	CC / Event B		*Bolboschoenus*, culm and its corm	Corm in highest mud below sand; culm probably extended through sand	Ambiguous: Culms likely grew up through sand lens unless corm lived within a few centimeters of pre-sand ground surface	Beta-146056	920 +/- 40	n/a	1030–1210
22	2000	41	5.2	CC / Event B		*Bolboschoenus*, culm and its corm	Corm in highest mud below sand; culm extends through sand	Ambiguous: Culms likely grew up through sand lens unless corm lived within a few centimeters of pre-sand ground surface	Beta-146057	1120 +/- 40	n/a	780–860

12	2000	41	5.2	CC / Event B		*Bolboschoenus*, culm and its corm	Corm in highest mud below sand; culm extends through sand	Ambiguous: Culms likely grew up through sand lens unless corm lived within a few centimeters of pre-sand ground surface	Beta-146058	890 +/- 50	n/a	1030–1260
18	2000	41	5.2	CC /Event B		*Bolboschoenus*, culm and its corm	Corm in highest mud below sand; culm extends through sand	Ambiguous: Culms likely grew up through sand lens unless corm lived within a few centimeters of pre-sand ground surface	Beta-146059	990 +/- 40	n/a	990–1160
22	1996	38	5.0	CC / Event B	-20	*Bolboschoenus*, ~30 culm bases, some with parts of corm	15–25 cm below sand lens	Ambiguous as maximum age for sand, if injected deeply	Beta-92272	1260 +/- 100	n/a	610–990

Table 2.2. Radiocarbon ages from other sites in the Duwamish estuary. Samples collected 2000 or earlier were collected by Brian Atwater. Calibrated ages are rounded to the nearest 10 years.

ID	Date collec-ted	Site	Event or event horizon	Height above marker (cm)	Plant genus, parts dated	Stratigraphic position	Interpretation	Lab number	Quoted age	Age with added variance	Calibrated age, 95% confidence, cal yr CE
24	9/3/17	SS	Event(s) C Dike	0	*Triglochin*, leaf base	base in stratum cut by dike	Minimum age for Event C3 dike	OS-137071	740 +/- 15	738 +/- 27	1230–1300
25	6/26/18	SN	SN strata		*Bolboschoenus*, corm and culm	32 cm above sand bed, within laminae	Minimum for sand deposition	OS-145726	190 +/- 15	190+/-27	1650–modern
26	6/26/18	SN	SN strata		*Bolboschoenus*	29.5 cm above sand bed, at lower end of laminae	Minimum for sand deposition	OS-145772	185 +/- 15	183+/-26	1660–modern
27	6/26/18	SN	SN strata		*Bolboschoenus*, corm	12 cm above sand bed	Minimum for sand deposition	OS-145727	380 +/- 15	380+/-26	1450–1630
28	6/26/18	SN	SN strata		*Triglochin*, leaf base	3.5 cm below sand bed	Close maximum for sand deposition	OS-145728	540 +/- 20	542+/-27	1320–1430
29	6/26/18	SN	SN strata		*Triglochin*, leaf base pieces	8 cm below sand bed	Maximum for sand deposition	OS-145730	475 +/- 15	476+/-26	1410–1460
30	8/7/17	KS	KS strata	-2	*Triglochin*, leaf base	base 2 cm below base of sand, top embedded 1-2 cm in sand	Close maximum for age for sand deposit	OS-147269	910 +/- 20	908+/-29	1040–1220
31	8/7/17	KS	KS strata	-2	*Triglochin*, leaf base	base 2 cm below sand, top embedded in sand	Close maximum for age for sand deposit	OS-145000	870 +/- 20	871+/-29	1050–1260
32	9/16/17	KCS	Event(s) C sand injection	1.3	*Bolboschoenus*, corm	base 1.3 cm above sand	Ambiguous for sand - dike injects into strata below injected *Bolboschoenus*, dike probably postdates a similar timeframe	OS-145520	385 +/- 25	384+/-32	1460–1630
33	9/16/17	KCS	Event(s) C sand injection	-5	*Bolboschoenus*, corm	base 5 cm below sand	Ambiguous for sand- dike injects into strata - Minimum for start of *Bolboschoenus* marsh - dike probably postdates a similar timeframe	OS-145729	390 +/- 15	388+/-26	1460–1630
34	3/19/97	KC	Event(s) C	0-10	*Bolboschoenus*, 18g corms, culms, rhizomes	0-10 cm above sand lens of event C5	Maximum for Event C5	QL-4936	336 +/- 15	n/a	1490–1640
35	9/2/17	KN	KN strata	106	*Triglochin*, leaf base	106 cm above sand, highest *Triglochin*	Minimum for *Triglochin* marsh	OS-145002	175 +/- 30	175+/-36	1660–modern
36	9/2/17	KN	KN strata	96	*Triglochin*, leaf base	96 cm above top of dike, lowest *Triglochin*	Maximum for *Triglochin* marsh	OS-145001	225 +/- 20	223+/-31	1640–modern
37	9/2/17	KN	KN strata	66	*Bolboschoenus*, corm	66 cm above top of dike, highest *Bolboschoenus*	Minimum for *Bolboschoenus* marsh	OS-145771	365 +/- 15	365+/-26	1460–1630
38	9/2/17	KN	KN strata	18	*Bolboschoenus*, corm	18 cm above top of dike	Minimum for *Bolboschoenus* marsh	OS-137070	445 +/- 30	446+/-36	1410–1620

39	9/2/17	KN	Event(s) C, KN strata	14	*Bolboschoenus*, corm	14 cm above top of dike, lowest *Bolboschoenus*	Minimum for *Bolboschoenus* marsh	OS-136965	445 +/- 15	446+/-26	1420–1480
40	10/4/18	KN	Event(s) C	-5	Detrital bark	5 cm below top of dike, in massive mud cut by dike	Maximum for dike	OS-14005	950 +/- 20	950+/-28	1030–1160
41	10/4/18	KN	Event(s) C	-18	Detrital bark	18 cm below top of dike, in laminae cut by dike	Maximum for dike	OS-145004	775 +/- 20	774+/-30	1220–1280

Table 2.3. Liquefaction and age control documented at other Puget Lowland sites.

Site, Locality	Studies	Environment	sedimentary evidence	max thickness of lenses	lateral extent	Reported limiting max (cal yr CE, 95% confidence)	Reported limiting min	Reported age range (cal yr CE)
Skokomish	Polenz et al., 2010; Martin, 2011; Martin and Bourgeois, 2012; Arcos, 2012	intertidal	sand dikes and blows	30 cm	~ 10 m		780–1000	
Lake Sammamish (Issaquah Creek)	Whisler et al., 2002; Martin, 2011; Martin and Bourgeois, 2012	fluvial	sand dikes and blows	50 - 100 cm	15 m	640–980	none	
Lynch Cove	Bucknam et al., 1992; Hemphill-Haley, 1996; Jovanelly and Moore, 2009, Martin, 2011; Martin and Bourgeois, 2012	intertidal	sand dikes and blows	84 -100 cm				680–1120
Snohomish (B)	Bourgeois and Johnson, 2001; Martin, 2011	intertidal	sand dikes and blows		traceable discontinuously for kilometers inland	800–980		
Snohomish (C)	Bourgeois and Johnson, 2001; Martin, 2011	intertidal	Sand dikes and one blow	1 cm	1 m			910–990
Snohomish (E)	Bourgeois and Johnson, 2001; Martin, 2011	intertidal	Sand dikes and blow		2 m	1400–1600		
Nisqually	Sherrod, 2001; Barhnardt and Sherrod, 2006	intertidal	deformed bedding and sand dike in cores		unknown	-420 – 890	none	
Nisqually, McAllister Creek	Sherrod, 2001; Barhnardt and Sherrod, 2006	intertidal	sand dike (2 cm) and sand blow		1.5 m	none	680–1030	
Burley	Sherrod, 2004	intertidal	sand blow			none	770–1000	

Table 2.4. Liquefaction features at the Duwamish delta

Event ID	Site	Sedimentary evidence	Modeled age range (95% CI, cal yr CE) rounded to nearest decade	Study	Oxcal sequence	Descriptive figure
A	VM	Convoluted beds at depth seen in sediment peels		Documented by Zehfuss (2005)		
B	FC	Sand dikes and blows	990–1150	This study	Appendix 2.1.2	Fig. 2.5, 2.6
C	FC	Sand dikes that crosscut Event B horizon	After 1030–1150	This study	Fig. 2.6	Fig. 2.5
C	KN	Sand dikes	After 1220–1280	This study		Fig. 2.12
C	SS	Sand dike	After 1230–1300	This study		Fig. 2.14
C	KCS	Sand injection that crosscuts laminae	After 1440–1630	This study		Fig. 2.10
C	KC	Sand dikes and blows	Before 1490–1630	Described and dated by B. Atwater, 2000		Fig. 2.8

Table 2.5. Attribution of liquefaction features at other sites and permissible correlation with Duwamish liquefaction features.

Site, Locality	Associated with interpretation of land level change?	Author's attribution	Studies	possible correlation to Duwamish
Skokomish	uplift attributed to Saddle Mountain fault zone	Saddle Mountain fault, based on uplift	Polenz et al., 2010; Martin, 2011; Martin and Bourgeois, 2012	n/a
Lake Sammamish (Issaquah Creek)	No	SFZ 923 CE	Whisler et al., 2002; Martin, 2011; Martin and Bourgeois, 2012	SFZ 923 CE; earlier permissible
Lynch Cove	abrupt uplift which was followed by subsidence	SFZ 923 CE, based on uplift	Bucknam et al., 1992; Hemphill-Haley, 1996; Jovanelly and Moore, 2009, Martin, 2011; Martin and Bourgeois, 2012	n/a (by age only, possible Duwamish B)
Snohomish (B)	subsidence	SFZ 923 CE	Bourgeois and Johnson, 2001; Martin, 2011	SFZ 923 CE
Snohomish (C)	No		Bourgeois and Johnson, 2001; Martin, 2011	Duwamish B
Snohomish (E)	No		Bourgeois and Johnson, 2001; Martin, 2011	Duwamish C(s)
Nisqually	No		Sherrod, 2001; Barhnardt and Sherrod, 2006	Duwamish B, C(s)
Nisqually, McAllister Creek	subsidence	SFZ 923 CE (Duwamish A) with local subsidence <0.5m	Sherrod, 2001; Barhnardt and Sherrod, 2006	n/a (by age only, possible Duwamish B)
Burley	uplift	SFZ 923 CE (Duwamish A) based on uplift	Sherrod, 2004	n/a (by age only, possible Duwamish B)

Chapter 3. **An unconsolidated marine terrace at Rialto Beach, Washington predates coastal deep-seated landslides and formed by progradation or uplift**

ABSTRACT

An unconsolidated marine terrace at the back edge of Rialto Beach, one of many such terraces along the northwest coast of Washington, dates to 1410–1800 cal yr CE and was produced either by beach progradation (requiring higher sediment supply than is available today) or by tectonic uplift. Rialto Beach and its terrace are above a stretch of the Cascadia subduction zone where there are few Holocene sea-level indicators and where modern geodetic deformation rates are unclear. The terrace, identified as a possible marine terrace by others based on its morphology, consists of a relatively flat platform that sits 1-3 m above the modern beach, below a steep slope that is peppered with landslides. The terrace is eroding rapidly toward the slope and hosts an established-but-dying Sitka spruce forest. My geologic field mapping of the terrace indicates that it is composed of stratified sand and beach cobbles, and that it is young. Radiocarbon ages of detrital wood within the terrace limit its maximum age to 1410 cal yr CE and a living tree on the terrace surface limits its minimum age to the decades prior to 1801 CE. The terrace post-dates all of the deep-seated landslides that occurred on the slope above, and pre-dates debris flows that have covered the terrace surface. The finding that all of the deep-seated landslides occurred prior to the formation of the terrace suggests they may have been destabilized by wave erosion at the toe of the slope. At Rialto Beach, stratigraphy and morphology of the terrace do not distinguish possible formation via uplift from formation by beach progradation at current sea level. If the terrace were formed exclusively as the result of tectonic uplift, the amount of uplift is likely confined to <3 m in magnitude and must have been relatively uniform across the 2.7-km stretch of Rialto Beach. If the terrace were formed via beach progradation, it would require a pulse of available sediment that began after 1410 cal yr CE and does not continue today. Neither explanation satisfies all the field data, but both explanations indicate that dramatic environmental change on the northwest coast occurred in the past few hundred years. Finally, I provide suggested strategies for study of the other similar terraces that exist across the northwest coast of Washington.

3.1 INTRODUCTION

The geologic record of coastal land-level change above subduction zones forms the basis for understanding rupture patterns of past earthquakes as well as tectonic deformation of the crust. Uplifted shore platforms along tectonically active margins have been used at many localities to shed light on subduction by interpreting earthquake histories (e.g., Chen et al., 2020; Ota et al., 1991) and interseismic strain (e.g., Merritts and Bull, 1989; Kelsey, 1990; Clark et al., 2010). Studies on both wavecut (e.g., bedrock) and wave-built (e.g., sandy or cobbly) marine terraces have used the elevation of old terraces compared with modern analogs to extract deformation histories of both crustal faults and plate boundaries (e.g., Berryman, 1993; Padgett et al., 2019). Many of these studies address accumulated uplift and fluctuating sea level on the timescale of 10^5 to 10^6 years (across the Pleistocene or longer) and do not directly address the occurrence of individual earthquakes. A subset of studies have attributed terraces to co-seismic uplift during one or more Holocene earthquakes, in many locations (e.g., Plafker et al., 1978; review by Ota and Yamaguchi, 2004; Ramírez-Herrera et al., 2011; Pinegina et al., 2013). Co-seismic uplift associated with Holocene earthquakes has thus far not been documented above the Cascadia subduction zone (CSZ) (Staisch and Walton, 2022).

In Cascadia, across the northwest coast of Washington, flat benches at the landward edge of pocket beaches can be seen in LiDAR at numerous localities (Fig. 3.1). These benches sit mostly around 6 m above sea level (NAVD88) (Fig. 3.2) and have been identified at individual sites by various authors (Daugherty and Fryxell, 1967; Haugerud, 2020; Riedel et al., 2021). The benches are relatively flat and truncate features on the slopes above, leading prior authors to infer that they are stranded shorelines. Most localities display only one such near-sea-level bench, though multiple steps of benches have been noted at a few sites (e.g., four possible steps of marine terraces were described at Cape Alava (Daugherty and Fryxell, 1967)). The benches are limited in lateral extent between rocky headlands; the longest bench, at 2.4 km long, is at Rialto Beach and is the subject of this study (Fig. 3.3). Herein, I refer to these low-elevation, limited-extent geomorphic benches as “terraces,” and distinguish them from other geomorphic terraces in the vicinity (e.g., glacial-outwash terraces or Pleistocene marine terraces).

These terraces exist on a stretch of the Cascadia margin where there are few geologic constraints on relative sea level during or between CSZ earthquakes (Fig. 3.1) (e.g., Engelhart et al., 2015; Staisch and Walton, 2022). Because of their location within this data gap, which is the largest land-level data gap in Cascadia (Staisch and Walton, 2022), the question of whether or not these terraces record tectonic uplift is of particular interest.

Prior to this study, which focuses on the terrace at Rialto Beach, only two of the ~50 other terraces on the northwest coast of Washington had been studied, at Cape Alava and Sand Point (Fig. 3.2). At Cape Alava, during excavation of the Ozette archaeological site in the 1960s and 70s, prior to recognition of subduction zone earthquakes in Cascadia, Daugherty and Fryxell (1967) described four steps of sandy terraces that extended up the hillslope to about 20 m above the modern beach (Friedman, 1976). They interpreted these as marine terraces that possibly recorded late-glacial sea-levels. At the pocket beach at Sand Point, Peterson et al. (2014) described a sandy terrace that sits at 6–9 m NAVD88 and determined it formed via beach ridge progradation that began around 1.5 ka and ended around 1270–1410 cal yr CE. Its maximum height (9 m NAVD88, 6.8 m above MHHW) they attributed to dune formation atop the prograded beach ridge plain.

This study focuses on the longest terrace along the northwest coast of Washington, at Rialto Beach (Fig. 3.1C). Here, I map and date the terrace and assess two hypotheses for its formation: shoreline progradation or tectonic uplift. Riedel et al. (2021) identified the terrace at Rialto Beach based on geomorphology and noted that wood eroding out of terrace scarps could be used for ^{14}C dating. He described the terrace to form a flat, forested bench above the upper edge of the modern beach, separating the beach from a steep, forested slope. The terrace extends parallel to shore for 2.7 km between the mouth of the Quillayute River and a bedrock headland known as Hole in the Wall (Fig. 3.3).

The terrace at Rialto Beach and the slope above have been the subject of several recent Master's projects. Bush (2020) mapped stratigraphy at one site at the terrace and used dendrochronology and ^{14}C dating to date deposits in the terrace and landslide. Freeman (2021) extended the chronology and mapped an adjacent landslide. Card (2023) mapped bedrock fractures in the host

rock of that landslide to assess slope stability and possible triggers for the landslide. Hill (2022) analyzed historic photos from the past 130 years to show that the modern Rialto Beach is retreating.

Here, I build on the prior research to present new results documenting the stratigraphy, sedimentology, and age of the Rialto Beach terrace and landslides, and reinterpret previously reported ages in order to evaluate the possibility that the terrace formed as a result of tectonic uplift or other processes. In doing so, I develop a stratigraphic framework that can be used to interpret other terraces and to date landslides along the northwest Washington coast.

3.1.1 Unconsolidated coastal deposits

The framework I present here for Rialto Beach relies on the interpretation of sedimentary facies of coastal deposits, particularly on the sedimentological and stratigraphic differences between beachface, beach ridge, and alluvial deposits. I also distinguish between deposits and landforms formed on prograding and retreating shorelines. Bourgeois and Leithold (1984) present a review of the sedimentary record from ancient and modern beaches to differentiate these deposits. According to their terminology, which I adopt here (Fig. 3.4), the *beachface* extends from mean lower low water (MLLW) to approximately mean higher high water (MHHW) and is formed by swash-backswash and surf, with contributions from longshore and rip currents. The *shoreface*, below MLLW, is not shown on the diagram in Figure 3.4. In both prograding and retreating shorelines, a constructed ridge (or berm) may separate the foreshore from the backshore. These ridges form at the upper end of the swash (near or above MHHW). Here, I use *beach ridge* to describe such ridges in prograding systems, and *retreat ridge* (or scarp-retreat ridge, where a scarp is present) to describe ridges in retreating systems. Beach ridges, though initially formed by wave swash, may accumulate aeolian sand as prograding shorelines move seaward. Beach progradation may result in the abandonment of earlier beach ridges as the shoreline builds seaward. The resulting landform, a beach ridge plain, is distinguished by shore-parallel ridges of sediment and intervening swales. Following Pinegina et al. (2013), I distinguish beach ridges (formed on prograding shorelines) from *scarp-retreat ridges*, features with similar morphology produced on retreating shorelines (Fig. 3.4B). Scarp-retreat ridges are piles of sediment tossed by waves atop and landward of a retreating shore scarp.

Other coastal deposits at Rialto Beach include alluvial deposits, eolian deposits, landslide, and debris flow deposits. The sedimentology of each of these deposits is distinct and reflects the different processes that emplace the sediments. In the absence of diagnostic biogenic signatures (as is the case at Rialto Beach), the size, shape, and sorting of clasts, and the characteristics of bedding distinguish among them. To interpret the terrace at Rialto Beach, it is necessary to differentiate beachface, beach ridge, and alluvial deposits. I review their characteristics below. I focus on sandy and gravelly beachface deposits, sandy and gravelly beach ridge deposits, and gravelly alluvial deposits, because these are the grain sizes present at Rialto Beach.

3.1.1.1 Beachface deposits

Beachface deposits, which may be coarse-grained or sandy, are emplaced within the swash zone. Coarse-grained beachface deposits are characterized by the presence of imbricated, disc-shaped clasts (Bourgeois and Leithold, 1984). Imbricated clasts dip seaward. Pebbles and cobbles are commonly segregated by size into well-defined, tabular beds. Where sandy, beachface deposits consist of evenly laminated sand (Reineck and Singh, 1980) with low dip angles and large lateral extent. Ripple bedding, undulating laminae, and heavy-mineral-rich layers may also be present. Eolian deposits, which may accompany beachface deposits, consist of well-sorted sand that may form planar bedding, cross-bedding, or ripple bedding. Bourgeois and Leithold (1984) consider bedded disc-shaped cobbles, in association with planar laminated sand rich in heavy minerals, to be diagnostic of gravelly beach deposits.

3.1.1.2 Beach ridge deposits

Beach ridges form at the upper end of swash by wave action and may grow taller as the result of dune formation (review by Tamura, 2012). At prograding shorelines, beach ridges or nearshore bars can build progressively seaward, producing morphologically distinct beach-ridge plains. Internal sedimentary structure of beach ridges varies depending on the mechanism of formation (e.g., accumulation of storm swash beach ridges or welding of intertidal bars) and consists of landward-dipping crossbeds and/or seaward-dipping foreset beds. The tops of beach ridges, if formed of cobbles, may exhibit landward-dipping imbrication on the seaward edge of the beach ridge and seaward-dipping imbrication on the landward edge.

3.1.1.3 Alluvial deposits

Gravelly beachface deposits can be distinguished from alluvial sediments by clast shape, imbrication, and sorting, as described by Clifton (1973). Disc-shaped and elongated clasts, diagnostic of beachface deposits, are less common in alluvial deposits. Imbrication of cobbles is also used to differentiate beach and alluvial deposits: because river flow orients clasts with upstream dips, beach cobbles typically dip seaward or parallel to the beachface, while imbricated alluvial cobbles dip upstream (landward) (Todd, 1996). Bedding in beach deposits is laterally more consistent and less lenticular than alluvial deposits. Sandy alluvial deposits may preserve channel-fill and cross-stratification. Gravelly alluvial deposits may also show channel fill. The clasts in beach deposits are better sorted into discrete beds than those of alluvial deposits (Clifton, 1973).

3.1.2 Unconsolidated shoreline deposits as records of land-level change

A major challenge in using unconsolidated shoreline deposits as records of deformation is establishing a reliable elevation datum of a shoreline, as the height of beach features is controlled by many factors (e.g., Tamura, 2012). Where bedrock wavecut platforms exist, the inflection point between the wavecut platform and the former sea cliff, often called the back edge or shoreline angle, is used as a proxy for MSL (Lajoie et al., 1986; Kelsey, 2015). However, at Rialto Beach and many other localities, such a bedrock platform is not visible in the available outcrops. Other studies in uplifted coastal deposits have identified characteristic elevations to use as elevation datums, like the crest of beach ridges (e.g., McSaveny et al., 2006) or establishment of vegetation (e.g., Pinegina et al., 2013). Rialto Beach lacks the diagnostic datums used elsewhere.

3.1.3 Geologic and tectonic background

Interpreting the origin of the terrace at Rialto Beach requires understanding of its geologic and tectonic context. In northwest Washington, geology and geomorphology are largely the product of subduction-zone and glacial processes. The coastline is characterized by steep, rocky headlands dissected by a handful of wide river valleys that drain the Olympic mountains. One such river, the Quillayute River, forms the southern boundary of Rialto Beach. The headlands, uplifted accretionary wedge sediments from the active subduction zone, consist of deformed

marine sediments and seafloor basalt (Gerstel and Lingley, 2000). These rocks were incised by alpine glaciers and partially covered by glacial sediment during at least six Pleistocene glaciations (Thackray, 2001). The Juan de Fuca lobe of the Cordilleran ice sheet also covered part of the outer coast. Its terminal extent, in the vicinity of Rialto Beach, is not well-known. Maximum Cordilleran ice extent is attributed to 16,000–15,000 cal yr BP (Haugerud, 2020). The maximum alpine ice extent is attributed to ca 70,000 cal yrs BP, and the most recent occurred ca 21,000 cal yr BP (Pazzaglia et al., 2003). Timing of deglaciation is not well constrained, but likely occurred rapidly, probably in the decades to centuries following maximum ice extent. The coast of Washington was formerly as much as 20 to 30 km to the west (Thackray, 1996) and has been eroding landward, leaving seastacks as evidence of former land positions.

Though this stretch of coastline lies atop the Cascadia subduction zone, the influence of coseismic and interseismic deformation on its morphology remains enigmatic. Ninety kilometers south of Rialto Beach, coseismic subsidence and tsunami inundation are well-documented by the burial of wetland soils in broad supratidal flats rich in fine sediment (e.g., Atwater and Hemphill-Haley, 1997). These environments are uncommon on the northwest Washington coast.

3.1.4 Relative sea level (RSL) in northwest Washington

Glacial isostatic adjustment (GIA) models indicate that relative sea level on the northwest coast of Washington has not fallen in the last 14,000 years (Yousefi et al., 2021). However, Rialto Beach is in a spatial data gap. The nearest geologic constraints on sea level from geology are at Neah Bay and Wa'atch, 45 km to the north, and the Copalis River, 100 km to the south (Fig. 3.1B) (Atwater, 1988; Hutchinson, 1992; Peterson et al., 2013; compiled by Engelhart et al., 2015). Analyses of geodetic constraints on modern interseismic strain have conflicting results (Newton et al., 2021; Miller et al., 2018). The Pacific Northwest Geodetic Array (PANGA) GPS station P816 at the Quillayute airport, 6 km inland from Rialto Beach, currently measures emergence of 1.2 mm/yr, though the measurement's weighted root mean square (WRMS) error, at 4.5 mm, is more than three times the signal (Pacific Northwest Geodetic Array, 2023). (A longer, but interrupted, record is available from PANGA GPS station p401, which records uplift of 0.5 mm/yr with WRMS error of 4.8 mm). Tide-gauge differencing at La Push suggests subsidence of 0-1 mm/yr (Newton et al., 2021). Highway leveling at Forks, Washington, 48 km

inland from Rialto Beach, suggests emergence of ~1 mm/yr (Newton et al., 2021). An interpolated tectonic model gives the cells at Rialto Beach 0-1 mm/yr vertical velocity, with an error around 1 mm/yr (Newton et al., 2021).

3.2 METHODS

3.2.1 Stratigraphy

The Rialto Beach terrace sits a few meters above sea level, and the seaward edge of the terrace is eroding, producing outcrops up to a few meters tall. These outcrops are ephemerally exposed, but commonly covered, as waves on the modern beach push cobbles and driftwood against them.

I mapped stratigraphy in the terrace face during field visits between 2018 and 2023, producing two >100 m-long levelled sketches at long outcrops and 24 measured sections elsewhere, including six pits dug down from the terrace surface (Fig. 3.3). In sketches, relative elevations were surveyed and tied to absolute elevation by centimeter-grade GPS. At measured sections, relative elevations were measured with a meter stick and tied to absolute elevation from either centimeter-grade GPS or LiDAR. Uncertainties in measured elevations were formally propagated by a root-mean-square calculation.

3.2.2 Estimating elevation of the modern beachface

In order to evaluate whether or not the surface of the terrace could have been produced by modern beach processes, it is necessary to evaluate the elevation of these processes.

Tidal datums provide one such reference. Local tidal datums were retrieved from the LaPush tide gauge (NOAA, 2020), which is located just to the south of Rialto Beach (Fig. 3.1C) and listed in Table 3.1.

Since local topography can influence the actual height of beach processes, and the height of the beach changes with the seasons (e.g., Miller, 2019), I used both field measurements and LiDAR to estimate a range of possible maximum beach heights (*tb* in Figure 3.4). In the field, I surveyed or measured the highest point of sand and gravel deposits where they met eroding outcrops. Surveying uncertainty is less than 1 cm. This measured height varies through time and

across the beach. Also from LiDAR collected in 2018, I drew 23 shore-normal profiles spaced every ~100 m across the beach. On each profile, I manually extracted the elevation of the top of the beach, defined as the uppermost point of the linear beach slope (*tb* in Fig. 3.4), at the inflection point where the steeper scarp-retreat ridge begins.

3.2.3 Difference in elevation between terrace-forming strata and modern beachface

I used a statistical test to evaluate whether there was a difference in elevation between the top of modern beach deposits (*tb* in Fig. 3.4) and the top of the terrace-forming strata excluding the soil developed atop these strata (*tt* in Fig. 3.4). This test, a two-sample t-test assuming unequal variances, uses the means and variances of two datasets to determine whether or not a difference in those means can be attributed to random chance (for a description of the t test, see Livingston, 2004). Here, the two datasets (n = 72 observations each) consisted of our field-observed elevations of the terrace-forming strata and the combined datasets that estimate elevations of the modern beach top. I calculated the t-test through the built-in function in Microsoft Excel using $p<0.05$ as the threshold for statistical significance.

3.2.4 Radiocarbon dating

I collected eight new radiocarbon samples at six sites (Table 3.2). These join eight samples collected or reported by Bush (2020) and Freeman (2021). All samples consist of detrital wood, conifer cones, and charcoal inferred to pre-date the material they were collected from. Samples were rinsed in the lab and cleaned under a microscope to remove rootlets and detritus not part of the sample itself. Pieces of wood commonly had networks of roots growing along the planes between each tree ring; all samples were separated into individual rings so these surfaces could be cleaned.

Radiocarbon determinations were made at the National Ocean Sciences Accelerator Mass Spectrometry Facility (NOSAMS) in Woods Hole, Massachusetts. I added variance (calculation in Appendix 3.1) to the radiocarbon errors reported by the labs. Error reported by the lab accounts for the repeatability of radiocarbon determination for the same sample (Luk, 2020). Added variance estimates reproducibility of multiple similar samples, accounting for other variance (Mark Roberts, pers. comm, 2019).

Ages in years CE were calibrated in Oxcal 4.4 (Bronk Ramsey, 2009; Bronk Ramsey, 1995) using the IntCal20 calibration curve (Reimer et al., 2020). Two modern ages were calibrated in CALIBomb (Reimer and Reimer, 2024) using the Bomb NHZ1 calibration curve (Reimer et al., 2004). All calibrated ages are reported as 95% confidence interval ranges of years CE rounded to the nearest 5 years.

3.2.5 Dendrochronology

Two live Sitka spruce were cored in 2021 using an increment borer (Table 3.3). These new cores supplement tree ring evidence presented by Bush (2020). Cores were mounted in a wooden frame and sanded to remove striations on the cores produced during coring. Rings were counted manually under 10x magnification. The number of rings estimates the age of the tree at the time of coring.

3.3 RESULTS

3.3.1 Morphology

The top of the Rialto Beach terrace sits at 4.4–7.1 m NAVD88 and separates the modern beach from the forested slope above (Figs. 3.3, 3.5, 3.6). The terrace is mostly 30–70 m wide and extends 2.7 km from the mouth of the Quillayute River to Hole in the Wall, a bedrock headland. The terrace is bisected by the mouth of Ellen Creek but is otherwise continuous (Fig. 3.5). Except at its seaward edge and at the mouths of gullies (which are discussed below), the surface of the terrace is relatively flat, mostly with less than 2 m of relief (Fig. 3.3).

At its landward edge, the top of the terrace commonly rises ~1–2 m directly adjacent to the slope edge (Fig. 3.3). The landward edge of the terrace surface truncates several deep-seated landslide scars visible in LiDAR. These landslides exhibit arcuate headscarps, benched topography, and sag ponds on their surface. However, with the exception of localized slumps, there is no geomorphic evidence for significant landslide deposits downslope of the landslides. Conversely, at the outlets of gullies, convex debris-flow fans cap the terrace surface. At their highest, these fans reach >8 m higher than the adjacent terrace surface.

The terrace is retreating, as evidenced by photogrammetry (Hill, 2022), repeated shoreline surveys (Troost et al., 2021), and reports from longtime residents (Jill Silver, pers. comm., 2020). Analysis of historic photos by Hill (2022) shows the terrace has been retreating consistently for the past 130 years. We observed rapid retreat during the six-year period of this study, with some new outcrops revealed each visit and some removed before the next. While all these lines of evidence point toward persistent terrace retreat, retreat of the modern beachface below the terrace, at least at the southernmost end of the beach, is not apparent in recurrent beach profiles collected by Miller (2019).

A scarp-retreat ridge formed by tossed-up cobbles and sand, up to 1.5 m high and 10–25 m wide, caps much of the retreating (seaward) edge of the terrace (Figs. 3.5 and 3.6). Where debris-flow fans build the terrace surface higher than 7 m NAVD88 (e.g., at LS2), and at the northernmost end of the beach, no ridge is present. An eroding scarp on the seaward edge of the terrace is ephemerally exposed but is commonly concealed by the scarp-retreat ridge (Fig. 3.4B).

The top edge of the modern beachface, as measured at the bases of outcrops and in LiDAR, ranges in elevation from 3 m to 4.5 m NAVD88 (Figs. 3.7, 3.8, 3.9). The beachface at Rialto Beach slopes seaward 4–5.2 degrees.

Ellen Creek crosses the terrace midway between the Rialto Beach parking lot and Hole in the Wall (Fig. 3.3). The outlet of the creek has incised through the terrace, and Ellen Creek base level is more than 1.5 m below the surface of the terrace at its mouth (Fig. 3.7). Where the creek mouth exits the terrace, it is commonly obstructed by logs and sediment, which sometimes impound the creek into a pond.

3.3.2 Stratigraphy

Materials in the terrace consist mostly of stratified beds of well-sorted sand and gravel, including cobbles. Locally, these stratified deposits, herein referred to as “terrace-forming strata,” are capped by debris-flow deposits or underlain by landslide deposits. The following stratigraphic framework was compiled from six years of observations and over 40 days on site. The descriptions below are listed in order from old to young. Most of the study was focused on the

unconsolidated materials that form or rest atop the terrace. I also describe bedrock, active beachface deposits and active fluvial deposits at Ellen Creek, though they were not a major focus of this study.

3.3.2.1 Bedrock

Bedrock comprising fractured sandstone and siltstone forms the slopes above the terrace, the sea stacks offshore, and the wavecut platform or platforms near modern MSL (Fig. 3.5). The strikes and dips of the bedrock vary along Rialto Beach. Bedrock consists of interbedded marine graywacke, sandstone, and siltstone, ranging from highly weathered to lightly weathered. Highly weathered zones can be peeled with a pocket knife (e.g., Selby 1993); lightly weathered zones are moderately fractured (Card, 2023).

Fragments of one or more wavecut platforms sit near MSL at the northernmost 250 m of Rialto Beach where they adjoin the bedrock headland, Hole in the Wall (Fig. 3.5). Offshore Rialto Beach, the platform(s) are neither extensive nor ubiquitous. Field surveys and LiDAR show that the platform(s)' surface sits mostly around 1.3 m NAVD88 and is rough, with tens of centimeters of variation in elevation. Adjacent to sea stacks, including Hole in the Wall, the flat surface of the platform(s) sits 1–1.5 m higher. Seastack surfaces are smoothed up to several meters above the surface of the platform(s). The three seastacks adjacent to Rialto Beach display an eroded concavity at 4 m NAVD88, 3 m above the wavecut surface at that site. In the kilometer north of Rialto Beach, the bedrock wavecut platform(s) are more widespread, elevations range from about 1.2 to 2.4 m NAVD88, and individual blocks top out several meters higher.

Elsewhere offshore Rialto Beach, individual rocks, possibly fragments of former platforms or seastacks, can be seen in the surf zone at low tides. Their surfaces sit at various elevations and appear mostly higher than the wavecut platform(s) described above. It is unclear whether the variations in elevation of bedrock in the surf zone represent variations in RSL or of variations in erosivity of the rock. It is also unknown whether the platform(s) near Hole in the Wall were formed by modern sea level or if they are inherited.

Bedrock has been mapped in gullies along the slope and in the streambed of Ellen Creek (Bush, 2020; Freeman, 2021; Card, 2023; this study). While bedrock presumably underlies the terrace-forming strata (section 3.3.2.1) and the landslide deposit described in section 3.3.2.2, we did not encounter this contact in any terrace outcrops or excavations.

3.3.2.2 Bedrock-rich landslide deposits

One landslide deposit was mapped underlying terrace-forming strata at the northern end of the Rialto Beach terrace (Fig. 3.16). The landslide deposit consists of friable, wet, chaotic, blue-gray clayey matrix, bearing sandstone-siltstone clasts of all sizes, ranging from <5 mm to >1.5 m (Figure 3.17). Clasts that are large enough to be identifiable are composed of fine-to-medium grained graywacke sandstone and siltstone jointed along bedding planes into angular <1 cm to 5 cm blocks with surface oxidation. The matrix is blue-gray silt and clay and exhibits some fabric that is deformed around the largest clasts. Between x = 5 m to x = 15 m along the sketch at T1 (Figure 3.17), the deposit is clast supported. North of x = 27 m (Figure 3.18), the deposit is matrix-supported in a blue-purple, clayey, wet matrix. The landslide deposit is vacant of organic debris except for one piece of wood which was exposed at x = 32 m.

The surface of this landslide deposit is truncated. Below, I describe evidence for truncation across the exposure from south to north. Between x = 5 m and x = 15 m (Figure 3.17), the deposit surface varies less than 20 cm in elevation, and a 1.5-m-diameter angular sandstone clast is flush with the horizontal surface of the landslide matrix. Near-vertical fabric in the landslide matrix is truncated by the upper contact. Where the exposure moves northward and landward, the elevation of the landslide deposit rises, but its surface remains smooth; another 2-m-diameter clast of fractured sandstone forms a flush surface with the matrix at x = 50 m (Figure 3.19). Clasts of landslide material are rarely seen in the overlying strata (described in section 3.3.2.3). Figure 3.20 shows the elevations of the truncated landslide surface as seen along the outcrop face (which varies in strike). Figure 3.21 shows an interpreted cross-section of the landslide surface perpendicular to the slope, where the depth to the landslide surface is projected along topographic contours to the location of the transect (the location of the outcrop and transect are shown in Figure 3.16).

3.3.2.3 Sand and gravel in the terrace (terrace-forming strata)

Sand with beds of gravel (including cobbles) forms the bulk of the terrace in all outcrops and excavations and is herein called the terrace-forming strata. Typically, the top 10-30 cm of this unit is altered by the overlying soil and consists of silty sand, in places stratified, with abundant charcoal and common fire-cracked rock. Below the soil zone, deposits range from moderately sorted to very well sorted and are commonly lightly to heavily oxidized (e.g., Fig. 3.15). Beds of sand and gravel range from <1 cm to >1 m thick; beds of cobble gravel typically are 10–60 cm thick (e.g., Fig. 3.12C and D). Sedimentary structures are common in all outcrops and include planar bedding, heavy mineral laminae, seaward-dipping imbrication of cobbles, cut and fill structures (e.g., Fig. 3.15), and stringers of cobbles and pebbles within bedded sand. At T1, where sand and cobbles cap the bedrock-rich landslide (see section 3.3.2.2 and Figs. 3.16, 3.17, 3.18 and 3.19), horizontally aligned, disc-shaped cobbles rest atop the truncated surface of the landslide. At EC (Ellen Creek, see section 3.3.2.8 and Fig. 3.22), sand, pebbles, and cobbles are horizontally bedded across 40 m of shore-perpendicular outcrop. At LS2 (see section 3.3.2.6 and Fig. 3.12), bedding of sand and gravel layers is truncated by overlying debris flow deposits.

The top of this unit (tt) ranges in elevation from 3 m to 7.1 m NAVD88 (including uncertainty; Figs. 3.7 and 3.8). Across the beach, the difference between the mean elevations of terrace-forming strata (tt) and the top of the modern beach deposits (tb) is 1.11 m. A paired t-test on these means rejects the null hypothesis ($p<<0.05$) that the elevations of these two datasets are statistically indistinguishable; additional hypothesis-testing t-tests show that the means differ by as much as 0.9 m. The means of the distributions are statistically different by up to 0.8 m (Appendix 3.2). Therefore, the terrace-forming deposits sit on average 0.8 m higher than the modern beach deposits. At most outcrops, terrace-forming strata are 0.5–1 m higher than the modern beach. At its highest point (above T1 and in pits at the landward edge of the terrace south of Ellen Creek), terrace-forming strata sit 3.1 m higher than the modern beach at the same locations. The terrace-forming strata tend to be finer than the modern beach deposits at the same locations.

3.3.2.4 Mud at the surface of the terrace

Two pits dug into freshwater wetlands on the surface of the terrace exposed 50 cm and 80 cm of massive dark brown mud below the soil and above the sand (Fig. 3.14; location in Fig. 3.3). The mud-sand contact exposed in both pits is abrupt and can be traced over one sand grain. At pit T5, the base of the mud above the abrupt contact contains sand. Moving upwards, the mud with sand grades to mud without sand. Eight centimeters above the base of the mud is one 4 cm thick patchy horizontal layer of sand. In pit T0, no sand in the mud was observed.

3.3.2.5 Soil

Sitka spruce, sword fern, salmonberry, and other freshwater forest species grow atop the terrace in a dark brown, organic-rich soil developed atop sand and cobbles. The soil is 10–40 cm thick in the outcrop face and in pits, and its top sits at 4.7–6.9 m NAVD88. It contains abundant detrital wood, charcoal, with scattered well-rounded cobbles including fire-cracked rock. Trees growing in this soil mostly post-date the Great Olympic Blowdown of 1921 (Bush, 2020), but one survivor was cored in 2021. The core did not reach the center of the tree, but 220 rings were counted in the recovered core, indicating the tree started growing on the terrace up to a few decades before 1800 CE (Table 3.3). In some places where scarp-retreat cobbles (see section 3.3.2.7) are piled atop the soil in a ridge, Sitka spruce roots on the <100-year-old trees rooted in the soil have formed a secondary higher root system atop the scarp-retreat ridge.

3.3.2.6 Active debris-flow deposits

Modern debris-flow deposits form muddy or clast-supported caps on terrace outcrops in at least three locations (locations are shown on Fig. 3.7). These deposits crop out along the seaward edges of gully fans visible in LiDAR and thicken towards the center of the fans. At the distal edges and bases of the fans (as seen in the outcrops that crosscut them), the deposits consist of mud with abundant organic debris.

The best exposure of debris-flow deposits is at the LS2 fan (Figs. 3.12 and 3.13). Below the mouth of a gully, the 150-mlong LS2 outcrop consists of debris flow deposits that cap soil and sand (described below) (Fig. 3.12). Muddy deposits at the base of the debris flow fan are horizontally stratified and coarsen upward to interbedded lenses of angular sandstone clasts that

reach 10 cm in diameter. The horizontally stratified mud at the base of the debris flow deposits is 0.6 m thick and contains cones, twigs, wood, conifer needles, and an abundance of charcoal (Fig. 3.13). The mud is overlain by 2.2 m of coarsening-upward, clastic deposits (Figs. 3.12, 3.13). Lenses (up to 6 m wide by 0.5 m thick) of angular sandstone clasts are mostly clast-supported and grade from pebble-sized clasts near the base to >10 cm clasts at the top of the fan. Clast-supported lenses are interfingered with lenses of silt and of mixed clast and silt.

3.3.2.7 Active beachface and scarp-retreat deposits

The modern beachface (Fig. 3.9A) varies in texture laterally, ranging from large cobbles to sand. Clasts are in some places are imbricated dipping seaward and elsewhere not obviously imbricated. Where springs emerge from the terrace and run down the beach forming shallow trenches in the beachface, I observed clasts with reversed imbrication, dipping landward. Upper beach deposits consist of bedded sand and cobbles and cobbles in a sand matrix. Sorting of heavy minerals, especially garnets, is common along the upper edge of the beach (Fig. 3.9C).

The scarp-retreat ridge (see section 3.3.1 and Fig. 3.9D) is composed of scarp-retreat deposits. These consist of cobbles in most places and of sand just north of Ellen Creek. Driftwood and other debris are common. Cobbles are well-rounded and are commonly disc shaped. They range in size from 2 cm to >10 cm and consist of several lithologies, primarily graywacke but also include granitic and metamorphic rocks. The clasts in the ridge are crudely sorted, as observed in one cross-section along the eroding outcrop at Ellen Creek. The gravel of the scarp-retreat ridge is highly mobile—the ridge atop the terrace varied in size and texture between visits to the site.

3.3.2.8 Active Ellen Creek deposits

Ellen Creek drains 16 sq. km of uplands to the north and east of Rialto Beach and emerges at the current beachface level through an incision in the terrace surface (Fig 3.10A). The active deposits described herein are from the channel bed and bars 300–400 m upstream from the creek mouth.

The bed of Ellen Creek, observed only in riffles (Fig. 3.10), consists of sandstone bedrock in some places overlain by a thin veneer of angular to rounded cobbles (Fig. 3.10B). Channel bars consist of sorted, angular to moderately rounded cobbles, gravels, and coarse sand. Disc-shaped and elongated clasts are present but are less common than spherical or irregularly shaped clasts (Fig. 3.10C). Channel banks at this location and downstream consist of bedrock strath terraces or fluvial terraces of unconsolidated sediments. The most downstream of these "fluvial" terraces appears in LiDAR to adjoin the Rialto Beach terrace that is the subject of this study (Fig. 3.5); however, outcrops along this terrace were not available. Where gravel crops out in channel banks, clasts do not exhibit obvious imbrication.

The configuration of the mouth of Ellen Creek varies substantially with time in response to the movement of large woody debris that accumulates at its outlet to the back edge of the modern beach (Fig. 3.11). These reconfigurations are demonstrated over the past 130 years by historic photos and maps (Hill, 2022) and by my field observations: Ellen Creek, upon exiting the terrace at beach level, has oscillated between swinging to the north or south before running down the beach. The map in Figure 3.11A shows the creek exiting to the north. An avulsion around 2018 resulted in the creek mouth bending to the south, which exposed new terrace outcrops (Fig. 3.11C) and abandoned channels (Fig. 3.11D). Occasionally, the beachface has buried the creek outlet, resulting in the creek traveling underground before reemerging on the beachface near MHHW. Frequently, the outlet of Ellen Creek is blocked by logs on the beach at the edge of the terrace so that the creek impounds; the height of this impoundment can reach nearly to the terrace level (Fig. 3.11B).

3.3.3 Chronology

I infer the timing of formation of landforms and emplacement of sediments at Rialto Beach from superposition, crosscutting relationships, radiocarbon ages, and ages of trees.

3.3.3.1. Deep-seated landslides predate terrace formation

Landslide scars on the slope above the terrace are visible in lidar and one landslide deposit was seen at site T1 (Figs. 3.3, 3.5, and section 3.3.2.7). Across the entire stretch of Rialto Beach, landslide scars on the slope terminate at the back edge of the terrace and there are no geomorphic

signatures of landslide deposits (e.g., hummocky accumulations) below their scars (e.g., Fig. 3.12A). Instead, the surface of the terrace below landslides is similar to the surface of the terrace where landslides are not immediately up-slope. Deposits of landslides are also not present at the surface of the terrace (as evidenced by strata in pits at LS2, pit T5, and pits T4 in Fig. 3.3). One landslide deposit was seen at the base of terrace stratigraphy at T1; it is truncated and overlain by the terrace-forming strata. This suggests that the deep-seated landslides – across the entire slope above Rialto Beach -- occurred first, and that their deposits were reworked or removed prior to the emplacement of the sands and gravels that form the bulk of the terrace.

Stratigraphic relationships, radiocarbon dates and tree coring suggest that the landslide at T1 is probably older than 1175-1400 C.E., but one radiocarbon age collected from within the landslide deposit is much younger. At T1, the landslide deposit underlies terrace-forming sand and cobbles. The terrace-forming sand in this site appears similar in age to this unit along the rest of Rialto Beach, based on three ^{14}C ages and the age of one living tree. Detrital wood and charcoal from within the sand at this site date to 1420–1480, 1175–1290, and 1300–1400 cal yr CE (Table 3.2 samples 13, 14, and 15, respectively). A tree living in the surface of the terrace 8 m to the south of the landslide deposit began growing in 1910 or earlier (Table 3.4).

One detrital ^{14}C age was retrieved from within the landslide deposit and is discordant with the three ages mentioned above. The age comes from a 90-cm-long, 10-cm-diameter, straight piece of wood with two broken ends, embedded 90 cm below the top of the unit and sticking out of the outcrop (sample 12, Table 3.2). Colorful cambium, but no bark, remained on its outside, suggesting it died less than a few years prior to its entrainment in the landslide. Radiocarbon dating of the outer few rings of the wood yielded an age of death of 1955 or 2016–2019 cal yr CE. This modern age was collected stratigraphically below samples with detrital ages from the 1400s, and below a tree (Privy tree in Table 3.3) which began growing 1910 CE or earlier. It is possible that the log represents an *in situ* sample that was contaminated with modern carbon or modern wood that recently became entrained in an old deposit (the sample was extracted from the landslide deposit just seaward of the outcrop face).

The possibility that the wood was entrained in the deposit when the landslide occurred, and therefore that the wood represents a maximum age for the deposit, cannot be ruled out, but is unlikely. No landslides can be seen in historic aerial photos from September of 1955 or since 2010, and the overlying ^{14}C age is consistent with ages collected elsewhere from the terrace-forming strata. Moreover, the general expectation when using radiocarbon dating that 5–10% of ^{14}C samples appear to be outliers (Blaauw and Christen, 2005). Therefore, in this dissertation, I interpret the age as an outlier and do not consider it further. Discounting this age is consequential, because if taken at face value, the age would imply that modern processes have produced part of the terrace, and therefore that no uplift is required to form the terrace.

3.3.3.2. Terrace-forming strata emplaced 1420–1800 cal yr CE

The ages of the sand and gravel that form the bulk of the terrace are constrained by eight samples of detrital wood and charcoal obtained from six sites (samples 9–16 of Table 3.2; Figs. 3.3, 3.7) and from trees that are living on the surface of the terrace (Table 3.3; Figure 3.3). Seven radiocarbon ages on detrital wood and charcoal range in age from 1055–1270 cal yr CE (Table 3.2, sample 1) to 1420–1480 cal yr CE (Table 3.2 sample 13). One radiocarbon age (Table 3.2, sample 11), on wood of a log partially exposed at the beach surface and partially buried in terrace sand, was modern. I assume this age represents an outlier; it is not included in the following discussion. Since all ages are detrital, the youngest ages represent the oldest possible age for the sand, indicating that the sands adjacent the samples must have emplaced no earlier than the early 1400s. The maximum age of ~1420 cal yr CE is supported by two radiocarbon ages from bedded sand at opposite ends of the beach (1420–1480 cal yr CE at T1 (Table 3.2, sample 13) and 1410–1460 cal yr CE at LS2 (Table 3.2, sample 5)).

Terrace-forming sand and gravel were deposited prior to the growth of trees atop them. A living Sitka spruce ("Cougar tree" of Table 3.3) on the terrace surface at site LS2 (Fig. 3.7) had >220 rings in 2021; only the outer third of the tree was cored. This tree started growing prior to 1801 CE, probably by at least a few decades. Another Sitka spruce ("Privy tree" of Table 3.3) at site T1 had 114 rings in one core and 124 in another, which reached the center of the tree, suggesting it started growing 1898–1901 CE. This tree is in addition to the 24 spruce trees cored and

reported by Bush (2020), all of which grew in the past 120 years and most of which post-date the Great Olympic Blowdown of 1921.

3.3.3.3. Debris-flow deposits emplaced 1680 cal yr CE to present

Preserved debris-flow deposits at LS2 (Fig. 3.12) are no older than 1680 cal yr CE and are still being emplaced. Radiocarbon samples from within the debris-flow deposits at LS2 were collected by Freeman (2021); the dates are recalibrated and reinterpreted here (Table 3.2; Fig. 3.13). The age of a conifer cone at the surface of the lowest debris flow deposits dates to 1680–1940 cal yr CE (sample 7 of Table 3.2). Three pieces of wood embedded in the same unit date to 1460–1635, 1675–1940, and 1410–1460 cal yr CE (samples 5, 6, 8 of Table 3.2). The cones and wood would have grown prior to being entrained in the debris flow. The wood may substantially predate the debris flow; the cone probably provides a closer maximum age. Radiocarbon results higher in the debris-flow section, and not reproduced here, suggest debris flows have continued to the present (Freeman, 2021), a possibility corroborated by dendrochronology at that site (Jessie Pearl, pers. comm, 2021). I observed an active debris flow deposit at the gully mouth to the south of LS2 in February, 2021 (Fig. 3.3).

3.3.4 Depositional environment of the terrace-forming strata

The mapping at Rialto Beach demonstrates that the terrace is composed of unconsolidated deposits. Below, I interpret the depositional environment of these deposits in order to evaluate hypotheses about the processes that produced the landform. Toward this end, I describe two outcrops in detail and summarize other observations. A long, shore-perpendicular outcrop at Ellen Creek (EC) suggests the terrace at this site consists of beachface deposits. Other parts of the terrace, including pits and long outcrops at LS2 and T1, display what may be beachface deposits, eolian deposits, or cobbly deposits of former beach ridges.

3.3.4.1. EC outcrop

The Ellen Creek (EC) outcrop consists of beachface deposits that top out 0.3–1.5 m above the nearest modern beachface measurements (Figs. 3.7, 3.22, 3.23). The EC outcrop has been exposed as a cutbank where Ellen Creek has incised through the terrace surface (Fig. 3.22), producing a 40 m-long, shore-perpendicular exposure. The outcrop is on the south bank of the

creek and extends east-west from the edge of the bluff to the terrace scarp at the modern beach (Fig. 3.23). The bank on the north side of the creek was not exposed during this study. During the six years of study at Rialto, the outlet at Ellen Creek experienced at least one major avulsion (around 2018) that changed the configuration of the creek outlet, producing new exposures. As a result, the LiDAR map (2018) does not show the configuration of the outcrop as photographed and measured in 2020 and 2021.

Sediments in this creek-bank outcrop (EC) consist of continuous and nearly continuous beds of stratified cobbles, pebbles, and sand (Fig. 3.22). The outcrop consists chiefly of subhorizontal beds 5–20 cm thick. Some gravel lenses are thinner and pinch out laterally. Strata dip gently seaward at an apparent dip of 1–2 degrees and are well-sorted. Cobbles, mostly disc-shaped and well-rounded, are commonly imbricated, dipping seaward. Some beds display cut-and-fill structures; otherwise, bedding is planar and largely parallel. In 2020, the outcrop displayed a prominent erosional surface about 90 cm below ground surface (Fig. 3.22B,C) which could be traced horizontally along the entire outcrop. This surface separated beds of chiefly sand (below) from beds of chiefly cobbles (above). Exposures retreated between 2020 and 2021, and the outcrop in 2021 did not display the obvious erosional surface, instead consisting of alternating beds of sand and cobbles, suggesting the erosional surface was limited in width. The top 20 cm of the outcrop consists of gray silty sand with abundant charcoal and alteration from the soil developed on top. Atop the seaward end of the outcrop are up to 20 cm of modern wave-tossed, well-rounded, unsorted cobbles.

Despite its location at a creek mouth, the outcrop at Ellen Creek does not show characteristic features of alluvial deposits, and more likely consists of beachface deposits than alluvium or eolian deposits. Eolian deposits are ruled out by grain size. The structure of the outcrop matches the tabular, well-sorted beds typical of clastic beach deposits (Clifton, 1973; Bourgeois and Leithold, 1984). The shape of the clasts is also typical of beach deposits: well-rounded, elongated and disc-shaped clasts are common. In multiple beds, these clasts are imbricated and dip seaward, in the expected direction for beach deposits but opposite what would typically be expected if the deposits were alluvial (Clifton, 1973, Reineck and Singh, 1980). The grain size, sphericity, and roundness of the clasts in the Ellen Creek outcrop are more similar to clasts of the

active beachface (described in section 3.3.2.7) than those in the active banks and bed upstream Ellen Creek (described in section 3.3.2.8). The erosional contact seen in 2020 and cut-and-fill structures could have been produced by Ellen Creek or a distributary crossing the beachface. However, the bulk of the outcrop is more consistent with beachface deposits than with alluvial deposits.

3.3.4.2 Pits and minor outcrops

Six pits dug in the surface of the terrace (Fig. 3.3) and numerous minor outcrops along the exposed terrace front (e.g., Fig. 3.15) support the interpretation that the terrace is composed of beachface deposits, but do not rule out possible components of eolian or beach ridge deposits. Strata generally consist of a thick forest soil developed onto bedded sand and cobble gravel. In some places cobbles are scattered amongst bedded sand but commonly the cobbles occur in layers. Bedding, where visible, is planar and horizontal to gently dipping. Some exposures contain cut-and-fill structures. Individual exposures did not provide enough evidence to distinguish beachface deposits from beach ridge deposits, as it was not possible to see whether beds extended from the seaward end of the terrace to the slope (as expected for beach deposits) or whether they were more limited in width (expected for beach ridge deposits). Eolian deposits could only be ruled out where stratified gravel is present.

These deposits exposed in pits at the surface of the terrace may have been disturbed by ancient or modern human activity, with evidence including an abundance of charcoal and fire-cracked rock. However, despite careful examination, we found no fragments of shells, bone, stone tools, or other material of possible archaeological significance.

3.3.4.3. T1 outcrop

At T1 (Fig 3.16), a N-S 160 m-long outcrop along the terrace scarp displays, from stratigraphically low to high, landslide deposits, a sand and cobble unit, and debris flow deposits. I will describe the outcrop in three sections from south to north. At the southern zone of the outcrop (x= -33–16 in Fig. 3.16), the exposure is approximately 15–20 m seaward of the slope. Landslide deposits at the base of the exposure (described in section 3.3.2.2) have an eroded upper contact and are capped by a ~1 m thick package of sand and cobbles that extends the

terrace surface. In the middle zone of the outcrop (x = 26–65 in Fig. 3.16), the outcrop sits closer to the slope: landward, the ground surface and surface of the landslide deposits rise and thicken, and the sand cap thins. In the northernmost zone of the outcrop (x = 90–128 m in Fig. 3.16), the landslide deposits are not present and the outcrop consists of sand capped by debris-flow deposits.

In the northern half of the southernmost end of the outcrop (x = 5–16 m, Fig. 3.17), the landslide deposits extend 0.7 m from the modern beachface to a flat, eroded top surface. The eroded top surface sits at 4.3 +/- 0.1 m NAVD88 with less than 20 cm of rugosity across both clasts and matrix. At x = 7 m, a 1.5 m diameter clast of fractured sandstone is flush with this surface (Fig. 3.17). Near-vertical fabric in the landslide matrix is truncated at the surface. The capping sand, 1.2 m thick, consists of clean, bedded sand with rare garnet laminae and few rounded cobbles. The cobbles are well-rounded, disc-shaped, horizontally aligned, and mostly located at the landslide-sand contact. The smooth surface of the landslide unit, including the flatness of the surface and remarkable lack of relief across clasts and matrix, suggests that the top of the landslide here was eroded. Later, sand and cobbles were emplaced on top.

The middle zone of the outcrop (x = 26–65 m, Fig. 3.18) strikes into the slope and shows the landslide deposits rising to maximum height of 6.7 m NAVD88. The surface of the landslide deposit remains smooth. As in other outcrops, a sand and cobble unit caps the landslide deposit. Here, this unit thins as the landslide surface rises landward. At the highest point of the sand (7 m NAVD88), the sand and cobble unit is 0.25 m thick. These are the highest sand and cobble deposits I saw anywhere along Rialto Beach and are higher than the surface of most of the terrace landform. The length of the sand and cobble unit exhibits planar bedding and common garnet laminae. Scattered, well-rounded cobbles, typically disc shaped, mostly 2–8 cm in diameter and up to 12 cm in diameter, are commonly present directly atop the truncated landslide (Fig. 3.19). Above one of the truncated boulders embedded in the landslide, a single stringer of <1 cm angular clasts of landslide material is interbedded with sand with garnet-rich laminae.

In the northern zone of the outcrop (x = 90–128 m, Figure 3.19), the landslide is not present. Instead, cobbles and sand are present at lower levels and are capped by a lenticular debris-flow deposit (described in section 3.3.2.6).

A cross-section of the landslide deposit and its cap of sand is shown in Figure 3.21. The cross-section is drawn across the southernmost portion of the outcrop; elevations from the middle portion of the outcrop, where the landslide and sand cap rise moving towards the slope, are projected onto the profile.

The surface of the landslide deposit was truncated by erosion. The erosive process that truncated the landslide deposit must have both smoothed the surface of the deposit and removed from the vicinity angular clasts of bedrock that form the boulders carried in the slide, as nearly none are seen amongst the overlying deposits. Erosive processes that could be responsible include waves or streams; below I evaluate these two possibilities.

Waves, in the form of storm waves or intertidal swash and backswash, would have the energy required to smooth the landslide surface and remove large clasts. The lowest parts of the landslide are easily within reach of modern storm waves, but typical storm erosion would remove the front face of a landslide deposit, not cut a flat platform onto its surface. Intertidal swash and backswash, which can cut flat platforms, would require RSL fall between the time that swash and backswash smoothed the surface and today. Flow of a stream would be capable of truncating the top of the landslide deposit, if stream power were sufficient to remove large clasts of angular sandstone and transport them elsewhere. No other geomorphic or sedimentary indicators of a large stream are present.

Below I evaluate depositional processes that could deposit bedded sand atop the truncated landslide deposit. The bedded sand includes common garnet laminae, scattered cobbles mostly along the base of the deposit, and at least one stringer of landslide material: angular clasts 1–2 cm interbedded with sand.

Depositional processes include storm waves, wind, tsunamis, or intertidal swash and backswash. Streams could also be responsible, but these are ruled out for the same reasons as mentioned above. The bedding of heavy minerals rules out storm waves that toss material up onto a berm or ridge (e.g., beach ridge deposits); the presence of cobbles rules out purely eolian processes. A combination of storm toss-up (occasionally tossing up cobbles) and eolian (bedding sand with heavy minerals) is possible but does not explain the stringer of landslide material interbedded in the sand. Tsunamis could deposit sand, cobbles, and landslide material, but the deposit lacks other characteristics of tsunamis, such as internal grading (e.g., Martin and Bourgeois, 2012). Deposition on a beachface provides a simple explanation for bedding sand, garnet laminae, disc-shaped cobbles, and a stringer of the underlying landslide. However, deposition on the beachface requires RSL fall.

If erosion or deposition of these sediments occurred on the beachface in the intertidal zone, RSL fall is required. The lowest smoothed platform of the landslide deposit sits 2.2 m above MHHW and 2.6 m above the modern wavecut platform (Fig. 3.21); the highest smoothed portion of the landslide deposit sits 4.2 m above MHHW and 5.4 m above the modern wavecut platform. The >3 m of relief on the surface of the landslide deposits casts doubt on its interpretation as a wavecut surface, though modern seastacks are smoothed up to ~3 m above the modern wavecut platform (Figs. 3.7, 3.21). To deposit beachface sediments atop the truncated landslide, RSL a minimum of 0.7 higher than today's would be required to reach the lowest part of the landslide; RSL 2.4 m higher would be required to reach the highest part of the landslide deposit.

3.4 DISCUSSION

3.4.1. General chronologic and stratigraphic framework

Geologic mapping at Rialto Beach supports the hypothesis that the terrace consists of beachface deposits with possible local presence of eolian or beach ridge deposits. Radiocarbon dates and tree rings show that the sediments in the terrace were deposited after 1420 cal yr CE and prior to 1800 CE. Geomorphic evidence indicates that the shoreline was at the seacliff prior to this time. The terrace sits just above the modern beachface at Rialto Beach and appears to be finer grained than the modern highest beachface, suggesting the processes occurring today are not the same as those that formed the terrace. Here, I first discuss a conceptual model for the sequence of events

leading to the formation of terrace and other deposits at Rialto Beach, then present two possible hypotheses for formation of the terrace itself: beach progradation at a time of higher sediment supply (with no sea-level change), and removal from shore processes due to relative sea-level fall (i.e., tectonic uplift).

3.4.2. Chronological model for landforms and sediments at Rialto Beach

3.4.2.1. Bedrock eroded to form modern bluff, seastacks, and wave-cut platform(s)

The bedrock that forms the uplands, headlands, slopes, and seastacks consists of Oligocene to Miocene marine sedimentary rocks, which have been substantially deformed (Tabor and Cady, 1978; Gerstel and Lingley, 2000). Following its initial accretion and uplift to form the western edge of the Olympic Peninsula, this bedrock would have presumably extended continuously from the top of the upland above Rialto Beach (where it has been mapped in gullies by Bush, 2020; Freeman, 2021, and Card, 2023) to the tops of the seastacks, and probably farther west (Thackray, 1996). Since that time, the bedrock mass has retreated, likely due to wave erosion, to form the individual seastacks and the wave-cut platform(s) that exist today. It is unknown whether the discontinuous patches of wave-cut platform offshore Rialto Beach (Fig. 3.5), which vary in elevation by 1–2 m, formed as a result of current sea levels or whether the platform(s) are inherited from prior sea-level(s). It is also unknown whether wavecut platform(s) that are discontinuously exposed in the surf zone continue at the same elevations back towards the bluff. (There is evidence for possible deformation of one such platform 0.8 km north of Hole in the Wall, as seen in LiDAR: the surface of what appears to be a wavecut platform forms a gentle antiform; the antiform trends perpendicular to the slope (Appendix 3.4; see also McCrory, 1996.)) It is not yet known why bedrock platforms are mostly absent in the surf zone offshore Rialto Beach: this may have to do with the mechanism or timing of erosion, local structures that juxtapose rocks of different erosivity, or variations in rock strength within the deformed rocks themselves.

3.4.2.2 Deep-seated landslides occurred as slope retreated; deposits largely removed by waves

Bluff retreat, probably by way of deep-seated landslides, occurred until the seacliff reached its current position. Waves undercut the bluff, probably destabilizing the slope and contributing to the triggering of deep-seated landslides now seen on the slope. Waves would have then

reworked or removed landslide deposits, as landslide deposits are largely not seen below the landslide scars that should have sourced them. The one exception found during this study is the landslide deposit seen within the terrace stratigraphy at T1, and the top surface of this is reworked. Radiocarbon ages from within the terrace—which postdates the bluff retreat and associated landslides-- show that bluff retreat and landslides occurred prior to 1420 cal yr CE. In section 3.4.3, I discuss further the implications of the finding that deep-seated landslides predate the terrace.

3.4.2.3 Terrace formed, stranding the seacliff and stabilizing the slope

Sometime following 1420 cal yr CE and prior to 1800 CE, the terrace-forming sands and gravels were deposited. The formation of the terrace itself (whether as deposition or by uplift) stranded the seacliff, stabilizing the slope. Though the deep-seated landslides have continued to adjust via smaller mass-wasting events to the present day, I observed no evidence for initiation of new or large-scale deep-seated landsliding that post-dates the formation of the terrace. The Sitka spruce forest established atop the terrace at least by decades prior to 1801 CE.

3.4.2.4 Debris flows, sourced from gullies, formed fans atop the stranded terrace surface

Debris flows at the outlets of gullies began to be emplaced atop the terrace no earlier than 1680 cal yr CE and continue to the present day. Debris-flow fans form aprons where gullies meet the surface of the terrace (Figs. 3.3, 3.12A). While debris flows likely also occurred prior to the formation of the terrace, when the shoreline was at the seacliff, debris-flow deposits onto the beachface would have been removed by waves. The terrace provides a platform on which debris-flow deposits can be preserved.

3.4.2.5 Terrace retreated

Historic maps and aerial photographs show that the terrace has been retreating at least for the past 130 years (Hill, 2022). Simultaneously, a scarp-retreat deposit has been tossed onto the retreating edge of the terrace; this deposit is reworked and re-established as the terrace retreats. Terrace retreat occurs perhaps most dramatically as a result of tree throw: trees standing on the edge of the terrace become undercut and eventually fall onto the beach, leaving sediment unprotected where the root ball used to be. Troost et al. (2021) estimate that at current rates, the

retreat could reach the seacliff in the next 25 years. If this occurs, the waves may undercut the bluff and result in a reactivation of deep-seated landslides on the slope.

3.4.3 Implications regarding ages of landslides

A new finding of this dissertation is that all of the deep-seated landslides sourced from the slope above Rialto Beach occurred prior to the formation of the terrace. In that prior period, waves were likely undercutting the base of the seacliff, contributing to seacliff retreat, which may have been characterized by deep-seated landslides along the bedrock-cored slope. This geomorphic configuration--landslides that predate the terrace(s) at their toes—can be seen in LiDAR at bluffs above many beaches along the northwest coast.

This finding motivates a different approach for modeling slope stability and landslide triggers along the northwest coast. Prior slope stability studies in this region, including at Rialto Beach, have assumed that the existing topography – in which the terrace is apparently buttressing the toe of the slope – is representative of the conditions under which the deep-seated landslides initially failed. The goal of these studies has been to identify landslides that required an earthquake (or other) trigger to fail, in order to find possible coseismic landslides that can be used for paleoseismology (Grant et al., 2022; Card, 2023). Results of these studies show that deep-seated landslides within the slope are largely too stable to fail without an earthquake trigger or exceptionally high groundwater levels. Given the new findings, presented in this dissertation, that the deep-seated landslides at Rialto Beach predate the buttressing terrace, the modeling by Card (2023) and Grant et al. (2022) likely overestimates the stability of the slope when the deep-seated landslides occurred at Rialto Beach and at other locations with analogous geomorphology. That is, the existing models likely overestimate the amount of perturbation required (i.e., peak ground acceleration or groundwater level) to trigger failure of these deep-seated landslides. Given this updated geomorphic perspective, it is yet to be determined whether the deep-seated landslides required an earthquake or groundwater trigger to fail, or whether undercutting by waves would have sufficiently destabilized the slope.

3.4.4. Origin of the terrace: what processes formed the terrace?

I interpret sand and gravel unit of the terrace at Rialto Beach to largely consist of beachface deposits, which requires that the terrace was not formed under current conditions. The position of the terrace sands and gravels higher than modern beach deposits requires RSL fall or beachface progradation under a different sediment regime.

Here, I discuss two hypotheses for the formation of the terrace: shoreline progradation at modern sea levels and RSL fall. Shoreline progradation at modern sea level requires a higher sediment supply to the beach. RSL fall does not require higher sediment supply but, instead requires tectonic uplift. I do not rule out either possibility and discuss strengths and weaknesses of both hypotheses.

First, I reject the alternative possibility that the terrace is related to glaciation. While there are abundant, large, flat outwash terraces in the Quillayute river valley and elsewhere in the region (Thackray, 2001), raising the possibility that the Rialto Beach terrace is related to glaciation, the young age (<~600 years) of the Rialto Beach terrace sediments rules out formation by glaciation-related processes.

3.4.4.1 Hypothesis 1: The terrace formed by shoreline progradation at modern sea level

Producing the terrace through shoreline progradation is contingent on a high sediment supply that does not continue today. That is, an influx of sand and gravel is required to induce beach progradation (instead of the retreat currently observed) and to deposit mostly sand high in the paleo-beachface and other deposits that make up the terrace (as opposed to mostly cobbles as seen high on the modern shoreline).

In this scenario (Fig. 3.24), progradation would have begun around or after 1410 cal yr CE as the result of a newly available supply of sediment. The terrace would have formed as the beachface built seaward at heights just above the modern beachface. Termination of the higher sediment supply by 130 years ago would stop progradation of the beachface and allow the erosional retreat observed today. Here I consider whether observations from Rialto and analogous locations permit or refute this hypothesis.

Outcrop EC

The Ellen Creek (EC) outcrop could consist of prograded beachface deposits, provided the slope of the beachface were much shallower during progradation than during the present-day erosional retreat, and provided the prograding beachface could accrete sediment ~0.7 m higher than the modern retreating beachface does. These two provisos are examined in the following paragraphs.

Evidence from nearby prograding shorelines suggests the first provision could be true. Seaward-dipping strata of modern prograding beachfaces along the Washington coast have dips similar to the 1–2 degrees seen in the paleo-beachface deposits of the EC outcrop (locations in Figs. 3.1), shallower than the 4–5.2 degree modern, retreating beachface. For example, south of Rialto Beach, a barrier spit adjacent Willapa Bay is prograding with sediment supplied by the Columbia River littoral cell (Meyers et al., 1996). Prograded strata from the past several hundred years, seen in ground-penetrating radar, are laterally extensive and dip seaward at 1–2 degrees. However, north of Rialto Beach, Hobuck and Tsoo-Yess beaches are also prograding, though with steeper dips similar to the retreating beachface at Rialto Beach (Miller et al., 2023). At Hobuck and Tsoo-Yess beaches, modern sandy prograding beachfaces dip seaward at <5 degrees. Ground-penetrating radar (Peterson et al., 2014) show strata that extend for tens of meters with dips of between 4 and 5 degrees. If the paleo-beachface of the EC outcrop were more similar to the modern beachface at Willapa Bay than those at Hobuck and Tsoo-Yess, then it is possible that the gently dipping strata could be explained as a prograded beachface.

It is unclear whether the second provision could be true or not. The beachface deposits in the EC outcrop are higher than the modern Rialto Beach beachface in the same area and also higher than modern prograding beachfaces at Hobuck, Tsoo-Yess, and Sand Point. Because the tidal ranges of these three sites are nearly equivalent, I compare them with respect to NAVD88. At Hobuck and Tsoo-Yess, Miller et al. (2023) measured modern beachface deposits up to 4 m NAVD88, with modern dunes extending higher. These beachfaces experience seasonal aggradation mid-way down the beachface: around the position of MHHW, summer beaches are ~1 m higher than winter beaches. There is also smaller amount of seasonal summer accretion lower on the beachface (Figure 4 of Miller et al., 2023). At Sand Point, Peterson et al. (2014) report

elevations of deposits from one transect. There, paleo-beachface deposits reach as high as 5.5–6 m NAVD88, 0.5–1 m higher than the modern beachface deposits, which reach 5.0 m NAVD88. Paleo-dune deposits, distinguished on the basis of grain size, reach meters higher. The paleo-beachface and modern beachface at Sand Point are at similar elevations to the paleo- and modern beachfaces measured at Rialto and presented in this study. The modern prograding beachface at Hobuck and Tsoo-Yess is about 1 m lower.

Is 1 m a geologically meaningful difference in elevation between a paleo-beachface and a modern beachface? Evidence from Hobuck (Miller et al., 2023) suggests that seasonal accretion on the order of 1 m might be expected. However, at Hobuck this seasonal accretion does not occur at the uppermost end of the beachface. Nonetheless, the possibility of seasonal accretion, especially if the EC outcrop represents an anomaly rather than a representative section of the terrace at Rialto Beach, suggests that beachface progradation could explain the terrace at its current elevation.

Outcrop T1

The outcrop at T1 could be produced by beach progradation if storms are responsible for truncating the top of the landslide deposit. Similarly, storm waves and wind at modern sea levels provide a mechanism for tossing cobbles atop the truncated surface and blowing sand atop them.

Lack of beach ridges

One issue with the beachface aggradation hypothesis is that the terrace at Rialto Beach lacks geomorphic beach ridges. Beach ridges 7–30 m wide can be seen in LiDAR at the modern prograding beaches at Hobuck and Sand Point (Fig. 3.3). The terrace at Rialto Beach, at >50 m wide, ought to be large enough to display beach ridges if they exist. It's possible that swales between beach ridges, if they existed, could have been filled with sediment so that linear ridges are not recognizable. More pits dug in the terrace surface, or multiple lines of ground penetrating radar, would have to be collected to determine whether or not this could be the case.

Sediment availability for progradation

A pulse of available sediment required to prograde the shoreline must have begun around or after 1410 cal yr CE must have ended by at least 130 years ago. A pulse of sediment supply of this magnitude and duration would represent a dramatic environmental change along this part of the coast. Such sediment could have been sourced from glacial outwash terraces in the drainages of Ellen Creek and the Quillayute River. Perhaps a storm or earthquake could have triggered many slope failures in these unconsolidated outwash deposits, introducing and abundance of sand and well-rounded cobbles into the streams. At Hobuck, a modern prograding beach that is also experiencing modern RSL fall, Miller et al. (2023) find that local rivers do not supply sufficient sediment for the observed progradation, and instead suggest that the RSL fall makes available nearshore sediments that can be transported to the shoreline.

If the other terraces along the northwest coast of Washington are analogous to the one at Rialto Beach, such a pulse in sediment supply would have to be regional in extent. This explanation is further complicated by the fact that several of these terraces are in isolated pocket beaches, not at the mouths of rivers or streams.

3.4.4.2 Hypothesis 2: The terrace formed as the result of RSL fall

Given the young age of the terrace (~600 years BP) and stability of sea levels during the past several thousand years (Yousefi et la., 2021), RSL fall requires tectonic uplift. The tectonic might have been abrupt or gradual. The terrace persisted long enough for a Sitka spruce forest to establish by at least 1800 CE. Fig. 3.25 provides an illustration of the events in this hypothesis.

EC outcrop

RSL fall provides a simple mechanism to strand the terrace at the EC outcrop and force the incision of Ellen Creek through those deposits to its current position. RSL fall also provides an explanation for how beachface deposits can crop out in the Rialto Beach terrace at elevations higher than the modern Rialto Beach, or beachfaces at Hobuck (Miller et al., 2023) and Sand Point (Peterson et al., 2014). However, uplift does not fit the evidence completely. If uplift alone produced the terrace, the beachface deposits within the terrace are analogous to the modern beachface. As discussed in section 3.4.4.1, the dip of beachface-deposit beds in the terrace dip

20–50% shallower than those in the modern beachface; uplift does not explain how the paleo-beachface might dip more shallowly than the modern beachface.

T1 outcrop

At T1, a higher RSL during the formation of the terrace provides a simple explanation for truncating the top of the landslide and emplacing sand and cobbles on top. If the landslide were deposited into the intertidal zone, waves could truncate the top and remove from the vicinity the angular bedrock clasts that constitute much of the deposit. Then, the sand and cobbles atop the truncated landslide, as well as beds of garnet-rich sand, could have been deposited as beachface deposits.

An issue with this interpretation lies in the apparent lack of an uplifted wavecut platform. As described in section 3.3.2.1, there is a bedrock platform (or platforms) near MSL, with elevations that vary by as much as 1.5 m. Does this variation represent a variation in sea level? It is unknown whether or not the platform was cut under modern sea levels or whether it is inherited. Nonetheless, there is no obvious uplifted wavecut platform at Rialto Beach.

Uplift would not trigger shoreline retreat

The modern Rialto Beach is retreating; this observation is not explained by uplift. Uplift typically triggers shoreline progradation, as is currently seen at Hobuck (Miller et al., 2023). If uplift occurred at Rialto Beach, other processes (e.g., possible modern RSL rise, which is not evaluated here) must be invoked to explain why the shoreline is currently retreating and not prograding.

Amount of uplift required

The top of terrace-forming strata lie 0.3–1.6 m above measurements of the modern beachface (Figs. 3.7 and 3.8). Outliers exist below the debris flow fan at LS2, where highest sand seen in the terrace deposit is 1–2 m lower than most of the sand mapped in the terrace, and at T1, where the terrace-forming strata, atop the landward edge of the truncated landslide, is 3 m higher than most terrace-forming strata found elsewhere along Rialto Beach.

Estimates of relative land-level change come from the outcrop at Ellen Creek and the truncated landslide at T1. At Ellen Creek, the creek has incised 1.5 m into beach sediments. If the current stream level in the creek represents base level at its outlet, this base level has fallen (i.e., the outlet uplifted) at least 1.5 m since the terrace's formation (Fig. 3.23). At T1, comparing the eroded surface of the landslide with the modern wavecut platform probably provides a maximum amount of uplift (Fig. 3.21). The wavecut platform is a modern erosive analog on the beach; probably the landslide was not eroded to an elevation lower than this modern platform. A projected seaward slope fit to measurements of the modern wavecut platform rests 2.6 +/- 0.1 m below the flat eroded surface of the debris flow.

It is unknown where on the beachface the sediments in the terrace formed; if the beach deposits now visible in the outcrop were formed midway down the beach or nearly to MSL, uplift could have been up to a few meters greater. However, given that the majority of the sand in the terrace sits within about a meter of the modern beach surface, and the landward-most edge of the terrace sits at most sites less than a meter or two higher, beach-wide uplift of > 2 m seems unlikely.

Use of ground penetrating radar at Rialto Beach, though logistically complicated, might provide evidence if whether the entire terrace is composed of seaward-dipping strata at the same elevation as those seen at Ellen Creek.

Gradual land-level change at current rates could account for height of terrace

Both glacial isostatic adjustment and modern interseismic strain drive land-level change on the northwest coast of Washington. In principle, both could contribute to the elevation of the terrace surface.

Observations along Cascadia show that in periods between great subduction zone earthquakes, land level gradually changes in response to accumulating strain above the locked megathrust (e.g., Newton et al., 2021). Interseismic land-level change is commonly opposite in sign to observed co-seismic change (e.g., gradual interseismic uplift following abrupt co-seismic subsidence; Wells and Simpson, 2001). It is unclear whether Rialto Beach is currently

experiencing interseismic emergence or subsidence, given that the uncertainties in the GPS data (4.8 mm/yr) exceed the emergence signal (1.2 mm/yr).

The magnitude of possible interseismic emergence is enough to account for the elevation of the beach deposits in the terrace, assuming a constant rate since the last great earthquake in 1700. At the measured rate of 1.2 mm/yr (Newton et al., 2021; Pacific Northwest Geodetic Array, 2023), the terrace would have emerged 0.39 m since 1700, which is similar to the smallest estimates of difference between the elevation of the terrace and elevation of the modern beachface. At the maximum rate given the uncertainty of the geodetic measurements (uplift of 6.0 mm/yr), the terrace would have emerged 1.9 m from its 1700 position. The minimum permissible rates estimated (-3.6 mm/yr), would indicate subsidence of 1.2 m since 1700. These estimates of deformation may not be realistic because of the uncertainties in the amount and direction of current vertical movement and because the postseismic deformation is not expected to occur uniformly through time. However, they show that it is permissible for the height of the terrace to be accounted for by interseismic strain.

Abrupt uplift could account for height of terrace

Uplift at Rialto Beach, if abrupt, could plausibly have been produced by an earthquake on the Cascadia subduction zone or unmapped crustal structures in the overriding plate. Here I consider alternative hypotheses that the terrace could have been produced by coseismic uplift on a local crustal structure or the CSZ.

Crustal faults can cause abrupt uplift, but there is currently inadequate information to evaluate whether uplift on a crustal structure could have produced the terrace at Rialto Beach. Bedrock structures in the region are poorly known because of glacial sediment and forest cover. Several studies in Cascadia attribute deformation of coastal terraces to shallow crustal faults (e.g., Padgett et al., 2019; Stanton et al., in prep). Published geologic maps do not identify any nearby active fault though bedrock exposure is poor due to dense forest cover and widespread glacial deposits, and thus the structures are poorly known. Near Rialto Beach, Thackray (1999) observed a Pleistocene terrace broadly folded in the Kalaloch syncline. The shallower limb of the fold

dips ~2 m/km; the steeper one dips more than 7 m/km. Deformation of this scale would be noticeable in the LiDAR across the 2.4 km at Rialto Beach, and no such deformation is present.

Deformation by crustal structure(s) could be more confidently evaluated by detailed geologic mapping of the slopes around Rialto beach or geophysical investigation to identify subsurface faults (e.g., Stanton et al., in prep). The broad extent of the terrace at Rialto Beach (forming a relatively flat surface over 2.4 km) would require a relatively broad zone of crustal deformation.

Deformation associated with subduction-zone earthquakes has been documented to produce broad, abrupt land-level change, e.g., subsidence in southwest Washington (e.g., Atwater and Hemphill-Haley, 1997). The terrace at Rialto Beach is among the southern-most of other coastal terraces, similar in elevation, that are observed over 100 km along the coast of northwest Washington. If these terraces can be attributed to uplift and not to other processes, and if they are of the same age as the terrace at Rialto Beach, it would be reasonable to infer that their uplift is the result of subduction zone deformation and not local structures.

If uplift is attributed to coseismic deformation during a CSZ earthquake, the ages presented here indicate that such an earthquake would have had to occur between 1410 and 1800 CE. Two possible earthquakes are inferred from existing records that overlap with that timeframe. The most recent, which occurred in 1700 (Satake et al., 1995), is evidenced by widespread coastal subsidence and tsunami deposits in marshes to the south, and on Vancouver Island to the north (Fig. 1A). Coseismic subsidence in 1700 has also been inferred at Neah Bay (Peterson et al., 2013), though the evidence at that site can be interpreted in other ways.

The offshore turbidite record has been interpreted to include a penultimate earthquake some time 1400–1560 CE (Goldfinger et al., 2017), though both the age of the turbidite deposit and whether or not it reflects a subduction zone earthquake have been the subjects of debate (e.g., Atwater and Griggs, 2012). Possible evidence against an earthquake within that timeframe comes from the tsunami record at Discovery Bay, which is thought to be a reliable recorder of CSZ tsunamis (Garrison-Laney, 2017). There, the penultimate event dates to 1350–1390 cal yr CE, prior to the formation of the Rialto Beach terrace.

The observations and radiocarbon ages from the Rialto Beach terrace cannot distinguish whether it might have formed in the 1400s or in 1700. If the terrace formed in an earthquake of the 1400s, it likely experienced interseismic deformation following that event then additional coseismic deformation in 1700, with the result that the uplift estimated here is the sum of two deformation events and two periods of interseismic strain. The possibility that all four of these time periods have different rates, amounts, and direction of deformation substantially complicates the interpretation.

If uplift at Rialto Beach (or elsewhere along the CSZ) were attributed to coseismic uplift during CSZ earthquakes, this finding would change the framework for modeling tectonic deformation and past earthquakes in the subduction zone. In subduction zones, the pattern of coseismic uplift and subsidence is controlled, at least in part, by the down-dip limit of slip during earthquakes (Hyndman, 2013). Coseismic uplift occurs closer to the trench, and subsidence occurs further inland. The transition zone between the two is thought to occur over the down-dip limit of slip. The lack of geologic evidence for coseismic uplift in Cascadia has led to assumptions that this transition zone is at the coastline or offshore (e.g., Hyndman & Wang, 1995). This interpretation has been used as an important constraint in earthquake models. Models of subduction zone earthquakes in Cascadia (Wirth and Frankel, 2019; Melgar et al., 2022) are constrained to avoid producing uplift, since none has been previously observed. The National Seismic Hazard Maps also use these assumptions, and shallow down-dip limits of slip account for 70% of the subduction zone's seismic hazard (Petersen et al., 2020). A recognition of coseismic uplift in northwestern Washington would inform these models, possibly allowing deeper slip limits in this region.

3.4.5. Is subsidence in 1700 permissible in the geologic record at Rialto Beach?

A subduction zone earthquake in 1700 produced subsidence to the south and north of Rialto Beach (Fig. 3.1). The terrace, with its age range of 1420–1800 cal yr CE, may have existed at the time of this earthquake. Does the stratigraphy preclude subsidence from having occurred in 1700?

Coseismic subsidence has left geomorphic evidence on coastal plains elsewhere, and these other sites bear some resemblance to the stratigraphy and morphology at Rialto Beach. In particular, subsidence has been blamed for the production of eroded scarps on relic shorelines, similar to Rialto Beach.

Along the Alaska subduction zone, coseismic subsidence in 1964 lowered a forested beach-ridge plain into the surf zone, initiating retreat of beach ridges in the plain (Kelsey et al., 2015). Evidence for subsidence came from Sitka spruce, formerly growing atop beach ridges, that were lowered into the surf zone. Spruce on the edges of the plain were killed and the beach ridges eroded landward, forming a retreating scarp. A scarp-retreat ridge (Kelsey et al. 2015 refer to this ridge as a new beach ridge) formed atop the lowered plain. This example has some similarities to the situation at Rialto Beach: both sites have a forested surface with a retreating seaward edge. Both sites emplace a modern ridge of wave-tossed cobbles on the seaward edge of the forested surface. However, unlike the Alaska site, the retreating terrace at Rialto Beach is not obviously a beach-ridge plain, and instead probably consists of beachface deposits, which form at lower elevations than beach ridges. The terrace at Rialto Beach notably lacks ridged morphology that is diagnostic of beach-ridge plains. Also, the rooted trees that cap the terrace are not in the surf zone. These differences suggest that different processes may be at play.

Eroded beach scarps have also been attributed to coseismic subsidence in Cascadia, at a beach barrier spit adjacent Willapa Bay (Meyers et al., 1996). There, ground-penetrating radar reveal buried scarps that truncate shallowly dipping sand deposits of a prograding barrier. These scarps were interpreted to evidence subsidence and a brief period of shoreline retreat before progradation began again. Meyers et al. (1996) attributed subsidence to earthquakes in 300 cal yr BP, 1100 cal yr BP, and several earlier events. The stratigraphy at that site has similarities to that at Rialto Beach: the shallow dips of the prograded barrier deposits (1–2 degrees) are similar to those seen in the outcrop at Rialto Beach, and the dip of the erosional surfaces (7 degrees) is similar to the dip of the modern beach at Rialto, which is eroding into the terrace. If the Rialto Beach terrace formed as a prograding beachface, perhaps subsidence triggered the start of terrace retreat, as occurred at the Willapa barrier spit.

Could subsidence have triggered the erosion of scarps (retreat of the terrace) at Rialto Beach? Such an explanation might explain the difference in dips between the old (prograding) beachface and the modern (retreating) beachface. However, the old beachface at Rialto Beach is already apparently higher in elevation than its modern counterpart. This suggests that if subsidence occurred, interseismic uplift would have to exceed the magnitude of the subsidence.

3.4.6 Recommendations for further work

Results presented here motivate further mapping and dating of terraces along the NW coast of Washington for comparison with Rialto Beach. It is particularly important to characterize the age of the terraces and the processes involved in their formation. If other terraces along the northwest coast are composed of unconsolidated sediments (and not bedrock), facies analysis should be undertaken in greater detail than in my study at Rialto Beach and paired with a detailed characterization of modern analogs. The wavecut platform(s) that sit around MSL could also be studied: current LiDAR does not sufficiently capture these platforms to evaluate their extent and whether they form one or multiple "steps." Additionally, paired geological and geophysical mapping to identify local structures is likely a necessary precursor to attributing the height of terraces to deformation on the Cascadia subduction zone.

If terraces appear to require tectonic uplift, the ages and elevations of these terraces could be used to test hypotheses about deformation on local crustal faults and folds and add spatially varying estimates of coseismic deformation from the megathrust. Filling the data gap in relative sea level histories along the northwest coast of Washington will also benefit GIA models, with possible implications for understanding mantle rheology or ice histories. The terrace at Rialto Beach shows that future mapping of similar terraces must evaluate the stratigraphy as well as the morphology of the terraces.

3.5 CONCLUSIONS

Geologic mapping of the marine terrace at Rialto Beach, on the northwest coast of Washington state, indicates that the terrace formed between 1410–1800 cal yr CE. I interpret the sand and cobble terrace to consist at least in part of beach deposits that sit slightly higher than the modern beachface. The terrace could have formed as a result of beach progradation or tectonic uplift.

Tectonic uplift may have been produced during subduction zone earthquakes or deformation on an unmapped crustal structure, or less likely, as interseismic uplift. Similar investigations, conducted at the other terraces in northwest Washington, should be undertaken to test whether or not other nearby terraces may be explained by the either of the two hypotheses presented here.

3.6 FIGURES

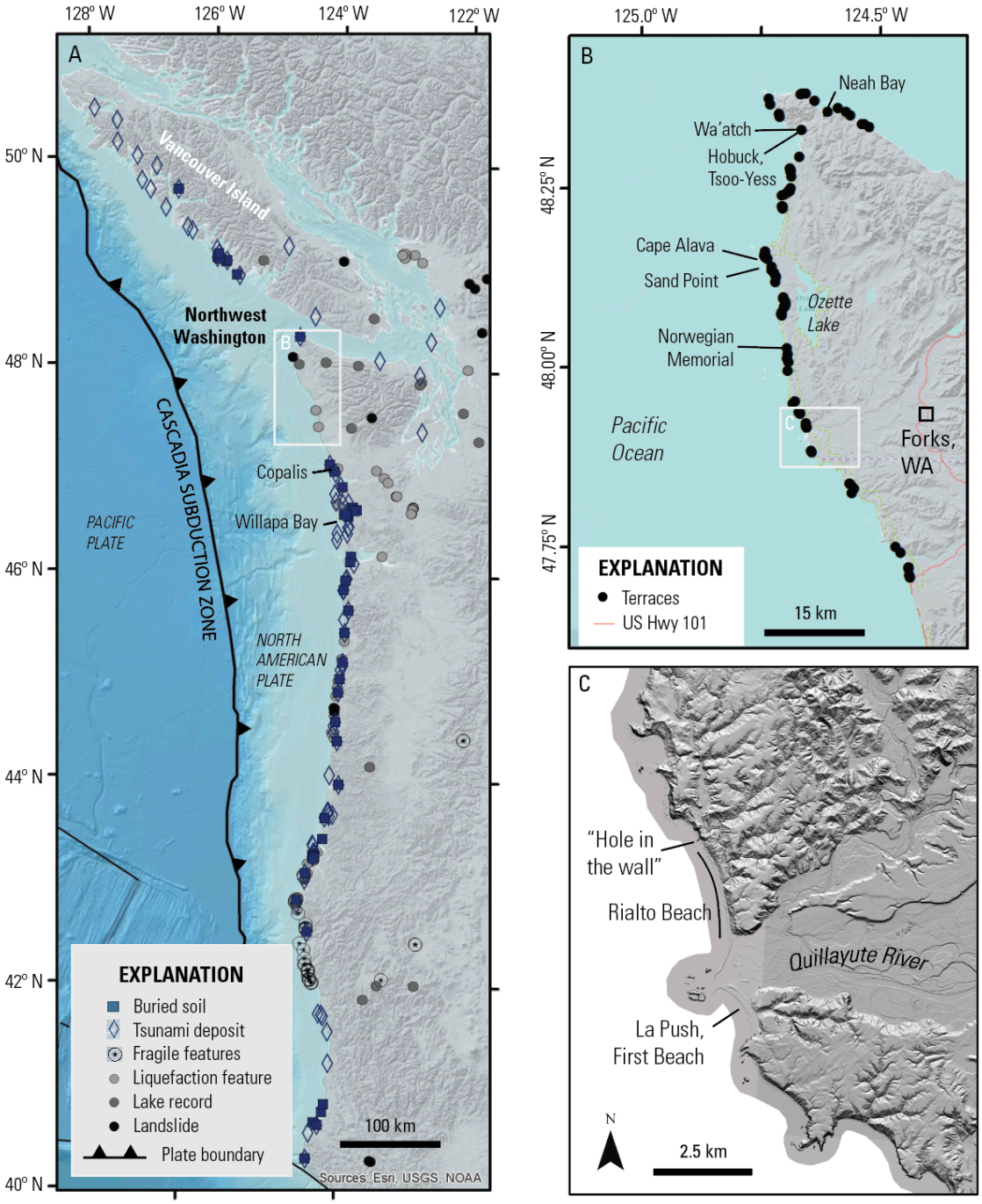

Figure 3.1. Index maps showing the location of northwest Washington and Rialto Beach above the Cascadia subduction zone. (A) Cascadia subduction zone and existing published coastal evidence for paleo-earthquakes (Staisch and Walton, 2022). Note the paleoseismic data gap in northwest Washington. (B) Northwest Washington, including locations of terraces similar to the one at Rialto Beach. Terraces are identified here in addition to those noted by Riedel et al. (2021). (C) Geomorphology in vicinity of Rialto Beach, including glacial outwash terraces in the Quillayute River valley. The gray apron around the shoreline is an artifact of LiDAR.

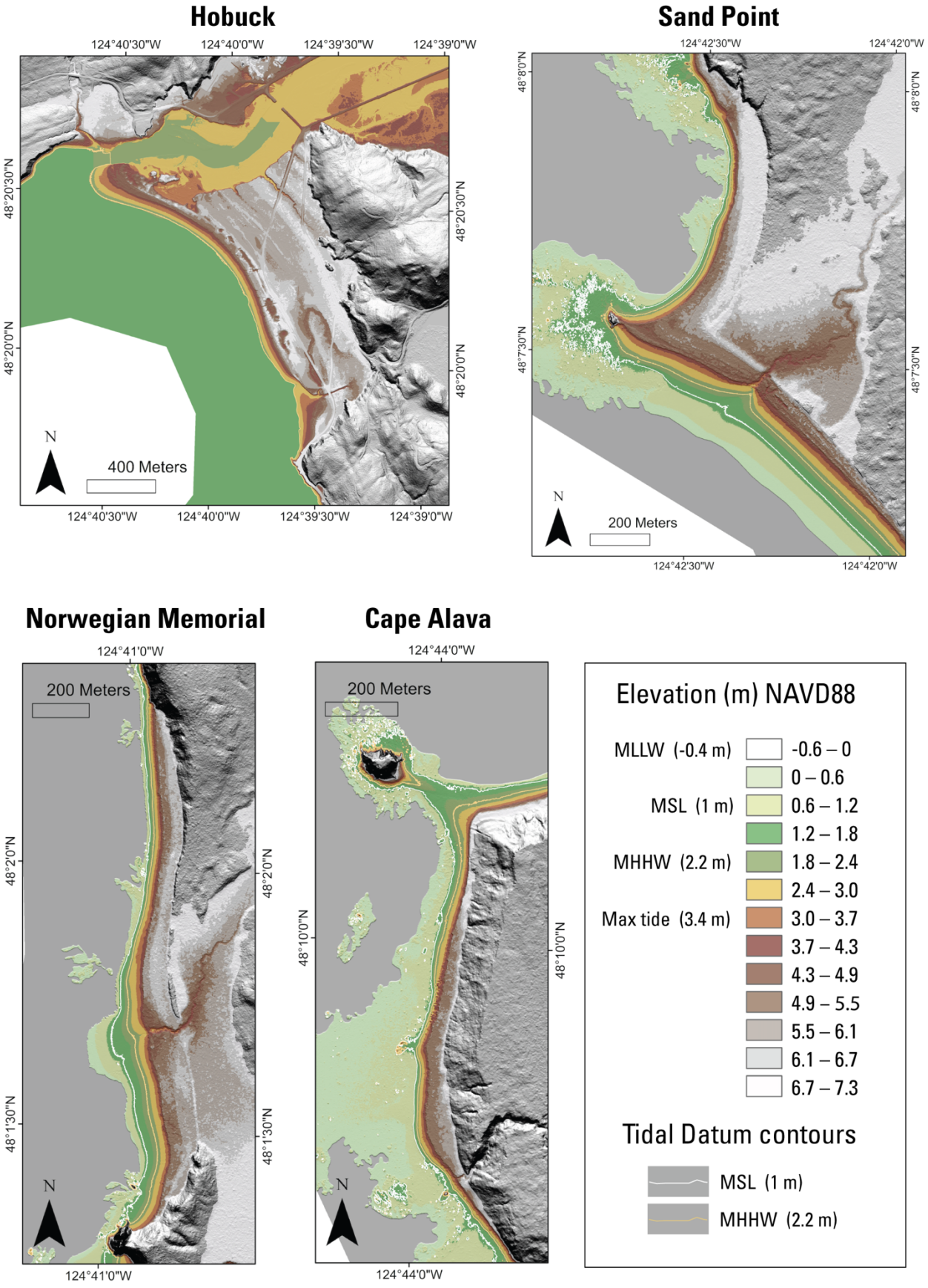
Hobuck
124°40'30"W
124°40'0"W
124°39'30"W
124°39'0"W
48°20'30"N
48°20'0"N
N
400 Meters
Sand Point
124°42'30"W
124°42'0"W
48°8'0"N
48°7'30"N
N
200 Meters
Norwegian Memorial
124°41'0"W
48°2'0"N
48°1'30"N
200 Meters
N
Cape Alava
124°44'0"W
48°10'0"N
200 Meters
N
Elevation (m) NAVD88
MLLW (-0.4 m)
MSL (1 m)
MHHW (2.2 m)
Max tide (3.4 m)
-0.6 – 0
0 – 0.6
0.6 – 1.2
1.2 – 1.8
1.8 – 2.4
2.4 – 3.0
3.0 – 3.7
3.7 – 4.3
4.3 – 4.9
4.9 – 5.5
5.5 – 6.1
6.1 – 6.7
6.7 – 7.3
Tidal Datum contours
MSL (1 m)
MHHW (2.2 m)

Figure 3.2. (prior page) Maps of beach-adjacent terraces along the coast of northwest Washington. At Hobuck, the shoreline is currently prograding and elevations above 4 m NAVD88 are attributed to dunes (Miller et al., 2023). At Sand Point, progradation of a berm started around 1.5 ka and terminated after 1270–1410 cal yr CE (Peterson et al., 2014). At Cape Alava, four possible treads of beach terraces have been identified (visible as small platforms around the northernmost headland) that do not resemble the rest of the terraces pictured (Daugherty and Fryxell, 1967). The terrace at Norwegian Memorial has not been studied. Elevations of the terraces and lower are shown in color; each color represents 1.6 m of elevation. Tidal datums MSL and MHHW from the La Push tide gauge are shown as contours. The tidal range is assumed to be similar at all these sites. Elevations around MLLW are not captured in LiDAR, as they sit below the water surface. Slopes, headlands, and uplands are shown in the original gray LiDAR (OPSW 2018; WA DNR).

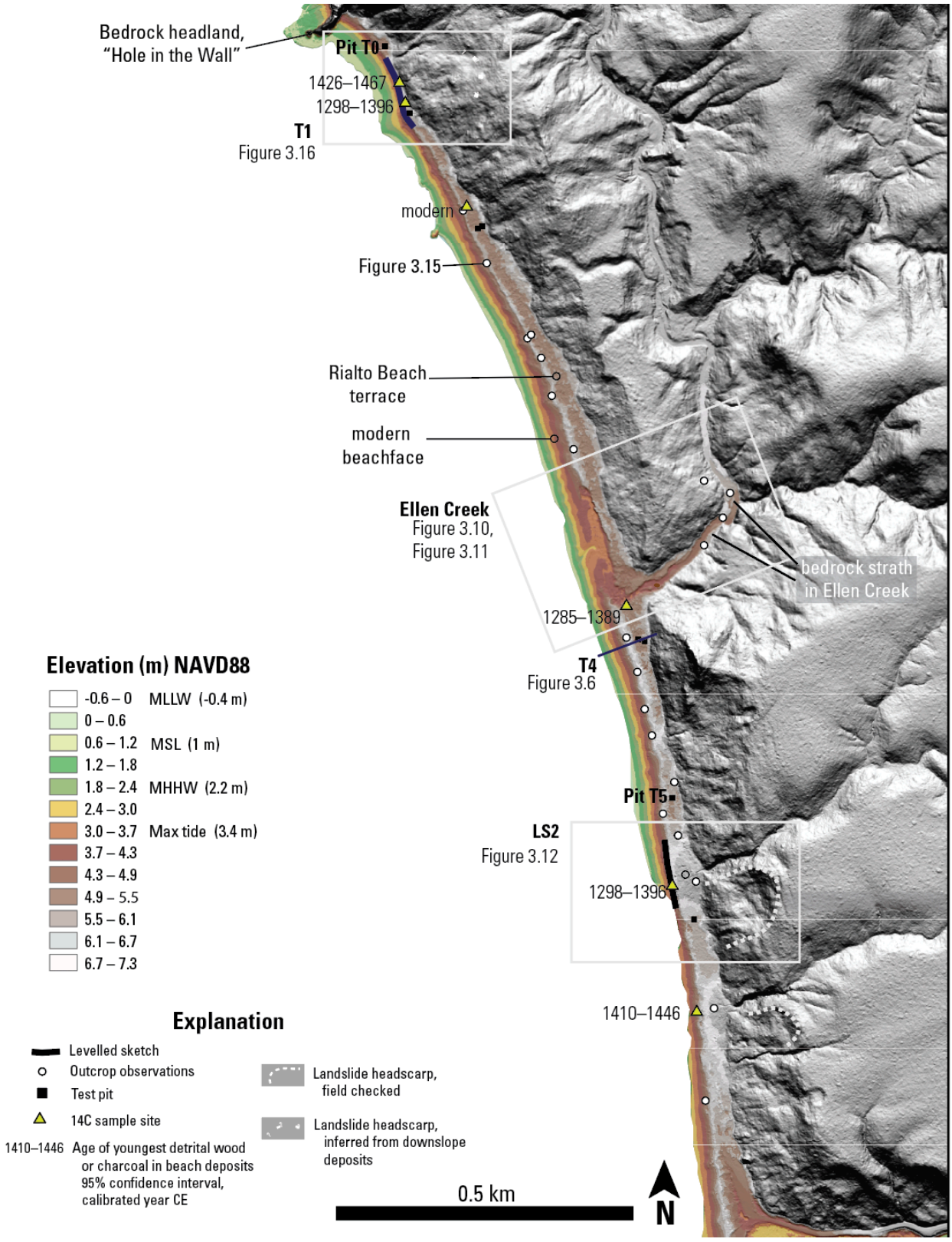

Figure 3.3. Map of Rialto Beach showing location of sketches, outcrop observations, test pits, and radiocarbon sample sites. Colored elevations show the low-elevation terrace and modern beachface.

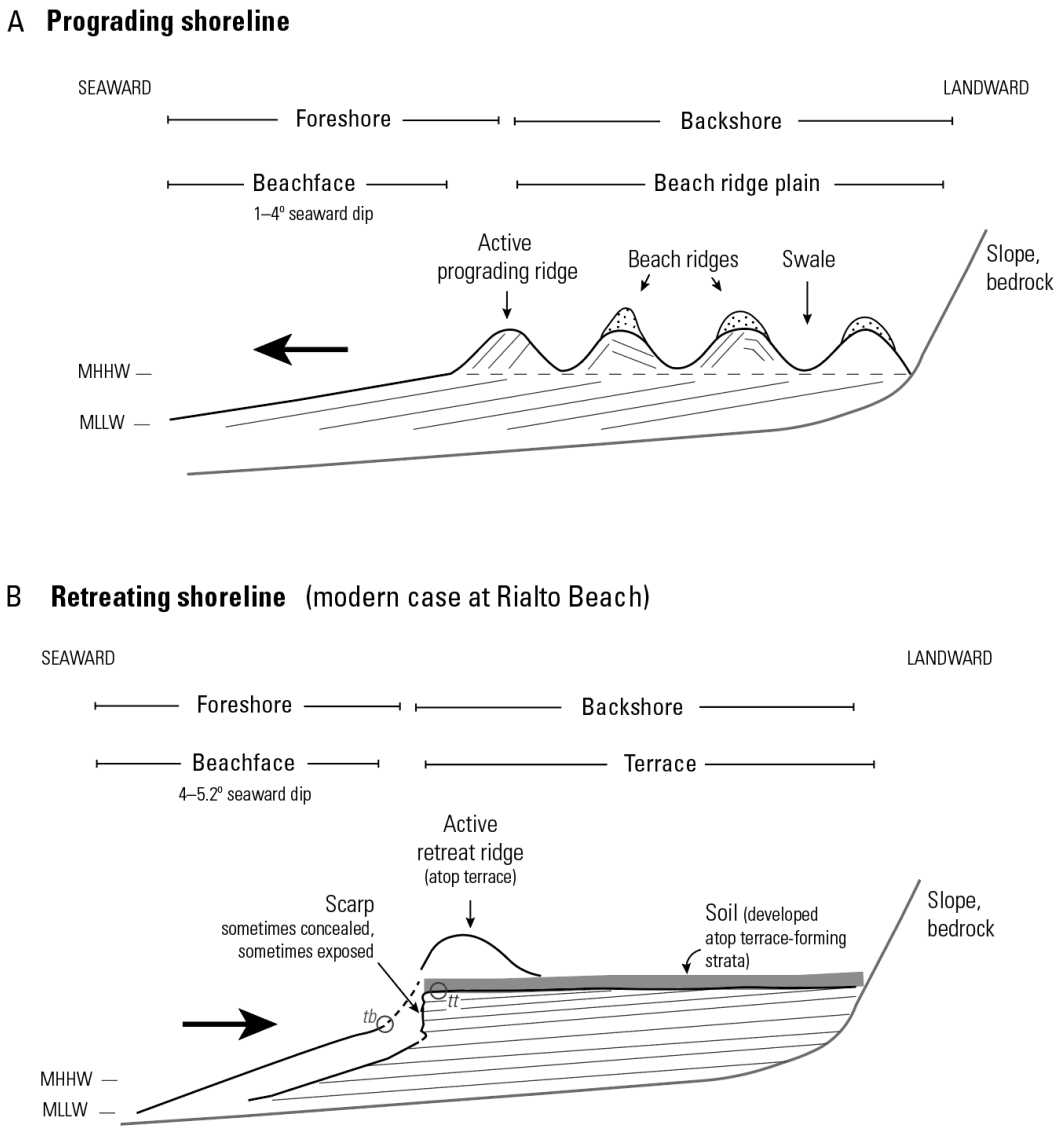

Figure 3.4. Schematic beach profiles showing morphology terms used in the text. (A) Illustration of a prograding shoreline that is built seaward by the lateral accumulation of beach ridges. The active beachface extends from approximately MLLW to MHHW. The accumulation of beach ridges forms the backshore, in this case a beach ridge plain. Beach ridges are initially formed by wave swash and may increase in height if the wave-worked sediments are capped by wind-blown sand. This cartoon shows several variations on internal stratigraphy of beach ridges (as summarized by Tamura, 2012); these variations would not necessarily be present on the same beach. The figure intends to show the variety of internal stratigraphy that is possible within beach ridges. (B) Illustration of the retreating shoreline at Rialto Beach. The backshore is formed by the terrace, which consists at least in part of shallowly seaward-dipping sands, gravels and cobbles with soil developed on top. The terrace is retreating landward, forming a scarp at its seaward edge. A ridge of cobbles and sand forms atop the retreating scarp (active retreat ridge). The retreating scarp is sometimes exposed and sometimes buried by this retreat ridge. The top of the terrace-forming strata (*tt*) is on average higher than the top of the modern beachface (*tb*), though *tt* is not higher than *tb* at all sites and times.

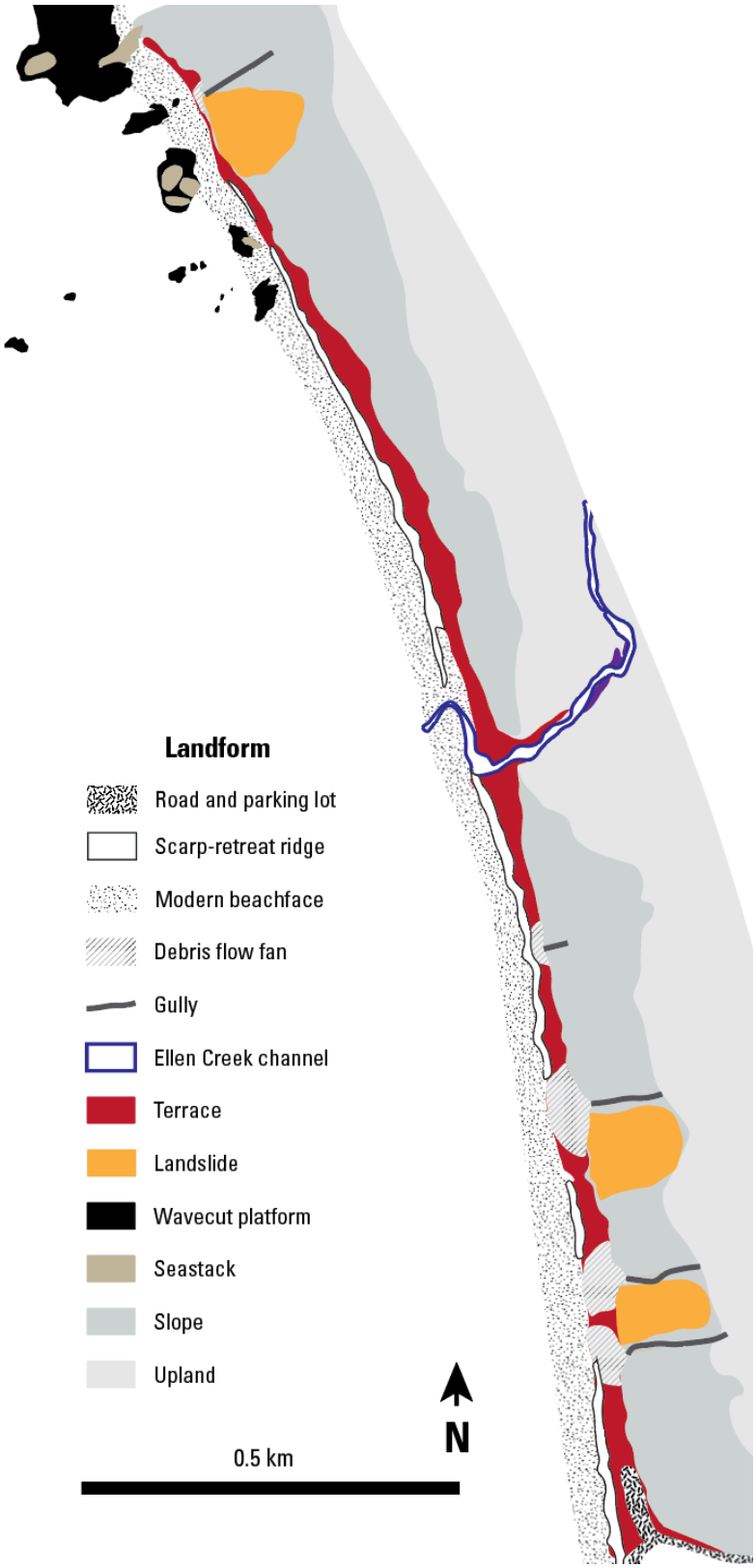

Figure 3.5 Geomorphic map of Rialto Beach, the Rialto Beach terrace, the slope, and the upland. The wavecut platform is cut into rock; the landslides mapped are only those featured in this study or prior studies (Bush, 2020; Freeman, 2021).

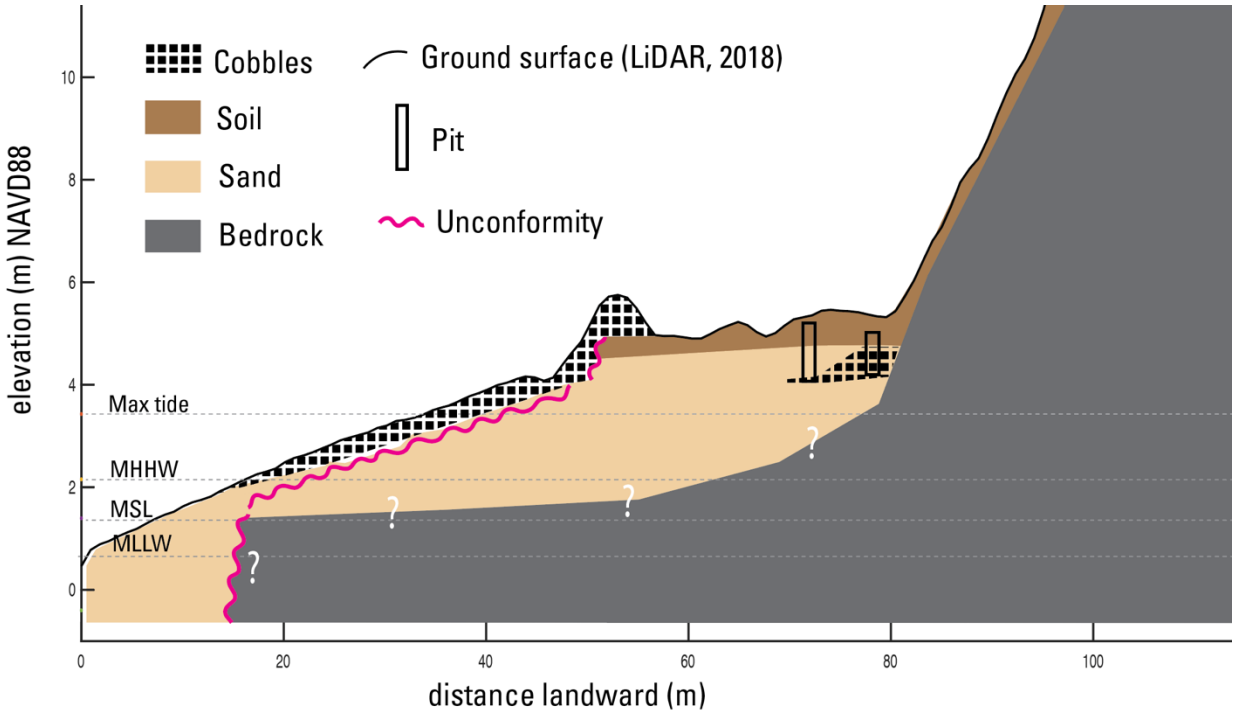

Figure 3.6. Characteristic slope profile at Rialto Beach, including the beachface, terrace, and upper slope. This particular profile was drawn from LiDAR at T4 (location in Fig. 3.2). Tidal datums are plotted at the elevations of Max tide, MHHW, and MSL. Because MLLW is more often than not underwater, it is typically not captured in LiDAR. The top of modern beach morphology forms around and just above the Max tide datum. Riedel et al. (2021) describe Rialto Beach as being sand-dominated in the lower intertidal zone and pebble-dominated higher in the intertidal zone.

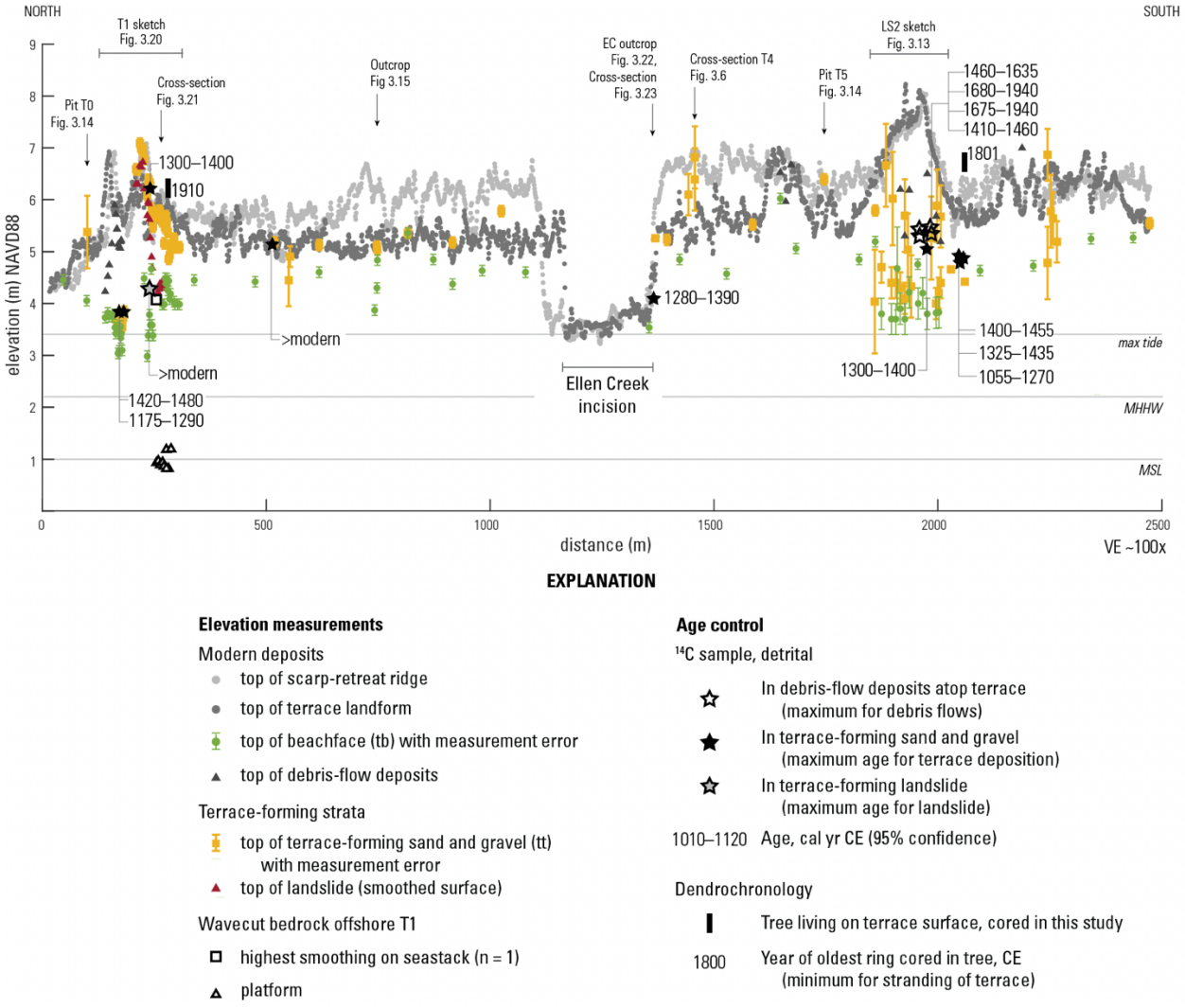

Figure 3.7. Shore-parallel elevation profiles along the terrace at Rialto Beach and locations of radiocarbon samples that date the sandy terrace deposits. Elevation uncertainty for terrace stratigraphy and modern beach deposits includes measurement uncertainty from LiDAR or GPS and levelling error. The other types of elevation measurements have similar errors which are not plotted.

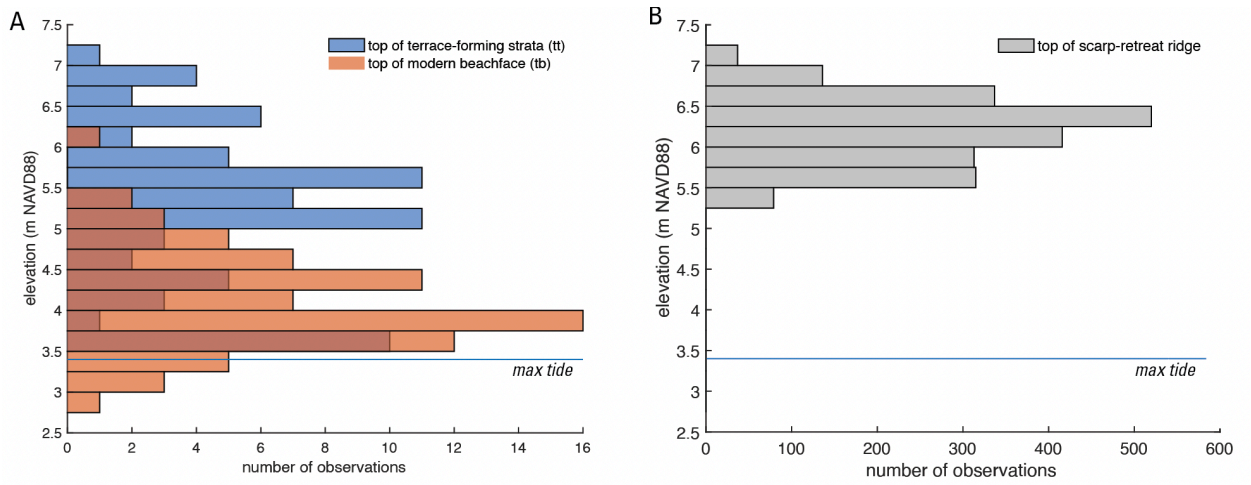

Figure 3.8. Histograms showing measured elevations of features along Rialto Beach. (A) Top of terrace-forming strata (tt) (n = 73), compared with the top of the modern beachface (tb) (n = 73). The means height of the top of the terrace-forming strata is statistically higher than the mean top of the modern beachface. The top of the modern beachface rests above the maximum tide level measured at the La Push tide gauge. (B) Top of modern scarp-retreat ridge, which sits atop the terrace. Elevation points were extracted from LiDAR (n = 2153). Modern deposits at Rialto Beach are emplaced at the elevations of the terrace. The wavecut platform near MSL sits around 1 m NAVD88.

Figure 3.9. Photos of modern beachface and retreat ridge deposits. (A) Bedded sands and rounded cobbles in modern beachface deposits, looking north. (B) Close-up photo of sands and cobbles of the modern beachface, showing some seaward imbrication in cobbles. (C) Sandy location of modern beachface with sorted garnets, looking landward. Large driftwood marks the retreat ridge. (D) Modern beachface and scarp-retreat ridge, looking landward toward terrace. The beachface consists of mixed sand and cobbles; the scarp-retreat-ridge is primarily cobbles and driftwood. Photo by Kathy Troost, used with permission. All photos were taken within the box labeled "T1" on Figure 3.3.

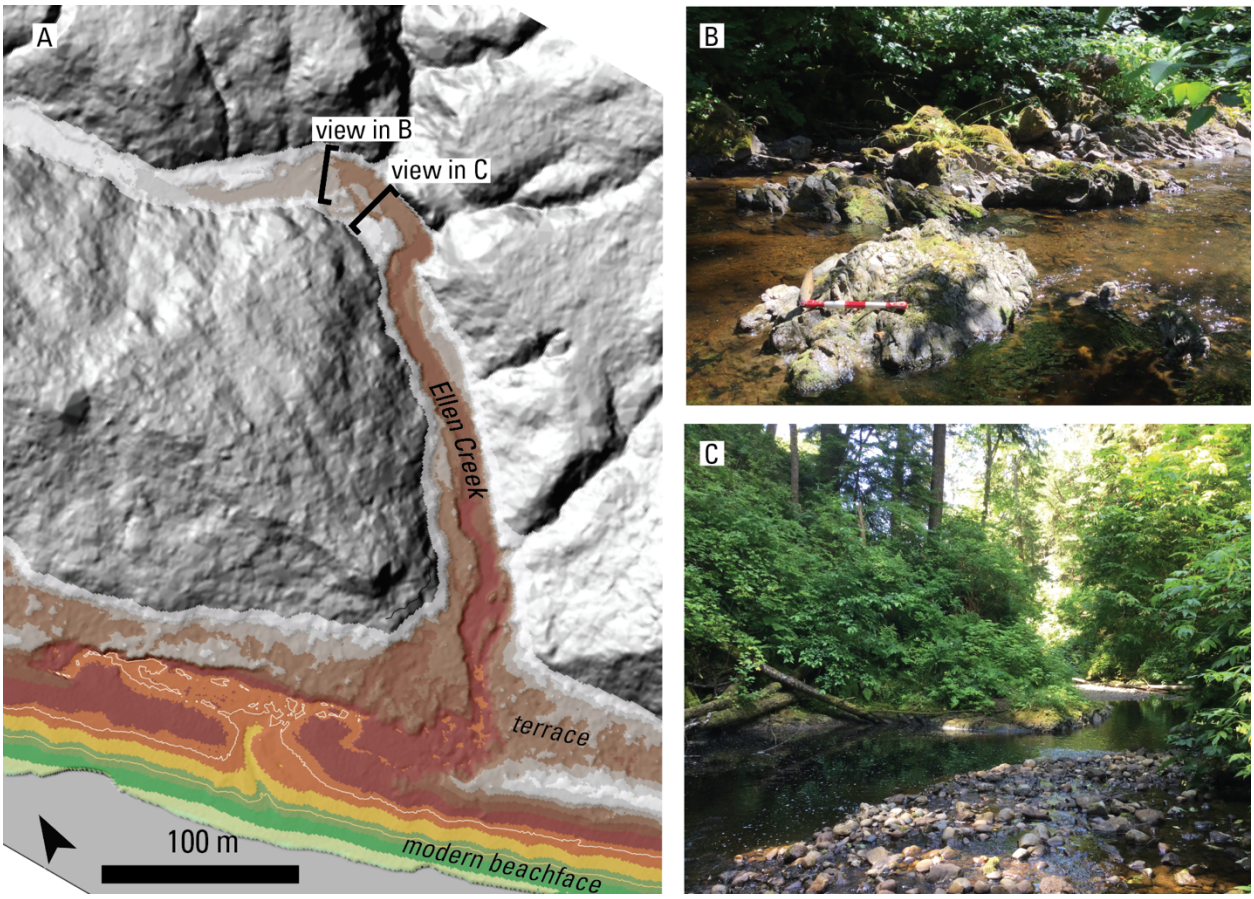

Figure 3.10. Location and photos of Ellen Creek streambed and bank observations. (A) Map showing locations and orientations of photos. Colored elevations of the Rialto Beach terrace and active beachface are the same as used in Figure 3.3. (B) Bedrock in the streambed and banks of Ellen Creek. Photo looks downstream. (C) Cobbles on a bar in Ellen Creek. Photo looks downstream.

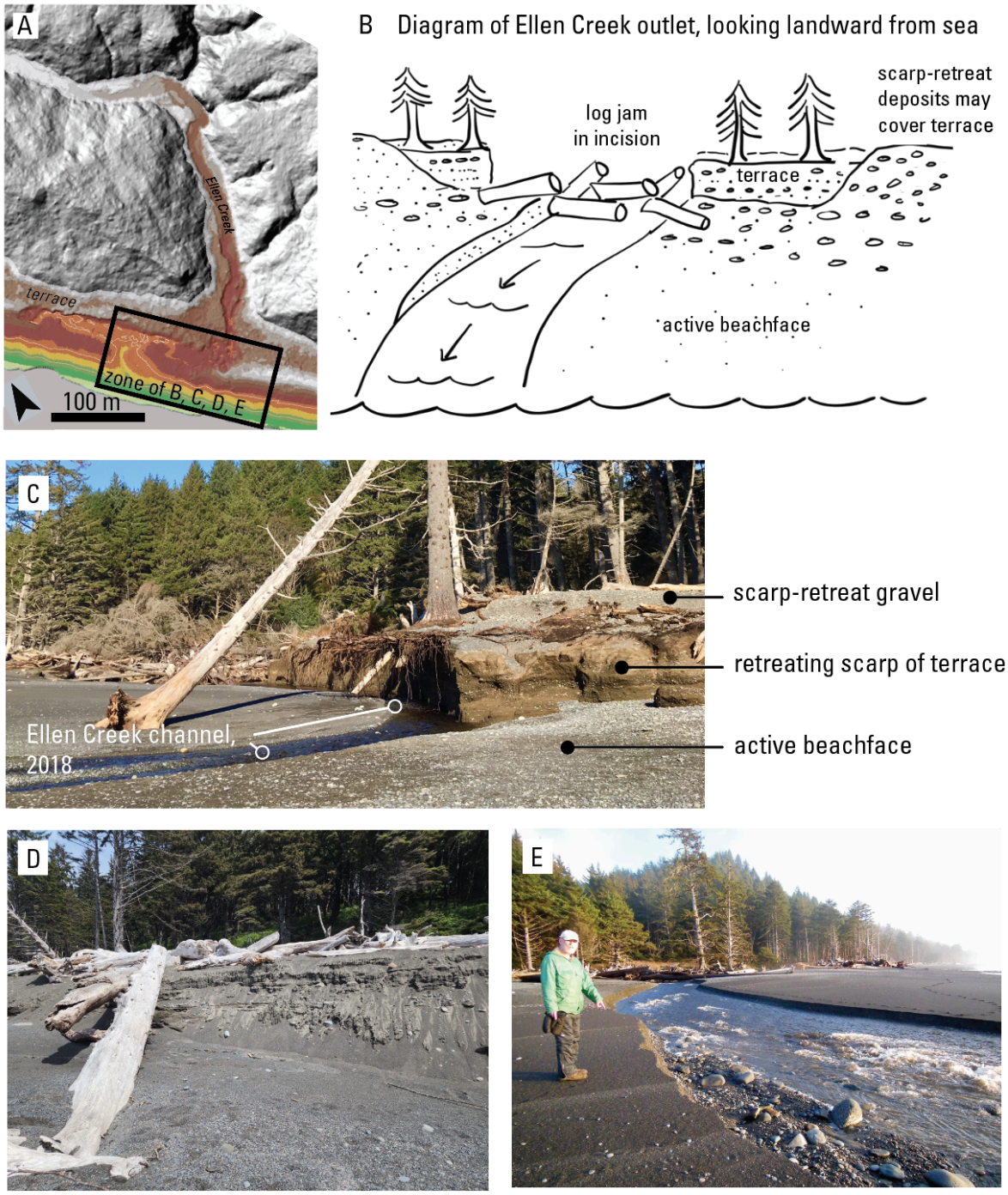

Figure 3.11. Configuration and deposits at the mouth of Ellen Creek. (A) Location of the mouth of Ellen Creek where it exits the terrace. Colored elevations of the Rialto Beach terrace and active beachface are the same as used in Figure 3.3. (B) Cartoon showing the mouth of Ellen Creek exiting the terrace at an incision that is commonly blocked by driftwood. (C) Photo of the retreating scarp of the terrace at the mouth of Ellen Creek. Photo by Joseph Reeves, 2018, used with permission. (D) Photo of an abandoned channel through modern sediments at the mouth of Ellen Creek. Photo by Kathy Troost, June 2023, used with permission. (E) Photo of the downstream end of Ellen Creek, where it runs down the beachface. The forested terrace can be seen in the background. Photo by Jill Rain, January 2013, used with permission.

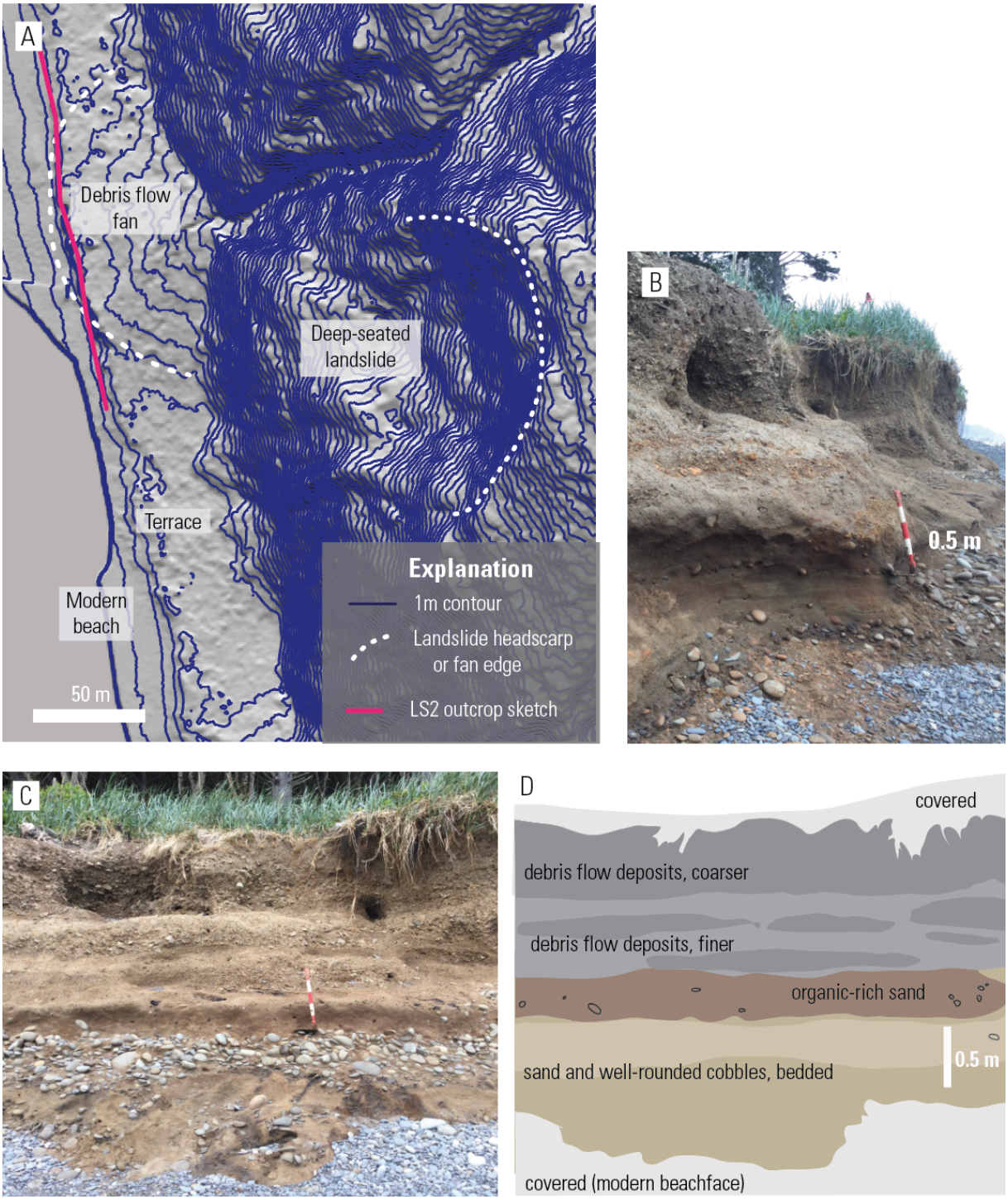

Figure 3.12. LS2 outcrop map and deposits. (A) Contour map over LiDAR showing location of outcrop (pink line) with respect to a debris flow fan at the mouth of a gully and a deep-seated landslide on the slope. No large landslide deposit is visible immediately below the landslide. (B) Photo showing oblique view of the outcrop, looking south. (C) Photo showing outcrop, taken facing toward the slope. (D) Sketch of outcrop shown in (C), showing debris flow deposits (lenticular) over bedded sand and cobbles.

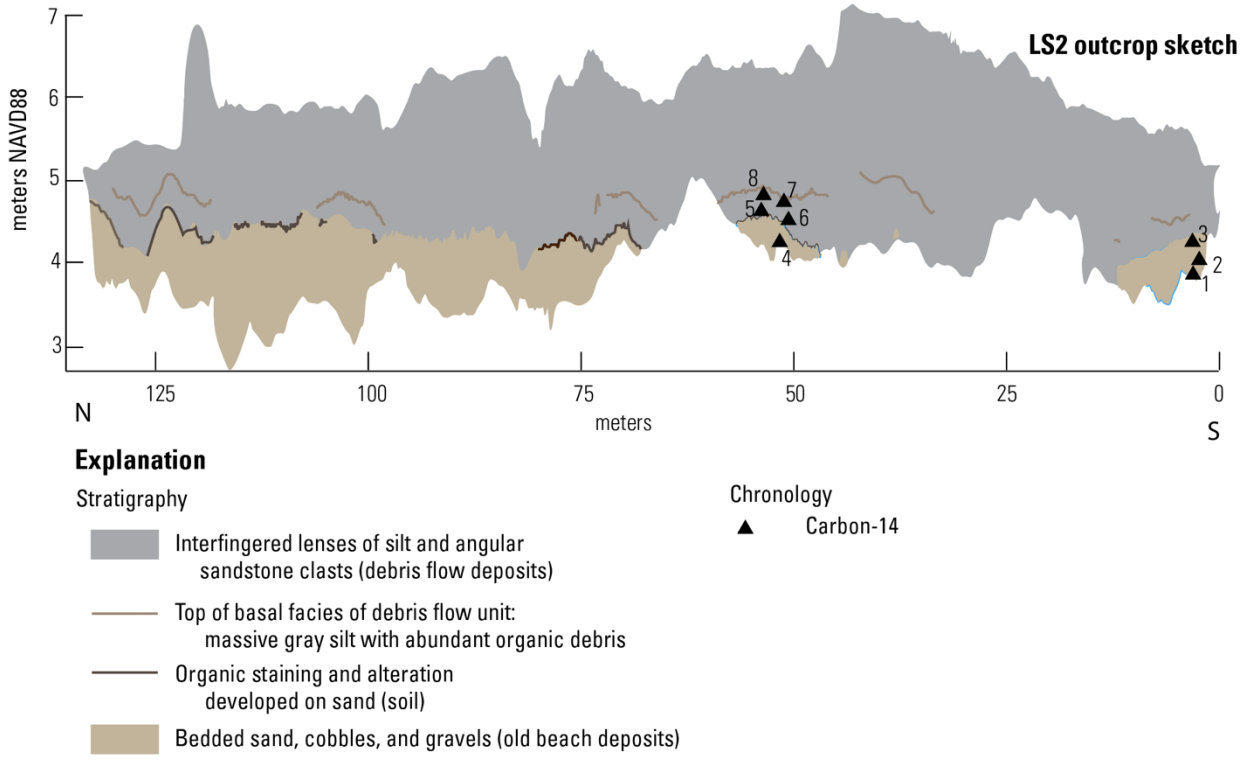

Figure 3.13. Stratigraphy and location of radiocarbon samples at LS2.

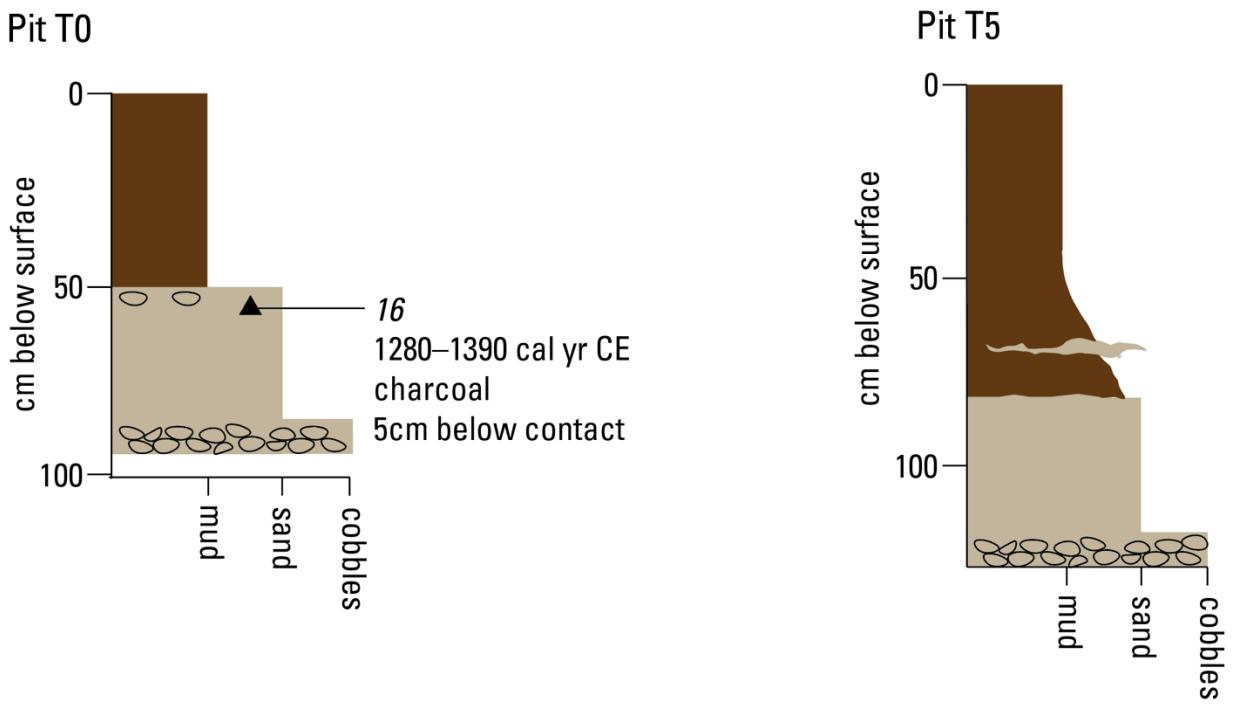

Figure 3.14. Sections of two pits showing mud atop sand. The location of the pits are shown in Figure 3.3. The radiocarbon sample at Pit T0 (sample 16) is listed in Table 3.2. In both pits, the mud-sand contact is abrupt and can be traced over one sand grain, though in pit T5, the lowest 30 cm of the mud contains sand.

Figure 3.15. Low-angle flat laminae and cut-fill structures in sand of terrace outcrop (location shown on Fig. 3.2). Shovel handle 0.5 m; red and white increments 10 cm each. Photo (left) and traced laminae (right). Roots of Sitka spruce cover the top 20-30 cm of the outcrop; modern beach sand forms the base of the outcrop. Note tossed-up modern beach cobbles on the outcrop in the left side of the photo. At this site, the top of the terrace sand sits 80 cm above the modern beach sand.

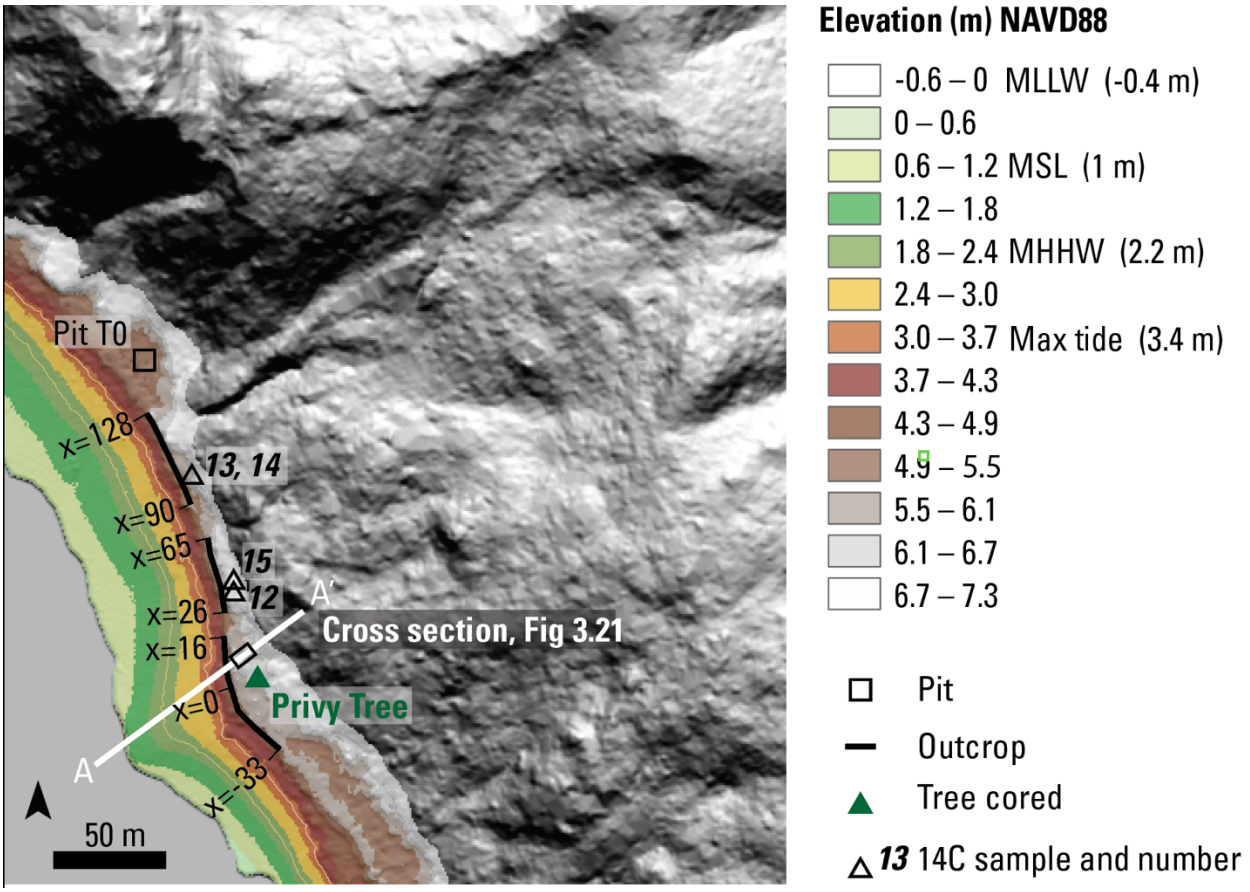

Figure 3.16. Map of outcrop T1 showing location of surveyed outcrop, the cross-section pictured in Figure 3.21., radiocarbon samples, two pits, and one cored tree. Radiocarbon sample numbers are keyed to Table 3.2. The location of this inset map is shown in Figure 3.3. Colored elevations of the Rialto Beach terrace and active beachface are the same as used in Figure 3.3.

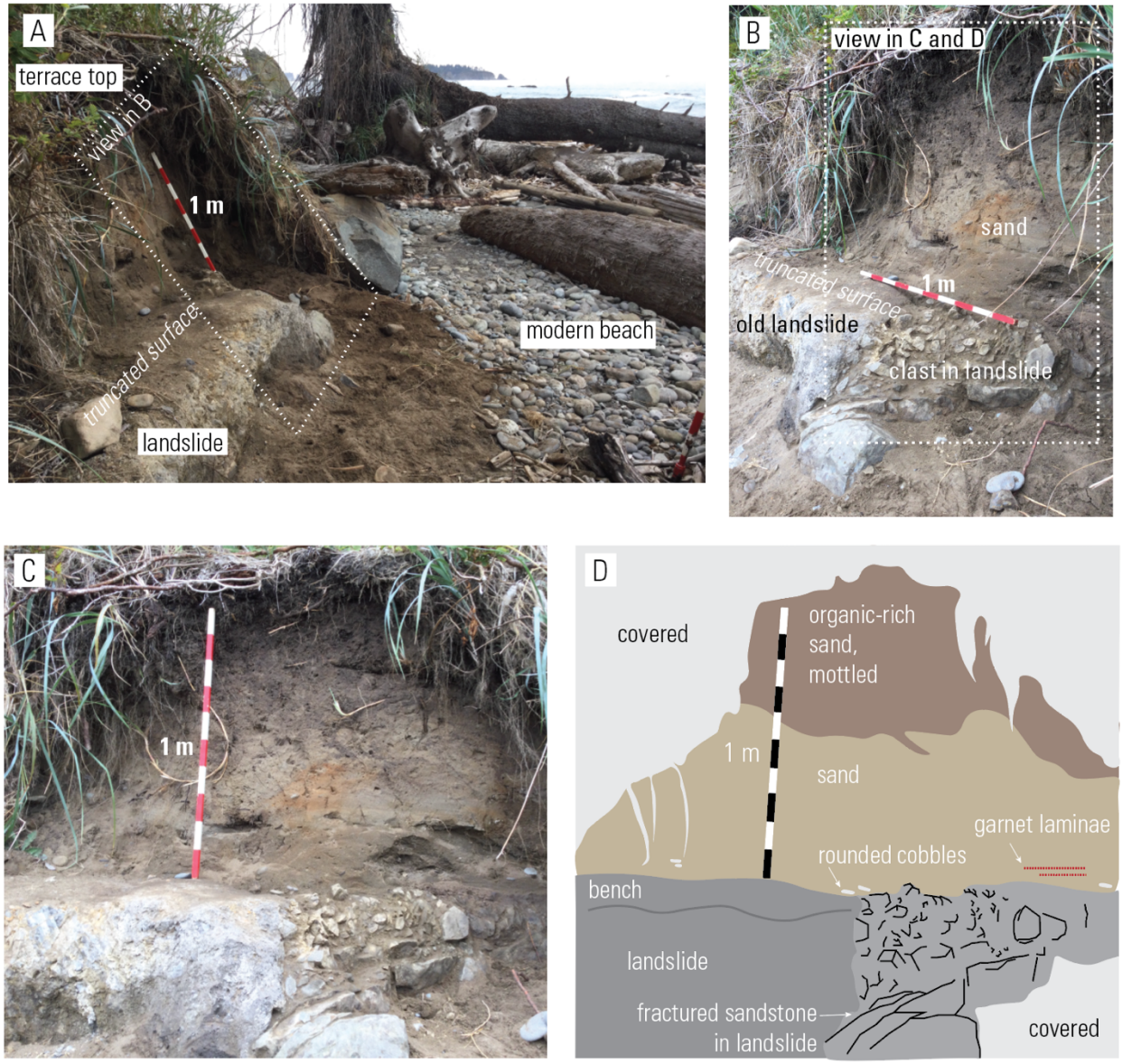

Figure 3.17. T1 outcrop at x = 5, where the truncated landslide and cap of sand are low in elevation. The location and coordinates of outcrop T1 are shown in Figure 3.16. (A) The truncated top of the landslide sits above the cobbles and accumulation of driftwood at the back edge of the modern beach. Sand forms a 1 m thick cap on the surface of the landslide. (B) Fractured sandstone clasts meet fine-grained landslide deposits at a flat surface with less than 20 cm of relief, providing the evidence that the landslide surface is truncated. The meterstick lies on the truncated surface. (C) Photo of outcrop; sketch in (D).

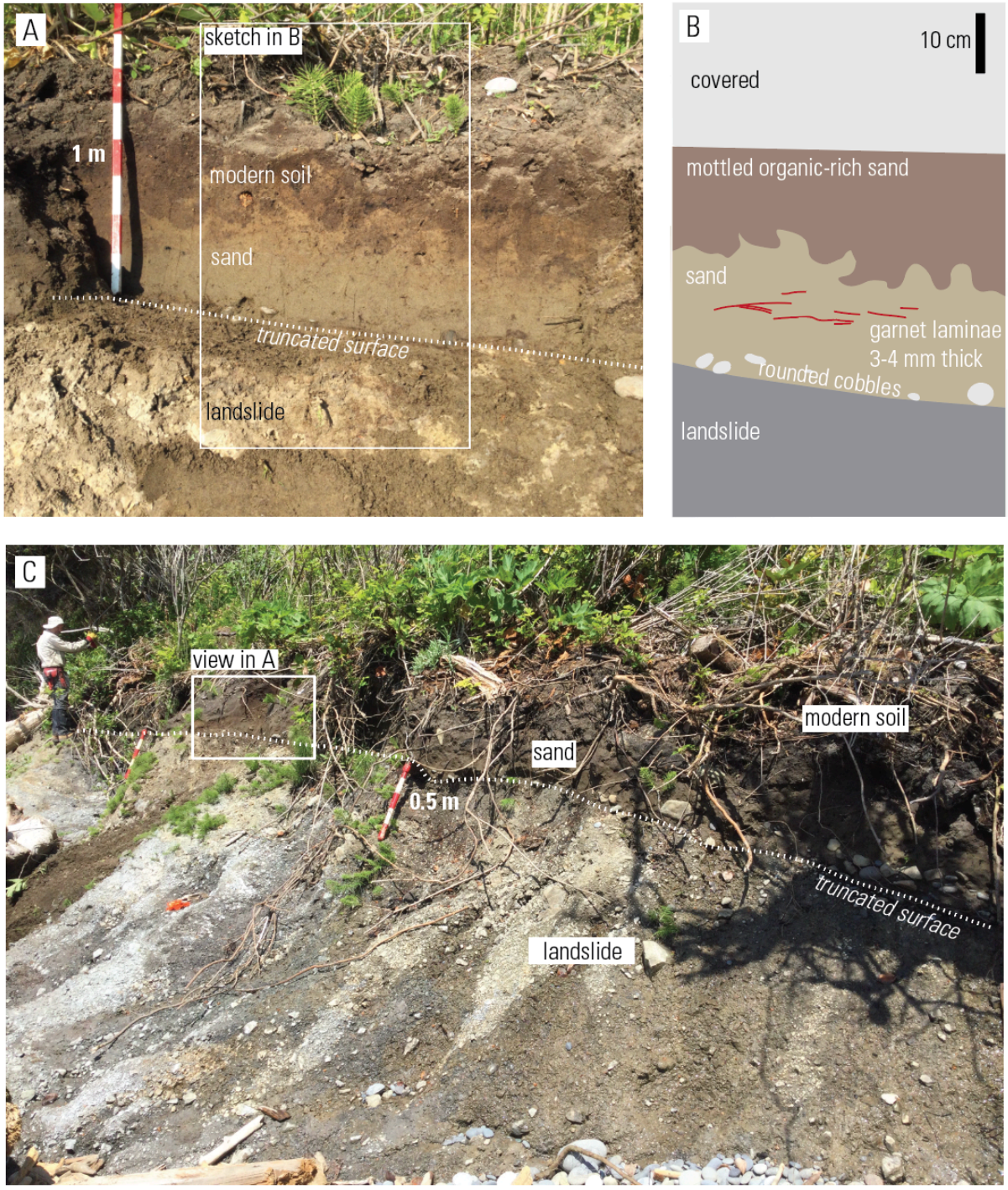

Figure 3.18. T1 outcrop at x = 33, where the truncated landslide and cap of sand rise in elevation where the outcrop trends closer to the slope. The location of the T1 outcrop and coordinates are shown in Figure 3.16 (A) The truncated landslide is capped by 50–70 cm of bedded sand with soil developed atop it. (B) Sketch of area shown in A. Sedimentary structures in the sand include undulating garnet beds 3-4 cm thick. Well-rounded graywacke gravels and well-rounded, disc-shaped cobbles 1–4 cm in diameter are at the base of the sand. (C) Context of the outcrop shown in (A) and (B). The truncated surface of the landslide rises landward and to the north (left in photo).

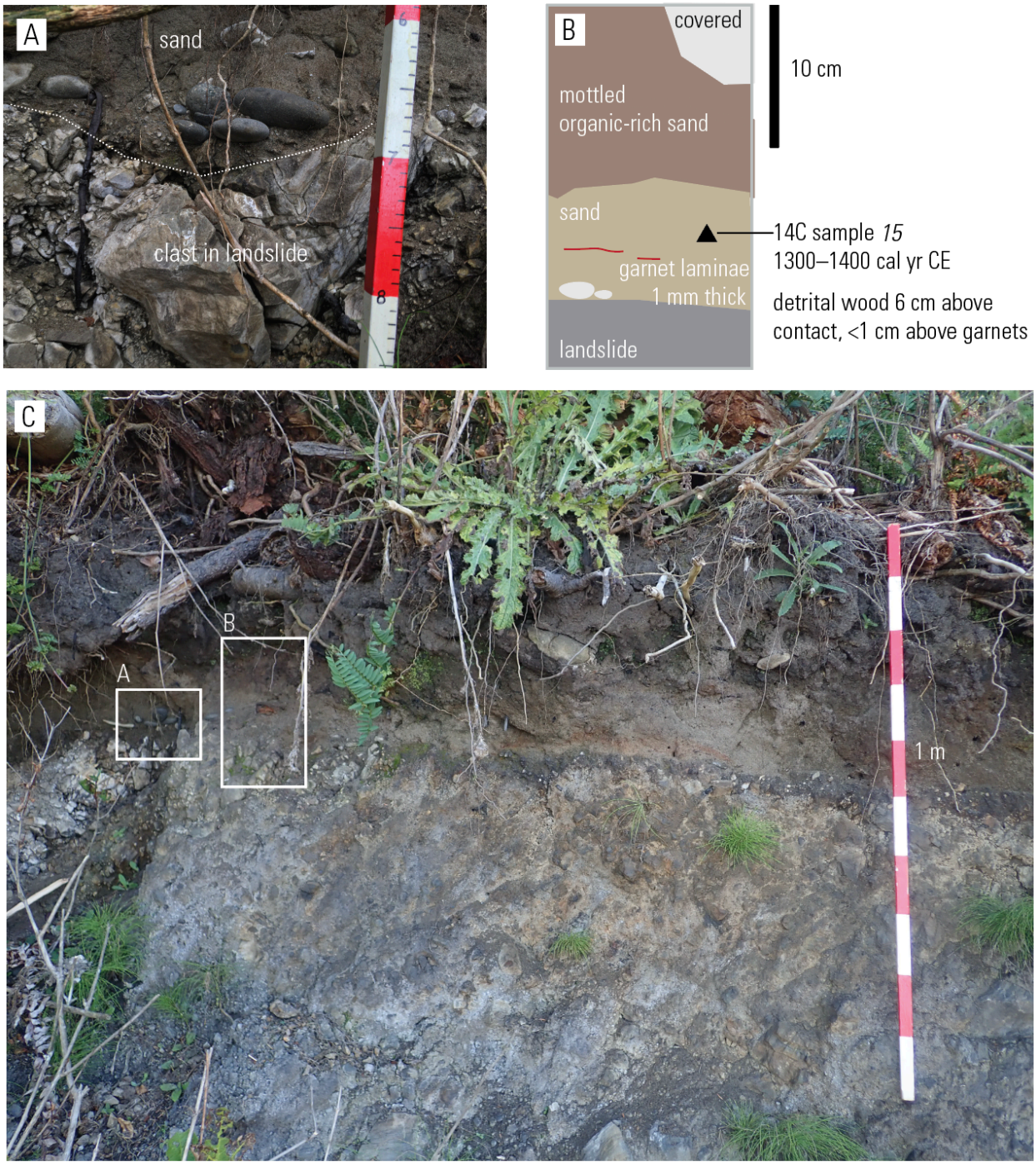

Figure 3.19. T1 outcrop at x = 39, where the truncated landslide and cap of sand are high in elevation. The location of the T1 outcrop and coordinates are shown in Figure 3.16. The truncated landslide is overlain by bedded sand with rounded cobbles and garnet beds. (A) Sand above truncated landslide (location in C) bears rounded cobbles and few pebbles of landslide material. (B) Sketch of the sand at 14C sample site 15 (location in C). Detrital wood of sample 15 was collected from within bedded fine sand 6 cm above the landslide-sand contact, less than 1 cm above two 1 mm-thick garnet laminae. The radiocarbon age of 1300–1400 cal yr CE predates the deposition of the bedded sand.

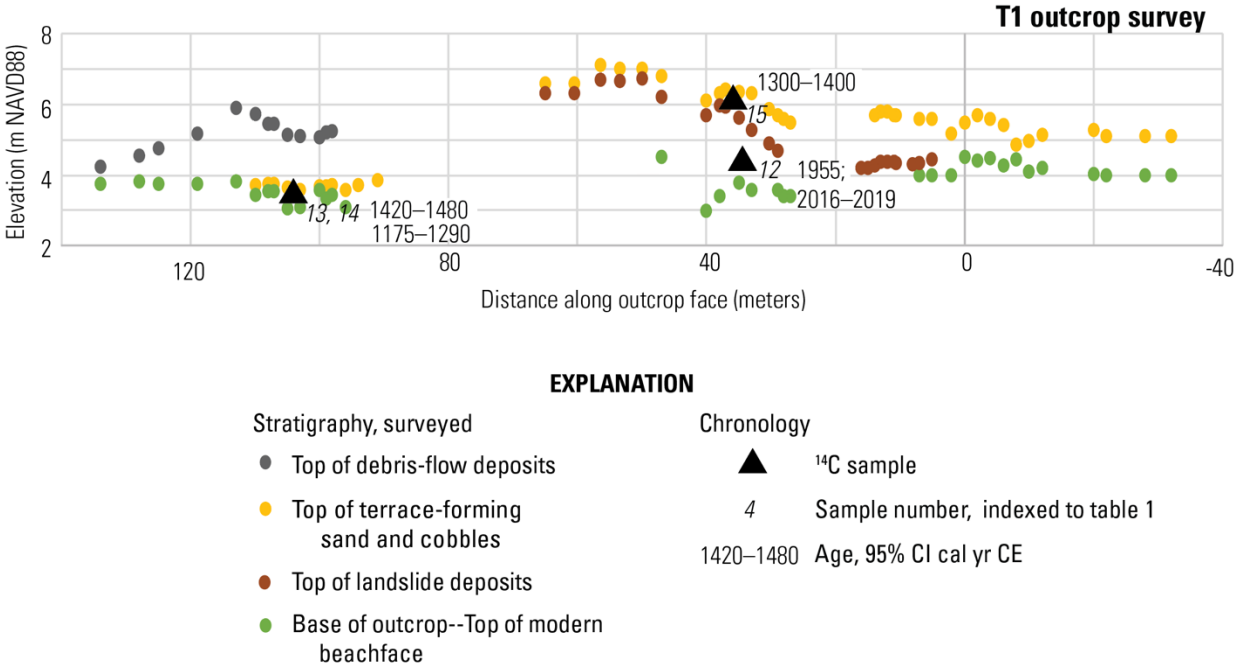

Figure 3.20. Slope-parallel stratigraphy and location of radiocarbon samples at T1.

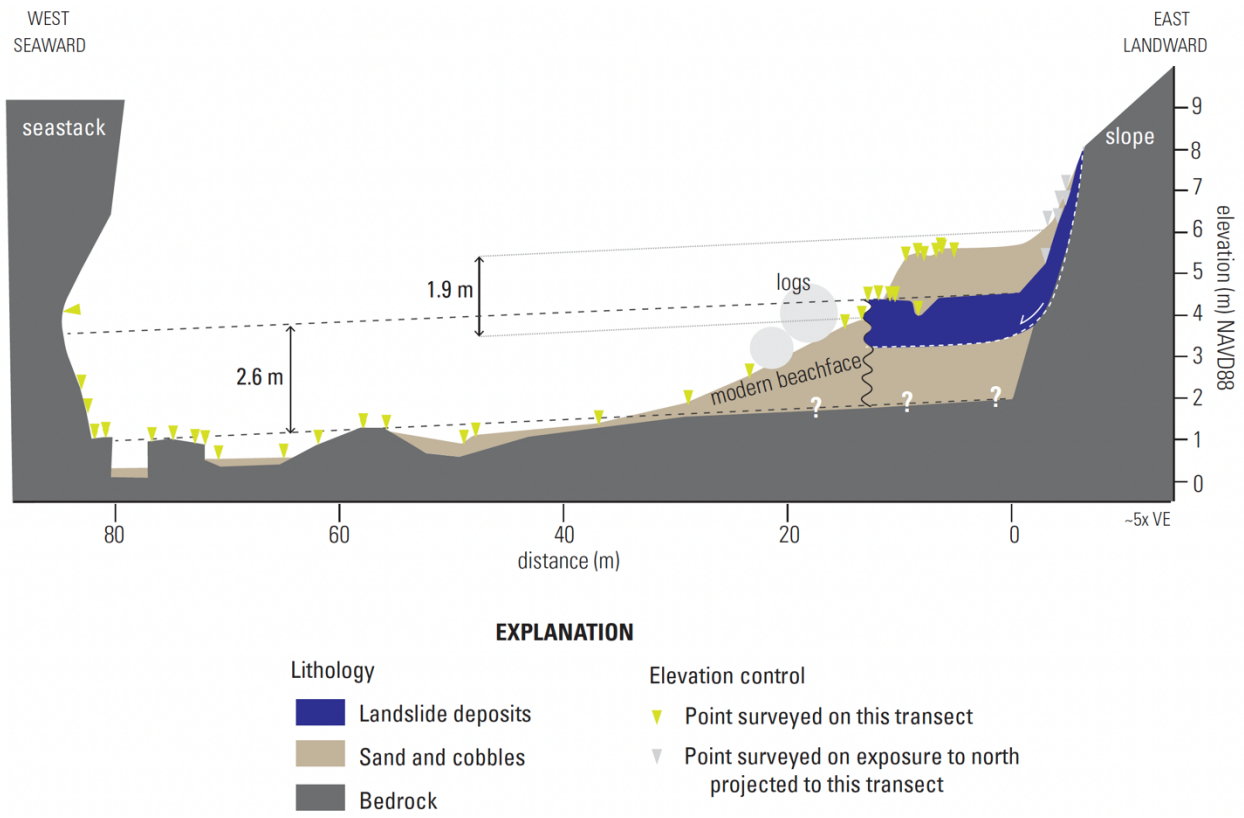

Figure 3.21. Slope-perpendicular transect at T1 based on levelling. Ground surface at the landward edge (x = -10–5 m) is derived from LiDAR. Stratigraphy is interpretive; survey points and deposit thicknesses at the far right end of the transect were projected along elevation contours from the outcrop survey to the north. Exposures of sand and cobbles were seen under the landslide deposit; it is unknown how thick these deposits are. Dashed lines show elevation differences between projected elevations in the modern beachface and in the terrace. The dashed line projects a line from bedrock exposed in the surf zone to where this would meet the seacliff. If the truncated top of the landslide is an analogous datum, the difference between these two is 2.6 m. The difference between the top of the modern beachface and the top of flat sand and cobble deposits on the terrace is 1.9 m. Smoothing of the seastack extends up to ~3 m above the flat wavecut platform; the point measured is the elevation of the concavity. Above this point, the seastack is angular and fractured.

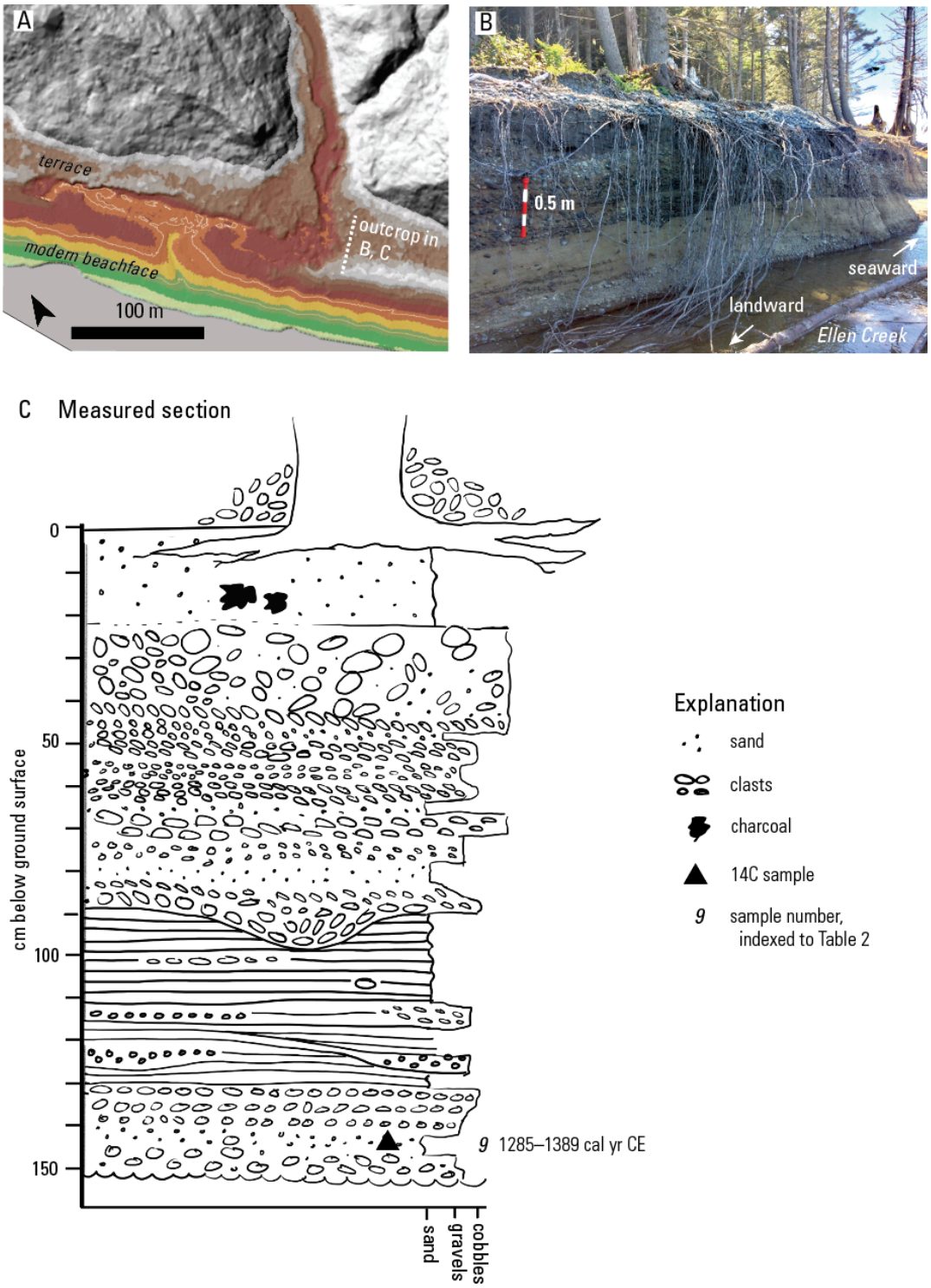

Figure 3.22. EC outcrop at the southern bank of Ellen Creek. (A) Approximate location of outcrop on the terrace. The outlet of Ellen Creek avulsed between the collection of the LiDAR (2018) and the photo (2021), changing the exposure and eroding part of the terrace. Colored elevations of the Rialto Beach terrace and active beachface are the same as used in Figure 3.3. (B) Photo of the EC outcrop in the southern creek bank. (C) Measured section along Ellen Creek, interpreted as beach deposits. The beds sketched dip seaward (to the right) 1–2º.

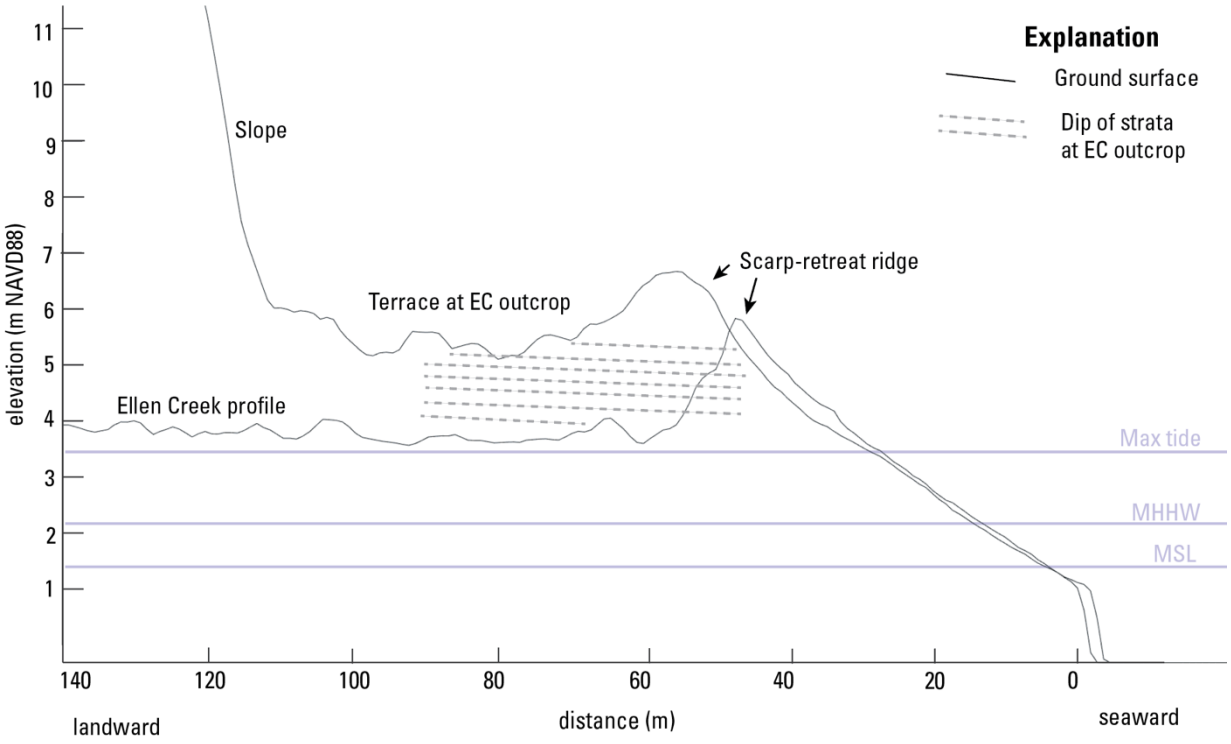

Figure 3.23. Cross-section of the terrace at Ellen Creek. Black lines show ground surface on the southern creek bank and along the creek itself. Dotted lines show the approximate extent, thickness, and dip of continuous strata observed in the creek-bank outcrop at Ellen Creek (EC outcrop). Exposures of the creek bank changed as the result of avulsions over the course of the study. The slope profiles ("ground surface") are derived from LiDAR from 2018, which shows different creek bank extents than were observed in later years. Ellen Creek exits onto the modern beachface around MHHW. Ephemerally, the mouth is blocked by large woody debris and cobbles.

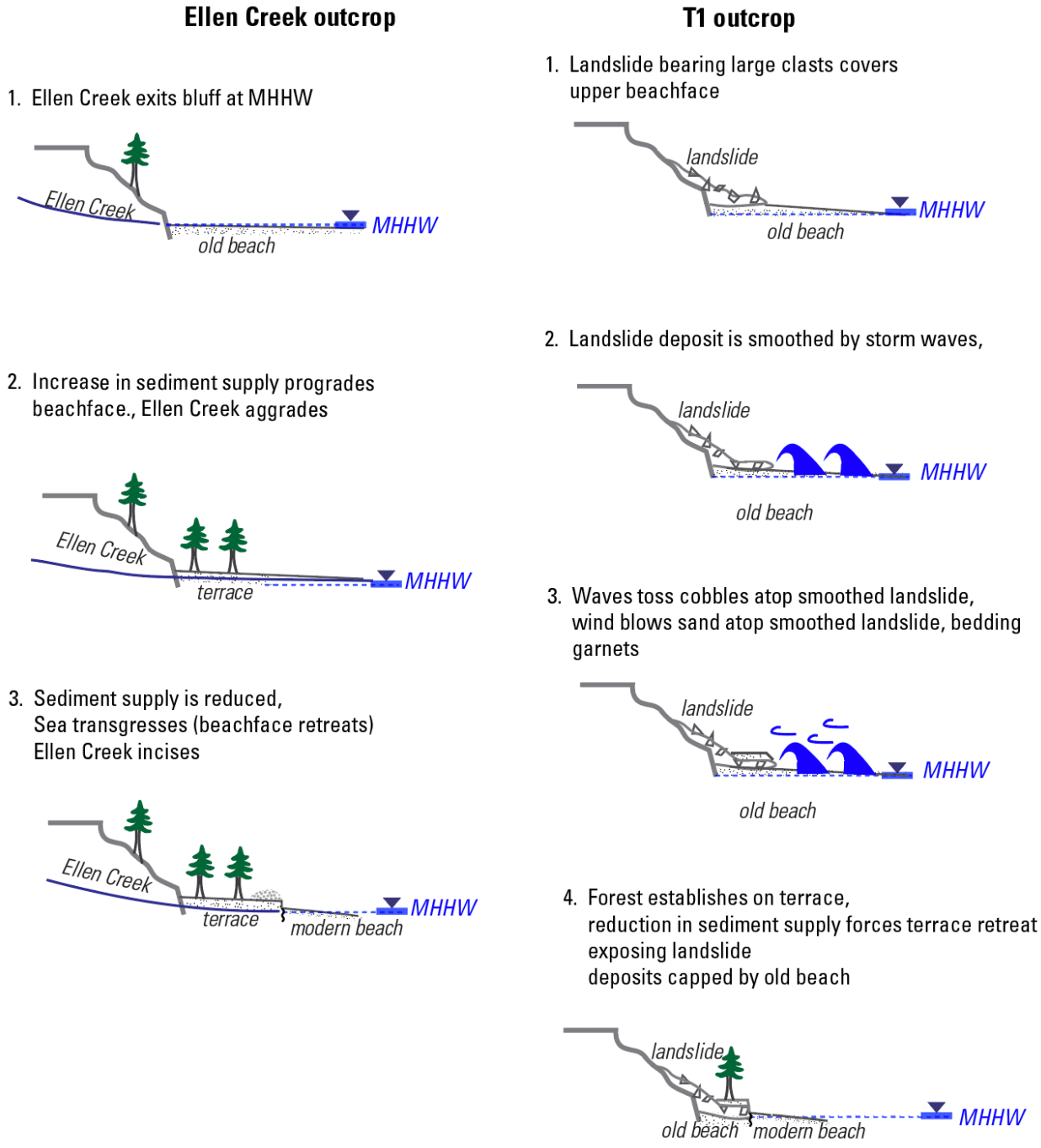

Figure 3.24. Diagram of how an increase in sediment supply can produce observed stratigraphy at Ellen Creek and T1.

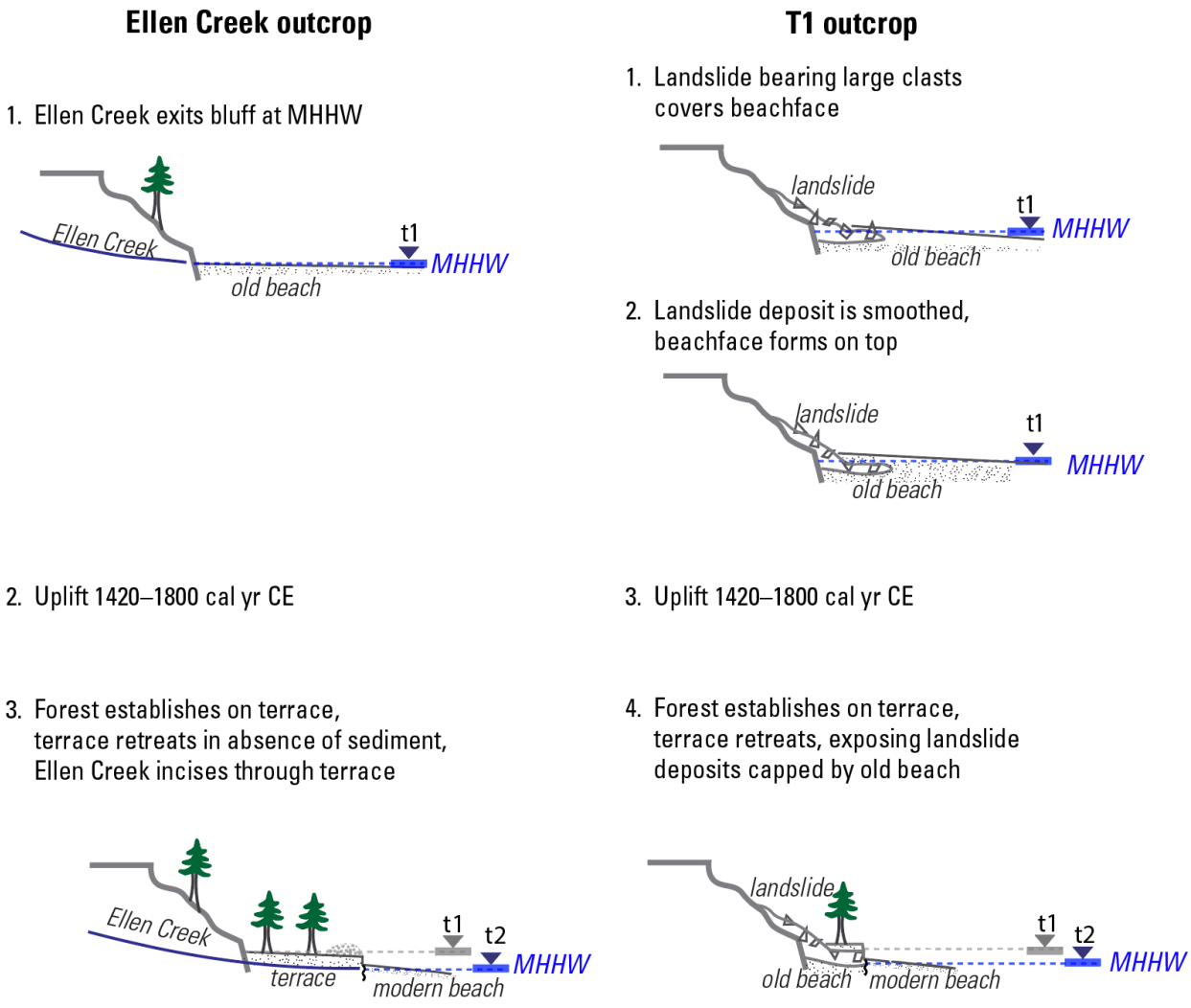

Figure 3.25. Diagram of how uplift can produce observed stratigraphy at Ellen Creek and T1.

3.7 TABLES

Table 3.1. Tidal datums at the LaPush tide gauge from 1983–2001 (NOAA, 2020).

Datum	Description and interpretation	Elevation m NAVD88
Max tide	Maximum flat-water height measured at the tide gauge. Measured Feb. 4, 2006. Includes storm surge and tide level but not wave height. Maximum upper limit of beach deposition during storms. Storm berms form above this level.	3.4 m
MHHW	Mean Higher High Water, approximate upper limit of beach deposits	2.2 m
MSL	Mean Sea Level, approximate level of wavecut platform	1.0 m
MLLW	Mean Lower Low Water	-0.4 m

Table 3.2. Radiocarbon samples collected at Rialto Beach

Index	Site	Field number	Reported by	Lab number	Lab-reported age (^{14}C yr BP)	Lab error (^{14}C yr BP)	Age with added variance (^{14}C yr BP)	Error with added variance (^{14}C yr BP)	Calibrated age rounded to nearest 5 (cal yr CE at 95% CI)	Inferred age context	Description of dated material
16	T0	ED-R2305-8	This study	OS-176404	660	15	662	26	1280–1390	maximum age for sand	charcoal, 5cm below mud-sand contact
15	T1	ED-R2210-1	This study	OS-171112	625	15	623	26	1300–1400	maximum age for sand	broken wood, in sand above bedded garnets
14	T1	ED-R2210-5	This study	OS-171113	820	15	822	27	1175–1290	maximum age for wave-worked sand	charcoal, in sand amongst bedded garnets
13	T1	ED-R2210-6	This study	OS-171111	445	20	446	27	1420–1480	maximum age for wave-worked sand	charcoal, in sand amongst bedded garnets
12	T1	ED-R230525	This study	OS-176403	>modern		-105	26	1955; 2016–2019	maximum age for old landslide	rings 2 and 3 of 80cm long straight stick with cambium, broken on both ends, embedded in old landslide. 90cm below top of debris flow, 160cm below surface of outcrop.
11	T2	ED-R2305-1	This study	OS-176402	>modern		-277	26	1956; 2011–2014	maximum age for wave-worked sand	twigs or possible roots with bark on underside of half-buried log

10	Ellen Creek	ED-R21EC 5 S-1	This study	OS-176405	130	15	130	26	1675–1940	maximum age for sand above bedrock strath	stick 8" by 1.5" diameter
9	Ellen Creek	KT 200-18 S-1	Bush (2020)	OS-147980	660	15	663	26	1280–1390	maximum age for wave-worked sand	Detrital wood
		additional 14C ages higher in the debris flow at LS2 are reported by Freeman (2021)									
8	LS2	S4-21	Collected by Freeman (2021), ages not reported	OS-160132	355	15	354	27	1460–1635	maximum age for start of debris flows (G)	Detrital wood
7	LS2	S5-20	Freeman (2021)	?	125	15	125	27	1680–1940	maximum age for start of debris flows (G)	cone exposed at surface of G (see Freeman, 2021), which drapes cobbles
6	LS2	S5-21	Collected by Freeman (2021), ages not reported	OS-160133	130	15	132	27	1675–1940	maximum age for start of debris flows (G)	Detrital wood
5	LS2	S7-20	Freeman (2021)	?	470	15	468	27	1410–1460	maximum age for start of debris flows (G)	charred wood at base of Unit G (see Freeman, 2021) where it drapes cobbles
4	LS2	S10-20	Freeman (2021)	?	625	15	625	27	1300–1400	maximum age for wave-worked sand	Detrital log in sand. No bark seen.

3	Sample Site 2	MAB-25-18-S2	Bush (2020)	OS-148121	490	20	488	32	1400–1455	maximum age for sand	charcoal in sand
2	Sample Site 2	MAB-25-18-S1	Bush (2020)	OS-147981	660	15	536	26	1325–1435	maximum age for sand	detrital wood in sand
1	Sample Site 2	MAB 24-18	Bush (2020)	OS-148122	845	25	843	33	1055–1270	maximum age for sand	detrital wood in sand

Table 3.3. Ages of cored trees (not including those reported by Bush, 2020).

Tree name	Month, Year cored	Number of rings	Center cored?	Start of tree growth	Location	Context
Cougar tree	October, 2021	220	No	<1801	Top of terrace at LS2, x=20 m	Postdates terrace, postdates LS2 landslide
Privy tree	March, 2023	Core 1: 114 Core 2: 124	Yes	1898–1910	Top of terrace at T1, x=-3 m, 6 m inland	Postdates terrace, possibly postdates T1 landslide

Table 3.4. Estimates of elevation change between terrace-forming strata and modern indicators of beach level.

Difference	**Min**	**Max**
Top of terrace-forming strata - Max tide	1.0 m	3.7 m
Top of terrace-forming strata - MHHW	2.3 m	4.9 m
Top of terrace-forming strata - top of modern beachface	0.3 m	1.6 m
Top of truncated landslide - top of modern wavecut platform	2.6 m	4.0 m
Amount of incision at Ellen Creek	1.5 m	n/a

Conclusions

Review

In review, this dissertation focused on the geologic record of earthquakes inferred from coastal geology and geomorphology at three localities in western Washington. In Chapter 1, I used marine geomorphology to evaluate the deformation history of the Seattle Fault Zone. In Chapters 2 and 3, I used field geology to evaluate geologic evidence for earthquakes and limitations to the record of such evidence.

In Chapter 1, I mapped submerged terraces in Puget Sound to constrain the 11,000-year deformation history of the Seattle fault zone, finding that there has been only one M~7.5 surface-deforming earthquake in this timeframe. Submerged terraces, visible in bathymetry in Puget Sound from Whidbey Island to Tacoma, were attributed by Haugerud (2017) to shorelines of a late-glacial sea-level lowstand that occurred no more recently than 11,000 years ago. I mapped terraces in bathymetry, measured depths, collected CHIRP seismic reflection data across benches, and used these data and other legacy seismic data to estimate the amount of sediment cover on the benches. I evaluated depths to the benches, and their offset across the fault zone, by fitting linear models to the data and interpolating amounts of deformation of onshore terraces. My mapping supports the interpretation that the terraces are former shorelines, as they form flat surfaces that sit at similar depths across Puget Sound. The terraces are offset upward across the SFZ, and the amount of the offset is similar in magnitude to offset produced in a SFZ earthquake that occurred 923–924 CE (Black et al., 2023). The broad-scale pattern of deformation that I mapped and quantified supports the structural interpretation that the SFZ forms the north end of block uplift that extends southward to the Tacoma Fault Zone. The results of this chapter indicate that the recurrence interval of the Seattle Fault Zone may be twice as long as current hazard estimates (i.e., half the number of earthquakes in the same timespan) and provide a broad-scale dataset for deformation that can be used as a backdrop for future localized studies.

In Chapter 2, I used morphology of sand features in the Duwamish estuary in Seattle to attribute some of the deposits to earthquake-induced liquefaction. In doing so, I demonstrated a method of dating liquefaction features with in-situ marsh plant fossils that provide exact stratigraphic precision. Radiocarbon ages of in-situ marsh plants around these deposits constrain the ages of

liquefaction to 990–1150 cal yr CE, before 1490–1630 cal yr CE, and after 1220–1280 cal yr CE, 1230–1300 cal yr CE, and 1460–1630 cal yr CE. Venting of sand at a ground surface was preserved in the available outcrops in the first two events listed. The earlier event, which occurred 990–1150 cal yr CE, vented sand over *T. maritima* leaf bases at a former ground surface. The ages of these leaf bases are the same as the age of the liquefaction event. Venting was not observed from known historic earthquakes at any outcrops, and only one outcrop displayed evidence for recurrent liquefaction. This locality, or at least the few available outcrops at this locality, display an incomplete record of regional earthquakes. The Duwamish estuary provides a counterexample to liquefaction records compiled from elsewhere, where recurrent liquefaction at individual outcrops has been used as an indicator that liquefaction preserves a complete earthquake catalog. Assumptions of completeness are necessary precursors to inferring that the absence of liquefaction features in an outcrop means that liquefaction has not occurred at the site.

In Chapter 3, I mapped and dated a terrace at Rialto beach on the northwest coast of Washington. Many similar terraces are located at the back edges of beaches across the northwest coast of Washington, and the terrace at Rialto Beach is the longest one. The terraces are of interest because they are located within the largest spatial gap in land-level data along the Cascadia subduction zone, and because the presence of terraces allows the possibility that regional coseismic or interseismic uplift occurs. I described the stratigraphy in the terrace and slopes above from outcrops, test pits, and a creek-bank exposure, measured elevations of the terrace-forming deposits and elevations of the modern beach features, and used radiocarbon dating and tree ring counts on live trees to date the terrace. My mapping indicates that the terrace is composed mostly of bedded sand and gravel, including beach cobbles, with soil developed on top, and that the terrace-forming strata sit on average higher than the modern beachface, but not higher than all modern beach processes. Locally, sand and gravel deposits that form the terrace overlie a landslide with a truncated surface and underlie coarse- and fine-grained debris-flow deposits. The terrace-forming sand and gravel were emplaced no earlier than 1055–1270 cal yr CE. Trees began growing on the surface of the terrace no later than 1801 CE. I developed a chronologic model for events that produced the landforms present at Rialto Beach and evaluated two hypotheses for formation of the terrace landform. I found that both tectonic uplift and beach

progradation due to a period of higher sediment supply could have emplaced the terrace-forming sediments and produced the terrace. I also found that deep-seated landslides on the slope above occurred prior to the formation of the terrace. To rule out or strengthen an interpretation of tectonic uplift, the other terraces along the coast of northwest Washington must be mapped and dated, and the elevations of modern processes (e.g., beachface deposition) must be measured.

Implications

This dissertation quantifies and dates aspects of earthquake hazards in western Washington and constructs frameworks for future paleoseismic work. Chapter 1 lengthened the recurrence estimate for earthquakes on the Seattle Fault Zone and contributed a new deformation dataset. It also provided a proof-of-concept that could be applied to estimate the deformation from other crustal fault zones in Puget Sound. Chapter 2 contributed new ages for the liquefaction catalog at Seattle, growing the existing catalog of liquefaction in this region. The findings from Chapter 2 demonstrated the benefits of working in a tidal marsh environment for dating liquefaction. Chapter 3 establishes that the terrace at Rialto Beach is young and provides a framework for assessing these unconsolidated terraces at other sites.

REFERENCES

Anderson, M., Lau, T., Sadowski, A., Polenz, M., Steely, A., von Dassow, W., Reedy, T., Horst, A., Amaral, C., 2023, The Doty Fault system: Finding and connecting active faults by integrating geologic mapping and geophysical data in Washington State, in Association of Engineering Geologists Program with Abstracts, Portland, Oregon, 126.

Angster, S.J., Sherrod, B., Pearl, J.K., Staisch, L., Johns, W., 2023, Paleoseismic evidence for Late Pleistocene and near Historic ruptures on north-verging faults within the Seattle Fault Zone: Implications for complex hanging wall deformation, in Association of Engineering Geologists Program with Abstracts, Portland, Oregon, 126.

Angster, S.J., Sherrod, B., Barnett, E., Bretthauer, J.L., and Anderson, M.L., 2020, 2020 Update to the Quaternary Fault and Fold Database for Washington State: U.S. Geological Survey data release, https://doi.org/10.5066/P9X2RR2T.

Arcos, M.E.M., 2012. The AD 900–930 Seattle-Fault-Zone Earthquake with a Wider Coseismic Rupture Patch and Postseismic Submergence: Inferences from New Sedimentary Evidence. Bulletin of the Seismological Society of America, 102(3), pp.1079-1098.

Armstrong, J.E., Crandell, D.R., Easterbrook, D.J., and Noble, J.B., 1965, Late Pleistocene stratigraphy and chronology in southwestern British Columbia and northwestern Washington: Geological Society of America Bulletin, v. 76, p. 321–330, https://doi.org/10.1130/0016-7606(1965)76[321:LPSACI]2.0.CO;2.

Atwater, B.F., 1988. Geologic studies for seismic zonation of the Puget lowland. National Earthquake Hazards Reduction Program, Summaries of Technical Reports, 25, 120-133.

Atwater, B.F., 1999, Radiocarbon dating of a Seattle earthquake to A.D. 900–930 [abstract]: Seismological Research Letters, v. 70, no. 2, p. 232.

Atwater, B. F., 2020, Data compiled from stratigraphic and tree-ring studies of late Holocene earthquakes and tsunamis at Copalis River, Grays Harbor, Willapa Bay, and Columbia River, Washington and Oregon. US Geol. Surv. Data Release.

Atwater, B.F., and Griggs, G.B., 2012, Deep-sea turbidites as guides to Holocene earthquake history at the Cascadia Subduction Zone—Alternative views for a seismic-hazard workshop: U.S. Geological Survey Open-File Report 2012–1043, 58 p., available at http://pubs.usgs.gov/of/2012/1043/.

Atwater, B.F., and Hemphill-Haley, E., 1997, Recurrence Intervals for Great Earthquakes of the past 3,500 years at northeastern Willapa Bay, Washington: U.S. Geological Survey Professional Paper 1576, Denver, Colorado, U.S. Nuclear Regulatory Commission, and Washington, U.S. Government Printing Office; sold by U.S. Geological Survey, Information Services, 108 p.

Atwater, B.F., and Moore, A.L., 1992, A tsunami about 1000 years ago in Puget Sound, Washington: Science, v. 258, no. 5088, p. 1614-1617, doi:10.1126/science.258.5088.1614.

Atwater, B.F., Tuttle, M.P., Schweig, E.S., Rubin, C.M., Yamaguchi, D.K., Hemphill-Haley, E., 2003, Earthquake recurrence inferred form paleoseismology, Development in Quaternary Science, 1: 331-348.

Bagley, C. B., 1929, History of King County, Washington (Vol. 1). S.N. Clarke Publishing Co, Seattle.

Barnhardt, W.A., and Sherrod, B.L., 2006, Evolution of a Holocene delta driven by episodic sediment delivery and coseismic deformation, Puget Sound, Washington, USA, Sedimentology: 53, 1211-1228.

Berryman, K.R., 1993. Distribution, age, and deformation of late Pleistocene marine terraces at Mahia Peninsula, Hikurangi subduction margin, New Zealand. Tectonics 12, p. 1365–1379.

Blaauw, M. and Christen, J.A., 2005. The problems of radiocarbon dating. Science, 308(5728), p.1551-1553.

Black, B.A., Pearl, J.K., Pearson, C.L., Pringle, P.T., Frank, D.C., Page, M.T., Buckley, B.M., Cook, E.R., Harley, G.L., King, K.J. and Hughes, J.F., 2023. A multifault earthquake threat for the Seattle metropolitan region revealed by mass tree mortality. Science advances, 9(39), p.eadh4973.

Blakely, R.J., Wells, R.E., Weaver, C.S. and Johnson, S.Y., 2002. Location, structure, and seismicity of the Seattle fault zone, Washington: Evidence from aeromagnetic anomalies, geologic mapping, and seismic-reflection data. Geological Society of America Bulletin, 114(2), pp.169-177.

Booth, D.B., Troost, K.G., and Tabor, R.W., 2015, Geologic map of the Vashon 7.5' quadrangle and selected areas, King County, Washington, U.S. Geological Survey, Scientific Investigations Map SIM-3328, 1:24,000.

Bourgeois, J., and Johnson, S.Y., 2001, Geologic evidence of earthquakes at the Snohomish delta, Washington, in the past 1200 yr: Geological Society of America Bulletin, v. 113, p. 482 494, doi: 10 .1130 /0016 -7606 (2001)113.

Bourgeois, J. and Leithold, E.L., 1984. Wave-worked conglomerates—depositional processes and criteria for recognition. *In:* Koster, E.H. and Steel, R.J. (Eds.). Sedimentology of Gravels and Conglomerates. Canadian Society of Petroleum Geologists, Memoir 10 (1984), p.331-343.

Bradley, W.C. and Griggs, G.B., 1976, Form, genesis, and deformation of central California wave-cut platforms. Geological Society of America Bulletin, 87(3), p. 433-449.

Bretz, JH., 1913, Glaciation of the Puget Sound Region: Washington Geological Survey Bulletin 8, 244 p., 3 plates.

Brocher, T.M., Blakely, R.J., and Wells, R.E., 2004, Interpretation of the Seattle uplift, Washington, as a passive roof duplex: Bulletin of the Seismological Society of America, v. 94, p. 1379–1401, doi: 10 .1785 /012003190.

Brocher, T.M., Parsons, T., Blakely, R.J., Christensen, N.I., Fisher, M.A. and Wells, R.E., 2001. Upper crustal structure in Puget Lowland, Washington: Results from the 1998 seismic hazards investigation in Puget Sound. Journal of Geophysical Research: Solid Earth, 106(B7), p.13541-13564.

Bronk Ramsey, C., 1995, Radiocarbon calibration and analysis of stratigraphy: The OxCal program: Radiocarbon, v. 37, no. 2, p. 425–430

Bronk Ramsey, C., 2009, Bayesian analysis of radiocarbon dates: Radiocarbon, v. 51, no. 1, p. 337–360

Bronk Ramsey, C., 2017, OxCal software version 4.3.2, https://c14.arch.ox.ac.uk/oxcal/OxCal.html

Bucknam, R. C., E. Hemphill-Haley, and E. B. Leopold, 1992, Abrupt uplift within the past 1700 years at southern Puget Sound, Washington, Science 258, p. 1611–1614.

Bush, C., 2020, Landslide ages and implications for a marine terrace at Rialto Beach, WA.: Seattle, University of Washington: Department of Earth and Space Sciences, MESSAGe technical report no. 081, 73 p.

Campbell, S., 1981. The Duwamish No. 1 site, A lower Puget Sound shell midden. Office of Public Archaeology. Institute for Environmental Studies, University of Washington, Seattle.

Card, K., 2023, Trigger mechanism of deep-seated landslide at Rialto Beach, WA: Using surface roughness relative ages, limit equilibrium analysis and co-seismic displacement: Seattle, University of Washington: Department of Earth and Space Sciences, MESSAGe technical report.

Collins, B.D., and Sheikh, A.J., 2005, Historical reconstruction, classification, and change analysis of Puget Sound tidal marshes: Puget Sound River History Project, Washington State Department of Natural Resources report, p. 321-328.

Chen, W.S., Yang, C.Y., Chen, S.T. and Huang, Y.C., 2020. New insights into Holocene marine terrace development caused by seismic and aseismic faulting in the Coastal Range, eastern Taiwan. Quaternary Science Reviews, 240, p.106-369.

Chleborad, A.F., and Schuster, R.L., 1998, Ground Failure associated with the Puget Sound Region earthquakes of April 13, 1949, and April 29, 1965, in Rogers, A.M., Walsh, T.J., Kockelman, W.J., and Priest, G.R., Assessing Earthquake Hazards and reducing risk in the Pacific Northwest, U.S. Geological Survey Professional Paper 1563, p. 373-440.

Clark, K., Berryman, K., Litchfield, N., Cochran, N., Little, T., 2010. Evaluating the coastal deformation mechanisms of the Raukumara Peninsula, northern Hikurangi subduction margin, New Zealand and insights into forearc uplift processes. New Zealand Journal of Geology and Geophysics 53, 341–358.

Clifton, H.E., 1973. Pebble segregation and bed lenticularity in wave-worked versus alluvial gravel. Sedimentology, 20(2), pp.173-187.

Daneš, Z. F., Bonno, M. M., Brau, E., Gilham,W. D., Hoffman, T. F., Johansen, D., Jones, M. H., Malfait, B., Masten, J., and Teague, G. O., 1965, Geophysical investigations of the southern Puget Sound area,Washington: Journal of Geophysical Research, v. 70, p. 5573–5579.

Daugherty, R.D. and Fryxell, R., 1967. Archaeological, geochronological, and ecological investigations of the Ozette Village Site Complex on the Northwest Coast of Washington. Department of Anthropology, Washington State University, Pullman, WA.

Dethier, D.P., Pessl, F., Jr., Keuler, R.F., Balzarini, M.A., and Pevear, D.R., 1995, Late Wisconsinan glaciomarine deposition and isostatic rebound, northern Puget Lowland, Washington: Geological Society of America Bulletin, v. 107, p. 1288–1303.

Emery, K.O., 1958. Shallow submerged marine terraces of southern California. Geological Society of America Bulletin, 69(1), p.39-60.

Engelhart, S.E., Vacchi, M., Horton, B.P., Nelson, A.R. and Kopp, R.E., 2015. A sea-level database for the Pacific coast of central North America. Quaternary Science Reviews, 113, pp.78-92.

EPA, 2014, EPA Superfund, Record of Decision: Lower Duwamish Waterway Superfund Site, EPA ID: WA00002329803, Seattle and Tukwila, King County, Washington.

Eronen, M., T. Kankainen, and M. Tsukada, 1987, Late Holocene sea-level record in a core from the Puget Lowland, Washington, Quat. Res. 27, 147–159.

Filiatrault, Andre, Uang, C.-M., Folz, Bryan, Christopoulos, Constantin, and Gatto, Kip, 2001, Reconnaissance report of the February 28, 2001 Nisqually (Seattle-Olympia) earthquake: San Diego, University of California, Department of Structural Engineering, 62 p. [http://www.eeri.org/lfe/pdf/usa_nisqually_ucsd_reconnaissance_report.pdf].

Finn, C., Phillips,W. M., and Williams, D. L., 1991, Gravity anomaly and terrain maps of Washington: U.S. Geological Survey Geophysical Investigations Map GP-988, scale 1:500,000 and 1:1,000,000.

Frankel, A.D., Mueller, C.S., Barnhard, T.P., Perkins, D.M., Leyendecker, E.V., Dickman, N., Hanson, S.L. and Hopper, M.G., 1996. National seismic-hazard maps: documentation June 1996 (No. 96-532). US Geological Survey.

Freeman, E., 2021, Age of a low-elevation marine terrace and landslide at Rialto Beach, WA. [MESSAGe technical report] University of Washington: Department of Earth and Space Sciences. No. 096, 41 p.

Friedman, E., 1976, An archaeological survey of Makah territory: a study in resource utilization. [Ph.D. dissertation] Washington State University, Department of Anthropology. 288 p.

Garrison-Laney, C., 2017. Tsunamis and sea levels of the past millennium in Puget Sound, [Ph.D. dissertation] University of Washington: Department of Earth and Space Sciences. 166 p.

Gerstel, W.J., and Lingley, W.S., 2000, Geologic map of the Forks 1:100,000 quadrangle, Washington, Washington Division of Geology and Earth Resources, Open File Report 2000-4, scale 1:100,000.

Gilbert, J.J., 1899, Seattle Bay and City, City and head of bay, Washington Territory: U.S. Coast and Geodetic Survey T-2421, scale 1:10,000.

Giona Bucci, M., Almond, P., Villamor, P., Ries, W., Smith, C. and Tuttle, M., 2017. When the earth blisters: Exploring recurrent liquefaction features in the coastal system of Christchurch, New Zealand. Terra Nova, 29(3), p.162-172

Goldfinger, C., Galer, S., Beeson, J., Hamilton, T., Black, B., Romsos, C., Patton, J., Nelson, C.H., Hausmann, R. and Morey, A., 2017, The importance of site selection, sediment supply, and hydrodynamics: A case study of submarine paleoseismology on the northern Cascadia margin, Washington USA. Marine Geology, 384, p.4-46.

Goldfinger, C., Nelson, C.H., Morey, A.E., Johnson, J.E., Patton, J.R., Karabanov, E.B., Gutierrez-Pastor, J., Eriksson, A.T., Gracia, E., Dunhill, G. and Enkin, R.J., 2012, Turbidite event history—Methods and implications for Holocene paleoseismicity of the Cascadia subduction zone (No. 1661-F). US Geological Survey.

Gower, H. D., Yount, J. C., and Crosson, R. S., 1985, Seismotectonic map of the Puget Sound region, Washington: U.S. Geological Survey Map I-1613, scale 1:250 000.

Grant, A.R., Struble, W.T. and LaHusen, S.R., 2022, Limits to coseismic landslides triggered by Cascadia Subduction Zone earthquakes. Geomorphology, 418, p.108477.

Haugerud, 2017, Late last-glacial shorelines in northwest Washington State, Geological Society of America Abstracts with Programs. Vol. 49, No. 6, ISSN 0016-7592 doi: 10.1130/abs/2017AM-304915

Haugerud, R.A., 2020, Deglaciation of the Puget Lowland, Washington, in Waitt, R.B., Thackray, G.D., and Gillespie, A.R., eds., Untangling the Quaternary Period—A Legacy of Stephen C. Porter: Geological Society of America Special Paper 548, p. 279–298, https://doi.org/10.1130/2020.2548(14).

Haugerud, R. A., Troost, K. G., & Laprade, W. T., 2017, Geology of Seattle, a field trip. From the Puget Lowland to East of the Cascade Range: Geologic Excursions in the Pacific Northwest, 49 p.

Herzig, E., Duvall, A., Booth, A., Stone, I., Wirth, E., LaHusen, S., Wartman, J. and Grant, A., 2023, Evidence of Seattle Fault Earthquakes from Patterns in Deep-Seated Landslides., Bulletin of the Seismological Society of America. https://doi.org/10.1785/0120230079

Hill, M, 2022, Historical shoreline change assessment of Rialto and First Beaches, Olympic Peninsula, Washington, [MESSAGe technical report] University of Washington: Department of Earth and Space Sciences.

Hitchcock, C.L., and Cronquist, A., 2018, Flora of the Pacific Northwest, second edition, Seattle, University of Washington Press, Seattle, WA

Hutchinson, I., 1992. Holocene sea level change in the Pacific Northwest: a catalogue of radiocarbon ages and an atlas of regional sea-level curves. Occasional Paper No. 1, Institute of Quaternary Research, Simon Fraser University, Burnaby, BC, 100 p.

Hyndman, R.D., 2013. Downdip landward limit of Cascadia great earthquake rupture. Journal of Geophysical Research: Solid Earth, 118(10), p. 5530-5549.

Hyndman, R.D. and Wang, K., 1995. The rupture zone of Cascadia great earthquakes from current deformation and the thermal regime. Journal of Geophysical Research: Solid Earth, 100(B11), p. 22133-22154.

Ishihara, K., 1985. Stability of natural soil deposits during earthquakes. Proceedings of the Eleventh International Conference on Soil Mechanics and Foundation Engineering, San Francisco, Vol. 1: p. 321-376.

Jacoby, G. C., P. L. Williams, and B. M. Buckley, 1992, Tree ring correlation between prehistoric landslides and abrupt tectonic events in Seattle, Washington, Science 258, 1621–1623.

James, T., Gowan, E.J., Hutchinson, I., Clague, J.J., Barrie, J.V. and Conway, K.W. (2009). Sea-level change and paleogeographic reconstructions, southern Vancouver Island, British Columbia, Canada. Quaternary Science Reviews, 28(13-14), pp.1200-1216.

Jara-Muñoz, J. and Melnick, D., 2015. Unraveling sea-level variations and tectonic uplift in wave-built marine terraces, Santa María Island, Chile. Quaternary research, 83(1), pp.216-228.

Jara-Muñoz, J., Melnick, D., Zambrano, P., Rietbrock, A., González, J., Argandoña, B., and Strecker, M.R., 2017, Quantifying offshore fore-arc deformation and splay-fault slip using drowned Pleistocene shorelines, Arauco Bay, Chile, J. Geophys. Res. Solid Earth, 122, 4529–4558, doi:10.1002/2016JB013339.

Johnson, S.Y., Dadisman, S.V., Childs, J.R. and Stanley, W.D., 1999. Active tectonics of the Seattle fault and central Puget Sound, Washington—Implications for earthquake hazards. Geological Society of America Bulletin, 111(7), pp.1042-1053

Johnson, S. Y., Hartwell, S.R., and Dartnell, P., (2014), Offset of latest Pleistocene shoreface reveals slip rate on the Hosgri strike-slip fault, offshore central California, Bull. Seismol. Soc. Am., 104(4), 1650–1662.

Jovanelly, T.J. and Moore, A.L., 2009. Sedimentological analysis of an ancient sand sheet of multiple origins at Lynch Cove, Puget Sound, Washington. Journal of Coastal Research, 25(2), pp.294-304.

Kayen, R.E., and Barnhardt, W.A., 2007, Seismic stability of the Duwamish River delta, Seattle, Washington, U.S. Geological Survey Professional Paper 1661-E, 11 p.

Karlin, R.E. and Abella, S.E., 1992. Paleoearthquakes in the Puget Sound region recorded in sediments from Lake Washington, USA. Science, 258(5088), p.1617-1620.

Karlin, R.E., Holmes, M., Abella, S.E.B. and Sylwester, R., 2004. Holocene landslides and a 3500-year record of Pacific Northwest earthquakes from sediments in Lake Washington. Geological Society of America Bulletin, 116(1-2), p. 94-108.

Kelsey, H., 1990. Late Quaternary deformation of marine terraces on the Cascadia subduction zone near Cape Blanco, Oregon. Tectonics 9, p. 983–1014.

Kelsey, H. M., 2015, Geomorphological indicators of past sea levels. Handbook of sea-level research, p. 66-82.

Kelsey, H. M., B. L. Sherrod, A. R. Nelson, and T. M. Brocher (2008). Earthquakes generated from bedding plane-parallel reverse faults above an active wedge thrust, Seattle fault zone, Geol. Soc. Am. Bull. 120, p. 1581–1597.

Kelsey, H.M., Witter, R.C. and Hemphill-Haley, E., 2002. Plate-boundary earthquakes and tsunamis of the past 5500 yr, Sixes River estuary, southern Oregon. GSA Bulletin, 114(3), p. 298-314.

Kelsey, H.M., Witter, R.C., Engelhart, S.E., Briggs, R., Nelson, A., Haeussler, P. and Corbett, D.R., 2015. Beach ridges as paleoseismic indicators of abrupt coastal subsidence during subduction zone earthquakes, and implications for Alaska-Aleutian subduction zone paleoseismology, southeast coast of the Kenai Peninsula, Alaska. Quaternary Science Reviews, 113, p.147-158.

Kovanen, D.J., Haugerud, R.A., and Easterbrook, D.J., 2020, Geomorphic map of western Whatcom County, Washington, U.S. Geological Survey, Scientific Investigations Map SIM-3406, 1:50,000.

LaHusen, S.R., Duvall, A.R., Booth, A.M., Grant, A., Mishkin, B.A., Montgomery, D.R., Struble, W., Roering, J.J. and Wartman, J., 2020. Rainfall triggers more deep-seated landslides than Cascadia earthquakes in the Oregon Coast Range, USA. Science advances, 6(38).

Lajoie, K.R., 1986. Coastal tectonics. In: Wallace, R.E. (Chairman), Active Tectonics. Studies in Geophysics. National Academies Press, Washington, DC, p. 95–124.

Lambeck, K., Rouby, H., Purcell, A., Sun, Y., and Sambridge, M., 2014, Sea level and global ice volumes from the Last Glacial Maximum to the Holocene: Proceedings of the National Academy of Sciences of the United States of America, v. 111, p. 15,296–15,303, https://doi.org/10.1073/pnas.1411762111.

Lawson, J.S., 1875, Duwamish Bay, (part of) Washington Territory, U.S. Coast and Geodetic Survey topographic map T-1406, scale 1:10,000.

Livingston, E.H., 2004. Who was student and why do we care so much about his t-test? 1. Journal of Surgical Research, 118(1), p.58-65.

Loeffler, R.D., Holmes, M.L. and Sylwester, R.E., 1989, September. In search of the Denny regrade: Fate of a Large Spoil bank in Elliott Bay, Puget Sound. In *Proceedings OCEANS* (Vol. 1, p. 84-89).

Lowe, D.R., 1975, Water escape structures in coarse-grained sediments. Sedimentology, v. 22, p. 157-204.

Ludwin, R.S., Thrush, C.P., James, K., Buerge, D., Jonientz-Trisler, C., Rasmussen, J., Troost, K. and De Los Angeles, A., 2005, Serpent spirit-power stories along the Seattle fault. Seismological Research Letters, 76(4), p. 426-431.

Luk, S., 2020, NOSAMS, "Radiocarbon data and calculations," https://www2.whoi.edu/site/nosams/radiocarbon-data-and-calculations, Accessed 21 Nov 2023.

Luzier, J.E., 1969, Geology and ground-water resources of south-western King County, Washington: Washington Department of Water Resources Water Supply Bulletin, v. 28, 260 p., 3 plates.

Martin, M. E., 2011, Coastal marsh stratigraphy as an indicator of past earthquakes, Puget Lowland, Washington State, Ph.D. Thesis, University of Washington, Seattle, Washington, 186 p.

Martin, M.E., Bourgeois, J., 2012. Vented sediments and tsunami deposits in the Puget Lowland, Washington—differentiating sedimentary processes. Sedimentology 59, 419–444.

Mazzotti, S., Dragert, H., Hyndman, R.D., Miller, M.M., and Henton, J.A., 2002, GPS deformation in a region of high crustal seismicity: N. Cascadia forearc, Earth Planet. Sci. Lett. 198, no. 1, p. 41–48, doi: 10.1016/S0012-821X(02)00520-4.

McCaffrey, R., King, R.W., Payne, S.J., and Lancaster, M., 2013, Active tectonics of northwestern U.S. inferred from GPS-derived surface velocities, J. Geophys. Res. 118, no. 2, p. 709–723, doi: 10.1029/2012JB009473.

McCaffrey, R., Qamar, A.I., King, R.W., Wells, R., Khazaradze, G., Williams, C.A., Stevens, C.W., Vollick, J.J. and Zwick, P.C., 2007. Fault locking, block rotation and crustal deformation in the Pacific Northwest. Geophysical Journal International, 169(3), p.1315-1340.

McCrory, P. A., 1996, Tectonic model explaining divergent contraction directions along the Cascadia subduction margin, Washington. Geology 24 (10), p.929–932. doi: https://doi.org/10.1130/0091-7613(1996)024<0929:TMEDCD>2.3.CO;2

McCulloch, D.S. and Bonilla, M.G., 1970. Effects of the earthquake of March 27, 1964, on the Alaska Railroad, U.S.G.S. Professional Paper No. 545-D.

McKenzie, K.A., Kelsey, H.M., Kirby, E., Rittenour, T.M., Furlong, K.P., 2022, Differential coastal uplift quantified by luminescence dating of marine terraces, central Cascadia forearc, Oregon, Quaternary Science Reviews, Volume 298: 107853, https://doi.org/10.1016/j.quascirev.2022.107853.

McSaveney, M.J., Graham, I.J., Begg, J.G., Beau, A.G., Hull, A.G., Kim, K., and Zondervan, A., 2006, Late Holocene uplift of beach ridges at Turakirae Head, south Wellington coast, New Zealand. New Zealand Journal of Geology and Geophysics, 49, p. 337–358.

Melgar, D., Sahakian, V.J. and Thomas, A.M., 2022. Deep coseismic slip in the Cascadia megathrust can be consistent with coastal subsidence. Geophysical Research Letters, 49(3).

Merritts, D.J., Bull, W.B., 1989. Interpreting Quaternary uplift rates at the Mendocino Triple Junction, northern California, from uplifted marine terraces. Geology 17, p. 1020–1024.

Meyers, R.A., Smith, D.G., Jol, H.M. and Peterson, C.D., 1996. Evidence for eight great earthquake-subsidence events detected with ground-penetrating radar, Willapa barrier, Washington. Geology, 24(2), p. 99-102.

Miller, I., 2019, Shoreline survey data collected at Rialto and Kalaloch Beaches, Washington State, 2018-2019. PANGAEA, https://doi.org/10.1594/PANGAEA.902570

Miller, I., Kaminsky, G. and Akamajian, A., 2023. Shoreline dynamics on a high energy beach associated with relative sea-level fall on the Pacific Coast, USA. In Coastal Sediments 2023: The Proceedings of the Coastal Sediments 2023, p. 364-378.

Miller, I.M., Morgan, H., Mauger, G., Newton, T., Weldon, R., Schmidt, D., Welch, M. and Grossman, E., 2018. Projected sea level rise for Washington state: A 2018 assessment. A collaboration of Washington Sea Grant, University of Washington Climate Impacts Group, Oregon State University, University of Washington, and US Geological Survey. https://cig.uw.edu/resources/special-reports/ sea- level- rise- in- washington- state- a- 2018-assessment/

Moernaut, J., Daele, M.V., Heirman, K., Fontijn, K., Strasser, M., Pino, M., Urrutia, R. and De Batist, M., 2014, Lacustrine turbidites as a tool for quantitative earthquake reconstruction: New evidence for a variable rupture mode in south central Chile. Journal of Geophysical Research: Solid Earth, 119(3), p.1607-1633.

Moore, G.L., Roland, E., Bennett, S.E., Watt, J., Kluesner, J., Brothers, D. and Myers, E., 2022, High-Resolution Marine Seismic Imaging of the Seattle Fault Zone: Near-Surface Insights into Fault Zone Geometry, Quaternary Deformation, and Long-Term Evolution. Bulletin of the Seismological Society of America, 112(5), p. 2715-2744.

Mosher, D.C. and Hewitt, A.T., 2004. Late Quaternary deglaciation and sea-level history of eastern Juan de Fuca Strait, Cascadia. Quaternary International, 121(1), p. 23-39.

Muller, J.R. and Harding, D.J., 2007, Using LIDAR surface deformation mapping to constrain earthquake magnitudes on the Seattle fault in Washington State, USA. In 2007 Urban Remote Sensing Joint Event (p. 1-7).

Mullineaux, D.R., 1970, Geology of the Renton, Auburn, and Black Diamond quadrangles, King County, Washington: U.S. Geological Survey Professional Paper 672, 92 p.

Mullineaux, D.R., Waldron, H.H., and Rubin, M., 1965, Stratigraphy and Chronology of Late Interglacial and Early Vashon Glacial Time in the Seattle Area, Washington: U.S. Geological Survey Bulletin 1194-O, 10 p.

Nelson, A.R., DuRoss, C.B., Witter, R.C., Kelsey, H.M., Engelhart, S.E., Mahan, S.A., Gray, H.J., Hawkes, A.D., Horton, B.P., and Padgett, J.S., 2021, A maximum rupture model for the central and southern Cascadia subduction zone—reassessing ages for coastal evidence of megathrust earthquakes and tsunamis: Quaternary Science Reviews, v. 261, p. 106922, doi:10.1016/j.quascirev.2021.106922.

Nelson, A.R., Johnson, S.Y., Kelsey, H.M., Wells, R.E., Sherrod, B.L., Pezzopane, S.K., Bradley, L., Koehler, R.D., and Bucknam, R.C., 2003a, Late Holocene earthquakes on the Toe Jam Hill fault, Seattle fault zone, Bainbridge Island, Washington: Geological Society of America Bulletin, v. 115, p. 1388–1403, doi: 10 .1130 /B25262 .1

Nelson, A.R., Johnson, S.Y., Kelsey, H.M., Sherrod, B.L., Wells, R.E., Okumura, K., Bradley, L., Bogar, R., and Personius, S.F., 2003b, Field and laboratory data from an earthquake history study of the Waterman Point fault, Kitsap County, Washington: U.S. Geological Survey Miscellaneous Field Studies Map MF-2423, http://pubs.usgs.gov/mf/2003/mf -2423/.

Nelson, A. R., Personius, S. F., Sherrod, B. L., Kelsey, H. M., Johnson, S. Y., Bradley, L.A., and Wells, R. E., 2014, Diverse rupture modes for surface-deforming upper plate earthquakes in the southern Puget Lowland of Washington State, Geosphere 10, no. 4, p. 769–796, doi: 10.1130/GES00967.1.

Newton, T.J., Weldon, R., Miller, I.M., Schmidt, D., Mauger, G., Morgan, H. and Grossman, E., 2021. An Assessment of Vertical Land Movement to Support Coastal Hazards Planning in Washington State. Water 2021, 13, 281.

NOAA, 2020, Datums for 9442396, La Push, Quillayute River WA. Accessed November, 2023. https://tidesandcurrents.noaa.gov/datums.html?id=9442396.

Obermeier, S.F., 1995. Preliminary limits for the strength of shaking in the Columbia River valley and the southern half of coastal Washington, with emphasis for a Cascadia subduction earthquake about 300 years ago. US Geological Survey Open-File Report 94-589, 46 p.

Obermeier, S.F., 1996, Use of liquefaction-induced features for paleoseismic analysis–An overview of how seismic liquefaction features can be distinguished from other features and how their regional distribution and properties of source sediment can be used to infer the location and strength of Holocene paleo-earthquakes. Engin. Geol., 44, p. 1–76.

Obermeier, S.F., Gohn, G.S., Weems. R.E., Gelinas, R.L., Rubin, M, 1985, Geologic evidence for recurrent moderate to large earthquakes near Charleston, South Carolina, Science, 227, p. 408–411.

Obermeier, S.F., and Pond, E.C., 1998. Issues in using liquefaction features for paleoseismic analysis: U.S. Geological Survey Open-File Report 98-28, 40 p.

Ota, Y., Hull, A.G. and Berryman, K.R., 1991, Coseismic uplift of Holocene marine terraces in the Pakarae River area, eastern North Island, New Zealand. Quaternary Research, 35(3), pp.331-346.

Ota, Y., S. Odagiri, H. Sasaki, and S. Mukoyama, 2006, Late Holocene deformation as deduced from the former shoreline height of marine terraces above the Seattle fault zone, Washington State, Jishin 58, 385–399.

Ota, Y. and Yamaguchi, M., 2004, Holocene coastal uplift in the western Pacific Rim in the context of late Quaternary uplift. Quaternary International, 120(1), p.105-117.

Pacific Northwest Geodetic Array, 2023, station P816, http://www.panga.cwu.edu/data/bysite/ Accessed 8 November 2023.

Padgett, J.S., Kelsey, H.M., Lamphear, D., 2019, Upper-plate deformation of Late Pleistocene marine terraces in the Trinidad, California, coastal area, southern Cascadia subduction zone. Geosphere 15, 1323–1341.

Pazzaglia, F.J., Thackray, G.D., Brandon, M.T., Wegmann, K.W., Gross, J., McDonald, E., Garcia, A.F. and Prothero, D., 2003. Tectonic geomorphology and the record of Quaternary plate boundary deformation in the Olympic Mountains. *In:* Swanson, T.W. (Ed.), Western Cordillera and Adjacent Areas. Geological Society of America Field Guide 4, 37–67.

Peterson C.D. and Madin, I.P., 1997, Coseismic paleoliquefaction Evidence in the Central Cascadia Margin, USA. Oregon Geology, 59, p. 51-74.

Peterson, C. , Kristensen, K. and Minor, R., 2014, Large-Scale Fluidization Features from Late Holocene Coseismic Paleoliquefaction in the Willamette River Forearc Valley, Central Cascadia Subduction Zone, Oregon, USA. Open Journal of Earthquake Research, 3, p. 82-99.

Petersen, M.D., Shumway, A.M., Powers, P.M., Mueller, C.S., Moschetti, M.P., Frankel, A.D., Rezaeian, S., McNamara, D.E., Luco, N., Boyd, O.S. and Rukstales, K.S., 2020, The 2018 update of the US National Seismic Hazard Model: Overview of model and implications. Earthquake Spectra, 36(1), p. 5-41.

Petersen, M.D., Shumway, A.M., Powers, P.M., Field, E.H., Moschetti, M.P., Jaiswal, K.S., Milner, K.R., Rezaeian, S., Frankel, A.D., Llenos, A.L. and Michael, A.J., 2023. The 2023 US 50-State National Seismic Hazard Model: Overview and implications. Earthquake Spectra.

Peterson, C.D., Cruikshank, K.M., Darienzo, M.E., Wessen, G.C., Butler, V.L. and Sterling, S.L., 2013. Coseismic subsidence and paleotsunami run-up records from latest Holocene deposits in the Waatch Valley, Neah Bay, northwest Washington, USA: Links to great earthquakes in the northern Cascadia margin. Journal of Coastal Research, 29(1), p.157-172.

Peterson, C.D., Butler, V.L., Feathers, J.K. and Cruikshank, K.M., 2014. Geologic records of net littoral drift, beach plain development, and paleotsunami runup, North Sand Point, Olympic Peninsula, Washington, USA. Northwest Science, 88(4), p. 314-328.

Pinegina, T.K., Bourgeois, J., Kravchunovskaya, E.A., Lander, A.V., Arcos, M.E., Pedoja, K. and MacInnes, B.T., 2013. A nexus of plate interaction: Vertical deformation of Holocene wave-built terraces on the Kamchatsky Peninsula (Kamchatka, Russia). Bulletin, 125(9-10), p.1554-1568.

Plafker, George, and Rubin, Meyer, 1978. Uplift history and earthquake recurrence as deduced from marine terraces on Middleton Island, Alaska, in Proceedings of Conference VI, Methodology for identifying seismic gaps and soon-to-break gaps: U.S. Geological Survey Open-File Report 78-943, p. 687-721.

PNSN. Deep Earthquakes. Accessed May 2018, https://pnsn.org/outreach/earthquakesources/deepearthquakes

Polenz, Michael; Czajkowski, J. L.; Legorreta Paulin, Gabriel; Contreras, T. A.; Miller, B. A.; Martin, M. E.; Walsh, T. J.; Logan, R. L.; Carson, R. J.; Johnson, C. N.; Skov, R. H.; Mahan, S. A.; Cohan, C. R., 2010 [revised 2011], Geologic map of the Skokomish Valley and Union 7.5-

minute quadrangles, Mason County, Washington: Washington Division of Geology and Earth Resources Open File Report 2010-3, 1 sheet, scale 1:24,000, with 21 p. text.

Pratt, T. L., Johnson, S. Y., Potter, C. J., Stephenson, W. J., and Finn, C., 1997, Seismic-reflection images beneath Puget Sound, western Washington State—The Puget Lowland thrust system hypothesis: Journal of Geophysical Research, v. 102, p. 27,469–27,490.

Pratt, T.L., Troost, K.G., Odum, J.K.,and Stephenson, W.J., 2015, Kinematics of shallow backthrusts in the Seattle fault zone, Washington State: Geosphere, v. 11, no. 6, p. 1948–1974, doi:10 .1130 /GES01179.1.

Ramírez-Herrera, M.T., Kostoglodov, V. & Urrutia-Fucugauchi, J., 2011. Overview of Recent Coastal Tectonic Deformation in the Mexican Subduction Zone. Pure Appl. Geophys. 168, p. 1415–1433. https://doi.org/10.1007/s00024-010-0205-y

Rasanen, R.A., Marafi, N.A., and Maurer, B.W., 2021a, Compilation and forecasting of paleoliquefaction evidence for the strength of ground motions in the U.S. Pacific Northwest, Engineering Geology 292, p.106-253.

Rasanen, R., Marafi, N., Maurer., B., 2021b, "Compilation and Forecasting of Paleoliquefaction Evidence for the Strength of Ground Motions in the U.S. Pacific Northwest: A Digital Dataset (Version 2)." DesignSafe-CI. https://doi.org/10.17603/ds2-fqkr-h615 v1

Reimer, Brown and Reimer, 2004. "Discussion: Reporting and Calibration of Post-Bomb14C Data", Radiocarbon 46, p. 1299-1304

Reimer, R.W. & Reimer, P.J. 2024 CALIBomb [WWW program] at http://calib.org accessed 2024-02-05

Reimer, P.J., Austin, W.E., Bard, E., Bayliss, A., Blackwell, P.G., Ramsey, C.B., Butzin, M., Cheng, H., Edwards, R.L., Friedrich, M. and Grootes, P.M., 2020, The IntCal20 Northern Hemisphere radiocarbon age calibration curve (0–55 cal kBP). Radiocarbon, 62(4), pp.725-757.

Reineck, H.E., and Singh, I.B., 1980. Depositional environments. Depositional Sedimentary Environments, Springer, Berlin, Heidelberg.

Riedel, J., S. Sarrantonio, and S. Dorsch., 2021, Geomorphology of coastal Olympic National Park. Natural Resource Report NPS/NCCN/NRR—2021/2260. National Park Service, Fort Collins, Colorado. https://doi.org/10.36967/nrr-2286564.

Rockwell, T.K., Keller, E.A. and Dembroff, G.R., 1988. Quaternary rate of folding of the Ventura Avenue anticline, western Transverse Ranges, southern California. Geological Society of America Bulletin, 100(6), p. 850-858.

Ruggiero, P., Kaminsky, G.M., Gelfenbaum, G. and Cohn, N., 2016. Morphodynamics of prograding beaches: A synthesis of seasonal-to century-scale observations of the Columbia River littoral cell. Marine Geology, 376, p.51-68.

Satake, K., Shimazaki, K., Tsuji, Y., Ueda, K., 1996, Time and size of a giant earthquake in Cascadia inferred from Japanese tsunami record of January 1700. Nature 379, p. 246–249.

Scharer, K., R. Weldon II, G. Biasi, A. Streig, and T. Fumal, 2017, Ground-rupturing earthquakes on the northern Big Bend of the San Andreas Fault, California, 800 A.D. to Present, J. Geophys. Res. Solid Earth, 122, p. 2193–2218 doi:10.1002/2016JB013606

Schuster, R.L., Logan, R.L. and Pringle, P.T., 1992. Prehistoric rock avalanches in the Olympic Mountains, Washington. Science, 258(5088), pp.1620-1621.

Selby, M.J., 1993. Hillslope Materials. Oxford University Press, 451p.

Shennan, I., Long, A.J., Rutherford, M.M., Innes, J.B., Green, F.M. and Walker, K.J., 1998. Tidal marsh stratigraphy, sea-level change and large earthquakes—II: submergence events during the last 3500 years at Netarts Bay, Oregon, USA. Quaternary Science Reviews, 17(4-5), p.365-393.

Sherrod, B.L., 2001, Evidence for earthquake-induced subsidence about 1100 yr ago in coastal marshes of southern Puget Sound, Washington: Geological Society of America Bulletin, v. 113, no. 10, p. 1299-1311.

Sherrod, B.L., Nelson, A.R., Kelsey, H.M., Brocher, T.M., Blakely, R.J., Weaver, C.S., Rountree, N.K., Rhea, B.S. and Jackson, B.S., 2003. The Catfish Lake scarp, Allyn, Washington: Preliminary field data and implications for earthquake hazards posed by the Tacoma fault. US Geological Survey Open-File Report, 455, p.14.

Sherrod, B.L., Brocher, T.M., Weaver, C.S., Bucknam, R.C., Blakely, R.J., Kelsey, H.M., Nelson, A.R., Haugerud, R., 2004. Holocene fault scarps near Tacoma, Washington, USA. Geology 32, p. 9–12.

Sherrod, B., and J. Gomberg, 2014, Crustal earthquake triggering by prehistoric great earthquakes on subduction zone thrusts, J. Geophys. Res. Solid Earth, 119, 1273–1294, doi:10.1002/2013JB010635.

Shugar, D.H., Walker, I.J., Lian, O.B., Eamer, J.B., Neudorf, C., McLaren, D. and Fedje, D., 2014. Post-glacial sea-level change along the Pacific coast of North America. Quaternary Science Reviews, 97, pp.170-192.

Staisch, L.M., and Walton, M.A., 2022, Cascadia subduction zone database: compilation of published datasets relevant to Cascadia subduction zone earthquake hazards and tectonics (2022): U.S. Geological Survey data release, https://doi.org/10.5066/P9O69X6E.

Stanton, K., Crider, J., Kelsey, H., & Feathers, J., 2023, The signature of accumulated permanent uplift, northern Cascadia subduction zone. Quaternary Research, 1-21. doi:10.1017/qua.2023.59

Stanton, K., Crider, J., Anderson, M., Lau, T., Staisch, L., Kelsey, H., (in prep 2023). Gravity and magnetic evidence for potentially active, transpressional crustal faulting, central Cascadia forearc. For Tectonics.

Struble, W.T., Roering, J.J., Black, B.A., Burns, W.J., Calhoun, N. and Wetherell, L., 2020, Dendrochronological dating of landslides in western Oregon: Searching for signals of the Cascadia AD 1700 earthquake. Bulletin, 132(7-8), p.1775-1791.

Styron, R.H. and Sherrod, B., 2021. Improving paleoseismic earthquake magnitude estimates with rupture length information: Application to the Puget Lowland, Washington State, USA. Bulletin of the Seismological Society of America, 111(2), p.1139-1153.

Tabor, R.W. and Cady, W.M., 1978. The structure of the Olympic Mountains, Washington: Analysis of a subduction zone (Vol. 1033). US Government Printing Office.

Tabor, R.W., Haugerud, R.A., Booth, D.B., and Troost, K.G., 2014, Lidar-revised geologic map of the Olalla 7.5' quadrangle, King, Kitsap, and Pierce Counties, Washington, U.S. Geological Survey, Scientific Investigations Map SIM-3277, 1:24,000.

Takada, K. and Atwater, B.F., 2004, Evidence for liquefaction identified in peeled slices of Holocene deposits along the lower Columbia River, Washington. Bulletin of the Seismological Society of America, v. 94, n. 2, p. 550-575.

Talwani, P. and Cox, J., 1985. Paleoseismic evidence for recurrence of earthquakes near Charleston, South Carolina. Science, 229(4711), p.379-381.

Tamura, T., 2012. Beach ridges and prograded beach deposits as palaeoenvironment records. Earth-Science Reviews, 114(3-4), p. 279-297.

ten Brink, U. S., J. Song, and R. C. Bucknam, 2006, Rupture models for the AD 900–930 Seattle fault earthquake from uplifted shorelines, Geology, 34(7), 585–588.

Thackray, G.D., 1996. Glaciation and neotectonic deformation on the western Olympic Peninsula, Washington. [Ph.D. Dissertation] University of Washington.

Thackray, G.D., 1999. Convergent-margin deformation of Pleistocene strata on the Olympic coast of Washington, USA. Geological Society, London, Special Publications, 146(1), p.199-211.

Thackray, G.D., 2001. Extensive early and middle Wisconsin glaciation on the western Olympic Peninsula, Washington, and the variability of Pacific moisture delivery to the northwestern United States. Quaternary Research, 55(3), pp.257-270.

Thorson, R.M., 1980, Ice-sheet glaciation of the Puget Lowland, Washington, during the Vashon stade (late Pleistocene): Quaternary Research, v. 13, p. 303–321, https://doi.org/10.1016/0033-5894(80)90059-9.

Thorson, R.M., 1981, Isostatic Effects of the Last Glaciation in the Puget Lowland, Washington: U.S. Geological Survey Open-File Report 81-370, 1 plate, scale 1:250,000, 100 p.

Thorson, R.M., 1989, Glacio-isostatic response of the Puget Sound area, Washington: Geological Society of America Bulletin, v. 101, p. 1163–1174, https://doi.org/10.1130/0016-7606(1989)101<1163:GIROTP>2.3.CO;2.

Thorson, R. M., 1993, Postglacial offset along the Seattle fault: Science, v. 260, p. 825–826.

Thorson, R.M., 1996, Earthquake recurrence and glacial loading in western Washington: GSA Bulletin, 108(9), p.1182-1191.

Todd, S. P., 1996, Process deduction from fluvial sedimentary structures, in: Advances in fluvial dynamics and stratigraphy, edited by: Car- ling, P. A. and Dawson, M. R., John Wiley & Sons Ltd, p. 299–350, 1996.

Troost, K. G., and D. B. Booth, 2008, Geology of Seattle and the Seattle area, Washington, in Landslides and Engineering Geology of the Seattle, Washington, Area, Geological Society of America Reviews in Engineering Geology, doi: 10.1130/2008.4020(01).

Troost, K. G., D. B. Booth, A. P. Wisher, and S. A. Shimel, 2005, The geologic map of Seattle—A progress report, U.S. Geol. Surv. Open-File Rept. 2005-1252.

Troost, K.G., Davis, E.J., Miller, I., Bush, C., Freeman, E., and Benson, M.A., 2021, Rapid Retreat of a Potentially Uplifted Coastal Terrace at Rialto Beach, on the Pacific Coast of Washington, Geological Society of America Abstracts with Programs, Vol. 53, No. 6, doi: 10.1130/abs/2021AM-371377.

Tuttle, M.P., 2001, The use of liquefaction features in paleoseismology: Lessons learned in the New Madrid seismic zone, central United States. Journal of Seismology, 5, p.361-380.

Tuttle, M.P., Villamor, P., Almond, P., Bastin, S., Giona Bucci, M., Langridge, R., Clark, K. and Hardwick, C.M., 2017, Liquefaction induced during the 2010–2011 Canterbury, New Zealand, earthquake sequence and lessons learned for the study of paleoliquefaction features. Seismological Research Letters, 88(5), p.1403-1414.

Tuttle, M.P., Hartleb, R., Wolf, L. and Mayne, P.W., 2019. Paleoliquefaction studies and the evaluation of seismic hazard. Geosciences, 9(7), p.311.

Tuttle, M.P., Sims, J.D., Dyer-Williams, K., Lafferty, I.R.H. and Schweig, E.S., 2000. Dating of liquefaction features in the New Madrid seismic zone. US Nuclear Regulatory Commission, p.78.

URS Corporation and BOAS Inc., 1987, The Duwamish No. 1 Site: 1986 Data Recovery. Report submitted to METRO, Contract No. CW/F2-82, Seattle, WA, U.S.A.

Waldron, H.H., 1967, Geologic map of the Duwamish Head quadrangle, King and Kitsap Counties, Washington, U.S. Geological Survey, Geologic Quadrangle Map GQ-706, 1:24,000

Walton, M.A., Staisch, L.M., Dura, T., Pearl, J.K., Sherrod, B., Gomberg, J., Engelhart, S., Tréhu, A., Watt, J., Perkins, J. and Witter, R.C., 2021. Toward an integrative geological and geophysical view of Cascadia subduction zone earthquakes. Annual Review of Earth and Planetary Sciences, 49, p.367-398.

Wells, R.E., Simpson, R.W., 2001. Northward migration of the Cascadia forearc in the northwestern US and implications for subduction deformation. Earth Planets Space 53 (4), 275-284.

Westdahl, F., 1901, Seattle Harbor, Washington: U.S. Coast and Geodetic Survey No. 6445, scale 1:20,000. Digitized by Puget Sound River History Project.

Whisler, J.E., Atwater, B.F. and Montgomery, D.R., 2002, December. Holocene liquefaction near the Seattle fault at the Issaquah Creek delta. In AGU Fall Meeting Abstracts (Vol. 2002, pp. S22B-1036).

Wirth, E.A. and Frankel, A.D., 2019, Impact of down-dip rupture limit and high-stress drop subevents on coseismic land-level Change during Cascadia Megathrust Earthquakes. Bulletin of the Seismological Society of America, 109(6), pp.2187-2197.

Youd, T.L., 1973, Liquefaction, flow, and associated ground failure. US Geological Survey Circular 688, 12 p.

Yount, J.C. and Gower, H.D., 1991, Bedrock geologic map of the Seattle 30' by 60' quadrangle, Washington, U.S. Geological Survey, Open-File Report OF-91-147, 1:100,000

Yousefi, M., Milne, G.A., Love, R. and Tarasov, L., 2018. Glacial isostatic adjustment along the Pacific coast of central North America. Quaternary Science Reviews, 193, p.288-311.

Yousefi, M., Milne, G.A. and Latychev, K., 2021. Glacial isostatic adjustment of the pacific coast of North America: The Influence of lateral earth structure. Geophysical Journal International, 226(1), p.91-113.

Zehfuss, P.H., 2005, Distal records of sandy Holocene lahars from Mount Rainier, Washington [Ph.D. thesis]: University of Washington, Seattle, 160 p.

Appendix 1. Supplement for Chapter 1

Table of Contents

A1.1. Sea-level predictions from published GIA models, including fit data from Puget Sound

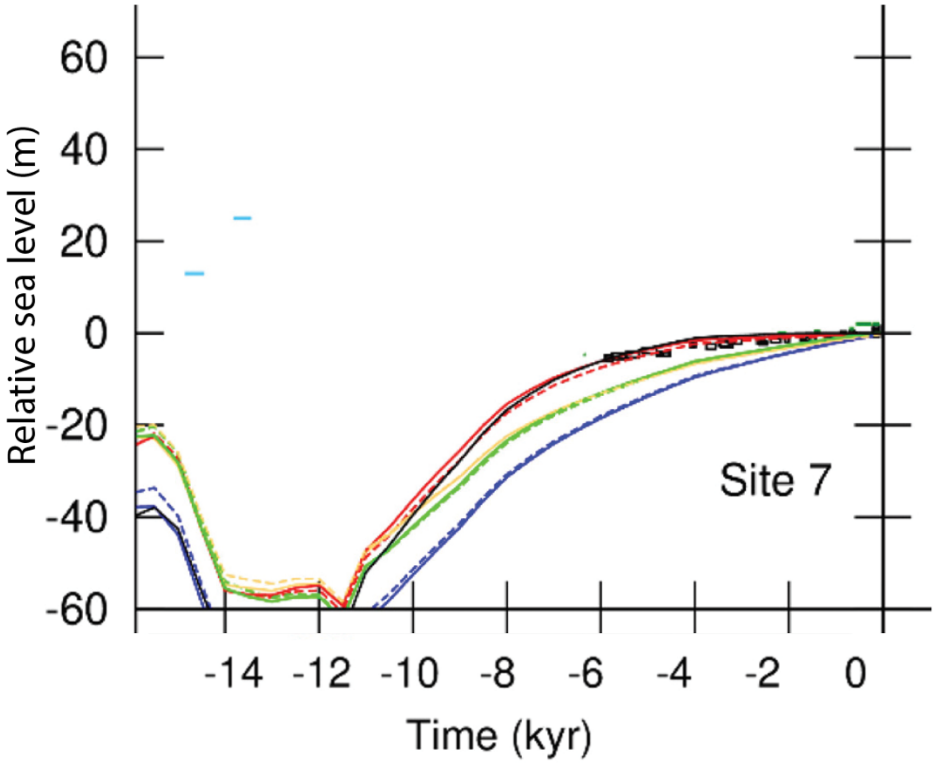

Figure A1.1. Sea-level predictions from published GIA models, including fit data from Puget Sound. This subplot ("Site 7", the Puget Sound region) is unmodified from Figure 9 of Yousefi et al. (2021). Long curves represent different GIA models that include various models of lateral earth viscosity. Short lines represent sea-level datapoints (Engelhardt et al., 2015). Unmodified from Yousefi et al. (2021).

A1.2. Histograms of pixel depths for mapped submerged terraces

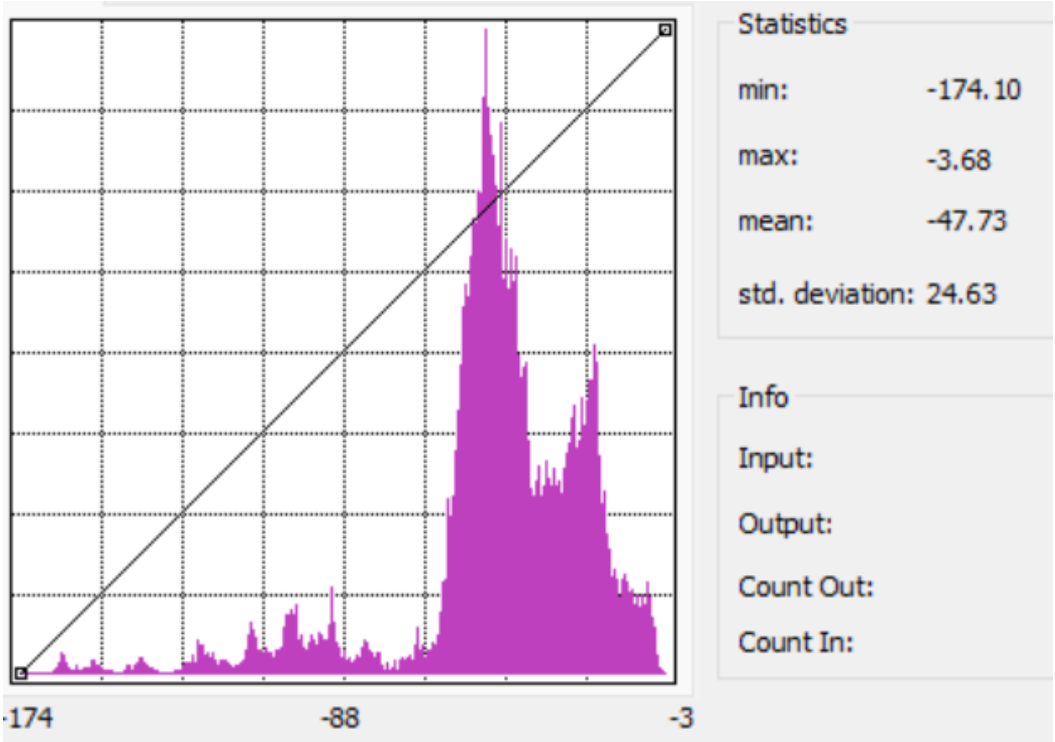

Figure A1.2. Histograms of pixel depths for mapped submerged terraces. Output window from ArcMap shows the number of pixels (y-axis) of various depths (x-axis) across mapped submerged terraces. Note that features mapped as submerged benches were located as deep as -174 m, but the majority of the benches are located above -66 m depth.

A1.3. Seismic reflection lines across terraces

2019 seismic survey

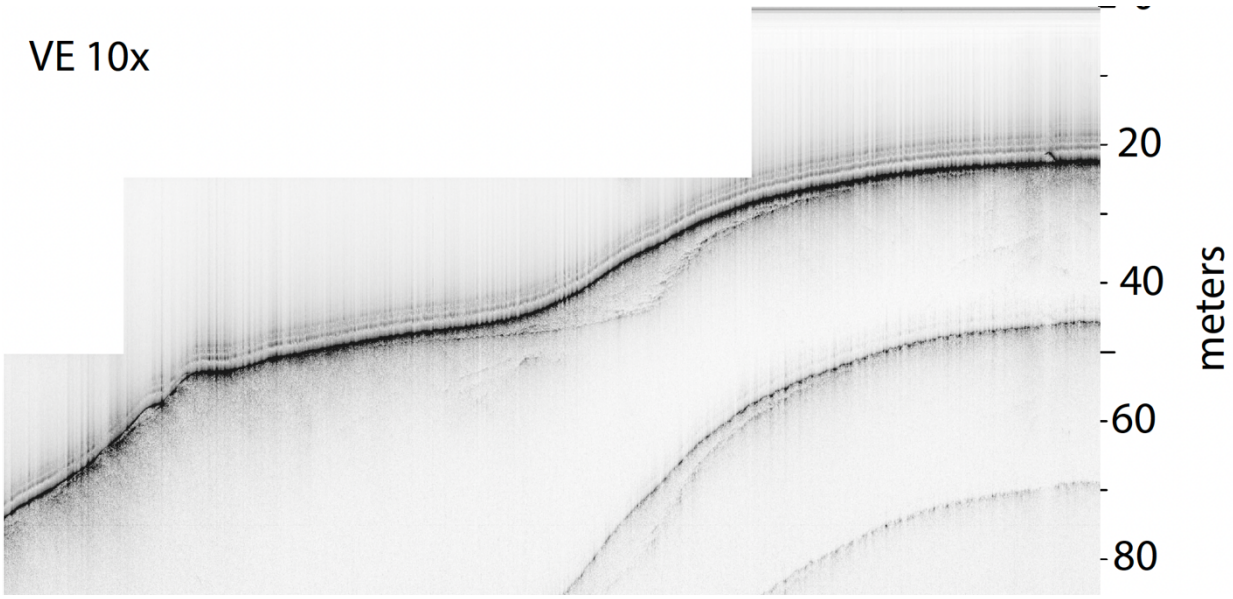

Figure A1.3.1. Line from 2019 seismic survey that crosses a submerged terrace. The location of this line is shown in the main text Figure 1.3.

Legacy non-digitized seismic line from R/V Onar seismic survey

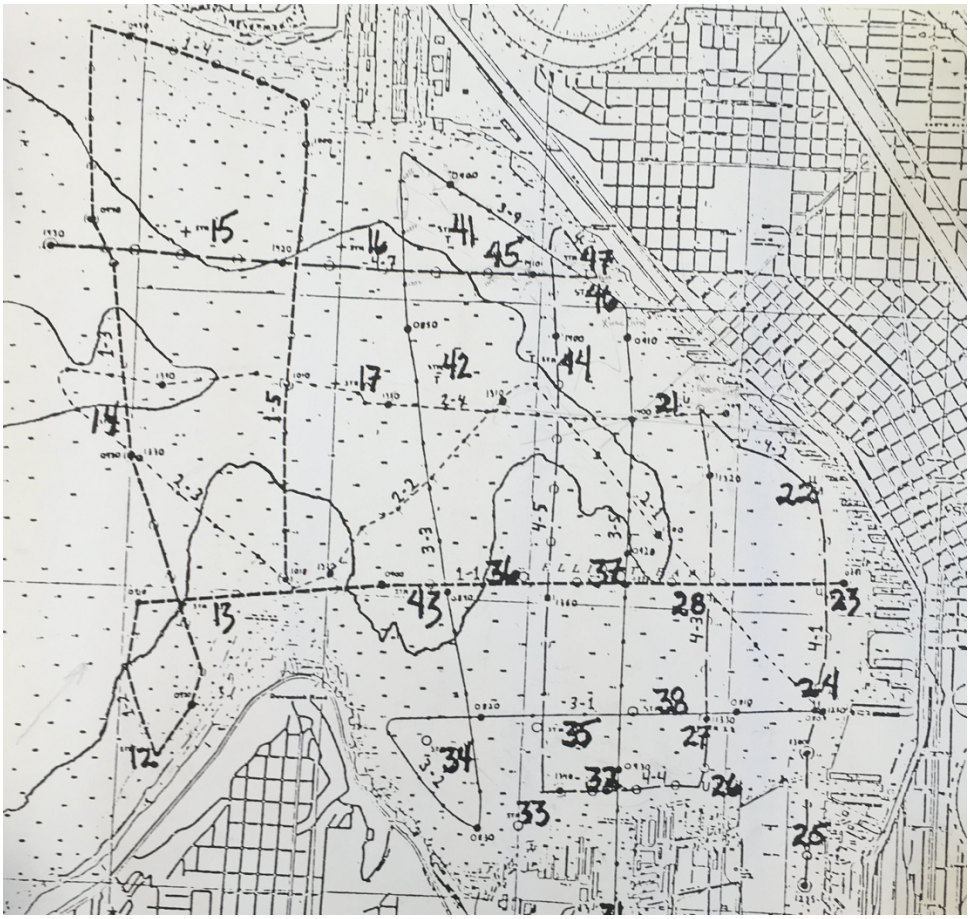

Figure A1.3.2. Location map showing line and point numbers from the survey by R/V Onar 1001 in April, 1982. This map is unmodified from the original. The perpendicular grid lines are streets in Seattle; heavy dotted and solid black lines represent tracklines locations (lines and shot points are numbered). These unpublished paper files are owned and stored by the UW Oceanography department.

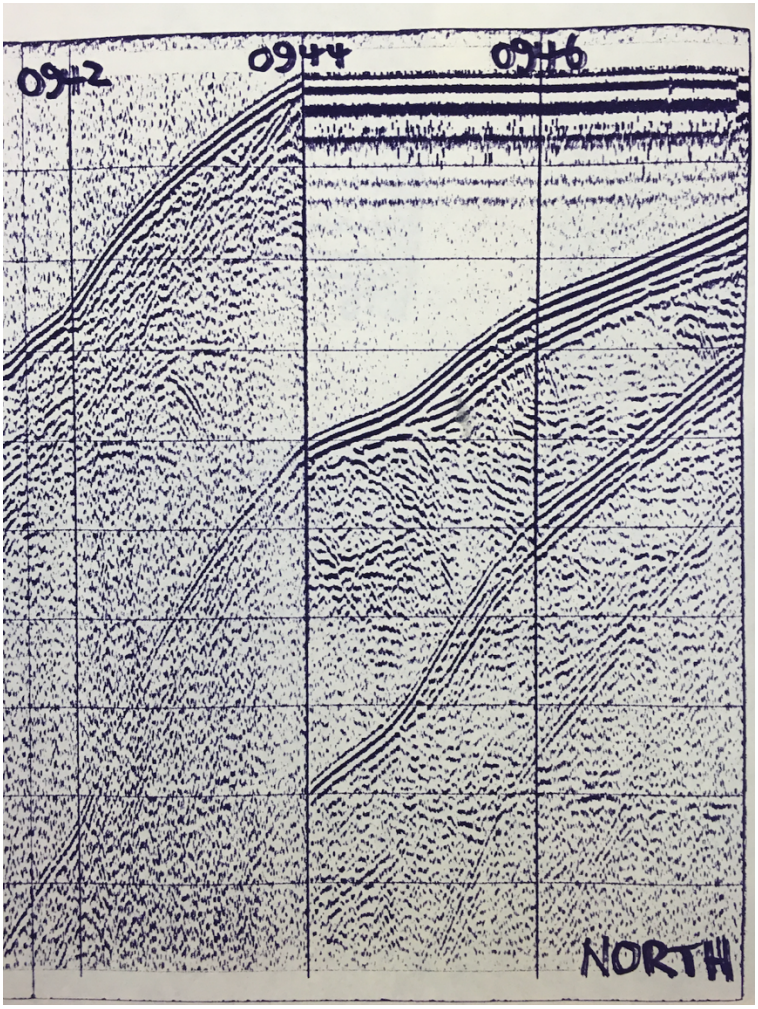

Figure A1.3.3. Line from the survey by R/V Onar 1001 in April, 1982 that crosses a submerged terrace offshore Magnolia. (Location shown in the Figure A1.3.1). These unpublished paper files are owned and stored by the UW Oceanography department.

A1.4. Formal error propagation

The uncertainty in the submerged shoreline angle depth (ε_d) includes the human error in determining ("picking") the location of the shoreline angle (ε_p), the error in the bathymetry (ε_b), and the error in the sediment cover thickness (ε_s):

$$\varepsilon_d = \sqrt{{\varepsilon_p}^2 + {\varepsilon_b}^2 + {\varepsilon_s}^2}$$

The uncertainty in difference in elevation between submerged shoreline angle depths and onshore uplifted terrace depths (ε_{diff}) includes all of the above and lidar error for the onshore datasets (ε_{ota}) described in Ota et al. (2006):

$$\varepsilon_{diff} = \sqrt{{\varepsilon_p}^2 + {\varepsilon_b}^2 + {\varepsilon_s}^2 + {\varepsilon_{ota}}^2}$$

Formal error propagation makes two assumptions that are not completely true in this case:

1. All error terms are independent. Bathymetry error (ε_b) and picking error (ε_p) are in theory not independent, but probably are effectively independent until bathymetric error gets large (>1m). To check this, I calculated correlation coefficient between picking error and bathymetry error for 154 picks; the result was -0.0311.
2. Errors are "small". Errors here are 1-10%.

A1.5. Interpolated elevations of emerged shorelines based on points measured by Ota et al. (2006)

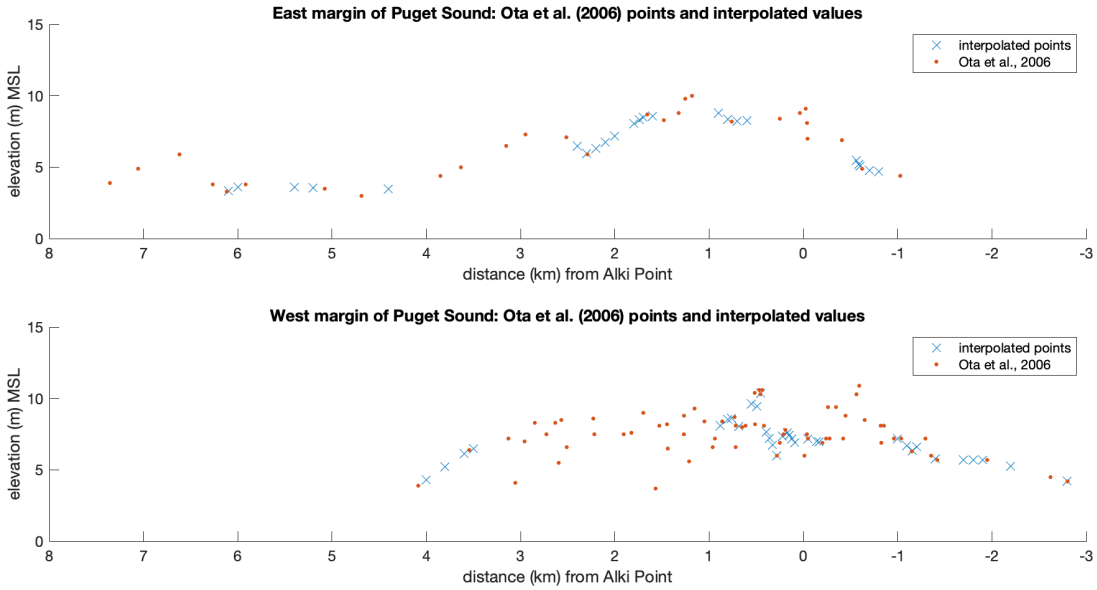

Figure A1.5. Interpolated elevations of emerged shorelines based on points measured by Ota et al. (2006). The emerged shorelines measured by Ota et al. (2006) are thought to represent the uplift that occurred in the Seattle fault earthquake 923–924 CE. Each interpolated point is the same distance from Alki Point (an approximately fault-parallel datum drawn between Alki Point and Restoration Point) as a measured profile on a submerged terrace. These interpolated points provide the offset values subtracted from the submerged terrace dataset.

A1.6. Linear models of glacial isostatic rebound

Equations

Table A1.6.1. A suite of linear models that fit points to the north of the SFZ were generated by Matlab, including Matlab's fit statistics. All lines generated are linear.

Fit lines generated by MATLAB			**Goodness of fit**						**Linear equation (slope-intercept form)**	
Conditions	**Data**	**Fit type**	**R-square**	**SSE**	**DFE**	**Adj R-sq**	**RMSE**	**# Coeff**	**m**	**b**
linear with normalized weights	e_fity vs. e_fitx with normweights	poly1	0.34552	1024	36	0.32734	5.3333	2	-0.3077	-53.34
linear no weights	e_fity vs. e_fitx	poly1	0.27842	454.75	36	0.25837	3.5541	2	-0.2718	-52.83
linear with weights for depth uncertainty	e_fity vs. e_fitx with e_weights	poly1	0.30902	69.24	36	0.28983	1.3868	2	-0.2853	-53.17
normweighted excluding one outlier near x = -10	e_fity vs. e_fitx with normweights	poly1	0.47223	505.17	35	0.45715	3.7991	2	-0.2824	-52.86
linear no weights excluding outlier x = -10	e_fity vs. e_fitx	poly1	0.39632	253.38	35	0.37907	2.6906	2	-0.2647	-52.37
midpoint of y weighted for depth exluding outlier x=-10	e_avg vs. e_fitx with e_weights	poly1	0.43308	36.43	35	0.41688	1.0202	2	-0.2708	-51.05
midpoint of y normweighted for depth excluding outlier x=-10	e_avg vs. e_fitx with normweights	poly1	0.47223	505.17	35	0.45715	3.7991	2	-0.2824	-51.36

Table A1.6.2. A suite of linear models that fit points to the north of the SFZ that I generated by hand.

Slope	Y-intercept (x = 0)	Comments
-0.29	-56	Eyeballed to catch the most points minus 2x Ota deformation
-0.4	-52.83	Eyeballed steepest line that fits the northern points
-0.25	-53	Eyeballed shallowest line that fits the northern points
-0.282	-54	Intervening lines
-0.282	-55	Intervening lines
-0.3	-54	Intervening lines
-0.3	-55	Intervening lines
-0.25	-55	Intervening lines
-0.22	-56.5	Lowest line
-0.3	-51	Highest line to fit high data on west margin of Puget Sound

Plotted with data

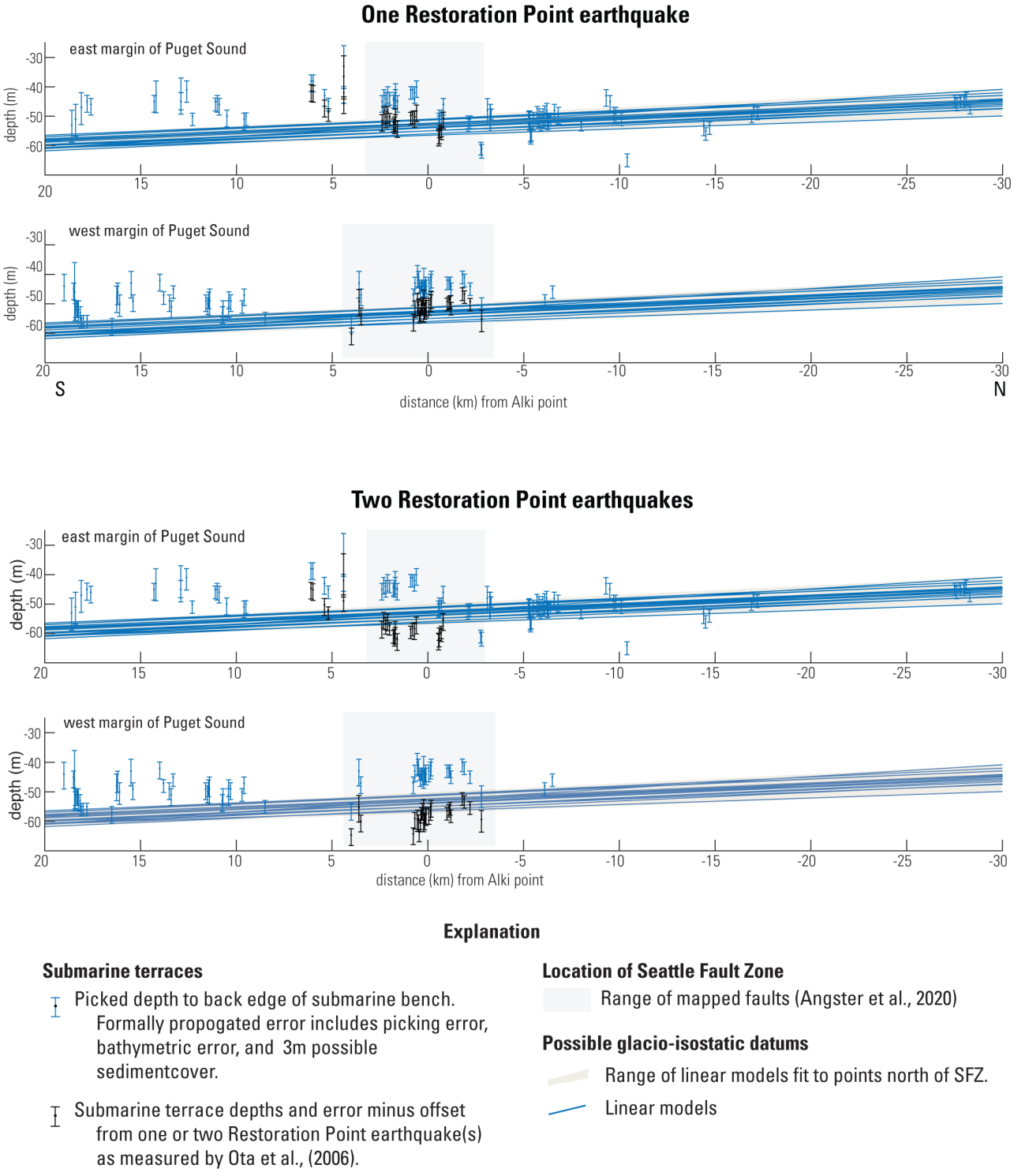

Figure A1.6. Linear models of isostatic rebound ("possible glacio-isostatic datums") plotted with data.

Appendix 2. Supplement for Chapter 2

Table of Contents

A2.1. Supplemental site information

A2.1.1. KS

Composite diagram showing stratigraphy and chronology at KS

KS – Sand repeatedly deposited about 1041–1260 cal yr C.E., probably by river.
Pasture soil buried c. 1914 C.E..

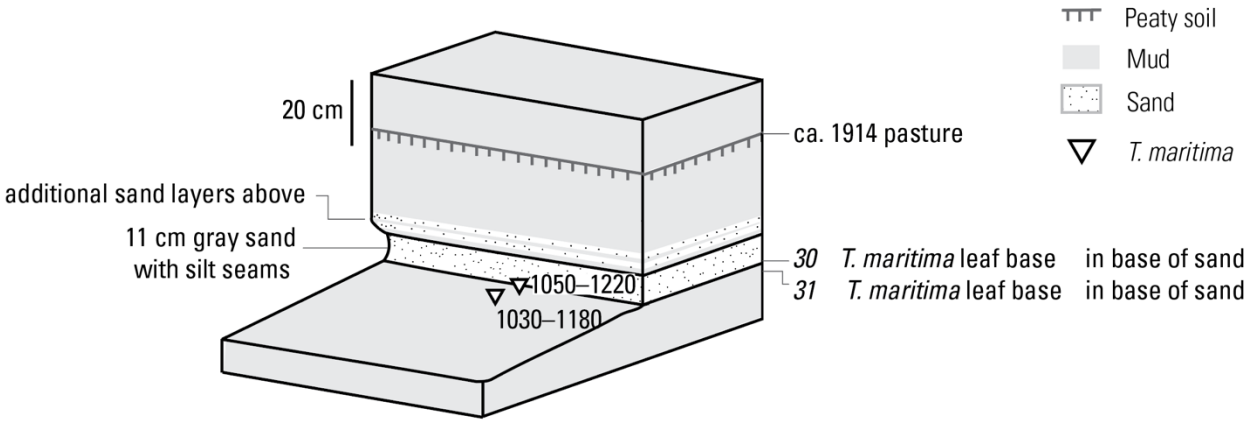

Figure A2.1.1. Composite diagram at site KS showing stratigraphy and chronology.

Photos and radiocarbon samples at KS

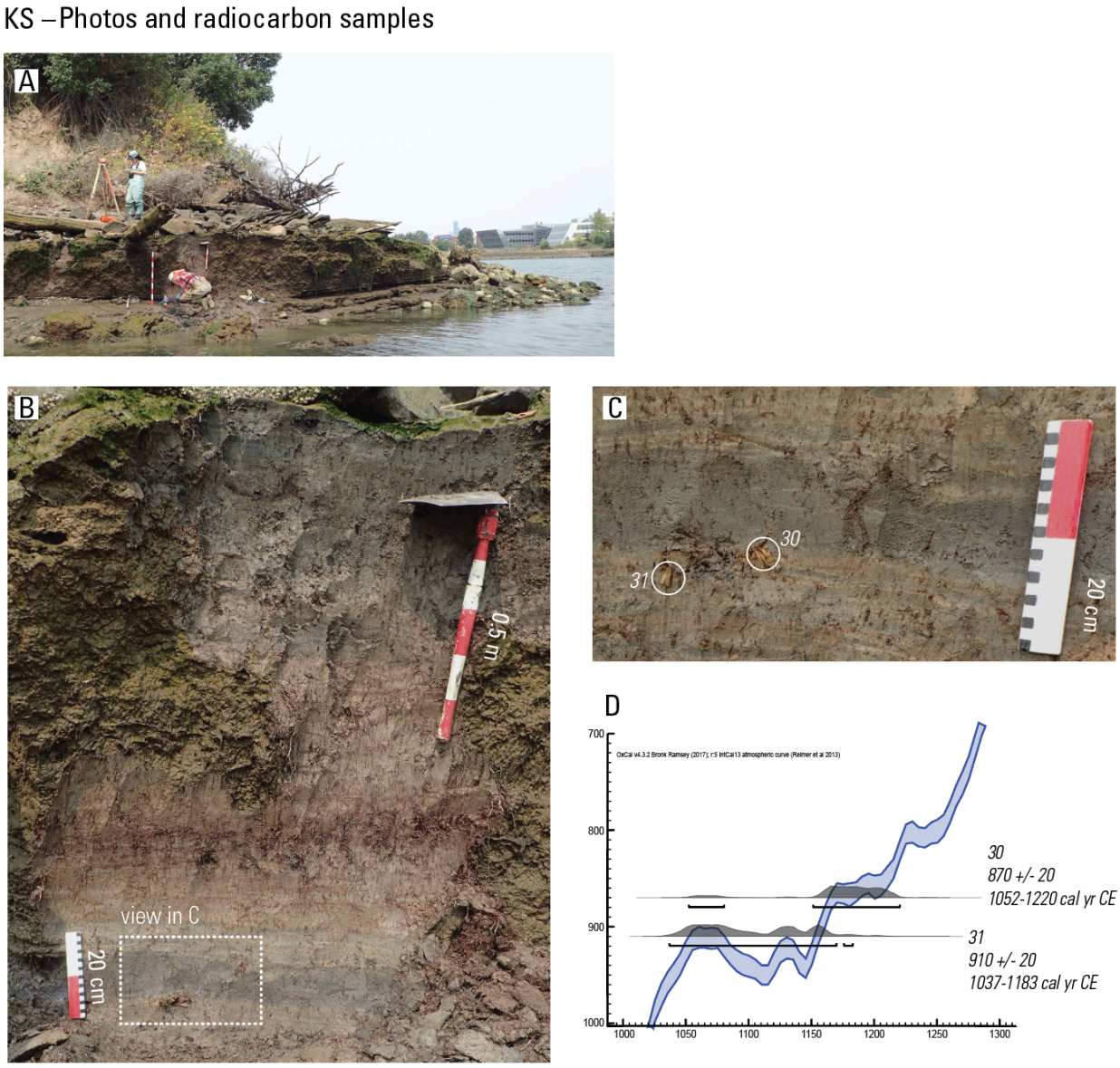

Figure A2.1.2. Photos and radiocarbon samples at KS. (A) Site overview photo. (B) Cleaned outcrop showing stratified mud and sand. (C) Photo showing *T. maritima* samples 30 and 31 below and at the base of a thick layer of stratified sand. (D) Oxcal output showing sample ages plotted on the radiocarbon calibration curve. The x-axis is the age in calibrated years CE; the y-axis is age in radiocarbon years.

A2.1.2 SN

Composite diagram showing stratigraphy and chronology at SN

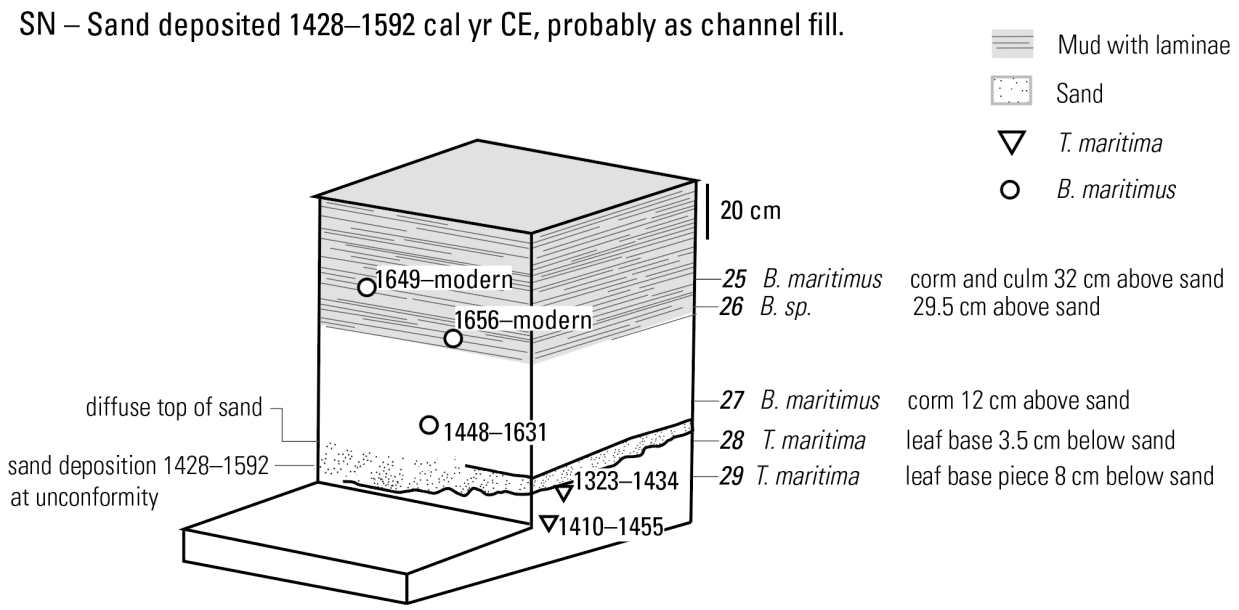

Figure A2.1.3. Composite diagram showing stratigraphy and chronology at site SN.

Photos at SN

Figure A2.1.4. Photos at site SN. (A) View of uncleaned outcrop, looking south. (B) Cleaned outcrop showing sand layer (dark gray) amongst mud and locations of radiocarbon samples (orange flags), not all of which were submitted for analysis. (C) Close-up of sand layer with clear lower contact and diffuse top. This layer might represent a channel fill rather than a layer of vented sand.

Oxcal sequence at SN

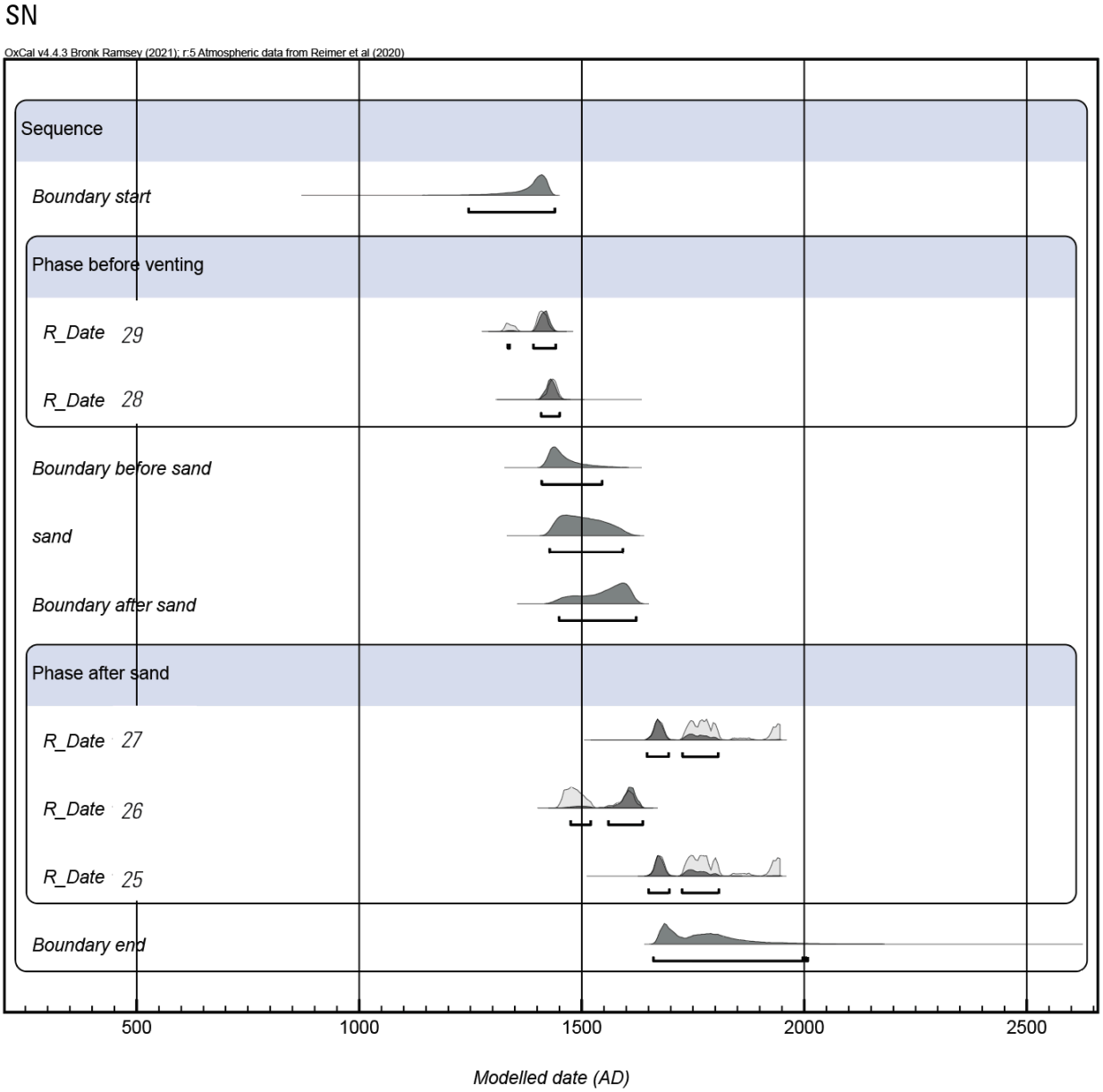

Figure A2.1.5. Oxcal sequence at site SN. Samples are labeled by number.

Photos at SS

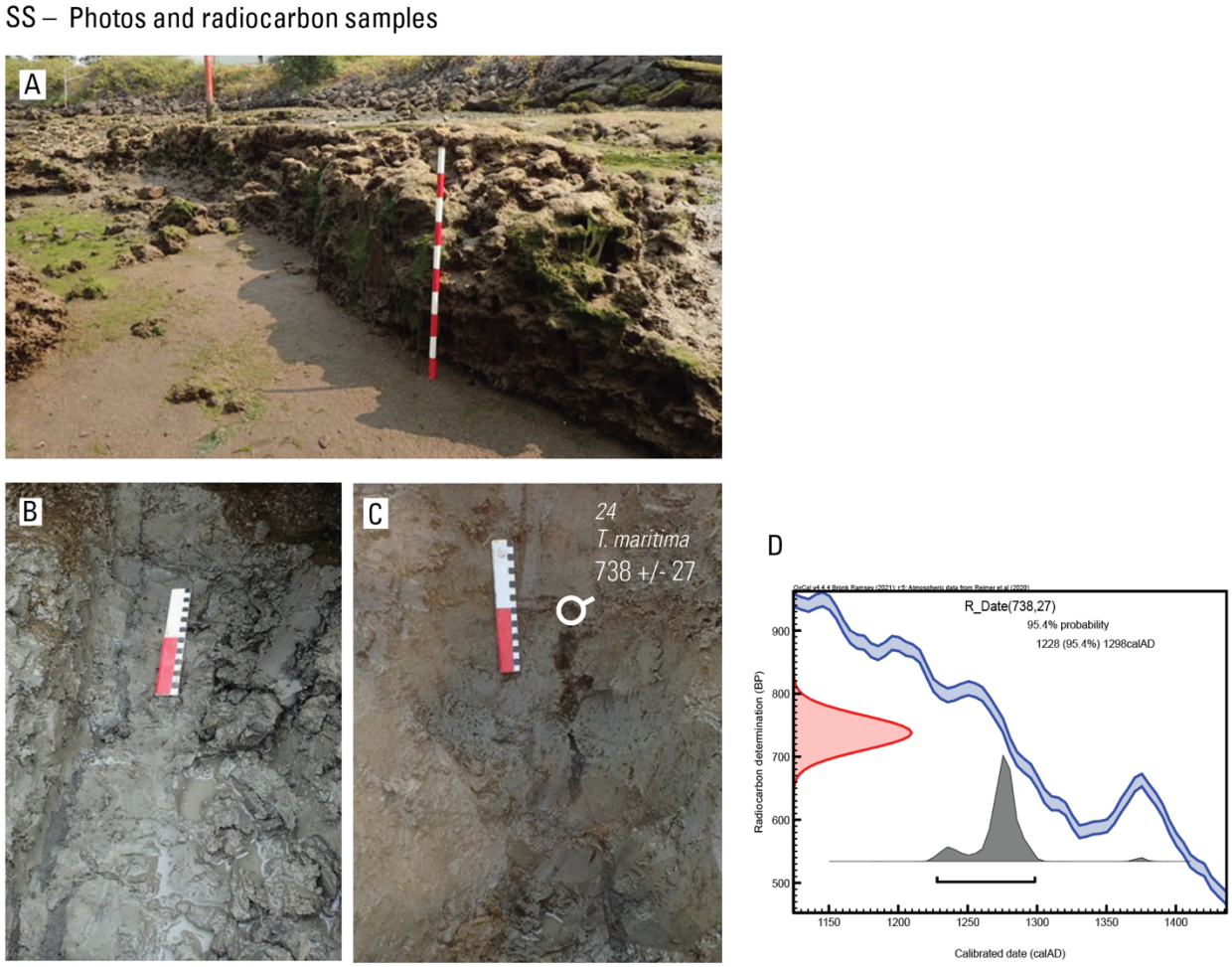

Figure A2.1.6. Photos at site SS. (A) View of uncleaned outcrop, looking north. The stick is 1 m long. (B) Photo looking down at dike (dark gray sand) crossing gray mud. The dike crosses vertically through the photo. The red and white scale is 20 cm long. (C) Photo looking at the outcrop; the dike climbs upward and crosses strata bearing radiocarbon sample 24 (white circle). The red and white scale is 20 cm long. (D) Oxcal output showing calibrated radiocarbon age for sample 24, plotted against the calibration curve.

A2.1.4 KC – 14C calibration

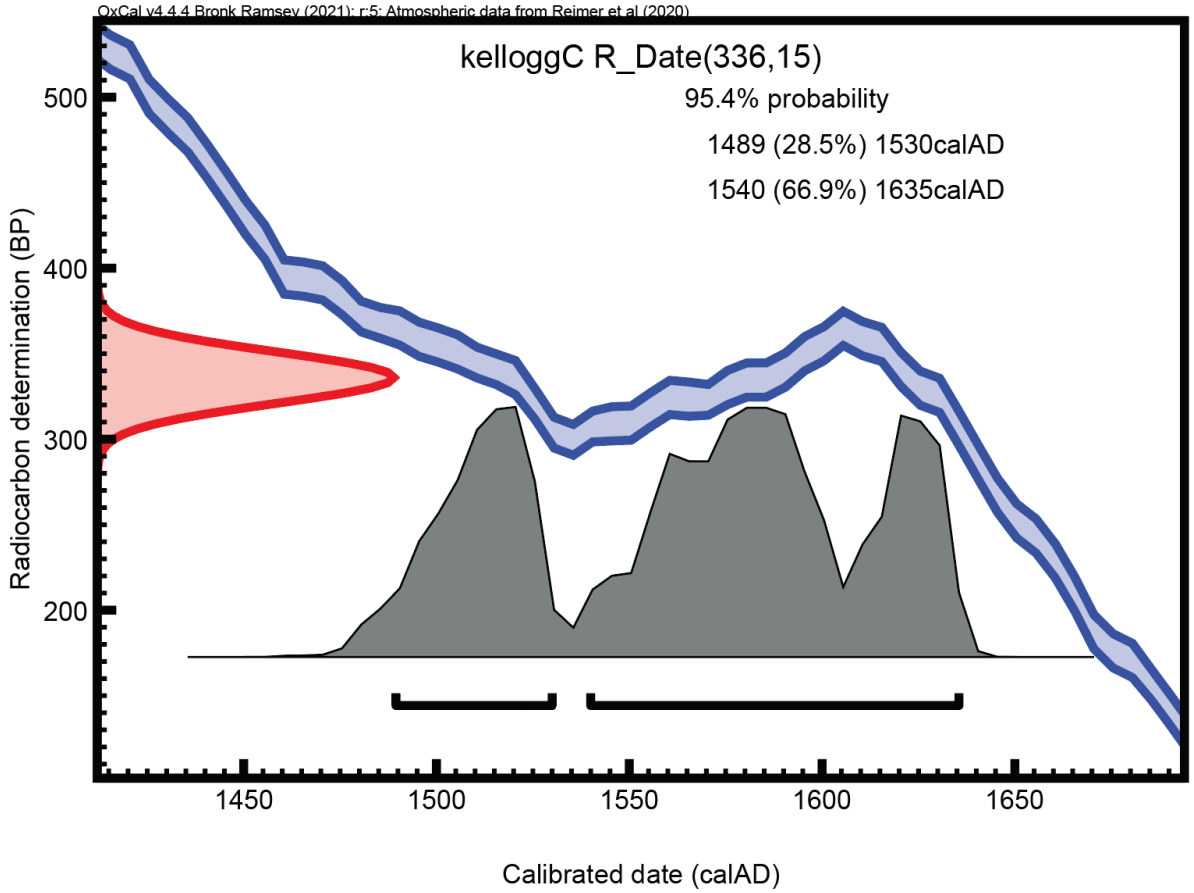

Figure A2.1.7. Oxcal output of radiocarbon calibration for the radiocarbon sample collected at site KC.

A2.1.5 KN – 14C sample photos

KN Photos and 14C samples

Figure A2.1.8. Photo of cleaned outcrop at KN showing a dike (dark gray sand) crossing laminated gray mud and location of radiocarbon samples. The sample numbers, ages, and calibrated ages are plotted on the photo.

A2.2 Alternate age calibrations for time of venting (constrained by three *T. maritima*) at Federal Center

I tested multiple methods for calibrating the 14C ages pertaining to the timing of sand venting at Federal Center. All methods return very similar age ranges. As described in the text, the vented sands drape several *in-situ* leaf bases of *T. maritima,* three of which were collected for 14C dating (Table 2.1.1). The *T. maritima* do not extend above the vented sand and likely died during the time of venting. Therefore, the age of these plants is representative of the timing of the earthquake. The following sections describe various methods for assessing the age of the *T. maritima* given their 14C ages.

Table A2.2.1. Radiocarbon samples used in this analysis.

Sample Number	**14C age**	**14C error with added variance**
106-31	1014	27
106-26A	994	27
106-29	951	30

Table A2.2.2 Age ranges for venting output by each of the methods tested. Age ranges are rounded to the nearest five years.

Method used	**95% confidence interval age range for time of venting (cal yr CE)**
2.1.1 Manual averaging replicate measurements	995–1160
2.1.2 Oxcal "combine" function (PREFERRED)	995–1150
2.1.3 Oxcal sequence with one overlying age	990–1120
2.1.4 Oxcal sequence with all nearby ages	995–1125

A2.2.1 Manually averaging replicate measurements

The three *T. maritima* leaf bases ought to be the same age, so it is reasonable to treat them as replicates of a single 14C sample. For this reason, a sum-of-squares method can be used to reduce the uncertainties of the radiocarbon determination. I used the sum-of-squares calculation presented by Scott et al. (2007) (pg. 340).

The results of this calculation are:
Combined mean (X) = 986
Standard deviation (s) = 32
Standard error of the mean (SEM) = 18.6
95% Confidence Interval Standard error of the mean = 37

Therefore, the combined 14C age is 986 +/- 37.
Calibrating in Oxcal gives the output age range of 995–1160 cal yr CE, after rounding to the nearest half-decade (Figure A2.1.1).

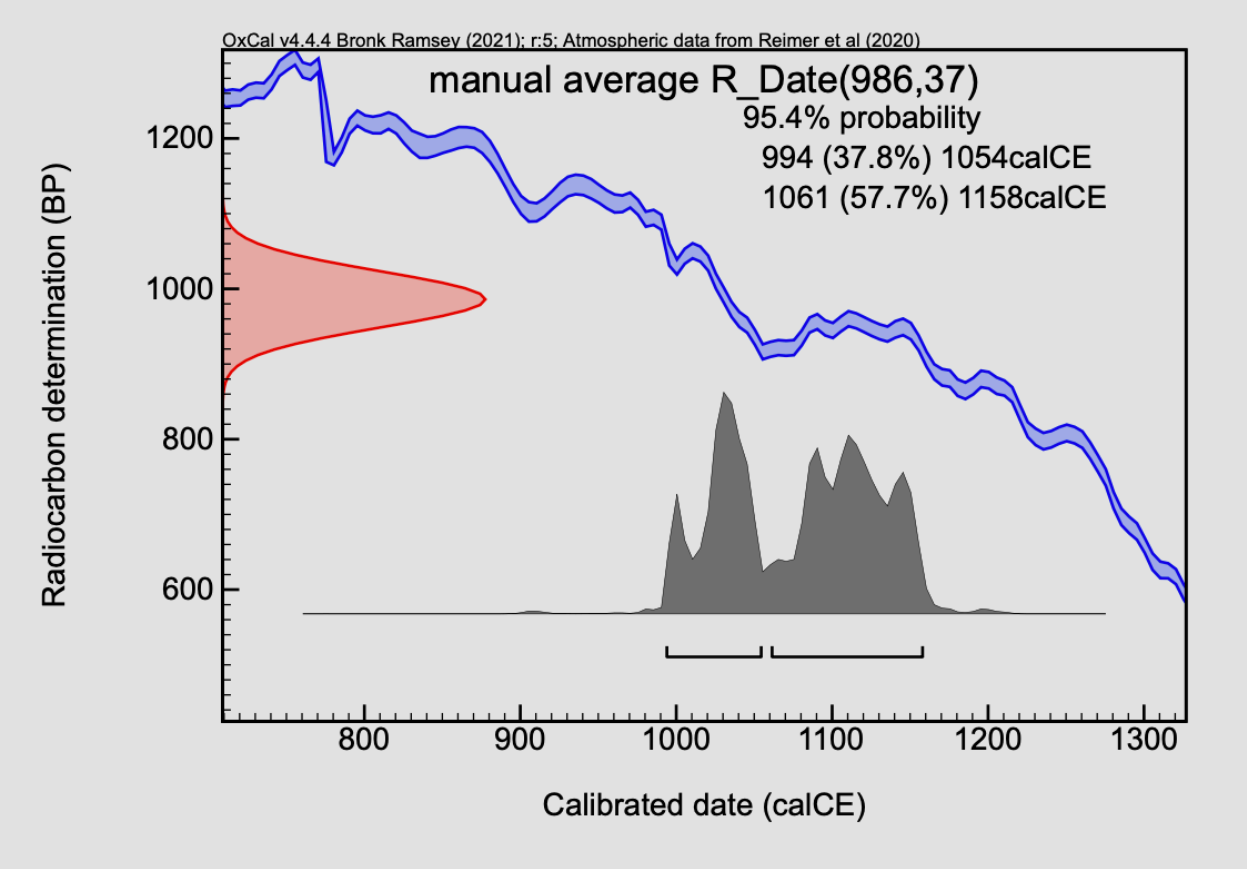

Figure A2.2.1. Oxcal output of manually averaged date.

A2.2.2 Oxcal "combine" function (PREFERRED)

Oxcal's "combine" function is another method to treat multiple samples as replicate samples. The output of this calibration (Fig. 2.1.2) gives an age range of 995–1150 cal yr CE.

Oxcal code for "combine" function

```
R_Combine("t_mound")
{
 R_Date("106-31", 1014, 27);
 R_Date("106-26A", 994, 27);
 R_Date("106-29", 951, 30);
};
```

Oxcal output for "combine" function

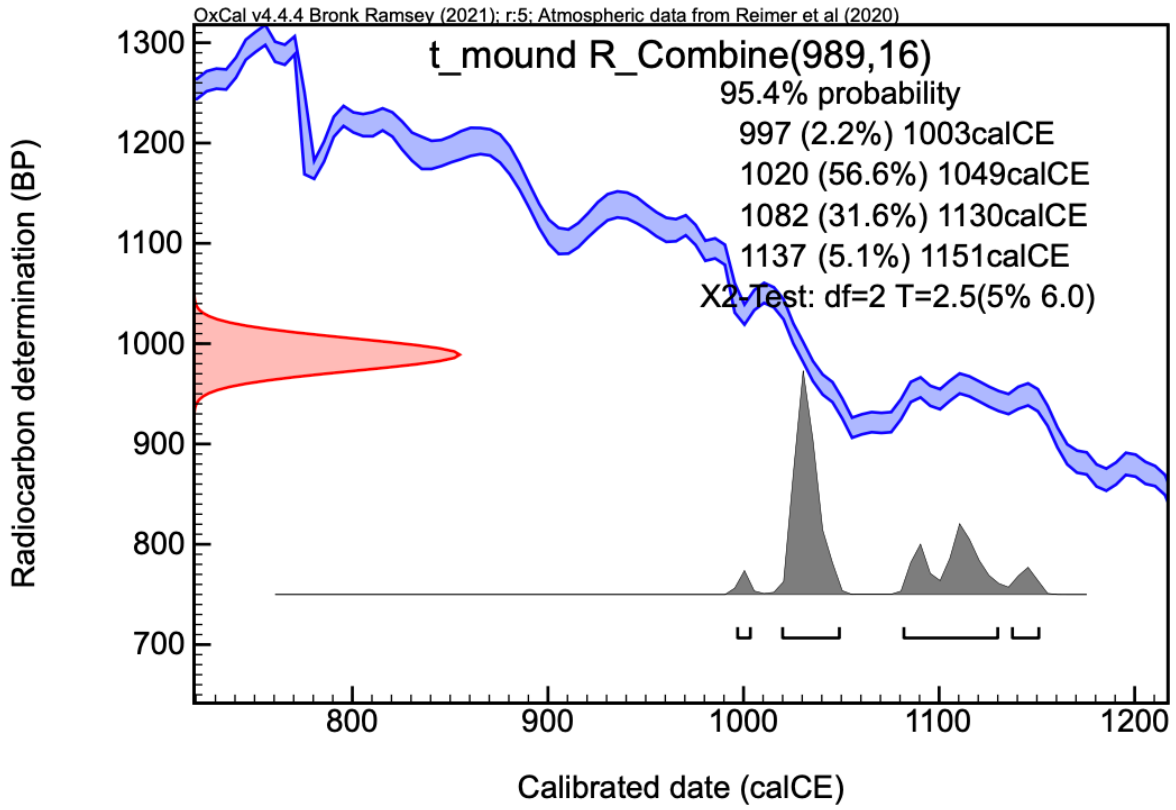

Figure A2.2.2. Oxcal output for combined age of three *T. maritima.*

A2.2.3 Oxcal sequence with one overlying age

Adding the closest overlying age restricts the minimum age of the possible venting to 990–1120.

Oxcal code (sequence with one overlying age)

```
Sequence()
{
 Boundary();
 R_Combine("t_mound")
 {
  R_Date("106-31", 1014, 27);
  R_Date("106-26A", 994, 27);
  R_Date("106-29", 951, 30);
 };
 R_Date("180716-6", 1018, 28);
 Boundary();
};
```

Oxcal sequence graphic (sequence with one overlying age)

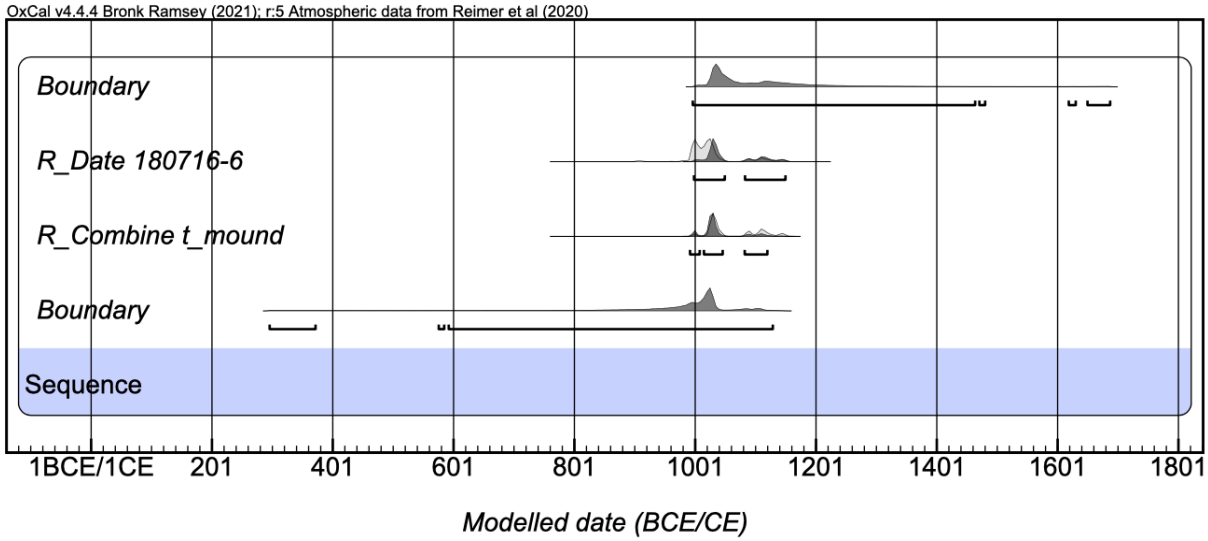

Figure A2.2.3. Oxcal sequence graphic for a sequence at site FC using the three *T. maritma* and the one close overlying age.

Oxcal output table (sequence with one overlying age)

Name		Unmodelled (BCE/CE)		Modelled (BCE/CE)		Indices A_{model}=76.7 $A_{overall}$=80.3					Controls		
		from_95.4	to_95.4	from_95.4	to_95.4	A_{comb}	A	L	P	C	Select	Page	Edit
Boundary				996	1689					98.6	6		
R_Date 180716-6		987	1150	998	1150		65.8			99.8	5		
R_Combine t_mound		997	1151	992	1120		111.5			99.8	4		
Boundary				293	1137					97.7	3		
▲ Sequence											2		

Figure A2.2.4. Oxcal output table for a sequence at site FC using the three *T. maritima* and the one close overlying age.

A2.2.4 Oxcal sequence with all surrounding ages

This sequence is described in the text and forms the basis for other reported ages.

Oxcal code (sequence with all surrounding ages)

```
Plot()
 {
  Sequence()
  {
   Boundary("start");
   Phase("T. maritima under DW-B")
   {
    R_Date("20",1014,27);
    R_Date("19",994,27);
    R_Date("16",951,30);
    Date("DW-B venting",,);
   };
   Phase("B. maritima after DW-B")
   {
    R_Date("21",1018,28);
    R_Date("17",962,26);
   };
   Date("LZ, max for DW-C1",,);
   Boundary("after LZ");
   Phase("after LZ")
   {
    R_Date("11",889,28);
    R_Date("15",936,26);
   };
   Date("LL",,);
   R_Date("10",613,40);
   R_Date("8",571,27);
   R_Date("7",554,29);
   Date("UZ",);
   R_Date("5",508,26);
   R_Date("4",440,26);
   R_Date("3",391,26);
   Date("brighter lamina 2",);
   R_Date("1",332,27);
   R_Date("2",356,29);
   Date("brighter lamina",);
   C_Date("pasture",1914,20);
   Boundary("end");
  }; };
```

Oxcal output graphic (sequence with all surrounding ages)

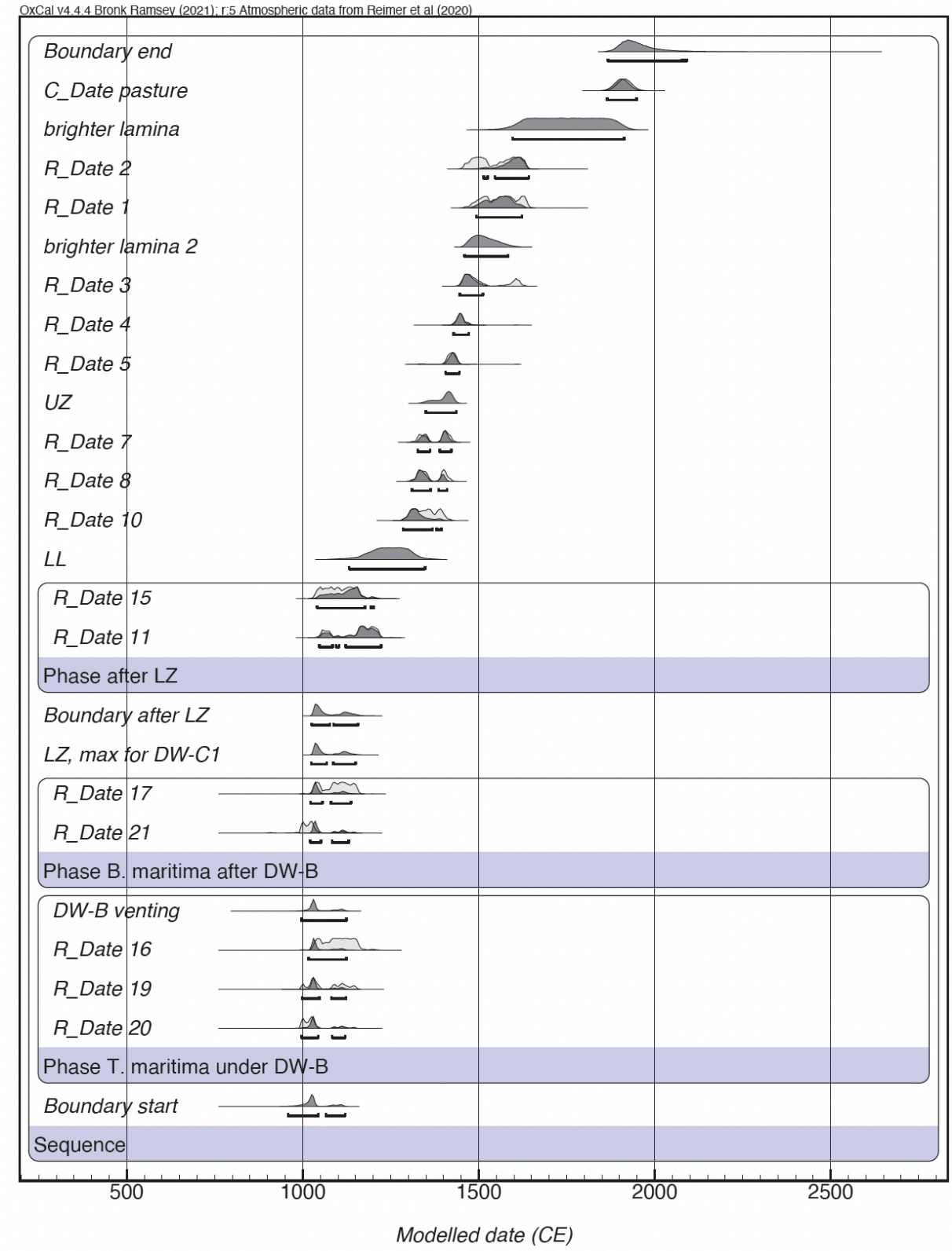

Figure A2.2.5. Oxcal sequence graphic for a sequence at site FC using all nearby radiocarbon ages.

Oxcal output table (sequence with all surrounding ages)

Name		Unmodelled (BCE/CE)		Modelled (BCE/CE)		Indices A_{model}=91.6 $A_{overall}$=95.8					Controls		
		from_95.4	to_95.4	from_95.4	to_95.4	A_{comb}	A	L	P	C	Select	Page	Edit
		Warning! Duplicate names - after LZ											
Boundary end				1867	2090					97.8	30		
C_Date pasture		1874	1954	1864	1948		96.1			99.6	29		
brighter lamina				1596	1913					99.6	28		
R_Date 2		1457	1635	1514	1642		101.8			99.8	27		
R_Date 1		1481	1639	1493	1623		105			99.8	26		
brighter lamina 2				1459	1583					99.9	25		
R_Date 3		1444	1624	1446	1511		122.9			99.9	24		
R_Date 4		1422	1480	1428	1471		110.3			100	23		
R_Date 5		1400	1445	1405	1445		102.8			99.9	22		
UZ				1349	1436					99.9	21		
R_Date 7		1318	1431	1326	1422		103.1			99.6	20		
R_Date 8		1310	1422	1310	1410		105.2			99.8	19		
R_Date 10		1293	1408	1285	1394		102.4			99.8	18		
LL				1131	1347					99.9	17		
R_Date 15		1031	1168	1041	1201		97.3			99.2	16		
R_Date 11		1045	1223	1047	1222		101.9			99.6	15		
▲ Phase after LZ											14		
Boundary after LZ				1025	1157					98.7	13		
LZ, max for DW-C1				1024	1150					98.9	12		
R_Date 17		1026	1158	1022	1137		105.1			99.2	11		
R_Date 21		987	1150	1021	1130		47.3			99.3	10		
				Warning! Poor agreement - A= 48.8%(A'c= 60.0%)									
▲ Phase B. maritima after DW-B											9		
DW-B venting				994	1124					98.5	8		
R_Date 16		1028	1162	1016	1124		73.3			98.6	7		
R_Date 19		993	1154	998	1121		145.7			98.9	6		
R_Date 20		990	1150	996	1120		102.2			98.5	5		
▲ Phase T. maritima under DW-B											4		
Boundary start				960	1120					95.7	3		
▲ Sequence											2		

Figure A2.2.6. Oxcal output table for a sequence at site FC using all nearby radiocarbon ages.

A2.3 Oxcal code for other age models

Site SN

```
Plot()
{
 Sequence()
 {
  Boundary("start");
  Phase("before venting")
  {
   R_Date("180626-10", 542, 27);
   R_Date("180626-12A", 476, 26);
  };
  Boundary("before sand");
  Date("sand");
  Boundary("after sand");
  Phase("after sand")
  {
   R_Date("180626-6", 190, 27);
   R_Date("180626-7", 380, 26);
   R_Date("180626-14", 183, 26);
  };
  Boundary("end");
 };
};
```

A2.4 References used in this supplement

Scott, E.M., Cook, G.T. and Naysmith, P., 2007. Error and uncertainty in radiocarbon measurements. Radiocarbon, 49(2), pp.427-440.

Appendix 3. Supplement for Chapter 3

Table of Contents

A3.1 Equations for adding variance to 14C samples measured at NOSAMS

Each ^{14}C age includes errors to account for variations that occur during ^{14}C measurements. Lab-reported errors estimate the reproducibility of a repeat measurements of a single sample; "added variance," described below, estimates reproducibility of replicate samples, including uncertainty introduced in collection or processing (Luk, 2020).

Added variance modifies the reported error for a sample. For a modern sample, the added variance calculated for NOSAMS for the years 2015 and 2016 was 2.6 per mille (Mark Roberts, pers comm, 2019). This value was used to inform the following equations for added variance error, where *Fmodern* and *Fme* are lab-reported values and Added Variance Error is the updated calculated error for a given age.

$$(1) \qquad Added\ variance = Fmodern * 0.0026$$

$$(2) \qquad Total\ error = \sqrt{(Fme^2 + Added\ variance^2)}$$

$$(3) \qquad Added\ Variance\ Error = \frac{8033 * Total\ error}{Fmodern}$$

A3.2 Results of t-test hypothesis testing in Microsoft Excel

I used hypothesis testing (t-test) to evaluate whether there was a difference between the top of the modern beachface (*tb*) and the top of terrace-forming strata (*tt*). Each dataset contains 73 observations. The results show that the means of these two distributions differ statistically by 0.8 m, but not by 0.9 m. I measured the top of the modern beachface in the field (mostly summertime) and from LiDAR (collected at a single point in time in 2018), so these measurements do not represent the full variability of the modern beachface. Future work should aim to more fully characterize the elevation of the modern beachface to re-evaluate whether it is lower than the paleo-beachface (terrace-forming strata).

Table A3.2.1. Output of Microsoft Excel t-test (two-sample assuming unequal variances, 2 tail) testing whether the means of tt and tb are statistically the same. The result is that these two distributions are statistically different.

Are the means equal? (2 tail test)	p<<0.05; t>tcrit	Result: Reject null hypothesis, means of tt and tb are not the same.
t-Test: Two-Sample Assuming Unequal Variances		
	tt (m NAVD88)	*tb (m NAVD88)*
Mean	5.229613447	4.11934113
Variance	0.906684927	0.368713614
Observations	73	73
Hypothesized Mean Difference	0	
df	122	
t Stat	8.399781393	
P(T<=t) one-tail	4.77435E-14	
t Critical one-tail	1.657439499	
P(T<=t) two-tail	9.54869E-14	
t Critical two-tail	1.979599878	

Table A3.2.2. Output of Microsoft Excel t-test (two-sample assuming unequal variances, 1 tail) testing whether tt and tb are statistically different by 0.5 m. The result is that these two distributions are statistically different by 0.5 m.

Are the means different by 0.5m? (1 tail)	p<<0.05, t>tcrit	Result: Reject null hypothesis, means of tt differ more than 0.5 from tb.
t-Test: Two-Sample Assuming Unequal Variances		
	tt (m NAVD88)	*tb (m NAVD88)*
Mean	5.229613447	4.11934113
Variance	0.906684927	0.368713614
Observations	73	73
Hypothesized Mean Difference	0.5	
df	122	
t Stat	4.617024107	
P(T<=t) one-tail	4.85592E-06	
t Critical one-tail	1.657439499	
P(T<=t) two-tail	9.71184E-06	
t Critical two-tail	1.979599878	

Table A3.2.3. Output of Microsoft Excel t-test (two-sample assuming unequal variances, 1 tail) testing whether tt and tb are statistically different by 0.8 m. The result is that these two distributions are statistically different by 0.8 m.

Are means different by 0.8m? (1 tail)	p<0.05, t>tcrit	Result: Reject null hypothesis: the means of tt and tb vary by more than 0.8 m
t-Test: Two-Sample Assuming Unequal Variances		
	tt (m NAVD88)	*tb (m NAVD88)*
Mean	5.229613447	4.11934113
Variance	0.906684927	0.368713614
Observations	73	73
Hypothesized Mean Difference	0.8	
df	122	
t Stat	2.347369735	
P(T<=t) one-tail	0.010258416	
t Critical one-tail	1.657439499	
P(T<=t) two-tail	0.020516831	
t Critical two-tail	1.979599878	

Table A3.2.4. Output of Microsoft Excel t-test (two-sample assuming unequal variances, 1 tail) testing whether tt and tb are statistically different by 0.9 m. The result is that these two distributions are not statistically different by 0.9 m.

Are means different by 0.9m? (1 tail)	p>0.05	NULL HYPOTHESIS - The means of tt and tb are not distinguishable by 0.9 m
t-Test: Two-Sample Assuming Unequal Variances		
	tt (m NAVD88)	*tb (m NAVD88)*
Mean	5.229613447	4.11934113
Variance	0.906684927	0.368713614
Observations	73	73
Hypothesized Mean Difference	0.9	
df	122	
t Stat	1.590818278	
P(T<=t) one-tail	0.057119224	
t Critical one-tail	1.657439499	
P(T<=t) two-tail	0.114238449	
t Critical two-tail	1.979599878	

A3.3 Table showing results for age calibration of >modern 14C samples

Field ID	Lab ID	Lab-reported age	Fmodern (reported)	fm err (reported)	Added variance (for modern sample, 0.0026)	Total error	Age (with added variance)	Error (with added variance)	Calibrated age, 95% CI (cal yr CE)
ED-R230525	OS-176403	>modern	1.0131	0.0020	0.0026	0.0033	-105	26	1955 or 2016–2019
ED-R2305-1	OS-176402	>modern	1.0351	0.0019	0.0027	0.0033	-277	26	1956 or 2011–2014

A3.4 Possible antiform in wave-cut platform(s) 0.8 km to the north of Rialto Beach

Evidence for a possible antiform consists of a symmetrical fall in elevation on the surface of a probable wave-cut platform (Figure A3.4.1). The fall in elevation can be seen in the surface to the north and south of the plotted symbol. This feature has not been field-checked; it could also represent a zone of more-resistant rock within the wavecut platform or an accumulation of sediment in this location at the time of the LiDAR flight. It is the only such symmetrical feature I noted in the nearshore LiDAR between Rialto Beach and Wa'atch.

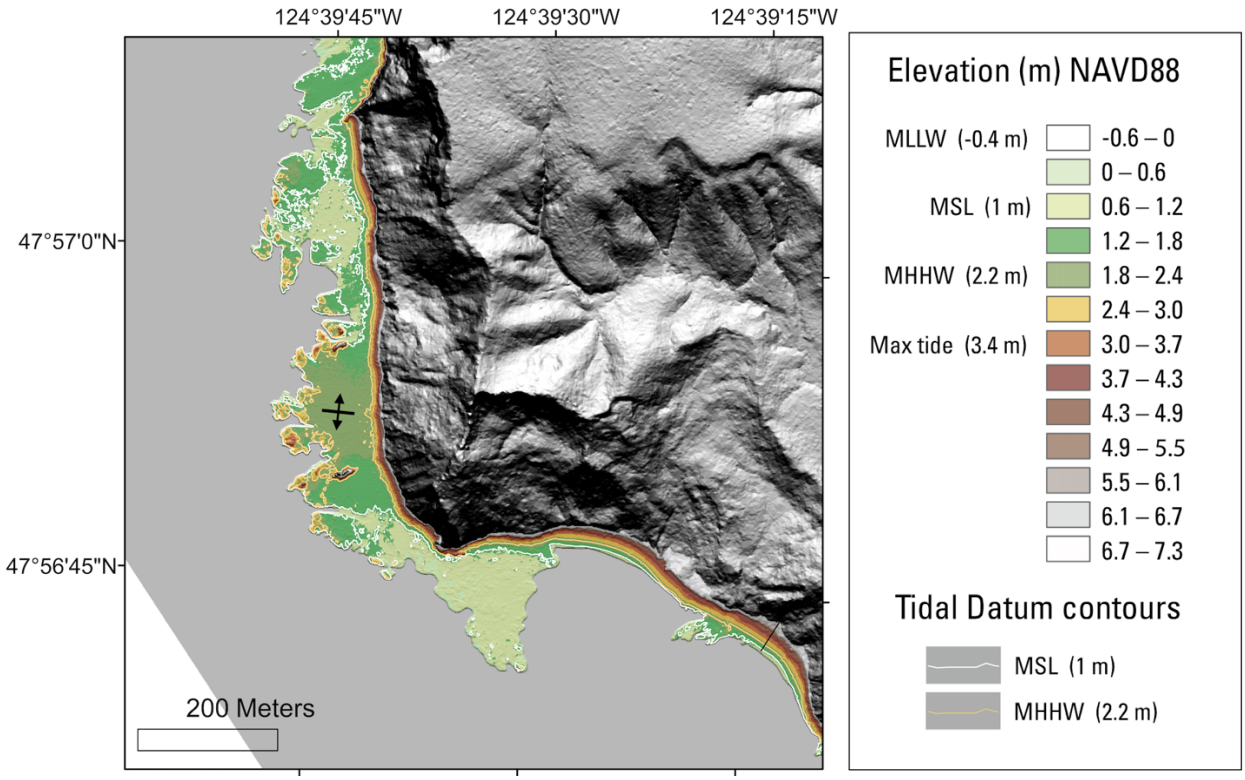

Figure A3.4.1. Map of slope and wave-cut platform(s) 0.8 km to the north of Rialto Beach, showing the location of the possible antiform. The trend of the possible antiform is annotated.